AD-A168 002 DEVELOPMENT OF FRACTURE MECHANICS MAPS FOR COMPOSITE MATERIALS VOLUME 1(U) DEUTSCHE FORSCHUNGS- UND VERSUCHSANSTALT FUER LUFT- UND RAUMF.. H W BERGMANN 1/3

UNCLASSIFIED DEC 85 AFWAL-TR-85-4150-VOL-1 F/G 11/4 NL

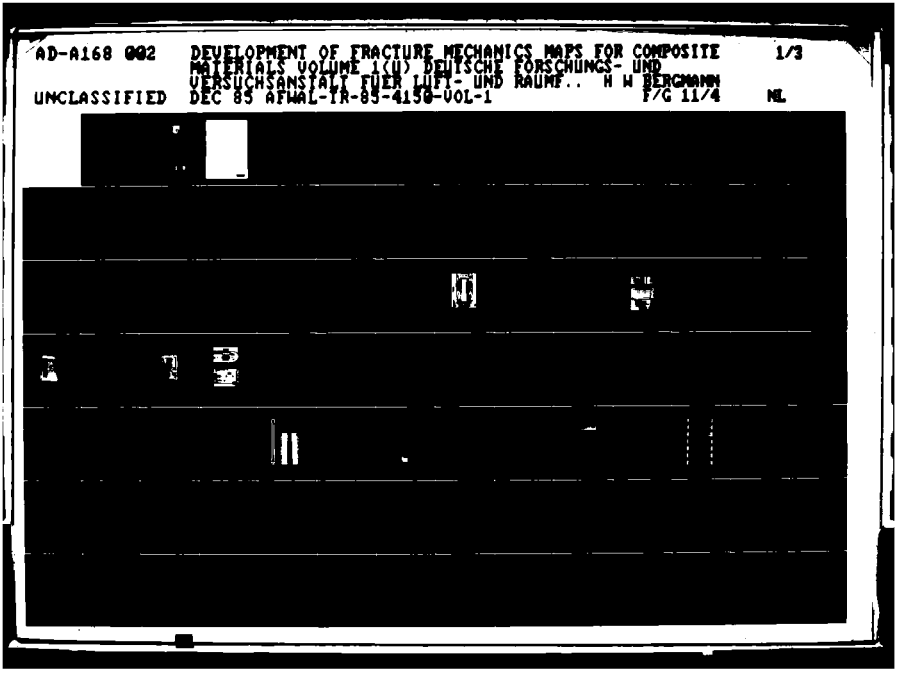

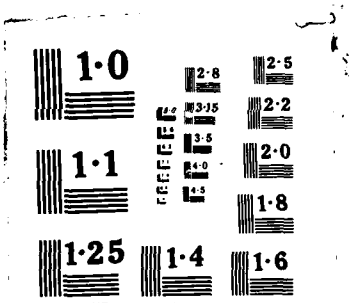
1·0
1·1
1·25
1·4
1·6
2·8
3·15
3·5
4·0
4·5
2·5
2·2
2·0
1·8

AFWAL-TR-85-4150
Volume 1

(1)

DEVELOPMENT OF FRACTURE MECHANICS MAPS FOR COMPOSITE MATERIALS

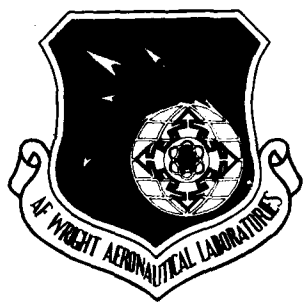

Dr. H. W. Bergmann

DFVLR - Institute for Structural Mechanics
Braunschweig, West Germany

December 1985

Final Report for Period January 1982 - January 1985

Approved for public release; distribution unlimited.

MATERIALS LABORATORY
AIR FORCE WRIGHT AERONAUTICAL LABORATORIES
AIR FORCE SYSTEMS COMMAND
WRIGHT-PATTERSON AIR FORCE BASE, OHIO

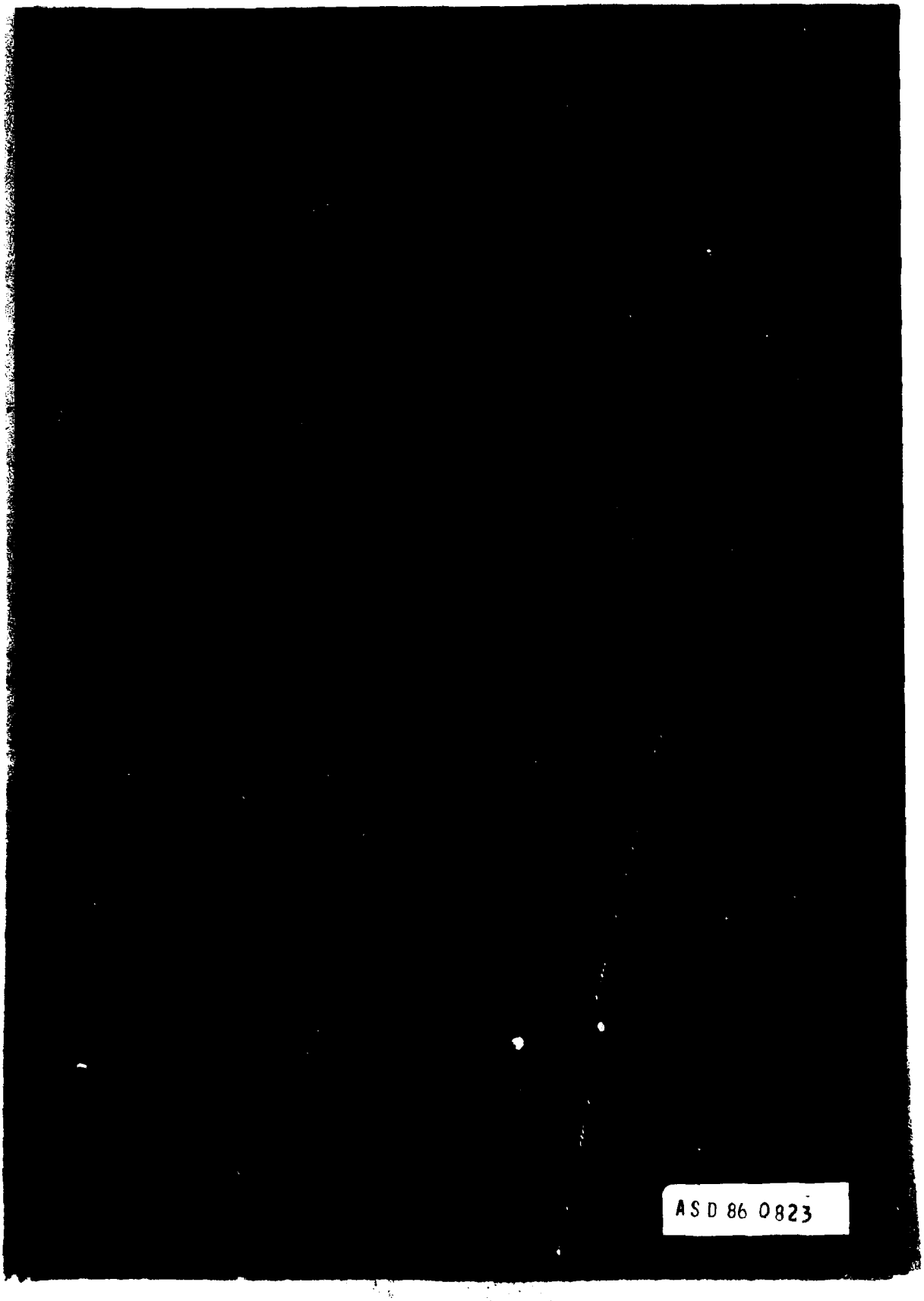
ASD 86 0823

UNCLASSIFIED

SECURITY CLASSIFICATION OF THIS PAGE

REPORT DOCUMENTATION PAGE

1a. REPORT SECURITY CLASSIFICATION: UNCLASSIFIED	1b. RESTRICTIVE MARKINGS: NONE
2a. SECURITY CLASSIFICATION AUTHORITY: N/A	3. DISTRIBUTION/AVAILABILITY OF REPORT: Approved for Public Release Distribution unlimited
2b. DECLASSIFICATION/DOWNGRADING SCHEDULE: N/A	
4. PERFORMING ORGANIZATION REPORT NUMBER(S): None	5. MONITORING ORGANIZATION REPORT NUMBER(S): AFWAL-TR-85-4150, Vol 1
6a. NAME OF PERFORMING ORGANIZATION: DFVLR - Institute for Structural Mechanics; 6b. OFFICE SYMBOL (If applicable): N/A	7a. NAME OF MONITORING ORGANIZATION: AFWAL/Materials Laboratory (AFWAL/MLSE)
6c. ADDRESS (City, State and ZIP Code): Braunschweig, West Germany	7b. ADDRESS (City, State and ZIP Code): Wright-Patterson AFB, OH 45433
8a. NAME OF FUNDING/SPONSORING ORGANIZATION: European Space Technology Committee; 8b. OFFICE SYMBOL (If applicable): N/A	9. PROCUREMENT INSTRUMENT IDENTIFICATION NUMBER: ESTEC/Contract No 4825/81/ML/AK(SC)
8c. ADDRESS (City, State and ZIP Code): Brussels, Belgium	10. SOURCE OF FUNDING NOS. — PROGRAM ELEMENT NO.: N/A; PROJECT NO.: N/A; TASK NO.: N/A; WORK UNIT NO.: N/A
11. TITLE (Include Security Classification): Development of Fracture Mechanics Maps for Composite Materials	
12. PERSONAL AUTHOR(S): Editor (Dr. H. W. Bergmann)	
13a. TYPE OF REPORT: Final; 13b. TIME COVERED: FROM Jan 82 TO Jan 85; 14. DATE OF REPORT (Yr., Mo., Day): 1985 Dec; 15. PAGE COUNT: see below (16)	
16. SUPPLEMENTARY NOTATION: Vol 1 (216) Vol 2 (204) Vol 3 (265) Vol 4 (192)	

17. COSATI CODES		
FIELD	GROUP	SUB. GR.
11	04	
01	03	

18. SUBJECT TERMS (Continue on reverse if necessary and identify by block number): Fiber Reinforced Composites, Dynamic Test, Thermal Cycling, Quality Control, Static Test, Stress Concentrations, Notched Specimens, Nondestructive testing

19. ABSTRACT (Continue on reverse if necessary and identify by block number)

The Institute for Structural Mechanics of the German Aerospace Research Establishment (DFVLR) has conducted a research program aimed at the characterization of the fracture behavior of carbon-fiber-reinforced epoxy resins. The research effort encompassed a comprehensive experimental and analytical investigation of the response of test specimens under a broad range of material, loading and environmental parameters. By combining an evaluation of global laminate properties with an investigation of micro- and macroscopic modes of failure, the understanding of the fracture and fatigue behavior of carbonfiber-reinforced composites was enhanced. It is expected that the results of the research program and their representation in the form of tables, figures, graphs and maps will assist the design engineer and lead to improved engineering concepts. (Keywords)

20. DISTRIBUTION/AVAILABILITY OF ABSTRACT: UNCLASSIFIED/UNLIMITED ☒ SAME AS RPT. ☐ DTIC USERS ☐	21. ABSTRACT SECURITY CLASSIFICATION: UNCLASSIFIED
22a. NAME OF RESPONSIBLE INDIVIDUAL: THEODORE J. REINHART	22b. TELEPHONE NUMBER (Include Area Code): 513/255-3691; 22c. OFFICE SYMBOL: AFWAL/MLSE

DD FORM 1473, 83 APR EDITION OF 1 JAN 73 IS OBSOLETE.

SECURITY CLASSIFICATION OF THIS PAGE

NOTICE

When Government drawings, specifications, or other data are used for any purpose other than in connection with a definitely related Government procurement operation the United States Government thereby incurs no responsibility nor any obligation whatsoever; and the fact that the government may have formulated, furnished, or in any way supplied the said drawings, specifications, or other data, is not to be regarded by implication or otherwise as in any manner licensing the holder or any other person or corporation, or conveying any rights or permission to manufacture use, or sell any patented invention that may in any way be related thereto.

This report has been reviewed by the Office of Public Affairs (ASD/PA) and is releasable to the National Technical Information Service (NTIS). At NTIS, it will be available to the general public, including foreign nations.

This technical report has been reviewed and is approved for publication.

FOR THE COMMANDER

Theodore J. Reinhart

THEODORE J. REINHART, Chief
Materials Engineering Branch
Systems Support Division

DEVELOPMENT OF FRACTURE MECHANICS MAPS

FOR COMPOSITE MATERIALS

Final Report

ESTEC/Contract No. 4825/81/NL/AK(SC)

Compiled and
Edited by: Dr. H.W. Bergmann, DFVLR

ESA Technical
Management: Dr. C. Stavrinidis, ESTEC

Authorized by: H. W. Bergmann .....

Dr. H.W. Bergmann
Director, Institute for
Structural Mechanics, DFVLR

January 1985

GERMAN AEROSPACE RESEARCH ESTABLISHMENT (DFVLR)

ABSTRACT

The Institute for Structural Mechanics of the German Aerospace Research Establishment (DFVLR) has conducted a research program aimed at the characterization of the fracture behavior of carbon-fiber-reinforced epoxy resins. The research effort encompassed a comprehensive experimental and analytical investigation of the response of test specimens under a broad range of material, loading and environmental parameters. By combining an evaluation of global laminate properties with an investigation of micro- and macroscopic modes of failure, the understanding of the fracture and fatigue behavior of carbonfiber-reinforced composites was enhanced. It is expected that the results of the research program and their representation in the form of tables, figures, graphs and maps will assist the design engineer and lead to improved engineering concepts.

STUDY MANAGEMENT

The research program involved a wide range of different disciplines and required the definition and coordination of a large number of subtasks. Dr. H.W. Bergmann, director of the DFVLR Institute for Structural Mechanics, served as Program Manager for the entire duration of the program from January 1982 to December 1984 and compiled and edited the final report.

ACKNOWLEDGEMENTS

The DFVLR Research Team acknowledges the assistance of ESTEC personnel in the conduct of the research program and in maintaining current awareness of ongoing developments in this field. Special appreciation is due the ESTEC Contract Manager, Dr. C. Stavrinidis, who conceived the request for proposal, supervised the contractual performance and provided helpful guidance at critical

stages of the research program. In this context the assistance through Engineering Systems International (ESI), supporting some of the analytical aspects of the contract, is specially appreciated.

The Program Manager acknowledges the responsiveness and cooperation of the numerous scientists and technicians, of the Institute for Structural Mechanics in the pursuit of the overall research effort. Appreciation is also expressed to the Section Heads of the Institute for Structural Mechanics Dr. Geier, Dr. Prinz and Dr. Niederstadt for their supervisory activities, and to the secretarial and drafting staff for the preparation of the document.

The authors of the individual sections of the final report are listed below:

Executive Summary : Dr.-Ing. H.W. Bergmann
Technical Report,
Section 1 : Dr.-Ing. H.W. Bergmann
Section 2 : Dr.-Ing. R. Prinz, Dipl.-Ing. K. Schmidt
Section 3 : Dipl.-Ing. M. Gädke
Section 4 : Dipl.-Ing. R. Schütze, Dipl.-Phys. J. Block
Section 5 : Dr.-Ing. H. Eggers, Dipl.-Ing. L. v.Bonin
Section 6 : Dipl.-Ing. M. Gädke
Section 7 : Dr.-Ing. L. Kirschke, Dr.-Ing. H. Eggers
Section 8 : Dipl.-Phys. H.C. Goetting
Section 9 : Dipl.-Ing. G. Kress, Dr.-Ing. L. Kirschke
Section 10 : Dipl.-Ing. W. Hartung
Section 11 : Dipl.-Ing. H. Twardy, Dipl.-Phys. J. Block
Section 12 : Dr.-Ing. G. Niederstadt
Section 13 : Dipl.-Phys. P. Nitsch
Section 14 : Dr.-Ing. H. Eggers, Dr.-Ing. K. Rohwer
Section 15 : Dr. J. Awerbuch
Section 16 : Dr.-Ing. R. Prinz

This Report consists of four Volumes:

Volume 1	-	I. Executive Summary II. Technical Report (Sections 1 - 8)
Volume 2	-	II. Technical Report (Sections 9 - 16)
Volume 3	-	Appendices A - E
Volume 4	-	Appendices F - K

VOLUME 1 - CONTENTS

VOLUME 2 - CONTENTS

VOLUME 3 - CONTENTS

VOLUME 4 - CONTENTS

DEVELOPMENT OF FRACTURE MECHANICS MAPS

FOR COMPOSITE MATERIALS

Final Report
- Volume 1 -

I. EXECUTIVE SUMMARY

EXECUTIVE SUMMARY

Recent years have witnessed an expanded utilization of fiber-reinforced composites. Among the variety of available fiber-matrix systems, carbonfiber-reinforced epoxy resins are most widely used in aerospace and other industrial applications. In the majority of cases these applications have been limited to stiffness-critical structures. There is now a rising demand for light-weight composites in strength-critical structures as well which poses entirely new challenges. Major areas of concern are an as yet incomplete understanding of the material response under adverse environmental conditions, the limited strain to failure of the epoxy resins, and the lack of acceptable principles of damage mechanics analogous to fracture mechanics in metals. In order to resolve these issues, the ESA initiated a comprehensive research program centering on the effects of material, loading and environmental parameters on the strength, toughness, fracture behavior, fatigue, etc. of carbonfiber-reinforced epoxy resins. Considering the wide range of available material systems, the variety of possible laminate configurations and the large number of different damage mechanisms, it is readily apparent that only a limited number of the existing problems can be solved in any one time-limited research program.

Before this background, the ESA-conceived research activities were important, and the requested confinement to an investigation of laminates subjected to tension loads was prudent. By concentrating on this load regime, a substantial degree of insight into the fracture process and failure modes of carbonfiber-reinforced epoxy resins could be gained. It would be equally prudent, however, to extend the research efforts into the compression load regime, where different fracture processes will produce different failure modes, in order to obtain a balanced understanding of the performance characteristics of composite materials.

The current research program commenced in January 1982 and terminated in December 1984. Within the scope of the contract the DFVLR Institute for Structural Mechanics addressed three major topics:

- experimental investigations in which reliable data were procured on the performance of laminates under a wide range of loading and environmental conditions;

- analytical investigations with the aim of developing physical or mathematical models as predictive tools for the forecast of the materials response and with which experimental data and observations can be reduced and interpreted;

- construction of relevant and usable design guides which display the advantages and disadvantages of a given material system, or which support the selection of an appropriate material system for specific design requirements.

The results and conclusions of the corresponding efforts are documented in this final report. The term fracture mechanics maps in the title of the report was interpreted to encompass all forms of visual aids such as tables, figure, charts and maps, useful for the description of fracture processes and failure modes of carbonfiber-reinforced laminates. The report is submitted in four volumes: Volumes 1 and 2 contain an executive summary and sixteen sections covering individual topics of the contracted work in a self-contained form; Volumes 3 and 4 are collections of appendices which expand on some of the research topics in more detail. The research program commenced on the premise that, in order to reduce data scatter and to identify the subtle influences of interacting parameters, very high standards in regard to the quality of the test specimen fabrication and the test facilities needed to be introduced and maintained. Special attention was also given to the traceability of the life history of all of the ca. 1800 specimens tested in the course of the program. Following a general introduction in Section 1, Sections 2 and 3 cover the above mentioned aspects.

Nondestructive inspection procedures were considered an indispensable part of the research program for quality assurance of the specimens prior to testing as well as for the detection and identification of developing damage patterns during and after testing. The techniques used are briefly described in Section 4.

Section 5 deals with several of the analysis tools used throughout the research program. Apart from the statistical treatment of test data, two finite-element computer programs are described which guided the interpretation of the fracture processes. Whereas the ASKA-program served well for standard stress analyses, the need arose for the development of a new program called LAMINA capable of coping with the intricacies of nonlinear laminate responses in an economically affordable fashion.

The heart of the report is contained in the subsequent Sections 6 through 13 which document the actual test results and the conclusions drawn from them. The accompanying figures are prepared such that they can serve as useful aids for engineering design practices.

The response of statically loaded un-notched test specimen is covered in Section 6. Since, because of the large variety of fibers, resins, volume fractions, stacking orders, etc., the characteristics of arbitrarily stacked laminates cannot be displayed summarily in the form of graphs or tables, it was attempted to deduce them from the characteristics of unidirectional laminates. The attempted forecasts are complicated by the nonlinear constitutive laws and the susceptibility to moisture and temperature effects of the matrix systems. The corresponding test program comprised the determination of all pertinent properties of unidirectional plies for three fiber-matrix systems under different temperature and moisture conditions. These properties form the basis for the analytical prediction of the response of multidirectional laminates. The predictions include the elastic moduli, the first-ply failure and the ultimate tensile strength of the laminates. They take into account the state of prestress induced by temperature and moisture. Additional tests were performed with multidirectional laminates to validate the analytical predictions and to support the failure analysis.

In Section 7 the behavior of notched test specimens under static loads is described. The test program included unidirectional on-axis and off-axis specimens as well as multidirectional specimens containing either a single central notch or two symmetrical notches at the specimen edges. During the loading of the speci-

mens the crack-opening displacements, the local strains and overall displacements, and the length of the cracks emanating from the notch tips were observed. The tests were supported by radiographical and fractographical investigations. Based on the test results, parameters were determined which characterize the state of damage and the influence of stacking order, type of notch, and length of crack. Parallel to the test effort, numerical calculations were performed with the aim of establishing failure criteria for incorporation into the computer program LAMINA. The analyses presupposed that for several of the test specimen configurations the precepts of linear elastic fracture mechanics are applicable. By means of the finite-element programs ASKA and LAMINA the states of stress at the crack tip were analyzed for different crack lengths at load intensities under which crack extension was observed. The critical stress intensity factors K_I^c and K_{II}^c were established by different evaluation methods and the strain energy release rate concept was found to be the most promising. Using this approach it was possible to identify the total energy release as well as the two energy release components which associate with the two crack opening types, from which K_i^c and K_{II}^c can be obtained.

Section 8 deals with the performance of mechanically fatigued un-notched specimens. Tests under four different environmental conditions were performed in order to investigate the influence of temperature and moisture on the fatigue strength and on the damage mechanisms in carbonfiber-reinforced laminates. Unidirectional on-axis laminates exhibited no significant degradation due to the combined effects of temperature and moisture. The presence of moisture at ambient temperature has a beneficial effect on the fatigue life because of the relaxation of the curing prestresses by the swelling of the matrix. Macromechanical damage like matrix cracks or delaminations could not be detected by means of NDT-techniques. In angle-ply laminates, elevated temperature alone as well as moisture alone led to significant degradations of the fatigue strength. An additional degradation is observed if both temperature and moisture are present simultaneously. Typical damage patterns are matrix cracks and edge delaminations in increasing degrees of severity which correspond to measured stiffness losses of the test specimens during

fatigue. Multidirectional laminates show, similarly to the unidirectional specimens, only slight degradations at elevated temperature, and slight improvements with increasing moisture contents. Even the simultaneous presence of both temperature and moisture has no severe influence on the fatigue strength. It can be stated, generally, that the fatigue properties of matrix-controlled laminates are sensitive to temperature and moisture, whereas the more fiber-controlled laminates show no significant degradative effects.

Conclusions from the testing of mechanically fatigued notched specimens are summarized in Section 9. In laminates containing notches or holes the formation of cracks and their subsequent progression are caused by stress concentrations in the vicinity of the discontinuities. The residual strength and stiffness of such laminates under cyclic loading was the primary aim of this investigation. In a preparatory study the nature of damage progression in on-axis unidirectional test specimens with two symmetrical edge notches under increasing numbers of load cycles with R = 0.1 was determined. The majority of the test effort was conducted with multidirectional laminates containing unloaded circular holes at the center of the test section. Matrix cracks and delaminations in and between adjacent plies of the laminates were observed and monitored by contrast-enhanced radiography. The strength and stiffness measurements after prescribed numbers of load cycles with R = 0.1 showed that the global stiffness of the test specimens diminished whereas the residual static strength continued to increase until shortly before failure. The strength increase is attributed to the relief of local stress concentrations due to the crack formation and progression in the plies of the laminate around the hole.

Section 10 contains a description of the performance of un-notched specimens thermally fatigued in a realistically simulated space environment. The potential problems arise from the different coefficients of thermal expansion of carbonfibers and polymeric resins which cause serious prestresses in the laminates. The magnitude of the resulting tensile stresses in the resins depends on the difference between the congealing temperature of the resins and the lower service temperature of the

laminates. Repeated exposures to very low temperatures may lead to accumulating damages particularly in laminates with high curing prestresses. In order to assess the effects of thermal cycling in a typical space environment on the mechanical properties of carbonfiber-reinforced laminates, and to study the potential mechanisms of damage, a test program was performed with cross-plied laminates prepared from five different fiber-resin systems. Several sets of test specimens were evaluated prior to and after exposure to various numbers of thermal cycles, in vacuum, between +100°C and -160°C. The test results showed that strength degradations of up to 20% occured in the expoxy-based laminates, and much more in the polyimide-based laminates, accompanied by corresponding stiffness degradations. Both types of degradation were traced to matrix cracking and interface deterioration.

The strain capabilities and the strain rate effects in neat epoxy resin and in carbonfiber-reinforced epoxy laminates were investigated in Section 11. The desirable increase of the failure strains of 180°C-curing resins under retention of high service temperatures is chemically incompatible and bey nd the state of the art. It is uncertain, therefore, whether the availability of advanced high-strength and/or high-strain carbonfibers in connection with the present generation of epoxy systems can offer significant advantages. Alternatively, the question arises what ranges of strain capability are needed to exploit the potential of the new carbonfibers. Investigations in this direction were made with a variety of matrix formulations and fiber types under ambient conditions, i.e., initially by-passing the issue of elevated service temperatures. The majority of the tension tests were performed with unidirectional ring-type specimens which led to consistent results. By increasing the matrix failure strain from $\varepsilon = 1.5$ % to $\varepsilon = 2.5$ %, strength improvements between 14 % and 54 % were shown to be possible. A second issue was the sensitivity of the strength and stiffness properties of the test specimens to different strain rates. With two specially constructed loading devices loading rates differing by four orders of magnitude could be applied. The tests showed, somewhat surprisingly, that for strain rates greater than $\dot{\varepsilon} = 1.0$ % per sec the strength values of

the test specimens remain constant regardless of the degree of ductility of the matrix.

Section 12 reports on the effects of radiative and oxidative environments on carbonfiber-reinforced epoxy resins. A limited effort only was made to assess the magnitude of degradation in three specific cases. A realistic simulation of electron beam irradiation as experienced during the service life of a spacecraft structure in a typical geostationary orbit showed that neither the tensile strength nor the elongation to failure of 1 mm thick laminates were impaired after 3×10^8 rads. A slight reddish tint on the laminate surfaces may be indicative of optical property changes. The long-time exsposure of test specimens to open atmospheric conditions led to matrix cracks and obvious deteriorations of the laminate surfaces. The direct cause was traced to UV-B irradiation, aided by the presence of both moisture and oxygen. The tensile strength diminished to 90% of the initial strength after an irradiation dose of 2000 J/cm^2 which is roughly equivalent to three calendar years. A clearly oxidative effect was observed on test specimens subjected to a sustained temperature of 120° C in the presence of air. The measured weight loss of 914C/T300 specimens was 3.3 % after 28900 hours and continuing still. At a sustained temperature of 100°C the rate of weight loss was considerably less but had an equally continuing trend. Optical investigations revealed no significant changes in the surface texture of the test specimens.

Apart from the observation of macromechanical fracture processes, a substantial portion of the research program dealt with the investigation of micromechanical failure modes. The results of fractographical studies of the fracture surfaces of test specimens are contained in Section 13. It became soon apparent that the topography of the fracture surfaces is not only affected by the nature or sequence of the dominant failure modes but also by such parameters as moisture content, variations of curing process, different stacking orders and strain rates. In view of the complexity of the issue the efforts commenced with the failure modes analysis of neat epoxy resins and proceeded to the investigation of environmental effects in uni- and multidirectional laminates. The topography of the fracture surfaces of the

tension-loaded neat resins was seen to depend on the curing process as well as on the moisture content. In curing cycles with low heating rates the formation of microcracks was observed. The fracture surfaces reveal that both the curing cycle and the moisture content affect the strain capability of the resin. A clear distinction between the two phenomena could not be made. With a known curing cycle, however, it is possible to deduce the moisture content of a specimen and, with a known moisture content, the nature of the curing cycle. In regard to fiber-reinforced laminates it became evident that the influence of different curing cycles, of test temperature and of moisture content on the matrix microstructure and on the fiber-matrix interface are identifiable. The fiber-matrix adhesion could be quantitatively evaluated in terms of the mean length of the pulled-out fibers.

Section 14 addresses the applicability of linear elastic fracture mechanics to carbonfiber-reinforced laminates. It must be understood that the principles of linear fracture mechanics were originally developed to describe the initiation and progression of cracks in isotropic and homogeneous materials. These principles cannot be applied directly to fiber-reinforced laminates because here, instead of a single crack, a damaged zone develops in which the material progressively deteriorates. Fissuring and meandering cracks extending through the thickness of the material form only shortly before ultimate failure, i.e., after the useful life of the structure. From this premise arises the need for the development of a new discipline - damage mechanics - capable of describing the behavior of damaged zones in fiber-reinforced structures prior to ultimate failure.

Generally accepted concepts of damage mechanics are still rare. Known to some extent are individual mechanisms of damage progression but their contributions, single or in combination, to the total state of damage are not well understood. Current research efforts, therefore, are directed toward the definition of characteristic strength parameters for carbon-fiber-reinforced resins by a combination of analysis and test.

Despite the seriousness of the arguments in section 14, many attempts have been made to develop simplified fracture models for

the prediction of the notched strength properties of composites. Section 15 contains a critical evaluation of such models which extend linear elastic fracture mechanics from metals to composites but do not actually address the micromechanical complexities in the crack extension process. Rather, they assume a self-similar crack extension, and the actual crack tip damage zone size is represented by an 'effective' damage zone size defined as a material parameter and to be obtained experimentally. Since these tests are tailored to the problem under investigation, they normally lead to good agreement between the predictions of a particular model and the actual strength of the notched laminates. Most of the models, therefore, are of pragmatic importance even though they by-pass the issue of specific failure modes. In order to evaluate the range of applicability and the accuracy of the more commonly used fracture models for notched laminates being subjected to uniaxial loading, a detailed evaluation was made of eleven different fracture models against a large amount of published test data. The collected experimental notched-strength parameters were then compared with the predictions from each of the fracture models. The comparisons were mostly poor because all of the fracture models consider the experimentally determined parameters as material constants whereas, in reality, they depend on stacking order, constituent properties and fabrication technique as well as on type of loading, specimen geometry and environmental conditions. Consequently, the parameters established for a particular condition are not of general validity and therefore not transferrable from one configuration to another.

The concluding Section 16 describes the nature and sequence of mechanisms of fracture in typical carbonfiber-reinforced laminates based on a multitude of observations. In contrast to metals, where fracture under static or fatigue loads results from the nucleation and growth of a single dominant flaw, the fracture of fiber-reinforced composites is characterized by the initiation and progression of multiple failures of different modes such as matrix cracks, interfacial debonding, fiber breaks and delaminations between adjacent plies of the laminates. The kinds of occuring faiiures, their distribution, time sequence and possible interaction depend on parameters such as the properties of

the fiber/matrix system, the stacking order and the curing process, the influence of the environment, etc. The problem is further complicated by the possibility of fatigue failure in the compressive as well as in the tensile load regime, and by different kinds of failure modes under static and dynamic load applications.

In order to gain insight into the mechanisms of the failure processes, the development of fatigue damage in unnotched multidirectional laminates was investigated under both tension and compression cycling. During and after fatigue loading specimens were examined for damage growth using light-microscopy, scanning electron microscopy, ultrasonic C-scans and x-radiography. Matrix cracking and edge delamination were found to be the dominant types of defects. Under fatique loading these defects propagated due to unfavorable interlaminar stresses to the point where the specimens ultimately failed by short buckling or shearing. The test effort was accompanied by finite-element calculations for the assessment of the state of stress in critical zones. A damage growth model was developed for edge delaminations which correlates well with the test results.

In summary it can be stated that the research program has led to a series of important recognitions, and that the assembled data will doubtless prove to be of advantage to the scientific community as well as to the practicing engineer. On the other side, an immense amount of work remains to be done requiring substantial amounts of additional time and effort. The problem is perceived in proper perspective by the reflection that the much simpler development of classical fracture mechanics has already required many thousands of manyears in more than two decades. The question is valid whether similar expenditures for fiber-reinforced composites are worth the gain. The answer must be guided by the recognition that a substantial amount of additional effort is inescapable if only for maintaining a strong position in the highly competitive international aerospace market.

DEVELOPMENT OF FRACTURE MECHANICS MAPS

FOR COMPOSITE MATERIALS

Final Report
- Volume 1 -

II. TECHNICAL REPORT
SECTIONS 1 - 8

1. INTRODUCTION

1.1 State of the Art

Recent years have witnessed a greatly expanded reliance on laminated composite materials whose specific strength, stiffness and fatigue characteristics are often superior to those of conventional metals. Research activities and application studies, generally, have focussed on fiber-reinforced polymer matrices. Among the large variety of available fiber-matrix systems, carbonfiber-reinforced epoxy resins are most widely used in many industries.

With respect to aerospace applications, a considerable number of structural components have already been placed into service. Most of them were restricted to so-called secondary structures with stiffness-critical service requirements. In such structures the operating stress levels are so low that the issues of durability and fatigue can be safely ignored.

There is now a growing demand for strength-critical structures but, before this demand can be met, a more thorough understanding is required of the way in which pertinent loading, environmental and material parameters affect the strength, toughness, fracture behavior, fatigue characteristics, etc. of carbonfiber-reinforced epoxy resins. A large number of tests relating to these aspects have been performed already in various parts of the world. Most of these tests, however, were addressed to specific design requirements and a comprehensive understanding of the material response has not yet evolved. Concurrently, analytical tools have been developed to predict the response of muldidirectional laminates from the properties of the constituent materials and their interactions.

A significant lack of comprehension still prevails with respect to the ultimate load-carrying capabilities of carbonfiber-reinforced epoxy resins and the associated failure processes. The identification and interaction of the many different failure modes and the mechanisms of damage progression in highly stressed

laminates were the objectives of the research efforts documented in this report.

1.2 Scope of the Research Program

The Institute for Structural Mechanics concentrated its efforts on the observation and description of failure modes and fracture processes in flat laminates with different stacking orders, both notched and unnotched, under static and cyclic load applications, and in environments typical for aerospace structures. In accordance with the contract requirements, the current research was essentially confined to the response of laminates in the tensile load regime. A limited number of tests were conducted under cyclic tension-compression and pure compression loads to demonstrate that different failure modes interact in different ways. It is therefore necessary to continue the research into the compression load regime in order to arrive at a more complete understanding of the behavior of fiber-reinforced composites.

In the planning stages of the research activities it was recognized that any specific composites problem can be resolved by means of a well-designed test program. However, new test series will become necessary for different structural configurations or different loading conditions unless the mechanisms of the fracture processes are known and their progression under changing parameters can be predicted. Insight into these mechanisms is also required for a successful treatment of the analytical aspects of the fracture phenomena. Considering the complexity of the issue it became apparent that a combined empirical/analytical approach to the comprehension of fracture processes was most appropriate. Accordingly, the research efforts centered on

- experimental investigations in which reliable data were procured on the performance of laminates under a wide range of loading and environmental conditions;

- analytical investigations with the aim of developing physical or mathematical models as predictive tools for the fore-

cast of the materials response, and with which experimental data and observations can be reduced and interpreted.

In the course of the research program approximately 1800 specimens were tested. The majority of the test specimens was extensively instrumented and the test conditions were carefully controlled in order to minimize data scatter. Modern nondestructive inspection techniques assured the detection and identification of developing defects throughout the program. Apart from the observation of macromechanical effects, a substantial portion of the research program dealt with the investigation of micromechanical failure modes.

With respect to analytical tools, it was realized that standard finite-element programs were inadequate to cope with the complexities of fracture processes in carbonfiber-reinforced resinous materials. Therefore, a special-purpose computer program was developed which incorporates a significant number of the required nonlinear in an economically affordable fashion. During its development some of the experimental aspects of the research program were supported by Engi eering System International under a special ESA-contract.

In context with the development of analytical models the question arose whether or to what extent the principles of linear elastic fracture mechanics are applicable for the treatment of composites problem. A significant effort was made the assess the merits of several of the currently used fracture models for notched laminates. As expected, the issue of fracture in carbonfiber-reinforced resins transcends the direct application or simple adaptation of classical fracture mechanics to merely a different class of materials. Rather, an entirely new frame of reference is required, partly because of the anisotropy and non-homogeneity of the material, and partly because of the large number of different kinds of damages. In fact, it may be appropriate to introduce the term damage mechanics for the fracture of composites in order to separate it from the much simpler fracture mechanics of metals.

1.3 Documentation of Results

The documentation of the research program is contained in this final report. The term fracture mechanics maps in the title of the research program was interpreted to include all forms of visual aids such as tables, figures, charts and maps useful for the description of fracture processes and failure modes in carbonfiber-reinforced epoxy resins.

The report is submitted in four volumes: Volumes 1 and 2 cover the following sixteen chapters of individual topics in a self-contained form; Volumes 3 and 4 comprise a collection of appendices which expand on several of the research topics. It is expected that this report will provide relevant and useable design guides for the selection and application of carbonfiber-reinforced epoxy resins for major structural components.

2. TEST FACILITIES

2.1 Summary

The bulk of the test program comprised the testing of ca. 1800 flat specimens under static loads, cyclic thermal loads and cyclic mechanical loads. It was recognized from the outset that a determination of the subtle effects of several parameters on the failure modes of carbonfiber-reinforced epoxy laminates mandated perfect test specimens as well as sensitive and reliable test facilities. On that basis especially the selected static and dynamic test machines reflected the latest developments in equipment and test system design and were adjusted such that they matched the specific requirements of the test program. Care was taken that correlating test series were executed on identical test machines to ensure compatibility of the test data. Special importance also had to be placed on the retention of constant environmental conditions during the mechanical load applications.

2.2 Thermal Cycling Facility

The thermal cycling tests were conducted in a space-rated test facility. The main components of this facility were a four-sided box-like structure rotatable about its vertical axis, provisions for infrared heating and radiation cooling from nitrogen-filled receptacles, and an airproof metallic shroud covering the entire assembly and allowing its operation in vacuum.

The specimens were mounted on two opposite sides of the box. By rotation of the box through ±90° the test specimens were exposed, alternately, to the heating and cooling devices inside the shroud. The rear side of the test specimens faced the walls of the box whose inside was permanently cooled. The interior of the shroud was evacuated and a pressure of 10^{-4} Pa maintained throughout the test. With this arrangement a test specimen temperature of 95°C was realized during the hot phase and of -155°C during the cold phase. Details of the test facility are visible in

Figs. 2.1 and 2.2. A typical thermal cycle extending over approximately 50 min is shown in Fig. 2.3.

2.3 Static Test Machine

The statically loaded un-notched specimens were subjected to tension, compression and bending loads under simultaneous environmental simulation on a computer-controlled universal testing machine equipped with a climate chamber (Fig. 2.4).

A microcomputer calibrated and controlled the test process and collected the data from 32 strain gage channels. The circuit diagram for the process control and the data acquisition is shown in Fig. 2.5. The maximum test load was 200kN and it was applied with crosshead speeds ranging from 0.0025 - 500 mm/min. The displacement measurements were obtained with an induction-type extensometer. Zero-point suppression could be introduced for both load- and displacement-controlled test modes. Load and displacement data were either recorded digitally or plotted by x-y-r corders.

2.4 Servohydraulic Test Machines

All of the mechanically cycled specimens and the statically loaded specimens containing notches were tested on servohydraulic machines with closed loop control allowing load, strain, displacement and velocity to be monitored as direct control parameters. The specimen loading sequence was regulated by servo-valves which control the oil flow to the actuator in proportion to electrical command signals.

The principle of the servohydraulic system used for the support of the test program is shown in Fig. 2.6. The oil flow produced by a power pack (1) capable of a supply pressure of 280 bar is led through the servo-valve (2) to a double-acting actuator (3) which applies the desired static tension or compression load, or a cyclic load sequence to the test specimen (4). Hydrostatic bearings of the actuator provided low friction, high side load

tolerance and self-centering action under increasing side loads. The feedback signal in the control circuit was correlated to the load intensity by an electric load cell (load control) (5), or by an extensometer (strain control) (6), or by a differential transformer in the piston rod (displacement control) (7). The voltages produced by appropriate transducers were amplified by signal conditioners (8) and displayed on an oscilloscope (9), recorded by an x-y-recorder, or stored digitally in a universal function generator/transient recorder (10), or in a computer (11). The difference between the command value and the measured value was amplified in the servo-controller (12) and used as error signal for the servo-valve control.

The stiffness of the frames of the test machines, the clamping of the movable crossheads and the grip attachments of the test specimens influence the test machine alignment or the backflash intensity. Therefore, very stiff two-column frames or cylindrical frames with cut-outs (Fig. 2.7) were used in conjunction with special grips clamped either mechanically or hydraulically. Fig. 2.8 depicts one of the five available servohydraulic test machines (System Schenck) in operation.

2.5 Environmental Simulation

The testing of specimens under simulated environmental conditions involves two steps: preconditioning to a desired moisture level and maintenance of that moisture level during testing at different temperatures.

The preconditioning for the static tests was accomplished by exposure of the specimens, including their tab-reinforced end sections, in temperature- and moisture-controlled climates, produced in receptacles filled with different saliferous water solutions kept at constant temperature. For cyclic load applications, however, the moisturized adhesive bondlines of the tabs tended to fail, requiring the design of a new preconditioning procedure, shown in Fig. 2.9, in which only the central part of the specimen is exposed to circulating steam at a temperature of 70°C ±2°C. The steam generator provides a relative humidity of

at least 95 %. Fig. 2.10 depicts the basic features of the facility.

During static testing the environmental conditions were maintained by placing the test rig with the full-length test specimen in a standard climatic chamber capable of independent temperature control between -55°C and 250°C, and moisture control between 0 and 95 % relative humidity. On account of the potential tab failures during cyclic testing, special climate chambers were constructed which are displayed in Fig. 2.11. The end sections of the test specimen are seen to protrude beyond the ca. 20×20×20 cm chamber so that the tabs and the grips are subjected to ambient conditions. Similar to the preconditioning approach, the desired test temperatures are obtained by circulation of hot air, and the moisture contents by injection of steam. The small size of the chamber has the additional advantage of low heat and minimal steam requirements. Several of these chambers were constructed for single and parallel operation at ambient temperature and wet conditions (28°C/95 % RH), hot and dry conditions (80°/5% RH) and hot and wet conditions (80°C/95% RH).

Fig. 2.1 Internal box-like structure of the thermal cycling test facility with mounted samples.

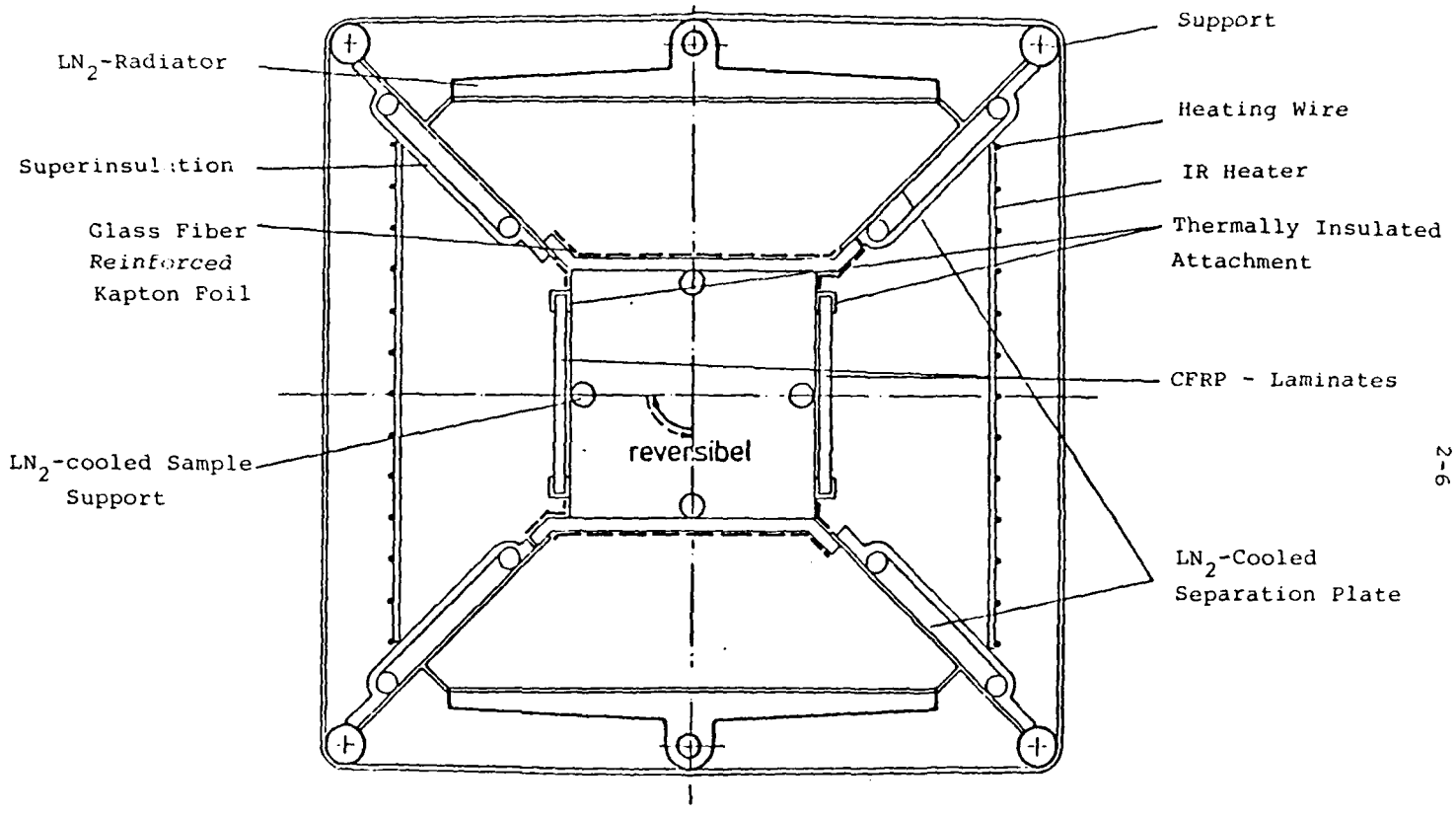

Fig. 2.2 Cross-section of test facility-hot phase mode.
(inside of metal shroud)

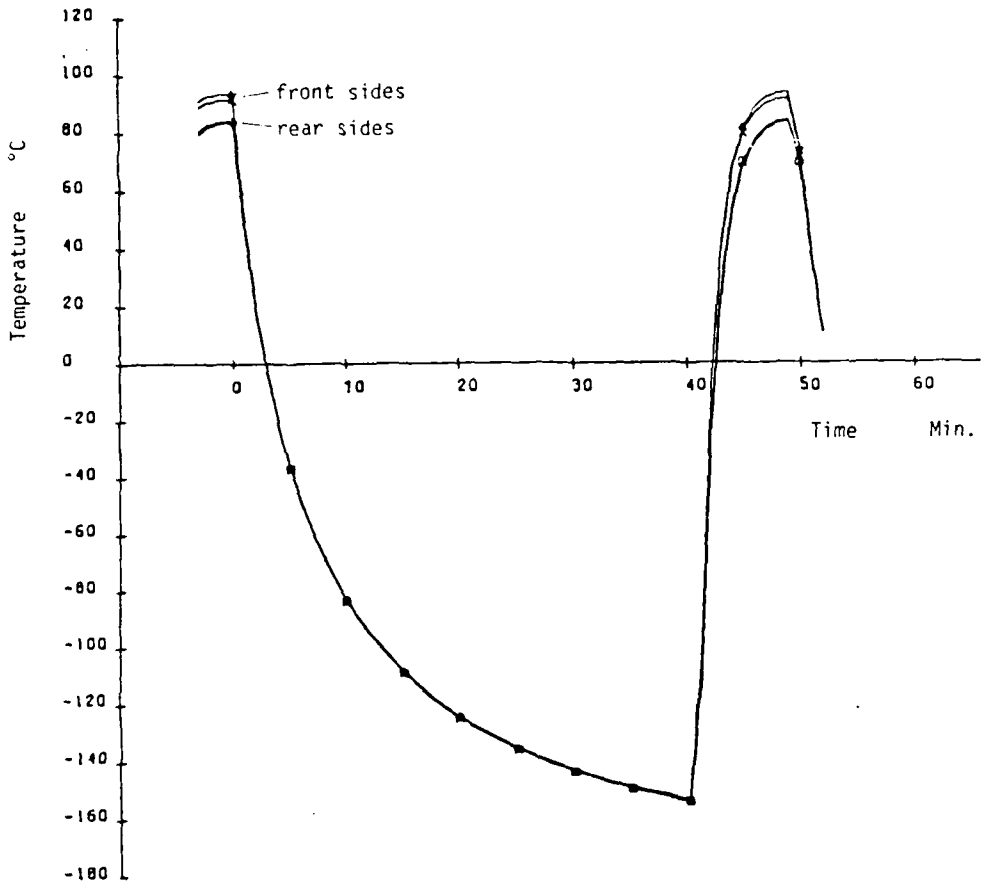

Fig. 2.3 Typical thermal cycle of surface temperatures versus time of two specimens.

Fig. 2.4 View of the static test machine.

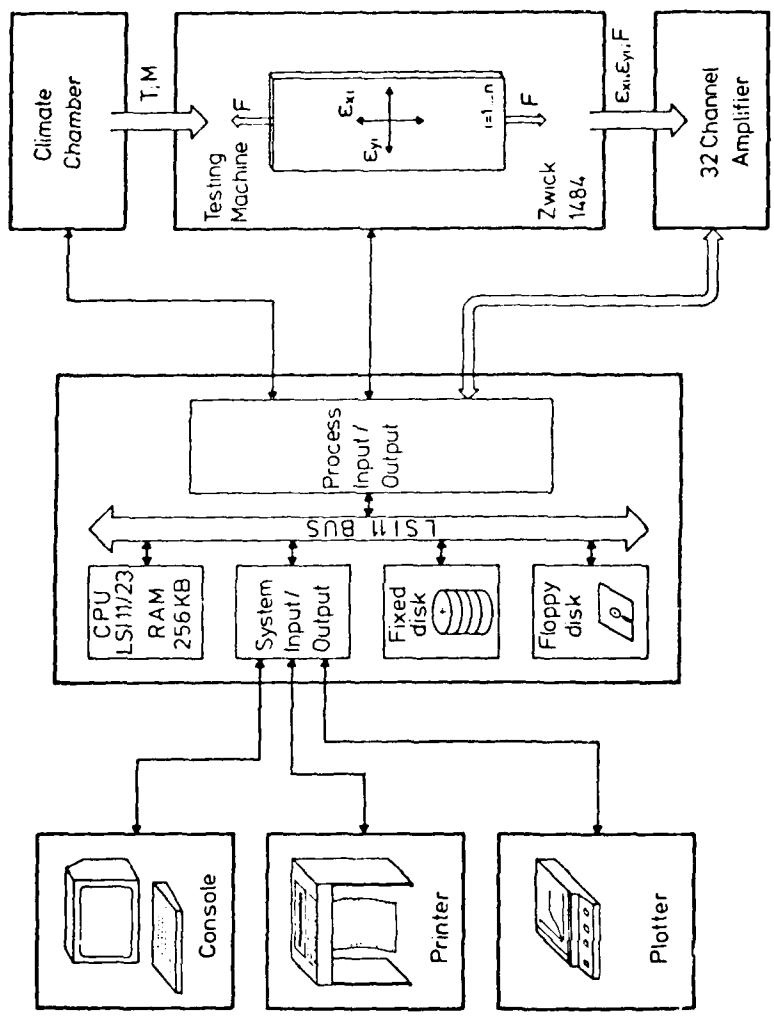

Fig. 2.5 Circuit diagram of process control and data acquisition.

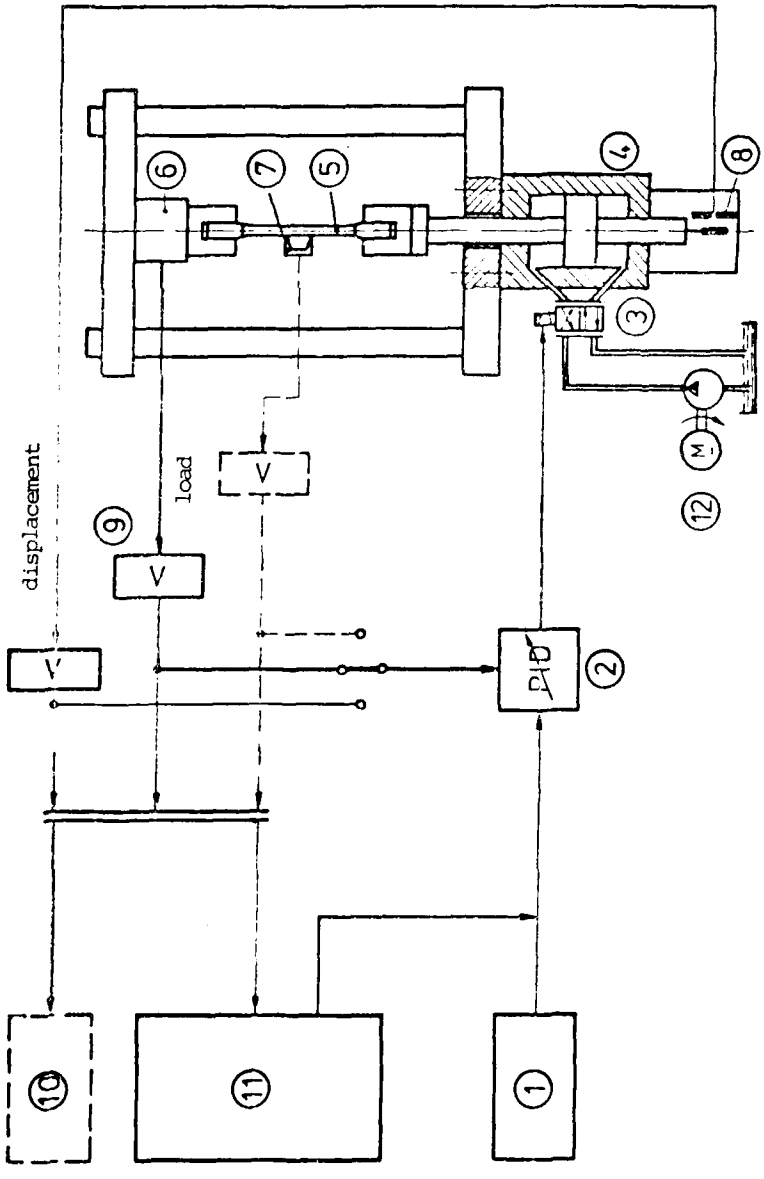

Fig. 2.6 Flow chart of the servohydraulic testing machines.

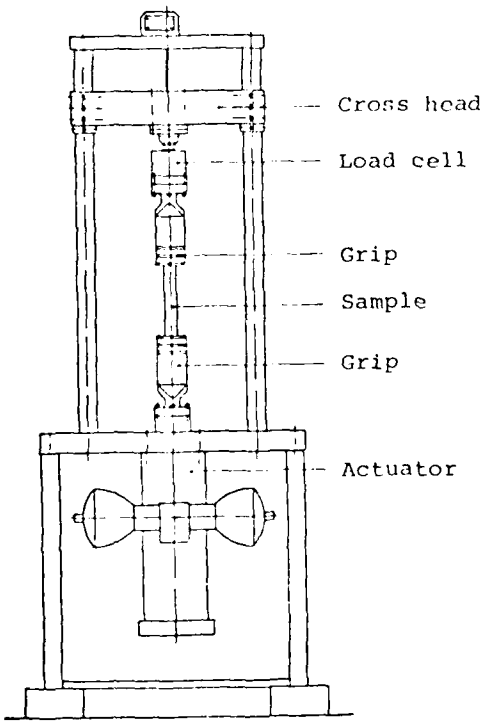

Test device with a two column frame.

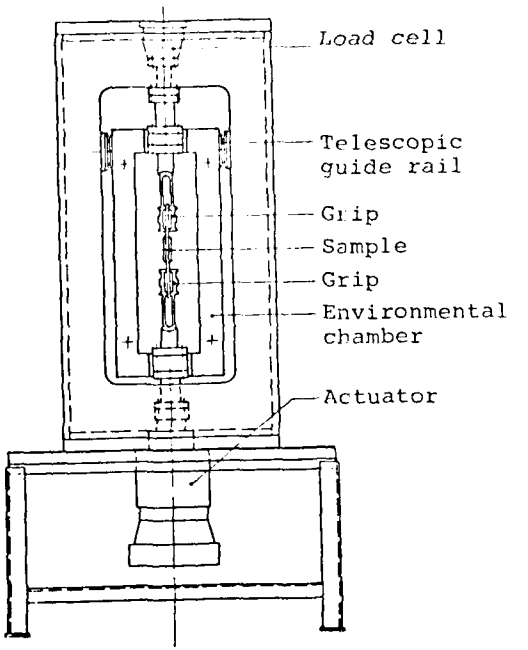

Test device with a cylindrical frame and cut-outs.

Fig. 2.7 Different types of test devices.

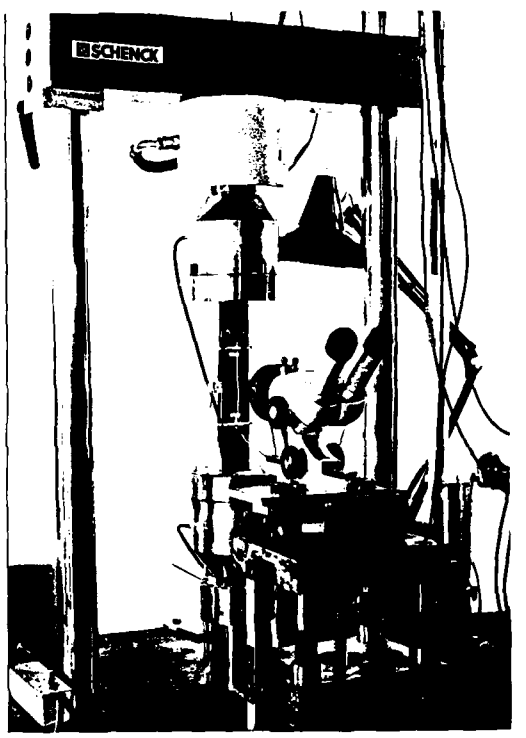

Fig. 2.8 View of an operating test machine.
(System Schenck)

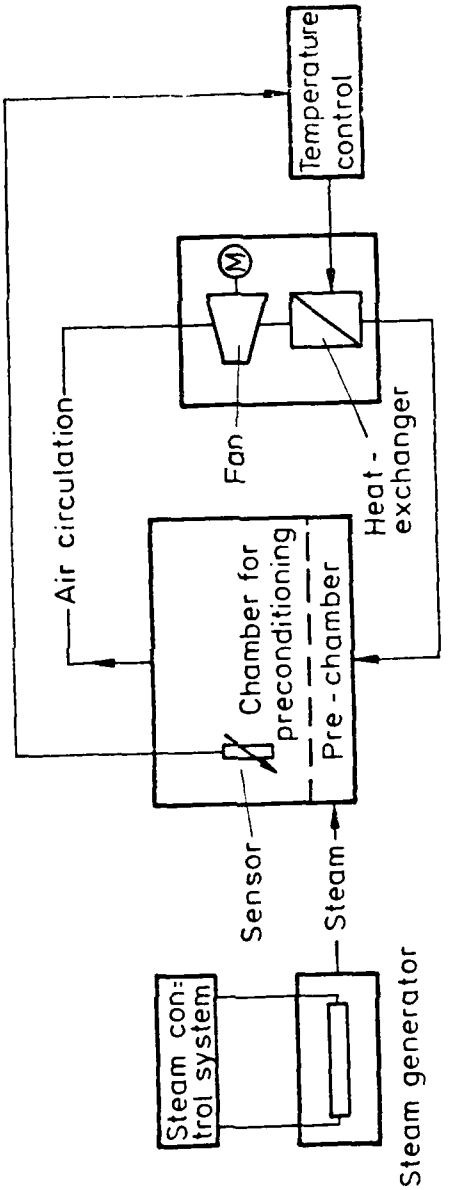

Fig.2.9 Flow chart of the preconditioning facility for CRP specimens

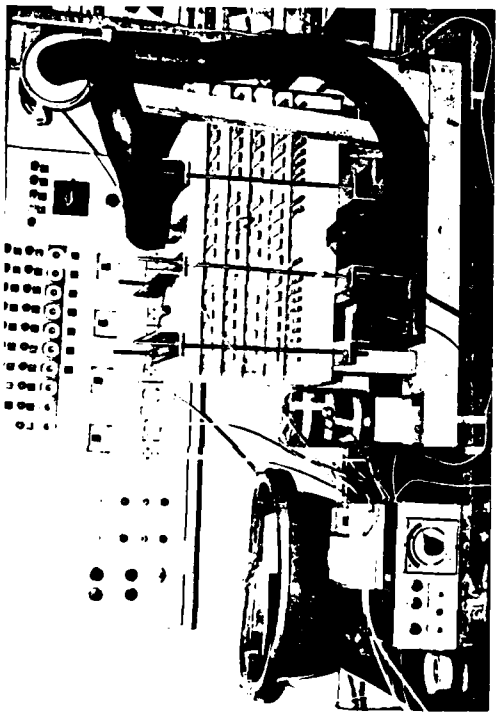

Fig.2.10 Chamber for preconditioning of test specimens.

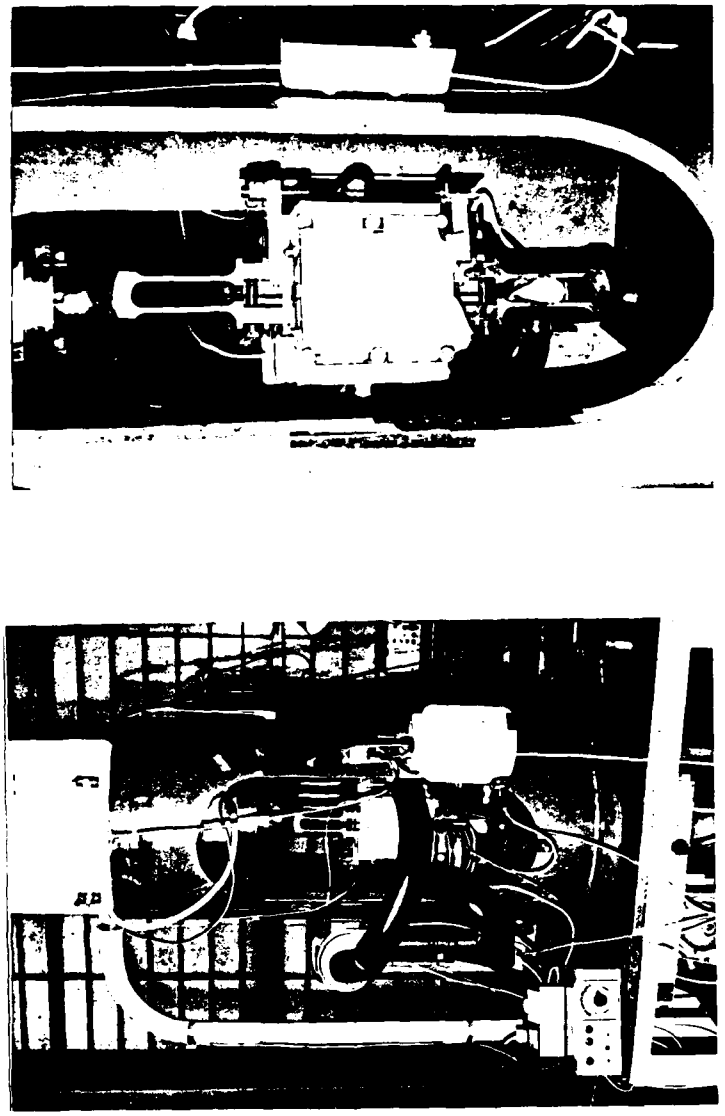

Fig. 2.11 Servohydraulic testing machine with inserted conditioning chamber.

3. TEST SPECIMENS

3.1 Summary

The proper interpretation of a test program extending over several years depends largely on the quality and uniformity of the test specimens. This is particularly true if the aim of the tests is the identification of parameters which only subtly influence the performance of carbonfiber-reinforced laminates.

Throughout the test program, therefore, the highest possible standard for all test specimens was maintained. Emphasis was placed on the quality control of incoming batches of materials, on the manufacture of laminates by a computer-controlled autoclave process, and on the traceability of the test specimen configuration and history.

3.2 Quality Control

The test program comprised the testing of specimens made from three different materials:

1. Fibredux 914C-TS-5 prepreg material from CIBA-GEIGY Ltd., consisting of surface-treated high-strength T300-6K carbonfibers and a 914-type epoxy resin with a curing temperature of 180 °C. The material was delivered in the form of unidirectional tapes on 30 cm wide rolls with a resin weight-fraction of 40 ± 2.5 % and with less than 1 % gaseous constituents. During the manufacturing process the surplus resin was bled out so that the cured plies had a mean fiber-volume content of 60 % and a thickness of 0.125 mm.

2. Code 69/T300 prepreg material from Fothergill & Harvey Ltd., consisting of surface-treated high-strength T300-6K carbonfibers and a Code 69-type epoxy resin with a curing temperature of 180 °C. The form of delivery and the ply properties correspond to 1.

3. T6T131-F550 prepreg material from Hexcel, consisting of surface-treated high-strength T300-6K carbonfibers and an F550-type epoxy resin with a curing temperature of 120 °C. The form of delivery and the ply properties correspond to 1.

Upon receipt of the various batches of material, representative samples were removed from the beginning and the end of each roll in order to ascertain the weight of unit areas of the resin and the fibers and that of the gaseous constituents. The degree of tackiness was determined by means of adhesion measurements and the amount of bled-outresin by weighing the laminates prior to and after curing.

The mechanical properties of cured sample laminates were established according to LN 29 971 at 23 °C and 50 % RH. The corresponding tests included the assessment of strengths and stiffnesses under bending, shear, tension and compression loads in 0°-, ±45°- and 90°-specimens. Fig. 3.1 is a typical record of the quality control tests.

3.3 Manufacturing Process

The majority of the test specimens consisted of 16 plies and had a mean thickness of 2 mm. The remaining specimens displayed 8, 7 and 4 plies with corresponding thicknesses of 1 mm, 0.875 mm and 0.5 mm. The stacking orders were as follows:

$[0°_{16}]$, $[90°_{16}]$, $[\pm 45°_4]_s$, $[0°/90°]_s$,

$[0°/\pm 45°/90°]_s$, $[90°/\pm 45°/0°]_s$, $[0°_2/+45°/0°_2/-45°/0°/90°]_s$,

$[\pm 15°_2]_s$, $[\pm 30°_2]_s$, $[\pm 45°_2]_s$,

$[5°_{8,16}]$, $[10°_{8,16}]$, $[15°_{8,16}]$, $[30°_{8,16}]$, $[45°_{8,16}]$.

The individual plies were cut from the prepreg roll in 400×400 mm squares and laid up on a steel platen. On both sides of the stack peel plies and bleeder plies were provided. The laminates were then cured in a computer-controlled autoclave according to the

supplier's recommended curing cycles. Fig 3.2 illustrates the curing cycle for the 914C/T300 system. Subsequently, the laminates made from the material systems 1 and 2 were postcured at 190 °C for 4 hours, and at 180 °C for 3 hours, respectively. The laminates made from the material system 3, cured at 120 °C, required no postcuring. The laminates were then non-destructively examined, provided with tabs and cut to proper dimensions with a water-cooled diamond saw.

3.4 Traceability

In order to interpret the test results correctly, special precautions were taken to ensure the traceability of all parameters affecting the test specimen performance. Apart from the quality assurance data of incoming materials, records were established and maintained identifying each of the manufactured laminates in terms of material charge, production date, dimensions, stacking order and other parameters enumerated in Fig. 3.3. Fig 3.4 traces the subsequent history of the laminate and includes references to non-destructive evaluation and the sectioning of the laminate. The latter is shown in more detail in Fig. 3.5 which, in addition to the specimen designation and location, prescribes the intended test condition for each specimen as well as the areas reserved for non-destructive evaluation.

Wareneingangskontrolle Ende Rolle 5 — Prüfzeugnis Nr. — DFVLR - Braunschweig Datum

Technische Lieferbedingungen nach LN oder 29 971	Name und Anschrift des Herstellers Ciba - Geigy GmbH		
Handelsname des Erzeugnisses Fibredux 914C-TS-5-40 %	Prepreglieferform Rolle 1-5		
Vollständige Bezeichnung des Prepregs 914-CTS-5-40 %	Prepregbatch-Nr. 75/50 956	Herstelldatum 19.10.82	
Lieferschein-Nr. A 05809	Liefermenge 80 kg	Lieferdatum 25.11.82	Prüfzeugnis d.Herst.Nr. CF 2968
Faser type Toray T 6K	Faserbatch-Nr. [illegible]	Dichte der Faser 1,74 g/cm³	
Harz type 914	Harzbatch-Nr. 70/9625	Dichte des Harzes 1,3 g/cm³	Harzgehalt im Prepreg 40 %

Laminat-Nr.	628 / ψ_{HF} = 12,32 %	629 / ψ_{HF} = 11,4 %	630 / ψ_{HF} = 12,32 %	631 / ψ_{HF} = 10,3 %	632 / ψ_{HF} = 11,68 %	
Faseranteil	Gew% 69,68 Vol% 60,92	Gew% 68,8 Vol% 58,2	Gew% 71,48 Vol% 61,97	Gew% 67,32 Vol% 58,43	Gew% 67,89 Vol% 60,62	Gew% Vol%

Prüfung nach LN 29 971 bei Raumtemperatur	Symbol	Einheit	Lam. Nr.	Sollwert LN 29 971	Istwerte untere Abweichung	Istwerte obere Abweichung	Mittelwert	Bemerkungen
Flächengewicht (Faser)	m_T	g/m²		131 ± 3	131,37	132,99	132,10	9.12.82
Flächengewicht (Faser+Harz)	m_P	g/m²		219 ± 14	214,90	216,50	215,47	[illegible]
Harzgehalt	ψ_H	Gew.%		40 ± 2,5	38,57	38,92	38,69	
Flüchtige Bestandteile	ψ_{Fl}	Gew.%		≤ 2	0,456	0,440	0,45	12.1.
Effektive Dicke	s	mm		0,125				
Harzfluß	ψ_{HF}	Gew.%		(≤ 12)			11,6	
Klebrigkeit	F_k	N/cm		(5)	0,390	0,726	0,558	
Biegefestigkeit	$\sigma_{bB}0°$	N/mm²	628	1270	1675	1735	1705	
Biegemodul	E_b 0°	KN/mm²	⊥	112-140	117,37	118,63	118,0	
Biegefestigkeit	$\sigma_{bB}90°$	N/mm²	⊥	70	116,0	119,2	117,6	
Biegemodul	E_b90°	N/mm²	⊥	8000	8315	8455	8385	
Zugfestigkeit	σ_B 0°	N/mm²	629	1250	1483	1603	1543	
Zugmodul	E_z0°	KN/mm²	⊥	125-145	Mittelwerte aus drei Messungen		135,367	0,304 Querkontraktionszahl
Interlam. Scherfestigkeit	τ0°/±45°	N/mm²	632	64	76,7	84,3	80,5	
Interlam. Scherfestigkeit	τ0°	N/mm²	628	80	97,0	99,0	98,0	
Druckfestigkeit	σ_{dB}0°	N/mm²	⊥		1010	1190	1100	
Druckmodul	E_d0°	KN/mm²	⊥		Mittelwerte aus drei Messungen		118,039	0,317 Querkontraktionszahl
Schubfestigkeit aus Zugvers.	τ0°	N/mm²	631	(100)	97,0	104,8	100,9	
Schubmodul " ±45°	G0°	N/mm²	⊥	(5300)	Mittelwerte aus drei Messungen		5414,5	0,731 Querkontraktionszahl

Fig. 3.1 Record of quality control tests.

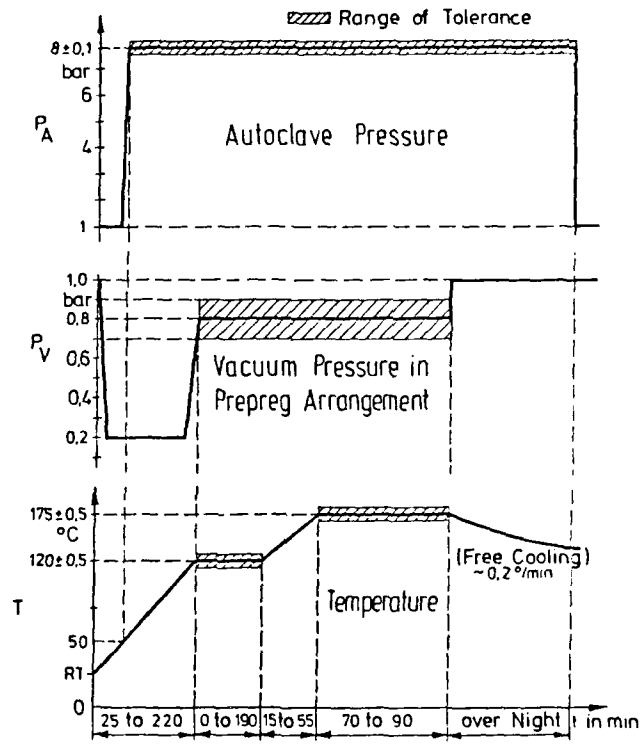

Fig. 3.2 Autoclave curing cycle for 914C-TS-5T.

Auftraggeber	Kostenträger
Lüerß	6P9

2. Herstellungsprotokoll für Prepreglaminate

Herstellungsdatum 10.5.83 — Platten-Nr. 252

Prepregsystem 914C-TS-5 Charge 25/50956 — Paket-Nr. IV/3

Lieferdatum 11.10.82

Prepreggew. vor d.Pressen 275,5 g, nach d. Pr. 240.2 g, Harzfluß

Position im Autoklaven: oben (X), unten

Meßplan für Istdicke (20, a, b):

086	090	088
088	089	089
087	0875	087

Laminataufbau

Abmessungen: a= 380 mm b= 380 mm Dicke,Soll= 0,875 Ist= ____

Lagen-Nr.	90° soll/ist	0° soll/ist	+45° soll/ist	-45° soll/ist	soll/ist	soll/ist
1	/	1/✓	/	/	/	/
2	/	/	2/✓	/	/	/
3	/	/	/	3/✓	/	/
4	4/✓	/	/	/	/	/
5	/	/	/	5/✓	/	/
6	/	/	6/✓	/	/	/
7	/	7/✓	/	/	/	/
8	/	/	/	/	/	/
9	/	/	/	/	/	/
10	/	/	/	/	/	/
11	/	/	/	/	/	/
12	/	/	/	/	/	/
13	/	/	/	/	/	/
14	/	/	/	/	/	/
15	/	/	/	/	/	/
16	/	/	/	/	/	/
17	/	/	/	/	/	/
18	/	/	/	/	/	/
19	/	/	/	/	/	/
20	/	/	/	/	/	/

Fig. 3.3 Record for identification of manufacture of laminates.

1 Lebenslaufkarte/Laufplan — Platten-Nr. 752

	Auftrag	Ausführung
2. Laminatherstellung		
2.1 Faser/Harz-System	914C-T5-5T	
2.2 Faserorientierungen	[0°, ±45°, 90°]s	
2.3 Schichtenzahl	-	
Datum/Zeichen	28.3.83 K	10.5.83 Hla
3. Zerstörungsfreie Prüf		
3.1 Prüfmethode	Röntgen	
Datum/Zeichen	28.3.83 K	
4. Probenherstellung	nach Schneidplan	
4.1 Prüfmenge/Zahl		
4.2 Probenart		26.5.83 Hla
5. Klimaprüfung	nach Plan	
5.1 Proben-Nr.		
5.2 Temperatur		
5.3 Feuchtigkeitsaufnahme		
Datum/Zeichen		
6. Festigkeitseigensch	nach Plan	
6.1 Proben-Nr.		
6.2 Belastungsart		
6.3 Temperatur		
6.4 Feuchtigkeitsaufnahme		
Datum/Zeichen		
7. Schwingfestigkeit		
7.1 Proben-Nr.		
7.2 Zahl der Lasten		
7.3 Art der Schwingbelastung		
7.4 Temperatur		
7.5 Feuchtigkeitsaufnahme		
7.6 Art der Bruchbelastung		
7.7 Temperatur		
7.8 Feuchtigkeitsaufnahme		
Datum/Zeichen		

Bemerkungen:

Die Druckproben vorerst nicht zuschneiden

752

T: 1'1.5'

Rö. Pr ++

Fig. 3.4 Record for history of a laminate with reference to nondestructive evaluation.

DFVLR Deutsche Forschungs- und Versuchsanstalt für Luft- und Raumfahrt e.V.

Forschungsbereich

SCHNITTPLAN

FK-Platte : 752

DFVLR-Bezeichnung: ESA - Standart 3

Laminataufbau: [0₂/90₂/±45]$_S$

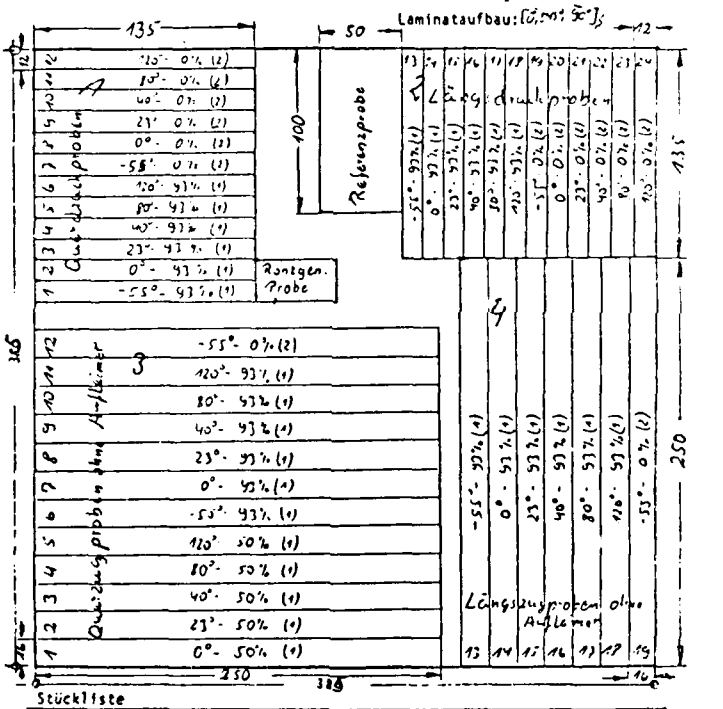

Stückliste

Stück	Abmessungen in mm	Orientierung zur Deckschicht	Probe	Bemerkung
12	250 x 16	senkrecht	1-12	
7	250 x 16	parallel	13-19	
12	135 x 12	senkrecht	1-12	Proben dürfen nach Schliff zusammengeklebt werden
12	135 x 12	parallel	13-24	-"-

Fig. 3.5 Record of intended sectioning of a laminate.

4. NONDESTRUCTIVE EVALUATION

4.1 Summary

The nondestructive evaluation of test specimens is mandatory to assure the absence of defects at the beginning of a test, and to monitor their initiation and growth during the test. In carbonfiber-reinforced laminates the problem arises to not only detect the presence of a defect but also to identify it with respect to kind, size and location [4.1]. Evidently, no single nondestructive technique can cover the numerous forms of potential damage in such laminates so that several complementary methods must be employed whose selection depends on the nature of the test program. The radiographic and ultrasonic techniques are well established and can, combined with each other, cover most of the interesting aspects of damage propagation by yielding well-focussed photographs and scans, respectively. X-ray photographs show even small cracks, whereas the ultrasonic C-scans are better suited for the detection of two-dimensional defects as delaminations. B th techniques are stationary (like the destructive test methods), i.e., the test specimens are inspected outside the test machine in a separate laboratory. The spatial resolution of both the radiographic and the ultrasonic technique is remarkable. On the other side, the *in-situ* techniques pursue the process of defect propagation immediately under load. They are characterized as quasi-nondestructive, i.e., the specimens are indeed damaged *during*, but not *by* their application. The acoustic emission analysis is particularly suited for the resolution of the damage progression process with respect to time and time-dependent parameters. The other *in-situ* technique used in the Institute of Structural Mechanics is the grating reflection technique which yields photographs showing the surface deformations of the specimens under evaluation. The individual strength, and weaknesses of these techniques are summarized in Fig. 4.1.

The potential of the acoustic emission and of the grating reflection technique are described in more detail in Appendices A and B.

4.2 Radiography

The radiographic principle allows the detection of variable mass distributions in laminates of uniform thickness which implies that radiography allows the detection of porosities, inclusions of foreign matter, and of matrix cracks. The central problem is the realization of sufficiently high degrees of contrast which, in view of the low molecular weight of the carbonfibers and the attendant inability to absorb high energy radiation, requires the application of low voltage X-rays in the range from 10-100 kV. The quality of radiographic investigations is influenced also by their lateral resolution which depends on the radiation source and the geometry of the test specimen.

In the case of externally accessible cracks or delaminations the contrast can be enhanced by the application of high density liquids such as tetrabromethane (TBE) or diiodinemethane capable of penetrating into extremely thin crevices, although care must be taken to guard against chemical reactions between the resin and the contrasting agent. Typical examples of radiographic records are displayed in Fig. 4.2, showing the crack formation in a notched tensile test specimen and the extent of an edge delamination, respectively, after diiodinemethane-treatment.

4.3 Ultrasonic Techniques

All ultrasonic techniques are based on the emission of an acoustic impulse into the test specimen and the evaluation of the measured energy flux. According to the kind of measurement one differentiates between the pulse-echo technique and the through-transmission technique. Both techniques have been in use for decades; however, their adaptation to carbonfiber-reinforced laminates is encumbered by the high sound attenuation of the material which leads to low signal-to-noise ratios. A modification of standard equipment requires at least highly damped transducers and a narrowband transmitter with variable pulse frequency. New investigations show a further improvement in using a receiver filter-technique (EF-System), which has been developed in the Institute of Structural Mechanics [4.2]. In order to

obtain reproducible coupling between transducer and laminate surface, the actual testing is performed under water.

Fig. 4.3 shows the ultrasonic test setup and identifies, schematically, four types of echo signals: 1) the front surface echo with the shortest transit time, 2) the defect echo in case a defect exists, 3) the back surface echo and 4) the bottom echo. In the pulse-echo technique the comparison of echo signals occurring between the front and back surfaces to prescribed threshold values is used as a criterion for the existence or non-existence of a defect at the point in question. Evidently, the location of the defect echo identifies also the depth of the defect. By systematic movements of the transducer the entire laminate can be scanned and the lateral extent of the defects made visible by yes-no or black-white signals at neighboring points in the form of a two-dimensional C-scan as shown, typically, in Fig. 4.4.

Alternatively, the intensity of the back-surface echoes or the bottom-surface echoes can be used as critical parameters for yes-no decisions. In the presence of a defect the echoes will be attenuated and returned to the transducer with diminished amplitudes whose comparison to nominal values will produce the desired C-scans. Instead of yes-no decisions it is also possible to record the inverse values of the amplitudes themselves and construct C-scans of the form shown in Fig. 4.5. From these figures it can be deduced that the ultrasonic facilities at the Institute for Structural Mechanics allow the reproducible identification of delaminations with diameters of $d \leq 0.5$ mm.

4.4 Acoustic Emission Analysis

The analysis of acoustic emissions resolves the irreversible process of damage progression with respect to time-dependent parameters. It supports the interpretation of individual phases of damage growth as well as the dynamics of the process as a whole [4.3].

Under sufficiently high loads mechanical energy will be released at critical locations of a test specimen, e.g., a crack tip. The

energy release is accompanied by the creation and propagation of acoustic waves which can be sensed by piezoceramic transducers and on account of the elongations of the piezoelectric crystals evaluated in terms of electric voltages. Fig. 4.6 is a representation of the electric signals associated with a typical acoustic emission and recorded with modern equipment. In the course of such an event the amplitudes of the acoustic wave exceed a predetermined threshold value a number of times which is referred to as count number. Recorded also can be the onset and duration of the event in real time, the peak amplitude, the rise time to reach the peak and the energy content of the event. It is further possible to perform frequency analyses of the acoustic wave at given points in time. Fig. 4.7 shows a typical acoustic emission evaluation in different ranges of time resolution.

The proper identification of these signals requires skill and experience. The Institute for Structural Mechanics has succeeded in using acoustic emission analyses for the location of acoustic emissions in slender test specimens and for the differentiation between fiber breaks and matrix cracks [4.4].

4.5 Grating Reflection Techniques

The principle of this optical in-situ technique is illustrated in Fig. 4.8 [4.5]. The human eye, or a camera, C, observes on the mirror surface of the test specimen the reflection of a regular illuminated grating, G. If the surface of the test specimen changes its slope locally then, at constant angle of view, a point P on the grating perceived previously will be replaced by a different point P', i.e., the initially parallel lines of the reflected grating move in consonance with the deformations of the test specimen. Fig. 4.9 shows the onset and progression of edge delaminations as registered by the distortions of the grating [4.6]. Apart from the significance of such qualititive indications it is also possible to obtain quantitative data by the evaluation of precise measurements.

4.6 References

[4.1] Hillger, W.
Schütze, R.
Non-Destructive Testing of CFRP Laminates. In: Damage Mechanics of Fibre-Reinforced Composite Materials. ESA-TT-758 (1982), pp. 9-46.

[4.2] Hillger, W.
Ultraschallprüfung von CFK-Laminaten mit hoher Auflösung und Reproduzierbarkeit in Impuls-Echo- und Durchschallungstechnik. Proc. 3rd European Conf. on NDT 15.-18. Oct. 1984 Florence, Vol. 5, pp. 12-22.

[4.3] Block, J.
Methods of Non-Destructive Testing of CFRP Laminates. In: Contributions on the Properties of Carbon Fibre Reinforced Composites. ESA-TT-849 (1984), pp. 105-154.

[4.4] Block, J.
Charakterisierung von Schadensfortschritten in CFK-Laminaten mittels Schallemissionsanalyse. DFVLR-IB 131-84/51 (1984).

[4.5] Ritter, R.
Hahn, R.
Contribution to Analysis of the Reflection Grating Method. Optics and Lasers in Engineering 4(1983), pp. 13-24.

[4.6] Schütze, R.
Goetting, H.C.
Ausbreitung von Randdelaminationen in multidirektionalen CFK-Laminaten unter quasistatischer Zugbelastung. DFVLR-IB 131-84/23 (1984).

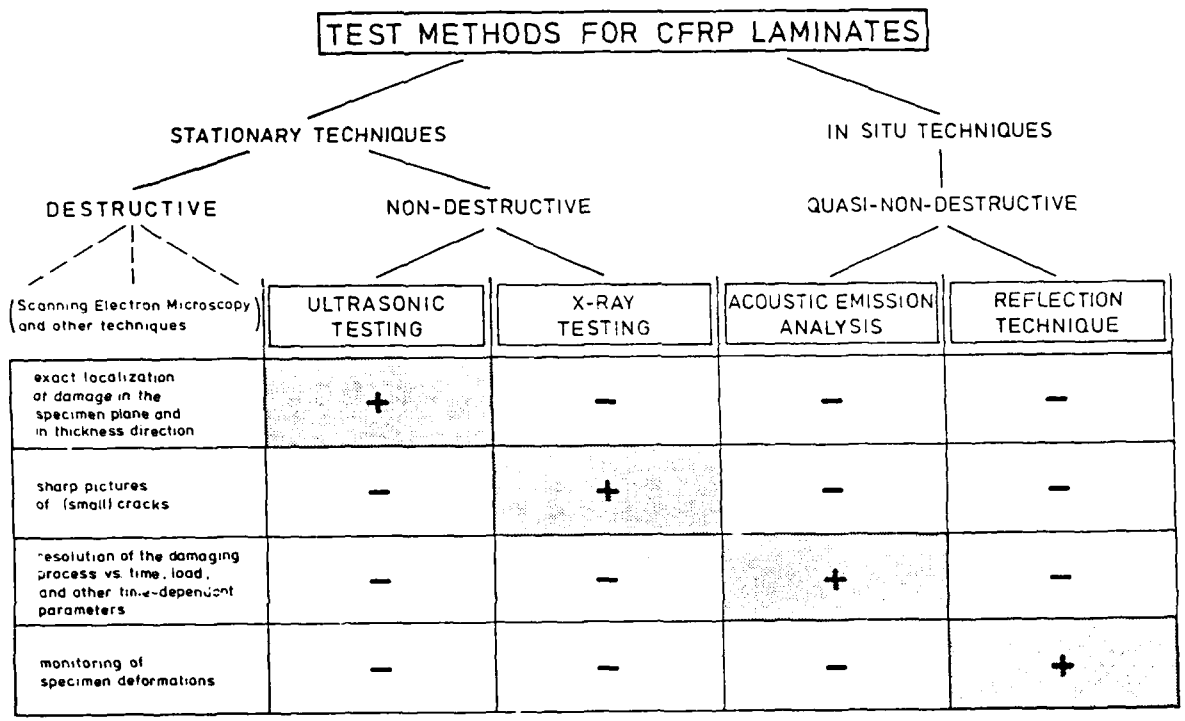

Fig. 4.1 Scope of the NDT techniques used in the Institute for Structural Mechanics.

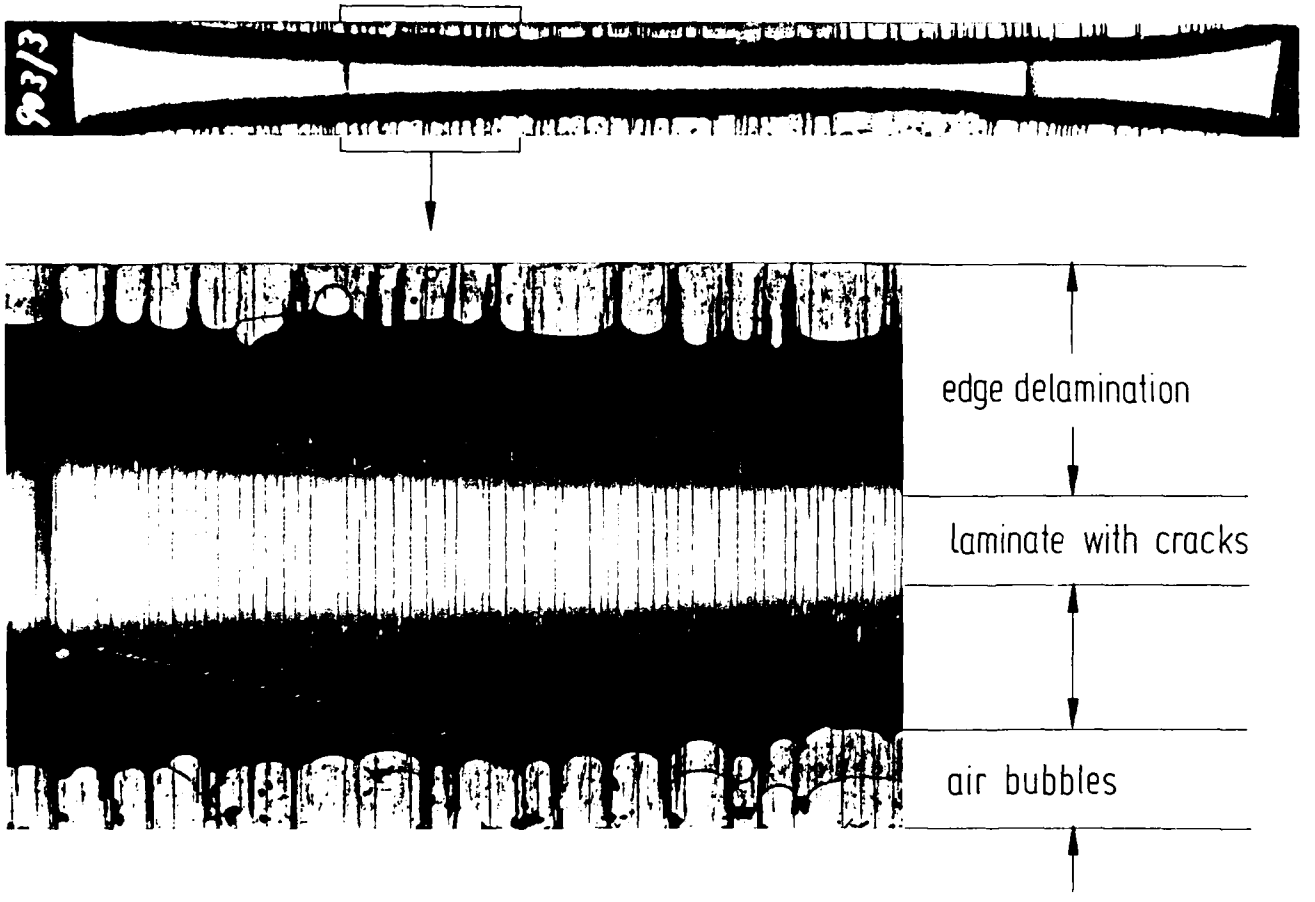

Fig. 4.2 X-ray photograph of a CFRP laminate with cracks and edge delaminations.

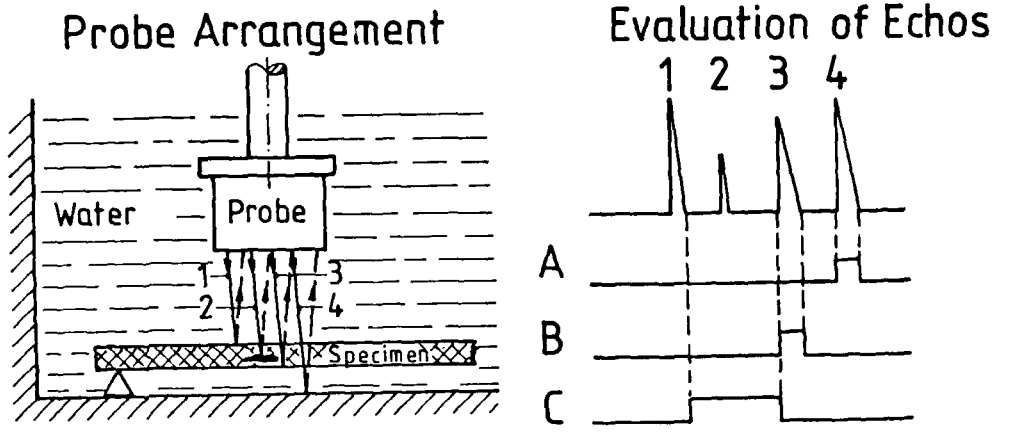

1 Surface Echo
2 Flaw Echo
3 Backwall Echo
4 Reflector Plate Echo

A Double-Transmission-Technique
B Double-Transmission-Technique
C Echo-Technique

Fig. 4.3 Principle of ultrasonic immersion techniques.

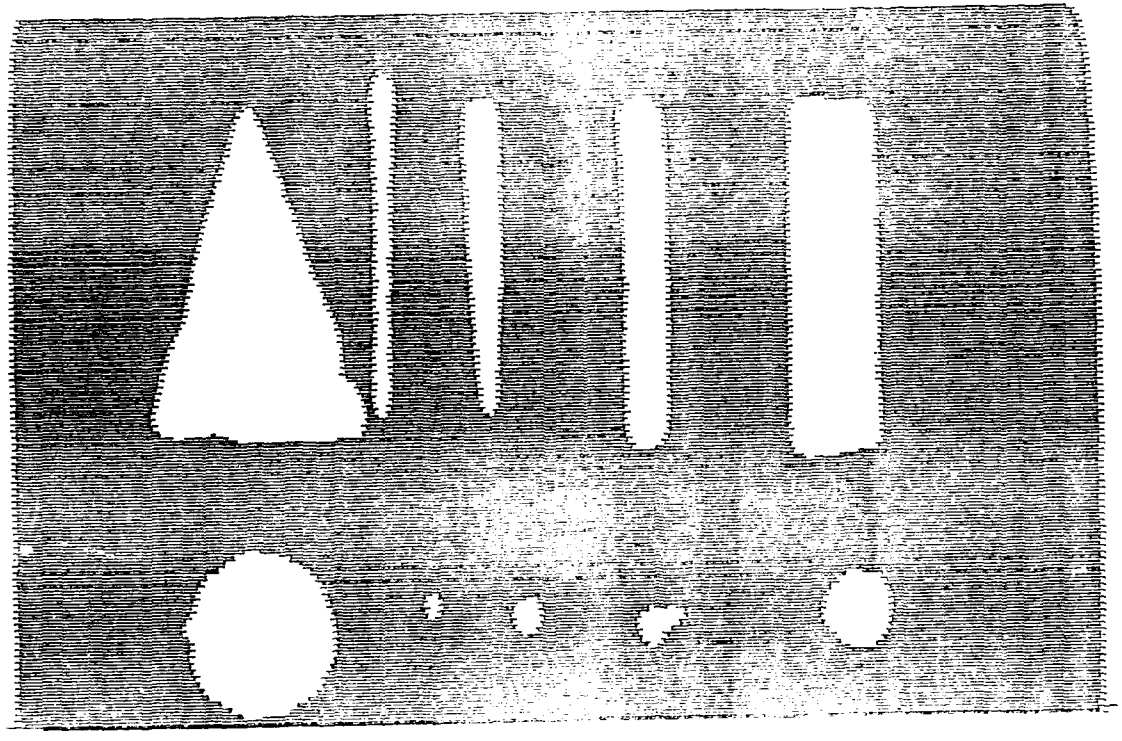

Fig. 4.4 Ultrasonic C-scan of a laminate with artificially inserted delaminations.

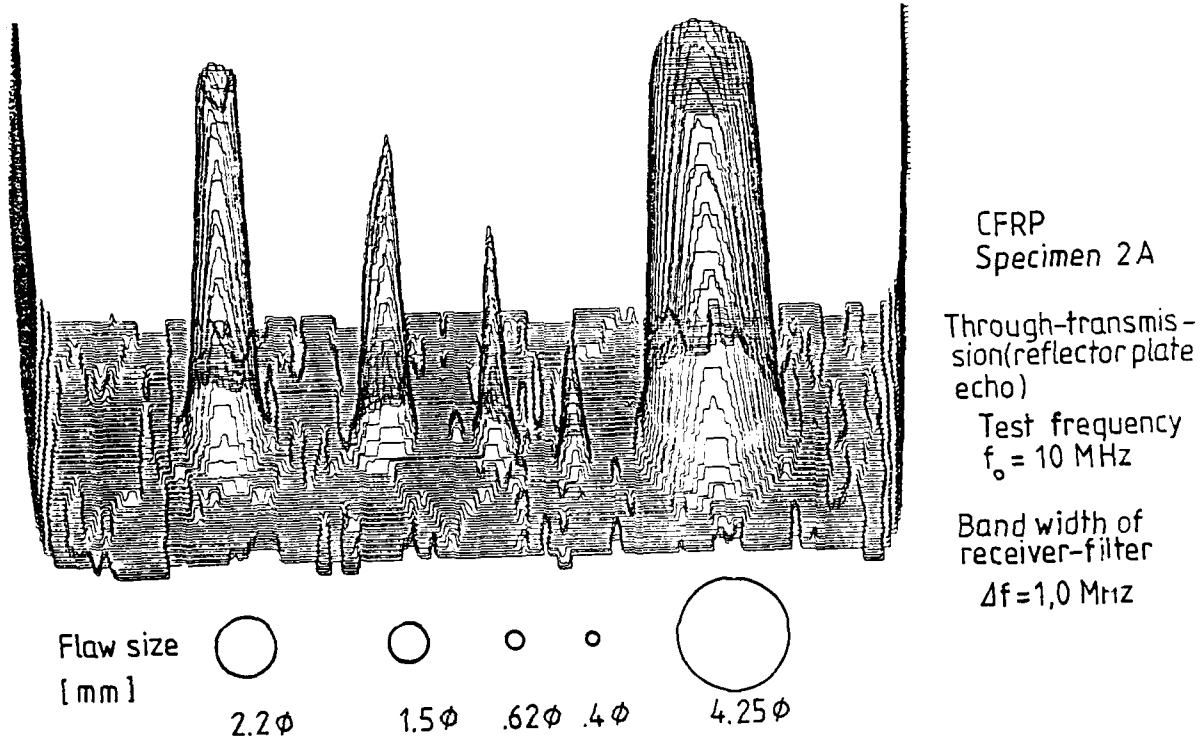

Fig. 4.5 Record of inverse ultrasonic amplitudes obtained from a laminate with circular delaminations.

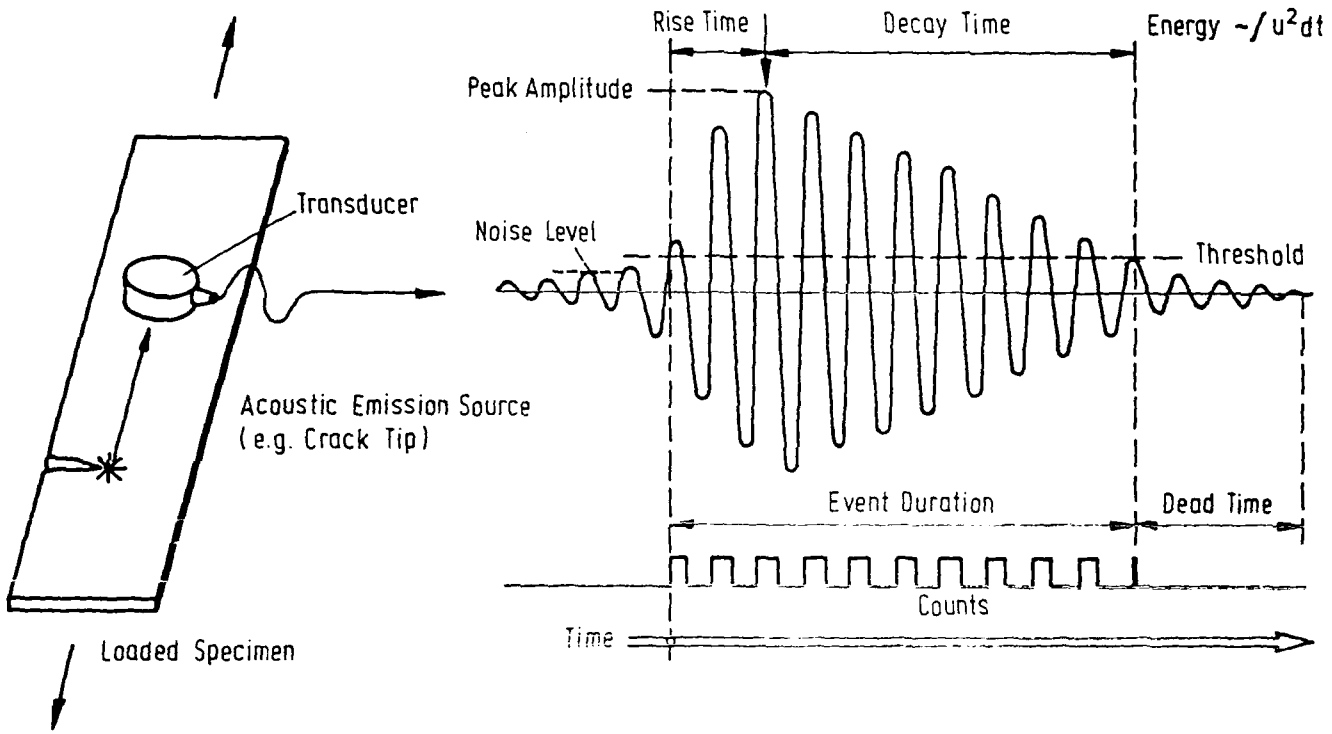

Fig. 4.6 Principle of acoustic emission analysis.

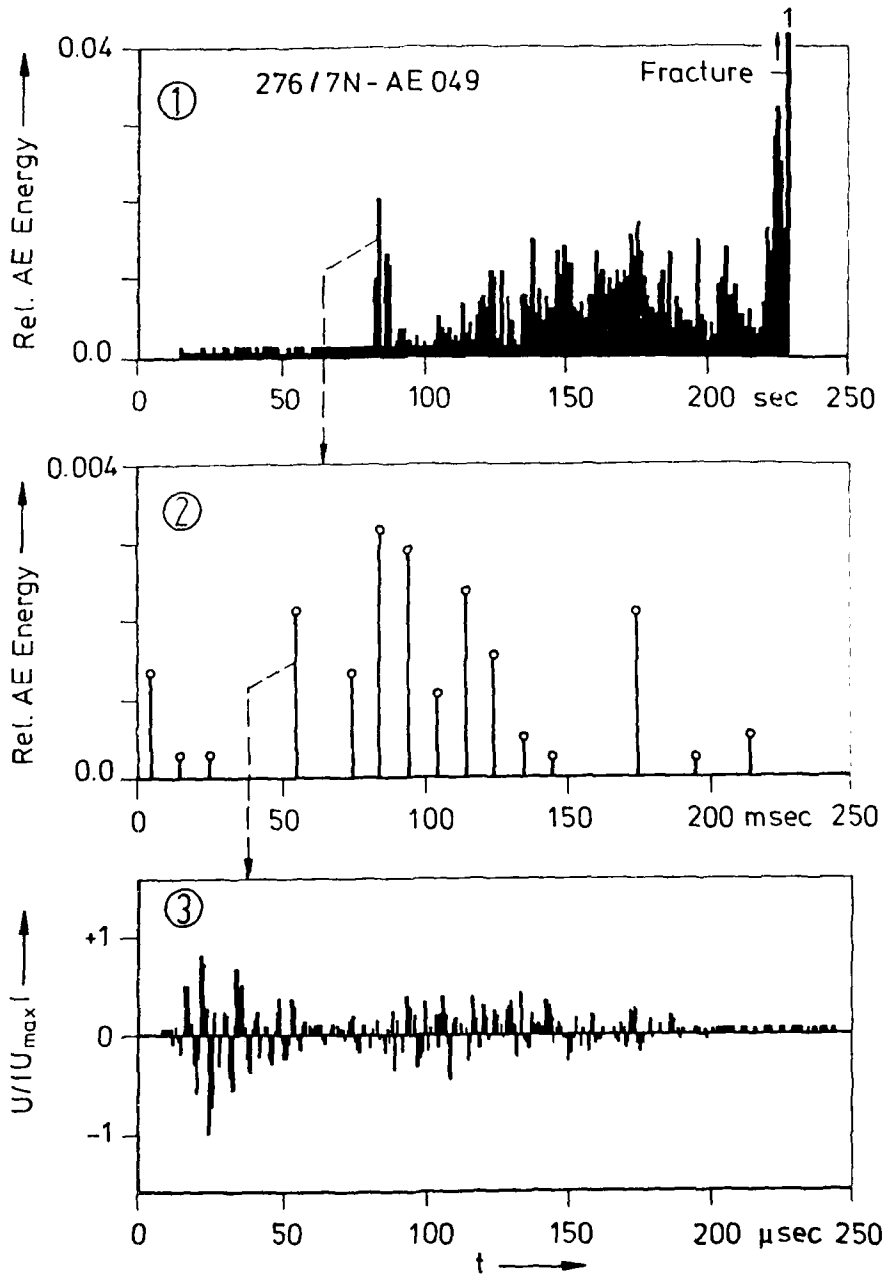

Fig. 4.7 Different ranges of time resolution for AE tests.

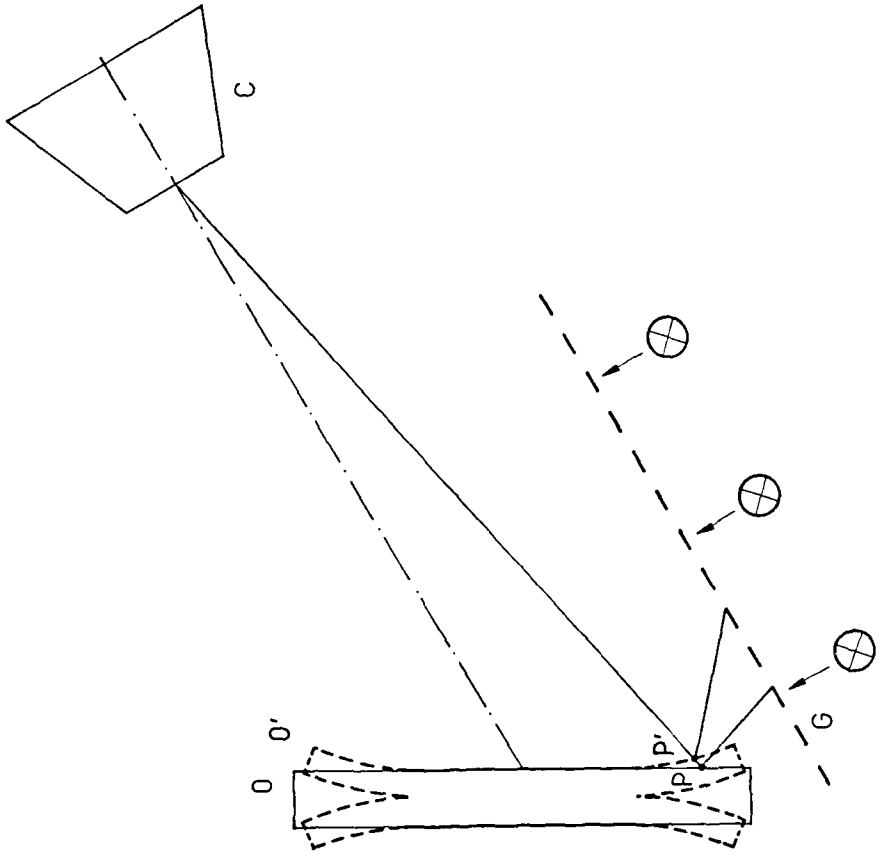

Fig. 4.8 Principle of grating reflection technique.

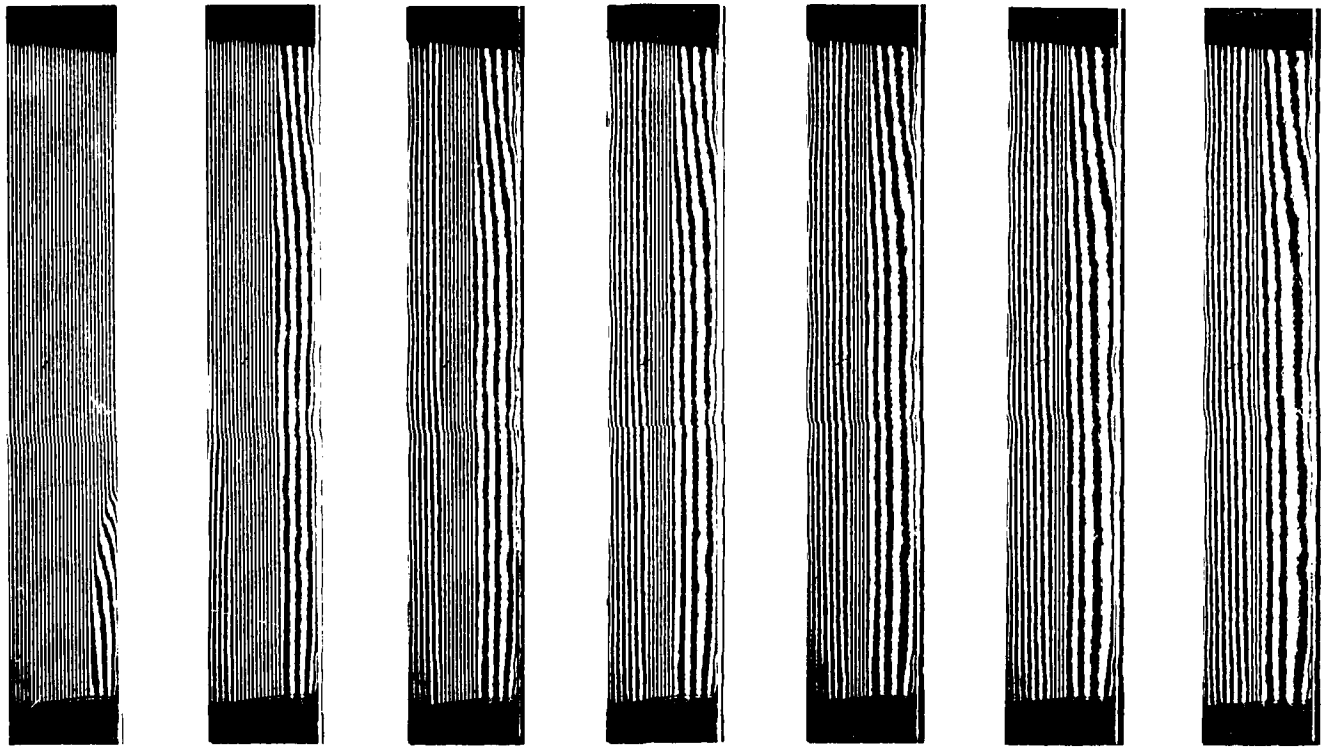

Specimen No 903/1 Stacking sequence $[0_2^\circ, +45^\circ, 0_2^\circ, -45^\circ, 0^\circ, 90^\circ]_s$

Fig. 4.9 Onset and growth of edge delaminations monitored by the grating reflection technique.

5. ANALYSIS TOOLS

5.1 Summary

In the course of the research program the need for analytical support arose in connection with the treatment of large numbers of test results and with the assessment of stress distributions leading to damage progression or fracture.

Carbonfiber-reinforced laminates, even when carefully prepared and tested under ideal conditions, exhibit a certain scatter in their characteristic values. The evaluation of such values by statistical means enhances the interpretation of the data and contributes to the understanding of the fracture processes.

With respect to stress analyses, the complexity of most problems defy closed-form solutions and require computerized finite- element techniques. In principle, general purpose programs like ASKA are capable of coping with most of the arising issues and were successfully utilized. However, the necessary degree of refinement of the element meshes leads to exorbitant computing costs especially in the iterative solutions of nonlinear problems. Another shortcoming of the standard codes is the lack of specific failure criteria for the tracking of damage propagation in laminated composites. For these reasons the development of a new special purpose-computer program LAMINA was initiated. Its basic component is a triangular hybrid plate element with degrees of freedom for bending and membrane action as well as for normal and shearing stresses on its upper and lower surfaces. A special condensation scheme was introduced for producing multilayer plate elements as well as substructures so that arbitrarily stacked laminates can be modelled in great detail with a relatively small number of degrees of freedom. Failure progression criteria are appended to the system of simultaneous equations in such a way that the tracking of the damage progression does not require repeated triangularization of the global stiffness matrix.

Appendix C "Eine effektive Teilstrukturtechnik angewendet auf Bruchprobleme" treats the development of the LAMINA program in more detail.

5.2 Statistical Data Treatment

The measured data sets from the experimental test series were subjected to a significance test (T-test) with the aim of determining whether observed differences in the properties of two random sample sets were due to accidental scatter or to the influence of environmental conditions. As a prerequisite for the T-test, a so called F-test was performed in which the variances of the two random samples sets were compared. This test determines whether significant or non-significant differences exist between the two variances and identifies the size of the sample sets for the T-test. The T-test ultimately compares the mean values of the random sample sets and establishes whether one of the environmental parameters is of influence or not. Both the T-test and the F-test were conducted on the basis of a confidence level of 5%. A requirement for the application of the significance test is an approximately normal distribution of the data sets resulting from static tests. In the case of fatigue data it was checked whether the measured life cycles fitted the Weibull-model based on a two parameter distribution law [5.1].

The results are graphically displayed in the form of probability diagrams, shown typically in Fig. 5.1, in which the distribution functions are represented as straight lines so that a linear regression of the measured test data can be expected. The level of confidence associated with the data sets, in context with a given distribution law, was identified by means of upper and lower confidence bands for the entire regression function. The confidence bands are based on a confidence level of 5% or 10%. The width of the confidence bands, of course, depends on the number of random samples and on the scatter of the individual data about the regression function; however, if the amount of scatter is within reasonable bounds, sets of 8-12 individual random samples suffice for rather narrow confidence bands. In the majority of cases it could be demonstrated that a normal distribution of static data

prevailed and that the failure rate of fatigue data follows the Weibull model. Fig. 5.2 contains characteristic scatter values, characteristic distribution parameters and an approximated density function.

5.3 Computer Program ASKA

Finite element programs have proven to be capable of solving a wide variety of structural problems. One of the most thoroughly developed codes available is ASKA (Automatic System for Kinematic Analysis), originated by the ISD at the University of Stuttgart. Of the many features in ASKA, only the linear static analysis part was used for two specific tasks [5.2].

For the assessment of the edge effect encountered in test specimens of multidirectional laminates, stress analyses were performed with physical models comprised of the pentahedron element PENTA18 and the hexahedron element HEXE27. Anisotropic material properties were assigned to every element. The approximation of the free edge stresses required up to 16 such elements over the thickness of one layer, resulting in stiffness matrices of very high orders. With the aid of a multilevel substructuring technique, the computational efforts could be considerably reduced. Special purpose programs were written for generating the input data as well as plotting the stress distributions.

In regard to stress intensity factors, ASKA was applied to determine this property for notched unidirectional laminates. Reliable results can only be achieved if the element grids show a considerable mesh refinement in the vicinity of the crack tip [5.3]. Such grids, mainly from the triangular membrane element TRIM6, were generated by a self-developed preprocessor which is capable of handling different fiber directions and different crack lengths. The analysis results served also as a guide line for the inclusion of a damage progression model into the LAMINA program.

5.4 Computer Program LAMINA

A detailed three-dimensional stress analysis in laminated composites necessitates a rather fine element grid in the plane of the laminate as well as in the thickness direction. The resulting systems of linear equations are large and their numerical solution is costly.

In the case of non-linear problems the system of equations must be solved iteratively with considerably increased numerical effort. The computer program PAM-FISS of Engineering System International (ESI) requires for a crack analysis, for example, a modification and new solution of the system of equations after every progression of the crack. The associated computing effort makes the solution of even more complicated problems without benefit of one or more axes of symmetry practically impossible.

Physically non-linear phenomena such as rupture, plastic flow, microcracks, friction, etc., may be interpreted as constraints which act on the linearly elastic structure. In finite element formulations these constraints augment the system of equations rather than change it, i.e. the matrix of coefficients needs to be assembled and partitioned only once (Fig. 5.3). In case of a propagating crack only the newly arising and the immediately preceding constraints must be newly formulated and partitioned. The resulting iterative process is very fast at the cost, however, of non-positive-definite systems of equations with varying order.

Relative to the overall structural dimensions the damaged zones in a laminate are small, so that major portions of the structure are linearly elastic and can be represented as substructures. The substructures are set up only once and then used repeatedly during the successive calculation process of the damaged zone. A rather simple modification of the equation-solving algorithm allows a straight-forward development of the substructures (Fig. 5.4 and Fig. 5.5). This new technique accommodates readily the method of boundary equations for the treatment of physical non-linearities as in both cases the external variables are treated identically.

For the efficient solution of such problems no computer program is currently available. An extension of existing finite-element codes did not appear sensible because an adaptation of such a code would further complicate the already intricate program organization for stepwise growing systems of equations. Therefore, the development of a special computer program with the acronym LAMINA was initiated.

The program LAMINA was conceived especially for the investigation of physically non-linear problems. The INCORE-version for linearly elastic structures has been completed and contains the following special features:

- the systems of equations must be symmetric but need not be positive-definite;
- variation of boundary values and load cycles are admissible;
- the number of unknowns in the systems of equations can be stepwise increased;
- an efficient substructure routine allows the partitioning and coupling of arbitrarily divided structural segments, the sequence of the unknowns to be coupled being unconstrained;
- identical elements or substructures are recognized and calculated only once;
- the calculation of I-integrals and energy release rates according to the crack closure method are included.

Presently a plot routine is being implemented for the graphic display of stress intensity factors. The program at this time operates with an extended beam element especially developed for a precise calculation of interlaminar stresses. Crack and fracture criteria are not yet automated parts of the program but can be simulated by appropriate coupling of substructures [5.4].

5.5 References

[5.1] v.Bonin, L. Die Untersuchung der Vertrauenswürdigkeit von gemessenen Festigkeitswerten an Probestäben aus CFK mit Hilfe statistischer Methoden (I). DFVLR-IB 131-84/11 (1984).

[5.2] ASKA Part I - Linear static analysis. User's reference manual, ISD-Report No. 73, UM202 (1971).

[5.3] Rohwer, K. Stresses and Deformations in Laminated Test Specimens of Carbon Fiber Reinforced Composites. DFVLR-FB 82-15 (1982).

[5.4] Eggers, H. Eine effektive Teilstrukturtechnik angewendet auf Bruchprobleme. DFVLR-IB 131-84/45 (1984).

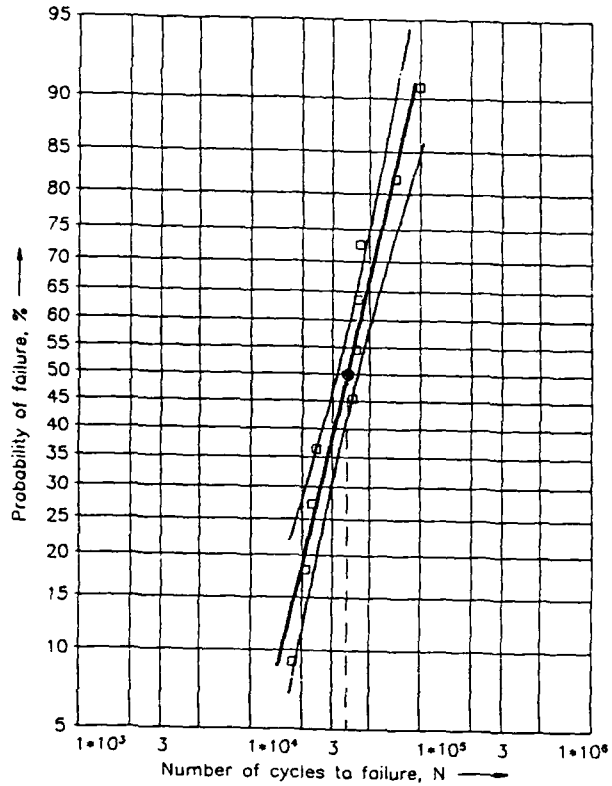

Fig. 5.1.a Cumulative frequency distribution as a linear function on normal distribution probability paper as a means for the estimation of the distribution function with the aid of measured values.

Coefficient of correlation for the probability of failure and number of cycles to failure in the probability paper of the normal distribution

$R_w = .971$

$N_{min} = 17670$ $N_{max} = 99865$ Range SW = 82195

Characteristic life parameter $N_{10\%} = 15187$ $N_{90\%} = 88791$

Extent of scatter $T = N_{90\%} / N_{10\%} \approx 5.846$

Standard deviation $\sigma = 36094$

Frequency distribution function

$$f(N) = 1.105 \cdot 10^{-5} \exp\left[- \frac{(N - 3.672 \cdot 10^4)^2}{2.606 \cdot 10^9} \right]$$

Expected value $E(N) = N_{50\%} = 36722$

Variance $Var(N) = \sigma^2 = 1.303 \cdot 10^9$

Coefficient of variation $V = \sigma / N_{50\%} = 9.829 \cdot 10^{-1}$

Distribution function and hazard rate not presentable.

Fig. 5.1.b Parameters and characteristic values of the approximated probability distribution.

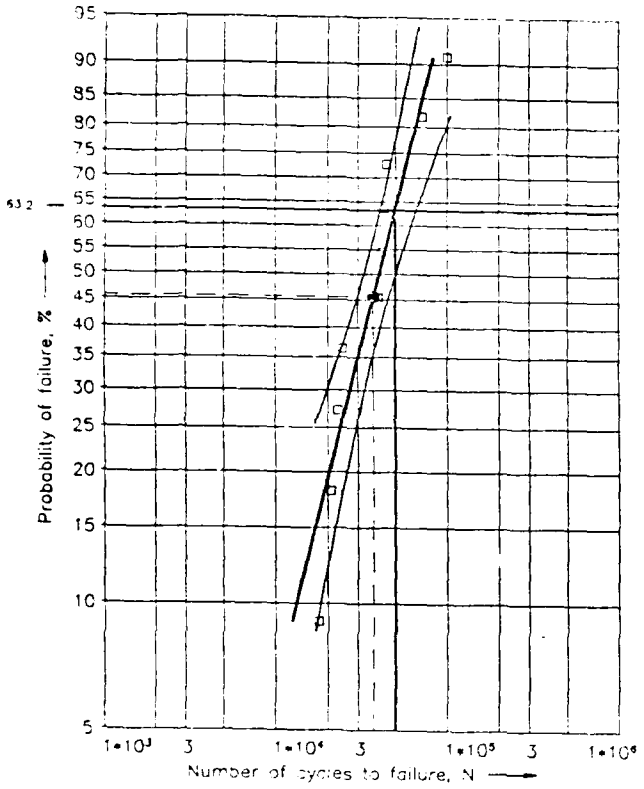

Fig. 5.2.a Cumulative failure frequency as a linear function on two parameter Weibull distribution probability paper as a means for the estimation of the distribution function with the aid of measured values.

[illegible] the probability of failure and the number of cycles to failure in the Weibull probability paper

R_e = .944

N_{min} = 17670 N_{max} = 99365 Range SW = 82195

Characteristic life parameter N_a = 49130

$N_{10\%}$ = 13078 $N_{90\%}$ = 93697

Extent of scatter T = $N_{90\%} / N_{10\%}$ = 7.165

Weibull shape parameter β = 1.700

Frequency distribution function

$$f(N) = 1.800 \cdot 10^{-8} \; N^{.700} \exp\left[-\left(\frac{N}{49130}\right)^{1.700}\right]$$

Weibull distribution function $F(N) = 1 - \exp\left[-\left(\frac{N}{49130}\right)^{1.700}\right]$

Hazard rate $h(N) = 1.800 \cdot 10^{-8} \; N^{.700}$

Expected value E(N) = 43845

Variance Var(N) = $7.007 \cdot 10^8$

Coefficient of variation V = $6.037 \cdot 10^{-1}$

Skewness S_3 = 1.977

Fig. 5.2.b Parameters and characteristic values of the approximated probability distribution. (Working life analyses)

Constrained functional :

$$\dot{j}^P = \dot{j}^E(\dot{\sigma}^{ij}, \dot{v}_i, \dot{\bar{p}}^i) - \int_{Fp} \dot{\varepsilon}^P \cdot (\dot{y}_{ij} \cdot \dot{\sigma}^{ij} - \frac{1}{2}\hat{H}\cdot\dot{\varepsilon}^P)\, dF = \text{stat.}$$

$\dot{\varepsilon}^P$ = Plastic strain increment

Finite transformation :

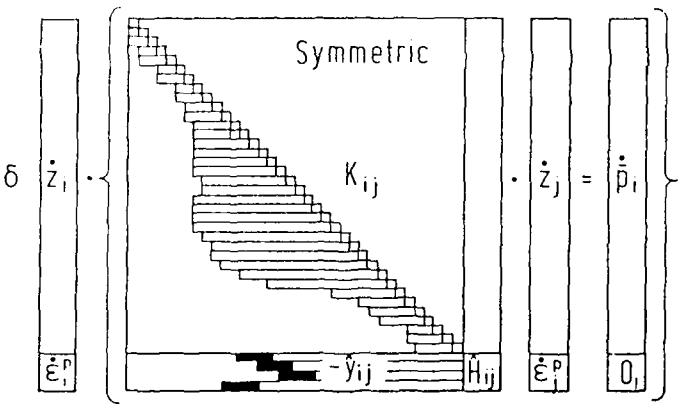

Figure 5.3 Finite transformation for a linear elastic structure augmented by yield conditions

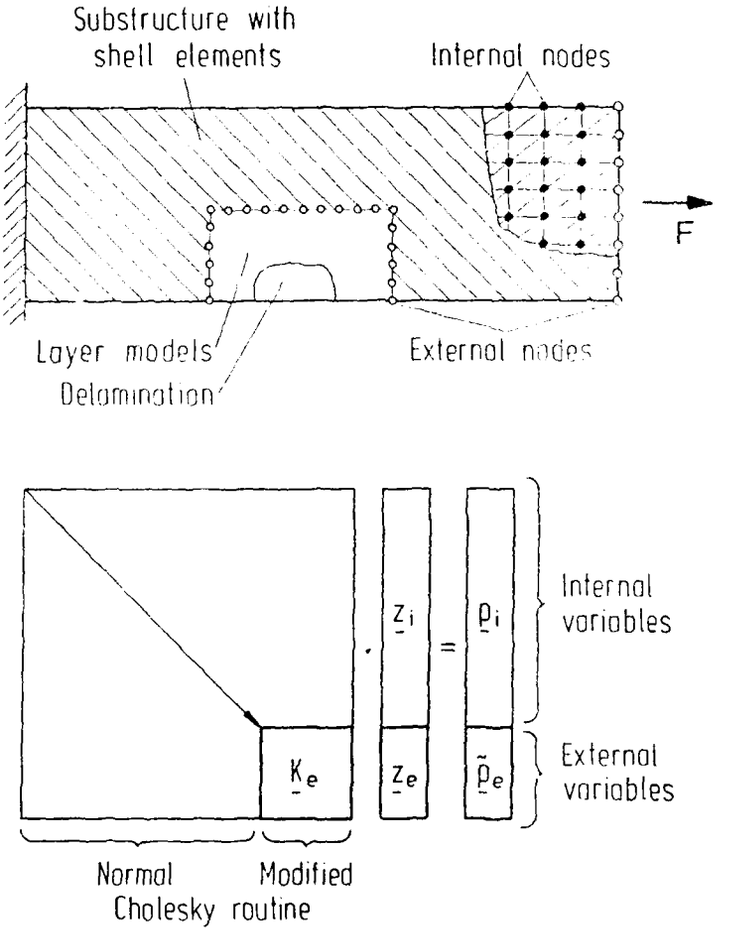

Figure 5.4 Substructure technique

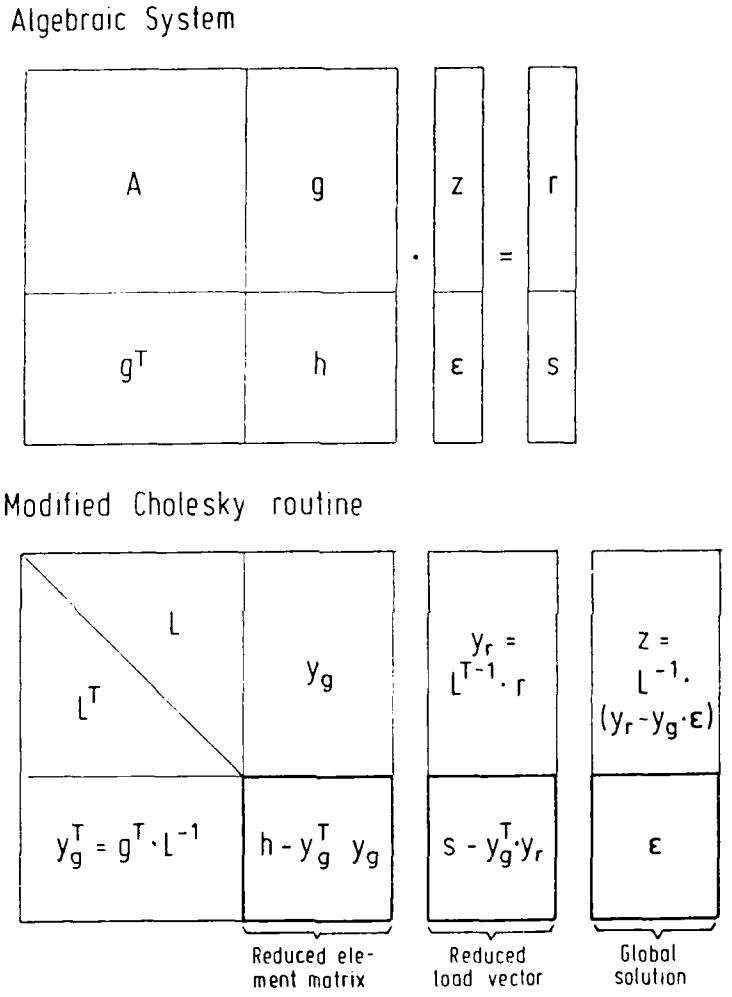

Figure 5.5 Modelling of substructures with a modified Cholesky-routine

6. RESPONSE OF STATICALLY TESTED UN-NOTCHED SPECIMENS

6.1 Summary

It is a major advantage of fiber-reinforced laminates that the fiber direction and the stacking order of the individual plies can be arranged such that they match the load paths of the structure. As the load paths differ from location to location, several different laminate configurations ought to be employed in the efficient design of a fiber-reinforced structure. Unless the properties of multidirectional laminates with arbitrary ply arrangements can be predicted analytically, they must be derived by time- and cost-consuming test programs. A promising approach to such predictions is the synthesis of multidirectional laminates based on the well-defined characteristics of unidirectional plies established by test. The attempted forecasts are complicated by the nonlinear constitutive laws of the laminates and by the susceptibility of the matrix systems to temperature and moisture.

6.2 Test Program

The corresponding test program comprised the determination of all pertinent properties of unidirectional plies for three fiber-matrix systems of carbonfiber-reinforced epoxies (CFRE) under the temperature and moisture conditions displayed in Fig. 6.1. These properties form the basis for the analytical prediction of the response of the multidirectional laminates identified in Fig. 6.2. The predictions include the elastic moduli, first ply failure and tensile strength of the laminates and take into account the state of prestress induced by temperature and moisture. Additional tests were performed with multidirectional laminates to validate the analytical predictions and to support the failure analysis. The following chapters focus on the essential features of the related efforts.

6.3 Influence of Moisture

Most polymeric materials absorb moisture by diffusion. In epoxy resins, e.g. Fibredux 914, the maximum moisture content may amount to 9 % of the initial dry weight. The absorbed water molecules influence the elastic modulus of the resin as well as its elongation as shown, typically, in Fig. 6.3. Another effect of moisture absorption is a volumetric change, the so-called swelling of the resin. The swelling strain is expressible as the product of the swelling coefficient α_Q and the change of moisture percentage ΔM [6.1],

$$\varepsilon_Q = \alpha_Q \, \Delta M.$$

Carbon fibers as such are unaffected by moisture, but in fiber-reinforced laminates they are subject to stresses and strains resulting from the fiber-matrix interaction. Swelling coefficients for unidirectionally reinforced laminates are displayed in Fig. 6.4 [6.2]. It is apparent that swelling occurs predominantly normal to the fiber direction, and that the deformation constraints in crossplied laminates can induce very sizable prestresses.

6.4 Influence of Temperature

The effects of temperatures on epoxy resins are similar to those produced by moisture. At elevated temperatures the stiffness properties diminish and the elongation to failure increases. The resulting volume changes are governed by the thermal strain

$$\varepsilon_T = \alpha_T \, \Delta T.$$

As in the case of moisture the carbon fibers remain dimensionally stable and produce interaction stresses in fiber-reinforced laminates. The strength reduction and the increase of shear deformation of a typical epoxy resin, and the coefficients of thermal expansion for three types of thermosetting resins are given in Fig. 6.5 and Fig. 6.6, respectively [6.3]. Using, at moderate temperatures, a mean value for the coefficient of thermal expan-

sion of the resin and the carbon fibers, the expansion coefficients for unidirectionally reinforced laminates can be calculated and are displayed in Fig. 6.7. Again, the more significant strains occur in the direction transverse to the fibers, so that a high state of prestress must be associated with crossplied laminates [6.4].

6.5 Properties of Unidirectional Laminates

Because of the discrepant thermal coefficients of carbon fibers and epoxy resins, prestresses are induced in the course of the curing process of the laminates by the difference between the lock-on and the ambient temperature. These prestresses affect to some extent the strength of laminates tested under different temperatures, however, no attempt has been made to account analytically for their presence. The test results of the laminates described in the subsequent sections are displayed in three-dimensional diagrams with temperature and moisture content as abscissae. The graphs represent the compensated functions of the mean values with standard deviations.

6.5.1 $[0°_{16}]$-Laminates under Tension

Figs. 6.8, 6.9 and 6.10 show that, in the -55 °C to +80 °C regime, the tensile strength in the fiber direction of dry test specimens increases with rising temperatures. Apparent explanations are the gradual reduction of the prestresses due to curing, and the diminishing brittleness of the resin which allows an alignment of the fibers and a better load distribution. Beyond 80 °C, however, the strength properties decrease because the shear transfer between fibers becomes less effective in the continually softening resin.

Specimens tested at constant ambient temperature and increasing moisture content also display improved tensile strength for similar reasons. The reduction of the curing prestress in this case is due to the swelling of the matrix, accompanied by a plastification of the resin. At constant moisture levels and increasing

temperatures the resin again softens to the point where the shear transfer between fibers suffers and results in reduced strengths.

The modulus of elasticity increases slightly with increasing loads, which is compatible with the improved load distribution due to fiber alignment [6.9]. At load levels close to rupture, the modulus of elasticity in all of the tested fiber-resin systems is fairly insensitive to higher temperature levels and moisture contents since the modulus depends predominantly on the fiber properties. Figs. 6.11, 6.12 and 6.13 show the corresponding numerical values. The scatter is probably due to the unavoidable modest variations of the fiber volume fraction.

6.5.2 $[90°_{16}]$-Laminates under Tension

In tests conducted under tensile loads applied transverse to the fiber direction, the three fiber-resin systems exhibit the somewhat inconsistent strength response observable in Figs. 6.14, 6.15 and 6.16. The reasons lie in the different degrees of ductility of the resins which tend to smooth the local stress concentrations in the resin, and in the different characteristics of the fiber-resin interfaces. Investigations of the fracture surfaces show that the reduction of the tensile strength at high temperatures and/or high moisture levels is essentially caused by weakening of the interface properties.

Figs. 6.17, 6.18 and 6.19 summarize the dependence of the transverse modulus of elasticity on temperature and moisture. Common to all systems is the degradation of the modulus at constant moisture content and increasing temperature, due to the softening of the resins. This effect is even more pronounced at higher moisture contents.

6.6 Properties of Crossplied Laminates

This type of stacking order is used for the determination of the shear properties of unidirectional laminates. The shear strength in the plane of an individual ply, often referred too as intrala-

minar shear strength, and the associated shear modulus can be deduced from the strength and strain measurements of [±45°]-laminates. Figs. 6.20, 6.21 and 6.22 display the shear strengths of the three fiber-resin systems as functions of temperature and moisture content. It is evident that the shear strengths at constant moisture levels degrade with increasing temperature. At constant temperatures up to 40 °C a slight improvement occurs in the presence of high moisture contents, while above 40 °C a general deduction is noticeable. An apparent contradiction is the loss of strength at high temperatures in the presence of an improved elongation to failure of the resin. The explanation is the degradation of the adhesive interface properties already noted in dry specimens which tend to deteriorate further in moist conditions.

The dependence of the shear modulus on temperature and moisture, given in Figs. 6.23, 6.24 and 6.25, is similar to that of the transverse modulus of elasticity. The softening of the resins leads to a reduction of the shear modulus which is especially pronounced at 120 °C in the simultaneous presence of high moisture levels.

6.7 Interlaminar Shear Tests

Interlaminar shear tests have been included in the test program to support the failure analysis of fractured laminates. The test were limited to short beam specimens with a free span to thickness ratio of 5. Figs. 6.26, 6.27 and 6.28 indicate clearly that the strength reduction in hot and moist environments is even higher than in the in-plane tests. The results support the supposition that in matrix-controlled failure modes the interface properties play an important role and counteract the positive effect of the plastification of the resins.

6.8 Prediction of Physical Properties of Multidirectional Laminates

The expressed purpose of the test program described in the preceding sections was to determine those properties of unidirectional laminates which would allow, by synthesis, the prediction of all pertinent physical properties of multidirectional laminates with ply orientations of 0°, ±45° and 90°. The inclusion of another angle would require additional computation work and checks by experimental testing.

6.8.1 Coefficients of Swelling

Fig. 6.4 contains the coefficients of swelling measured parallel and transverse to the fibers of unidirectional laminates. With these data the swelling coefficients α_Q for multidirectional laminates can be calculated by the known relationships of the lamination theory. The resulting coefficients for laminates with ply directions of 0°, ±45° and 90° and a fiber volume of 60 % are shown in Fig. 6.29 in the form of a carpet plot [6.6]. The swelling strains relate to a moisture content expressed in weight percent and have the form

$$\varepsilon_Q = \alpha_Q \times 10^{-2} \Delta M.$$

6.8.2 Coefficients of Thermal Expansion

The calculation of the coefficients of thermal expansion for multidirectional laminates, based on the properties of unidirectional laminates, is in all respects similar to that of the coefficients of swelling. With the appropriate data from Fig. 6.7, the coefficients of thermal expansion for laminates with ply directions of 0°, ±45° and 90° and a fiber volume content of 60 % as displayed in Fig. 6.30 [6.5]. The thermal strains follow from the equation

$$\varepsilon_T = \alpha_T \Delta T.$$

A comparison of the effects of thermal expansion and swelling transverse to the fibers of a unidirectional laminate shows that a change in moisture content of $\Delta M = 1$ % produces a strain equivalent to a temperature change of $\Delta T = 120$ °C.

6.8.3 Moduli of Elasticity

With the experimentally determined properties $E_{\parallel} = E_1$, $E_{\perp} = E_2$, $G_{\parallel} = G_{12}$, $\nu_{\parallel} = \nu_{12}$ and $\nu_{\perp\parallel} = \nu_{21}$ as functions of temperature and moisture, the stiffness and flexibility coefficients of multidirectional laminates can be determined by the lamination theory [6.7 - 6.8]. The prerequisites are balance and symmetry about the midplane of the laminate, and a membrane state of stress. For laminates with ply directions of 0°, ±45° and 90° the modulus E_{xx}, for example, in an environment of 23 °C and 50 % relative humidity, is displayed in Fig. 6.31 [6.5]. If the sum of the 0° and ±45° percentages identified in the figure is less than 100 %, then the difference represents the percentage of 90° plies. Similar diagrams can be established for the C_{ij} of the individual plies in dependence of temperature and moisture.

Fig. 6.32, 6.33 and 6.34 contain comparisons of calculated and measured moduli of elasticity for several stacking orders. Within reasonable limits the moduli are unaffected by moisture and temperature [6.9].

6.8.4 Strength Predictions

The strength properties of unidirectional and multidirectional laminates can be predicted through interaction failure criteria either in the stress or in the strain domain [6.7]. Such criteria assume a macroscopic homogeneity of the material and contain analytical relationships for the strength properties under compound stresses. The strength of multidirectional laminates depends on the strength of its individual plies. Under increasing load one of the plies will fail initially (first-ply failure) to be followed successively by the failure of other plies, the failure of the last ply signalling the fracture of the laminate.

The quadratic interaction criterion has the general form

$$F_{ij}\sigma_i\sigma_j + F_i\sigma_i = 1$$

or, in term of strain components,

$$G_{ij}\varepsilon_i\varepsilon_j + G_i\varepsilon_i = 1$$

with the tensors F_{ij}, F_i, G_{ij} and G_i representing the strength components in the fiber direction and normal to the fiber direction, and the shear strength. The interrelationship between the individual strength components is given in [6.7, 6.10].

The introduction of a factor R leads to

$$\sigma_i = R\ \sigma_i^m \quad \text{and} \quad \varepsilon_i = R\ \varepsilon_i^m$$

where σ_i and ε_i represent the allowable and σ_i^m and ε_i^m the mechanically induced stresses or strains. The substitution into the failure criterion produces a quadratic equation for the determination of the factor R which, in case of linear dependence between applied and allowable stresses, is synonymous with a safety factor.

Temperature changes and moisture absorption give rise to prestresses σ_i^p, or prestrains ε_i^p which must be superimposed on the mechanical stresses and strains. With

$$\sigma_i = R\ \sigma_i^m + \sigma_i^p \quad \text{and} \quad \varepsilon_i = R\ \varepsilon_i^m + \varepsilon_i^p$$

the failure criterion, in terms of strains, now assumes the form

$$G_{ij}(R\ \varepsilon_i^m + \varepsilon_i^p)(R\ \varepsilon_j^m + \varepsilon_j^p) + G_i(R\ \varepsilon_i^m + \varepsilon_i^p) = 1.$$

The solution for R yields the factor by which the mechanical loads, at constant temperature and moisture, can be increased before failure occurs.

Corresponding calculations and comparisons to test results for $[0°/90°]_s$-laminates are summarized in Fig. 6.35. In dry speci-

mens the calculated first-ply failure levels in the 90°-plies, represented by dotted lines, clearly rise with increasing temperature. In moist specimens the same tendency exists with a shift to substantially higher ply failure levels, i.e., under unidirectional static tension loads the presence of moisture is decidedly advantageous. The predictions for laminate fracture are given by the solid lines in the figure.

Fig. 6.36 shows similar relationships for $[0°/\pm45°/\overline{90}°]_s$- laminates with ply-failure predictions for the 90°- and ±45°-plies as well as laminate fracture. Evidently, the ±45°-ply failure, in the presence of high temperature and moisture levels, is preceded by the rupture of the 0°-plies.

Fig. 6.37 reflects the response of $[90°/\pm45°/\overline{0}°]_s$-laminates. The trends of the first-ply failures correspond to those in Fig. 6.36 with generally lower stress levels due to the reduction of the number of 0°-plies.

6.9 Mechanisms of Damage

A major issue in all of the static tests was the observation of the nature of the mechanisms leading to first-ply failures in the laminates. The investigations centered on the formation of matrix cracks in various environments, and on the failure of the interface between fiber and resin.

6.9.1 Formation of Matrix Cracks

The strain levels associated with first-ply failure and with laminate failure of $[0°/90°]_s$-laminates subjected to uniaxial tension loads are depicted in Figs. 6.38, 6.39 and 6.40 in dependence on temperature and moisture content. The strain measurements were carried out by strain gages applied in the two principal directions of the laminate. After the detection of the first failure in the 90°-plies, additional cracks were observed to form under increasing load until the laminate failed as a whole. After the tests, all specimens were examined by contrast-enhanced

radiography to verify the strain gage responses and to ascertain the locations of the cracks. The mean crack distance, $\bar{a}_r$, was determined from the mean number of cracks per mm of the cracked length of the test specimens. At high enough moisture contents the strain capability of the 90°-plies exceed that of the 0°-plies and the cracks, correspondingly, vanish. A comparison with Fig. 6.35 shows that the actual first-ply failure strains of the $[0°/90°]_s$-laminates are significantly higher than the calculated first-ply failure strains which were based on $[90°_1]$-laminate measurements. Apparently, the external 0°-plies provide a smoother stress distribution in the internal 90°-plies as well as lateral support. In view of this conclusion, the current practice of predicting first-ply failure on the basis of the failure strains of $[90°_n]$-laminates may have to be reevaluated as being overly conservative.

The photomicrographs of polished sections of failed test specimens depicted in Fig. 6.41 are further evidence that both temperature and moisture retard the crack formation in 90°-plies and must be considered, in context with the described test program, as positive influences [6.11].

6.9.2 Failure of Fiber-Resin Interface

In the preceding sections, first-ply failures were identified with the development of cracks in the 90°-plies of a laminate. No attempt was made to differentiate whether the failures were induced by lack of cohesion between resin particles, or by lack of adhesion at the fiber-resin interface. The distinction is important because improvements of the resin formulations to raise the ply failure level will be of no avail if the interface properties are deficient, and vice versa. Therefore, an attempt was made to investigate the influence of temperature and moisture on the morphology of the fracture surfaces of the tension test specimens. Fig. 6.42 shows that at -55 °C and 0 % moisture the fibers are fully imbedded in the resin and the adhesion is strong enough to cause clean rupture planes of the fibers. Apparently, the laminate failed due to lack of cohesion in the resin. At -55 °C and moisture saturation at 93 % relative humidity, the fracture sur-

faces of 90°-laminates have a different appearance. Adhesion of the resin to the fibers is still evident but the inclination of the fiber rupture planes to the fiber axis indicates a lower quality of the interface properties which is consistent with the reduced strength data in Fig. 6.14.

Microphotographs of tests performed at 120 °C are displayed in Fig. 6.43. At 0 % moisture the interface shows some degree of deterioration but the fiber rupture planes are still normal to the fiber axis. Specimens tested after saturation in 93 % relative humidity and at 120 °C, however, exhibit fracture modes of a different kind. The fiber surfaces are now clean and no evidence of fiber ruptures can be found, indicating a drastic degradation of the adhesive bond at the interface. The correspondingly low strength properties of 90°-laminates in hot-wet conditions, shown also in Fig. 6.14, have often been explained as an undesirable synergistic effect of the epoxy resins. In the light of the described observations it appears more reasonable to interpret the degradation as an interaction of two quite different phenomena and to concentrate on the improvement of the interface properties in hot-wet environments.

6.10 References

[6.1] Lo, S.Y., Hahn, H.T. Chiao, T.T. — Swelling of Kevlar 49/Epoxy and S_2-Glass-Epoxy Composites. Proc. of 4th Conf. on Composite Materials 25.-28. Oct. 1982 Tokyo, pp. 987-1000.

[6.2] Gitschner H.W. — Dissertation RWTH-Aachen, DS 8011 (1980).

[6.3] Jones, F.R., Mulheron, M. Bailey, J.E. — Origins of Thermal Strains in Polyester Laminates. Proc. of 4th Conf. on Composite Materials 25.-28. Oct. 1982 Tokyo, pp. 1045-1052.

[6.4] Niederstadt, G., Nitsch, P. — Diffusion, Wärmedehnung und Quellung von CFK (Zusammenfassende Darstellung). DFVLR-IB 131-84/06 (1984).

[6.5] Bieling, U. — Dissertation RWTH-Aachen, DS 8305 (1983).

[6.6] Niederstadt, G. — Besonderheiten beim Konstruieren mit Kohlenstoff-Fasern. Kunststoffe 74 (1984) H. 11, S. 686-691.

[6.7] Tsai, S.W., Hahn, H.T. — Introduction to Composite Materials. Westport: Technomic Publishing Company, 1980.

[6.8] Jones, R.M. — Mechanics of Composite Materials. Washington D.C.: Scripta Book Company, 1975.

[6.9] Gädke, M. Ermittlung mechanischer Eigenschaften kohlenstoffaserverstärkter Kunststoff-laminate in Abhängigkeit von den Umweltbedingungen Feuchtigkeit und Temperatur. DFVLR-IB 131-84/19 (1984).

[6.10] Gädke, M. Kennwertbestimmung für faserver-stärkte Werkstoffe. In: Beiträge zum Verhalten kohlefaser-verstärkter Verbundstrukturen. DFVLR-Mitt. 83-16 (1983), S. 9-99.

[6.11] Bergmann, H.W. Mechanisms of Fractures in Fiber Reinforced Laminates. In: Advances in Fracture Research. Proc. of 6th Int. Conf. on Fracture (ICF6) 4.-10. Dec. 1984 New Delhi, India, Vol. 1, pp. 569-585.

Physical Property			$\sigma;\tau;E;G;\varepsilon;\gamma;\nu_i;\alpha_S;\alpha_T$						
Parameter Variation			Tension, Compression, Temperature, Moisture						
Direction	Material	%r H	Temperature in °C						
			-55	0	23	40	80	120
X (0°)	914C-TS-5T	0						
		50						
		93						
Y (90°)	Code69 - T300	0						
XY (±45°)		50						
ZX (ILS)		93						
	T6T 131-12-F 550	0						
		50						
		93						

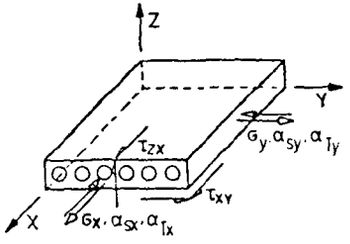

Fig. 6.1 Test program for the determination of physical properties of unidirectional CFRE-laminates.

Mechanical Property				$\hat{G};\hat{\tau};\hat{E};\ \hat{\varepsilon};\ \hat{\nu}$					
Loading Condition				Tension					
Direction	Material	Stacking Sequence	°C / %rH	-55	0	23	40	80	120
X	914C-TS-5T	$[0°/90°]_s$	0						
			50						
			93						
Y		$[0°/\pm 45°/\overline{90}°]_s$	0						
			50						
			93						
ZX		$[90°/\pm 45°/\overline{0}°]_s$	0						
			50						
			93						

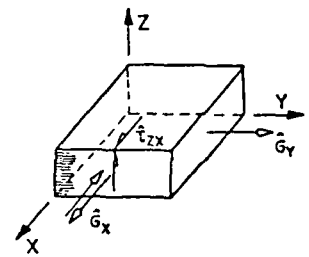

Fig. 6.2 Test program for the determination of mechanical properties of multidirectional CFRE-laminates as functions of moisture content and test temperature.

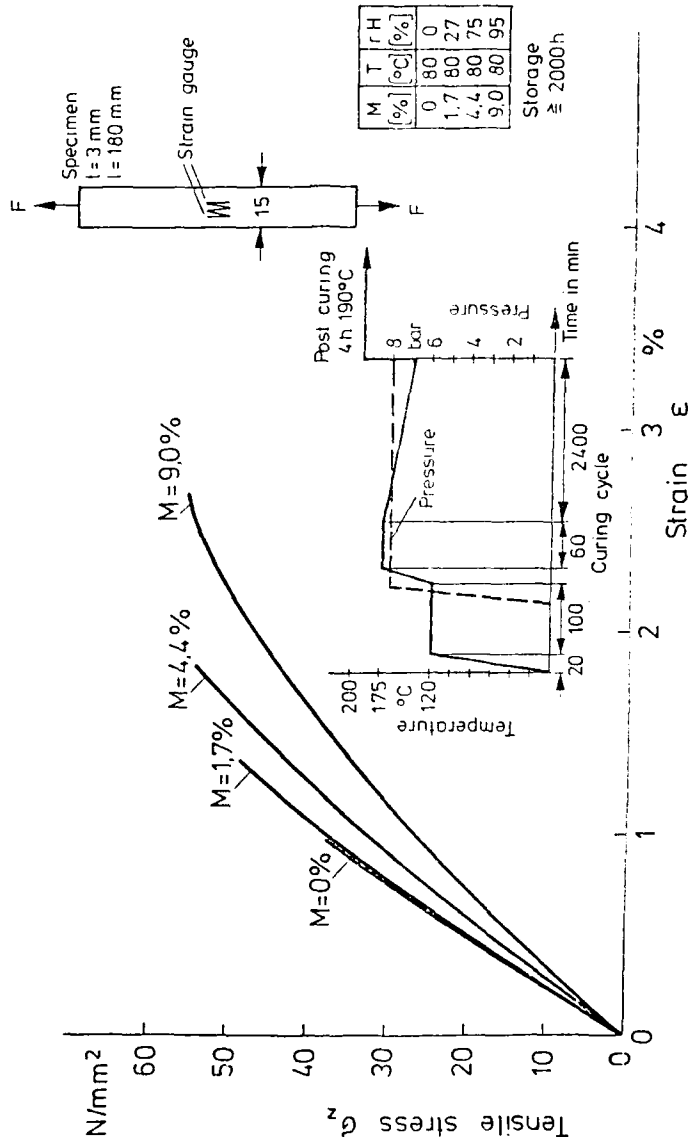

Fig. 6.3 Stress-strain curves of Fibredux 914 (neat resin) for different moisture contents tested at RT.

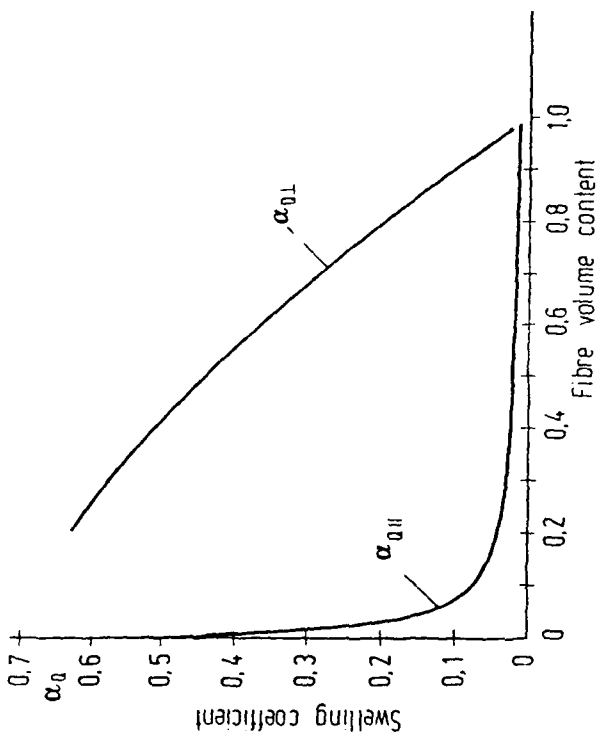

Fig. 6.4 Swelling coefficients of unidirectional CFRE as function of fiber volume fraction.

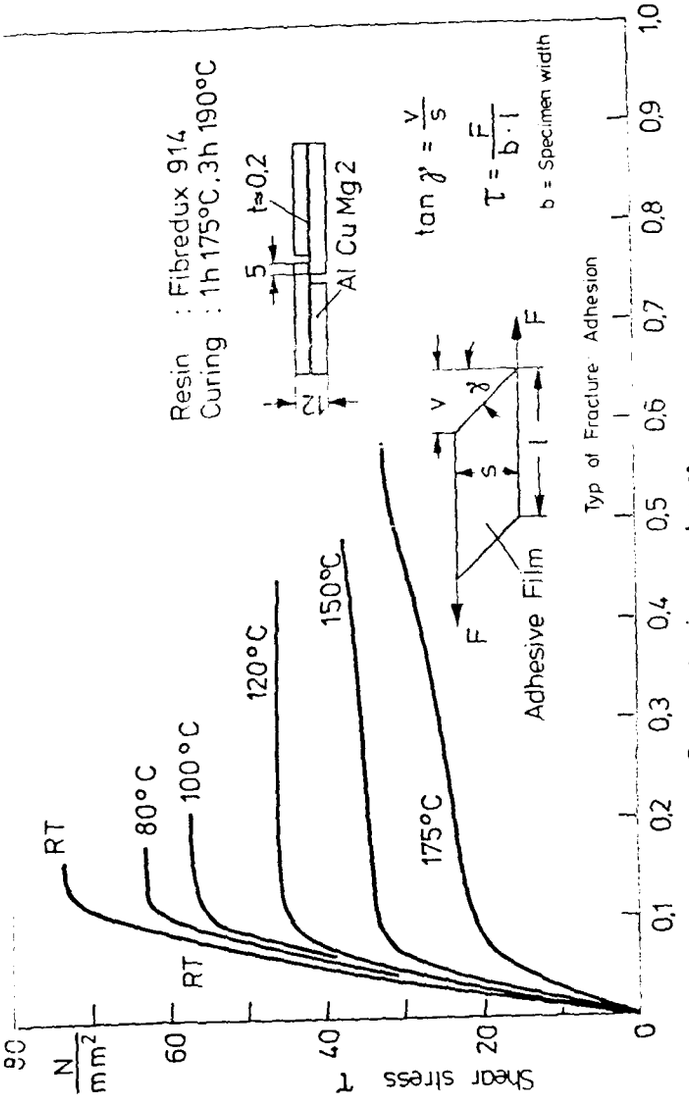

Fig. 6.5 Shear stress-strain curves of Fibredux 914 (neat resin) as function of test temperature.

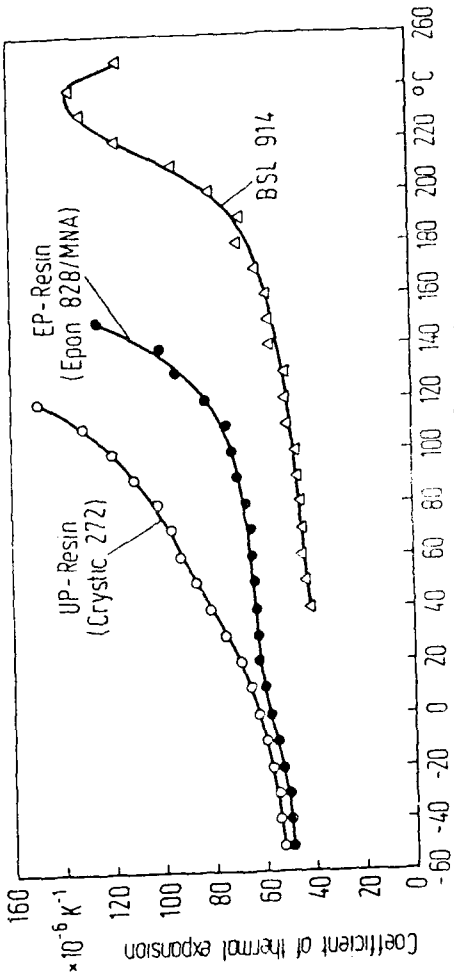

Fig. 6.6 Coefficients of thermal expansion of polymers as function of temperature.

AD-A168 002 DEVELOPMENT OF FRACTURE MECHANICS MAPS FOR COMPOSITE MATERIALS VOLUME I(U) DEUTSCHE FORSCHUNGS- UND VERSUCHSANSTALT FUER LUFT- UND RAUMF.. H W BERGMANN 2/3

UNCLASSIFIED DEC 85 AFWAL-TR-85-4150-VOL-1 F/G 11/4 NL

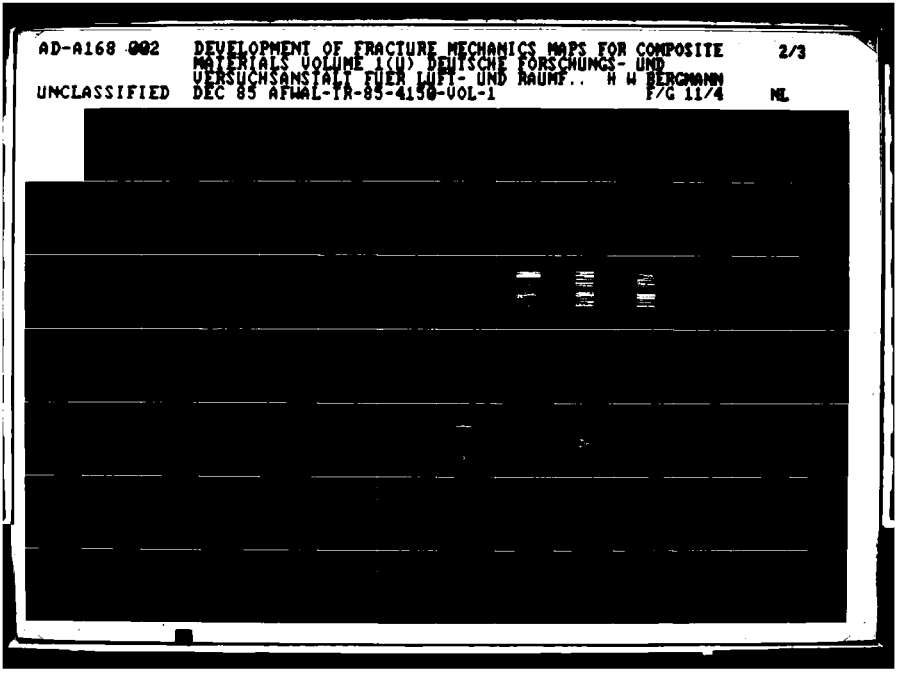

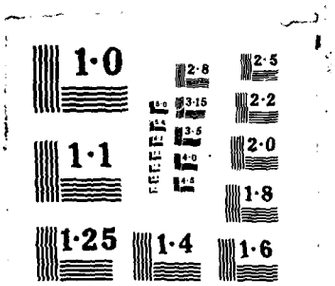
1·0
1·1
1·25
2·8
3·15
3·5
4·0
4·5
1·4
2·5
2·2
2·0
1·8
1·6

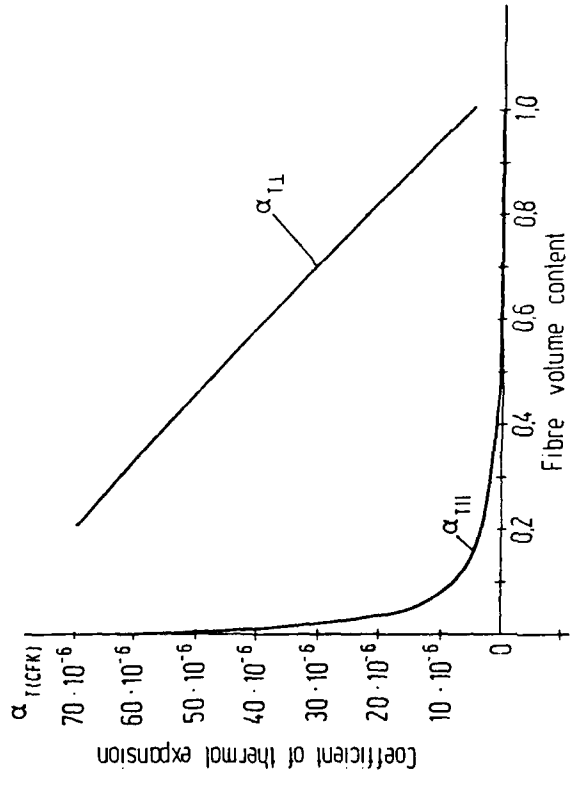

Fig. 6.7 Coefficient of thermal expansion of unidirectional composites as function of fiber volume fraction.

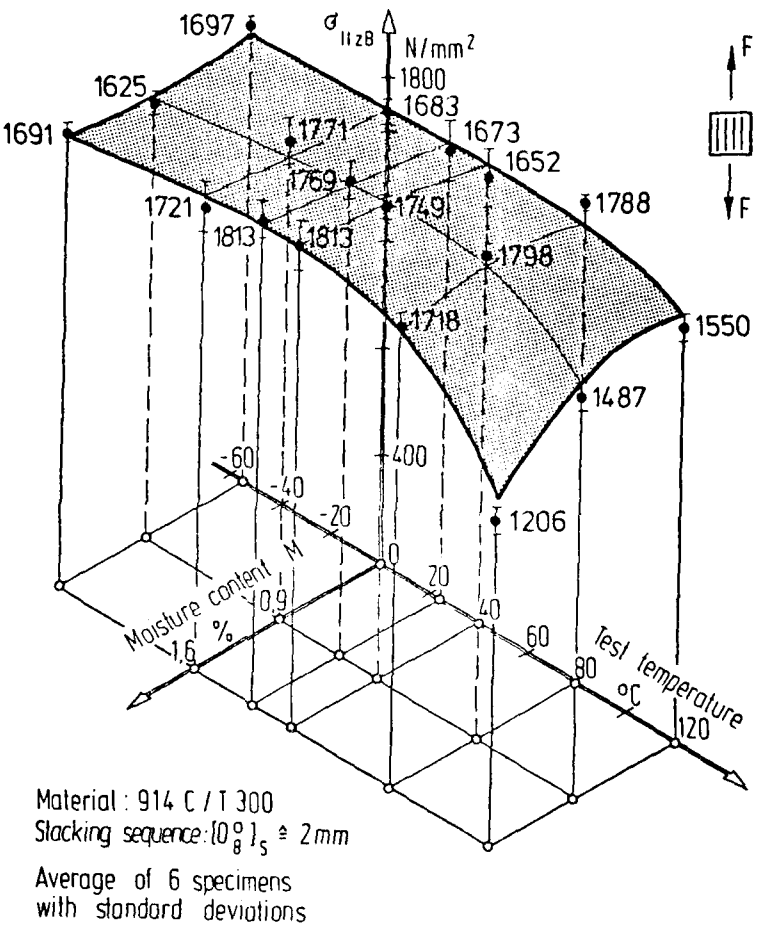

Fig. 6.8 Longitudinal tensile strength of CFRE-laminates as function of test temperature and specimen moisture content.

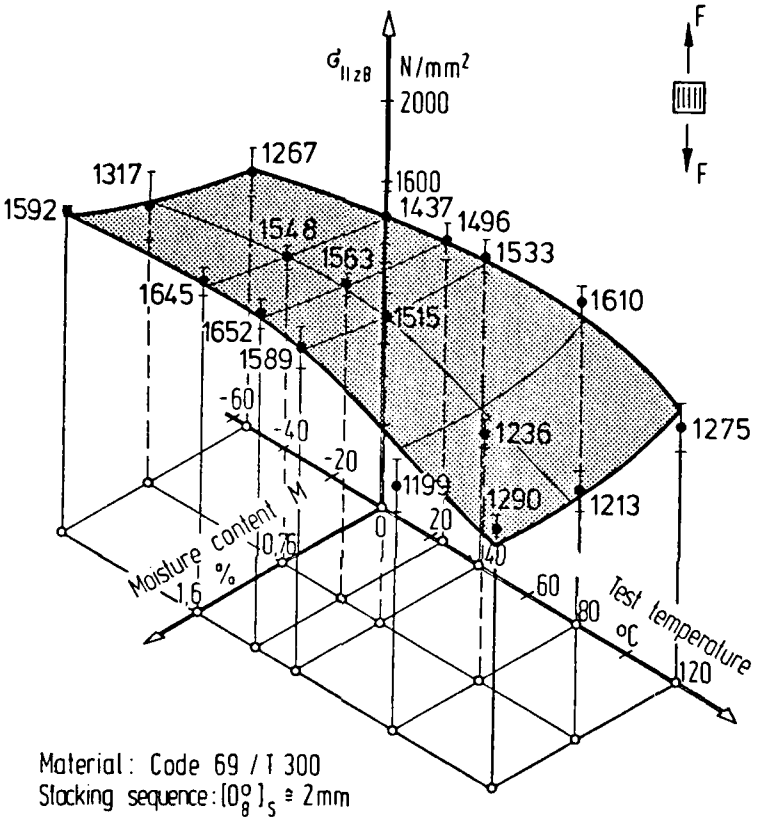

Fig. 6.9 Longitudinal tensile strength of CFRE laminates as function of test temperature and specimen moisture content.

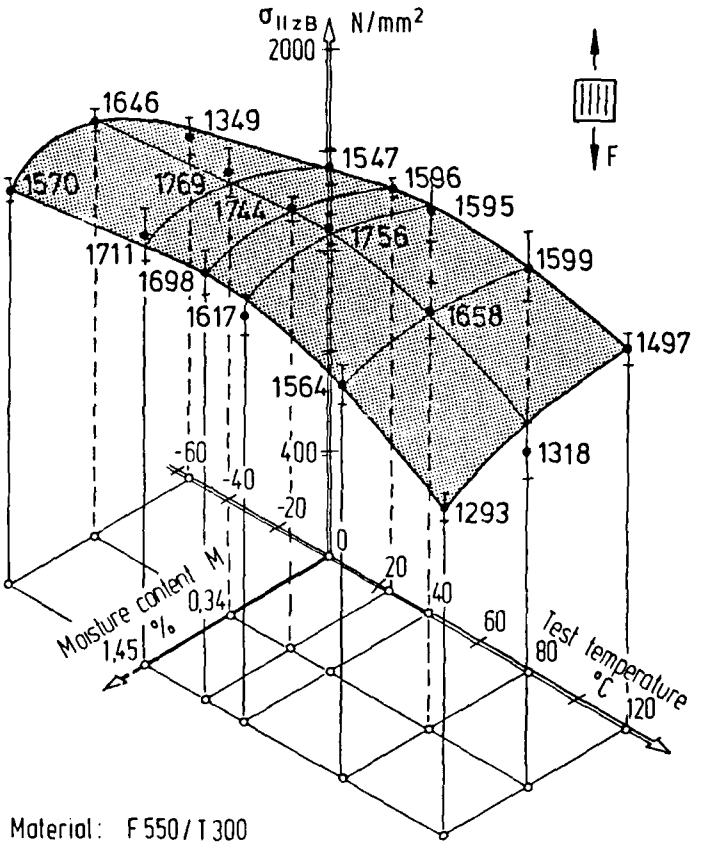

Material: F 550 / T 300
Stacking sequence: $[0°_8]_s$ ≙ 2 mm
Average of 6 specimens
with standard deviations

Fig. 6.10 Longitudinal tensile strength of CFRE laminates as function of test temperature and specimen moisture content.

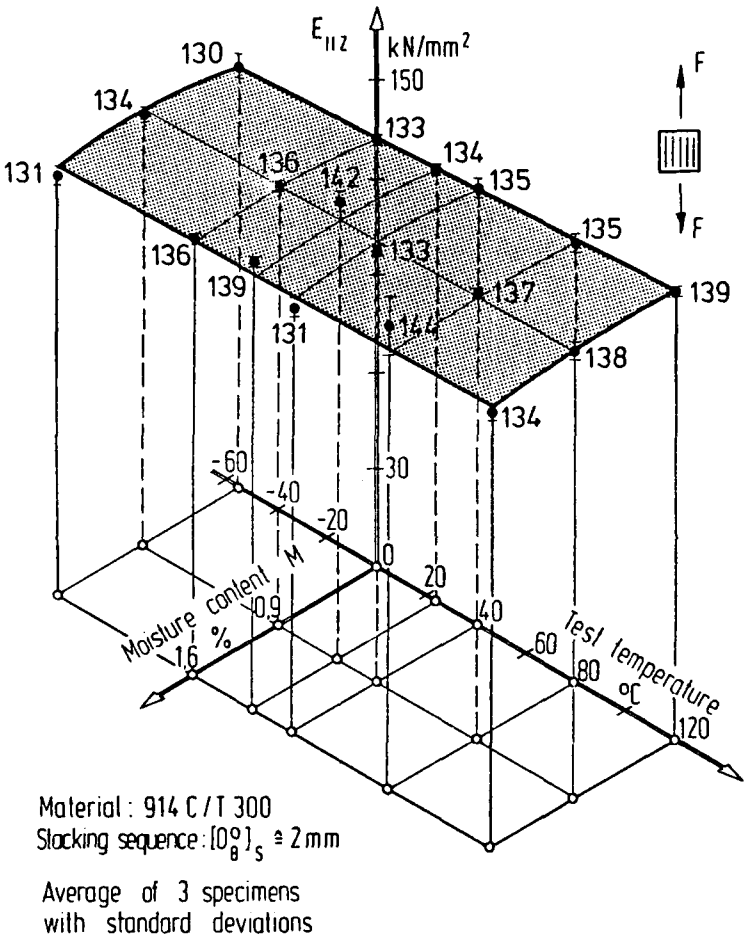

Fig. 6.11 Longitudinal modulus of elasticity of CFRE laminates as function of test temperature and specimen moisture content.

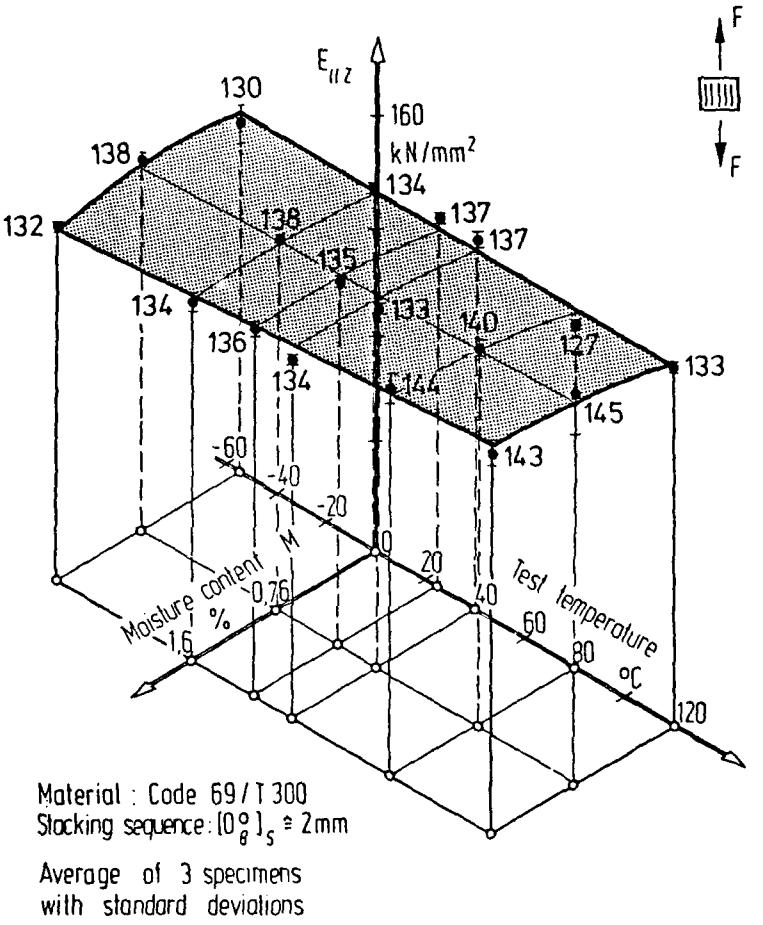

Fig. 6.12 Longitudinal modulus of elasticity of CFRE laminates as function of test temperature and specimen moisture content.

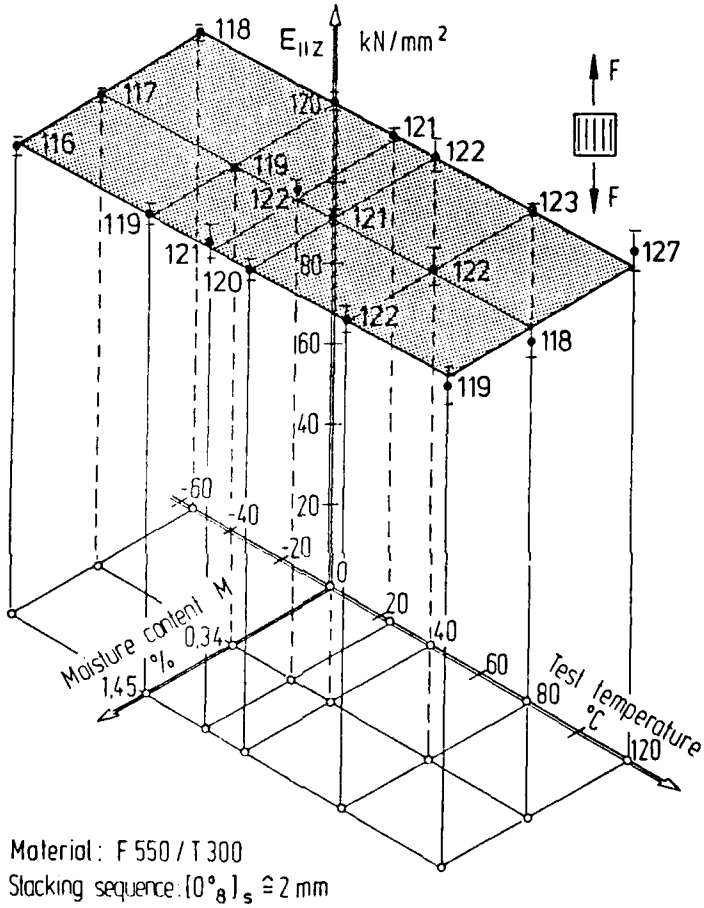

Material: F 550 / T 300
Stacking sequence $[0°_8]_s$ ≙ 2 mm
Average of 3 specimens
with standard deviations

Fig. 6.13 Longitudinal modulus of elasticity of CFRE laminates as function of test temperature and specimen moisture content.

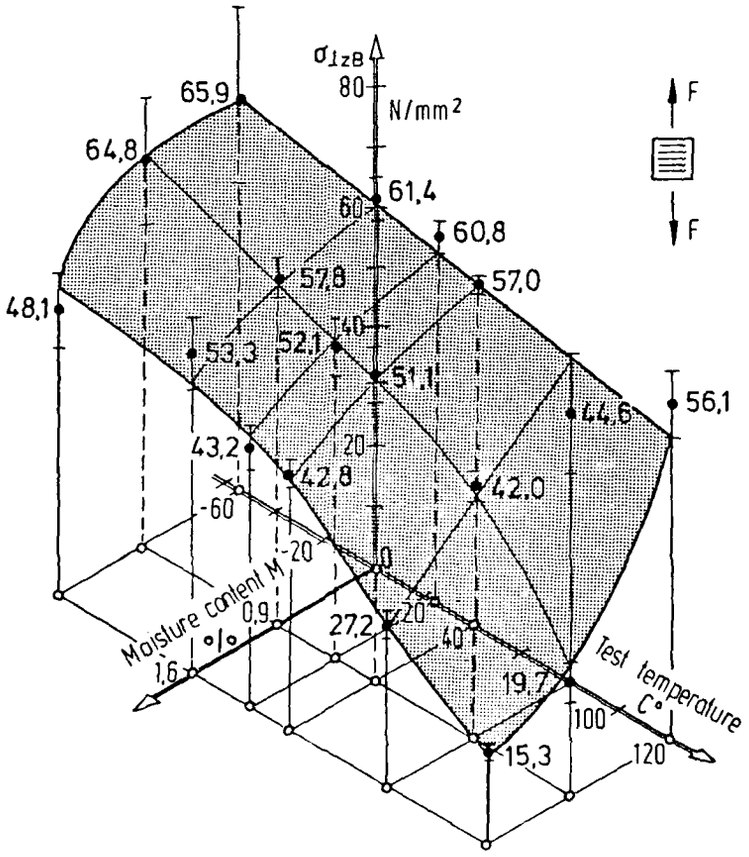

Material: 914 C / T 300
Stacking sequence: $[90°_8]_s$ ≙ 2 mm
Average of 6 specimens
with standard deviations

Fig. 6.14 Transverse tensile strength of CFRE laminates as function of test temperature and specimen moisture content.

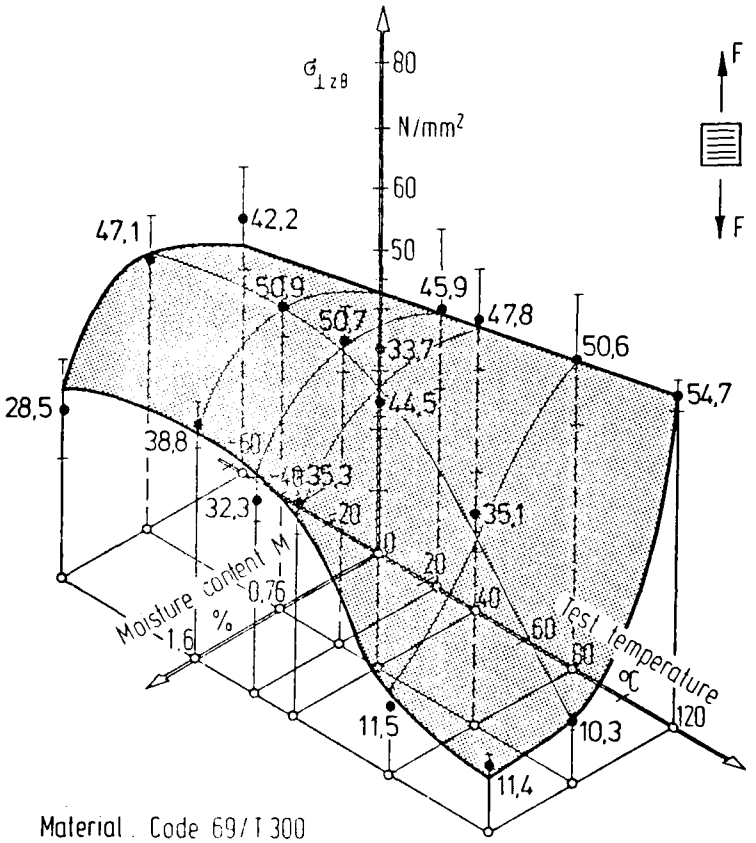

Fig. 6.15 Transverse tensile streng'h of CFRE laminates as function of test temperature and specimen moisture content.

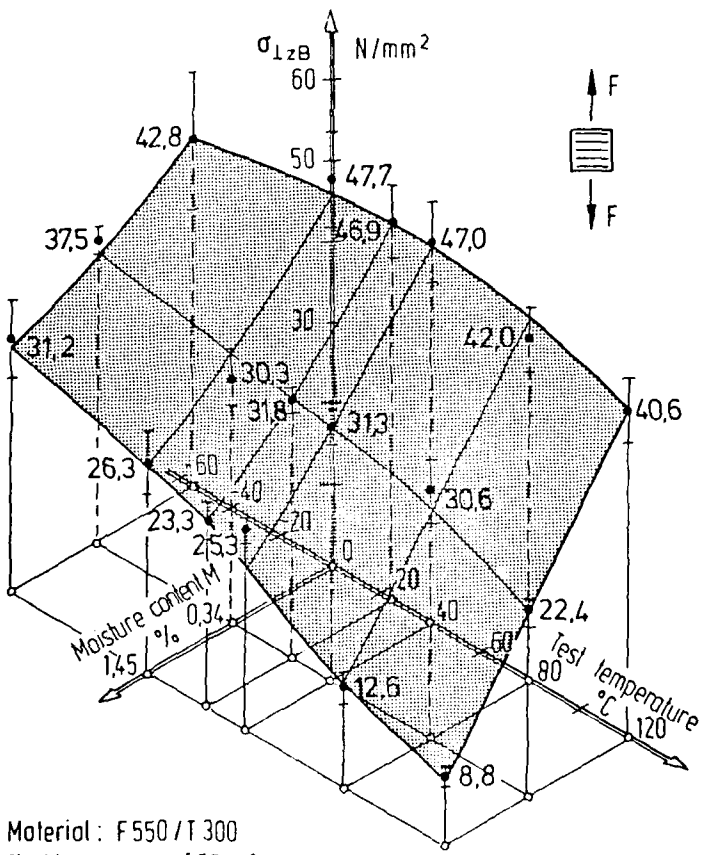

Fig. 6.16 Transverse tensile strength of CFRE laminates as function of test temperature and specimen moisture content.

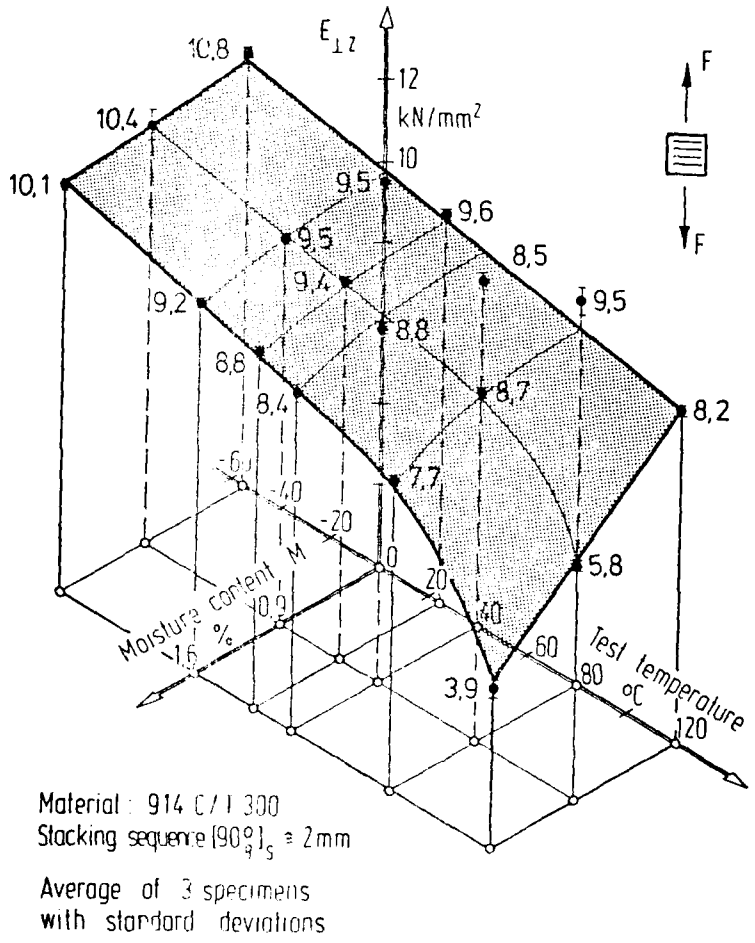

Fig. 6.17 Transverse modulus of elasticity of CFRE laminates as function of test temperature and specimen moisture content.

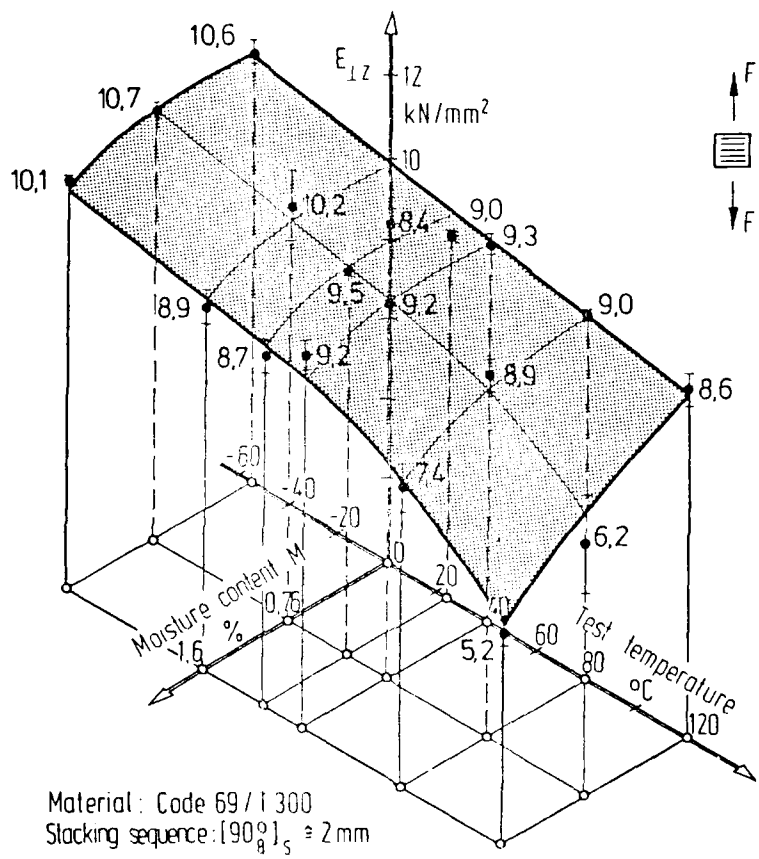

Fig. 6.18 Transverse modulus of elasticity of CFRE laminates as function of test temperature and specimen moisture content.

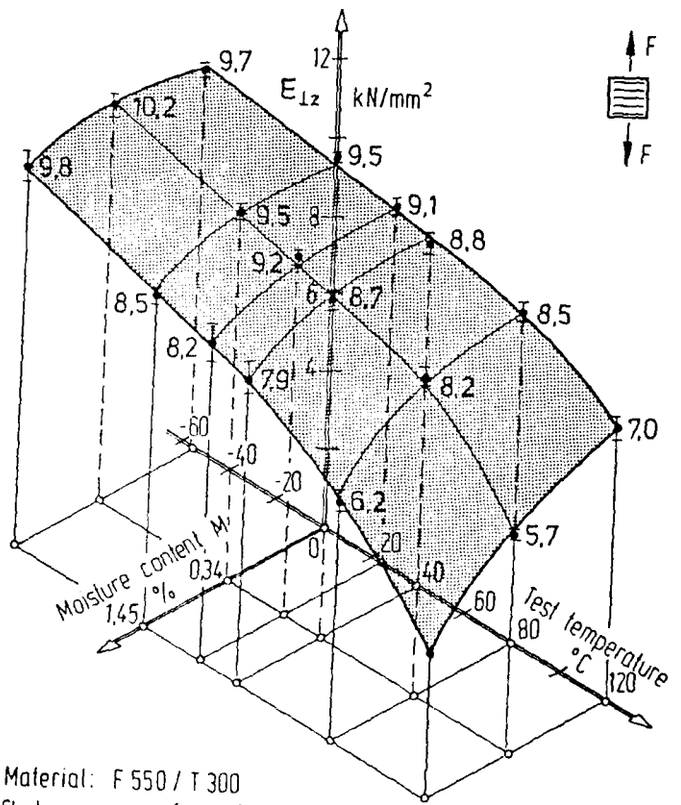

Material: F 550 / T 300
Stacking sequence: $[90°_8]_s$ ≙ 2mm

Average of 3 specimens
with standard deviations

Fig. 6.19 Transverse modulus of elasticity of CFRE laminates as function of test temperature and specimen moisture content.

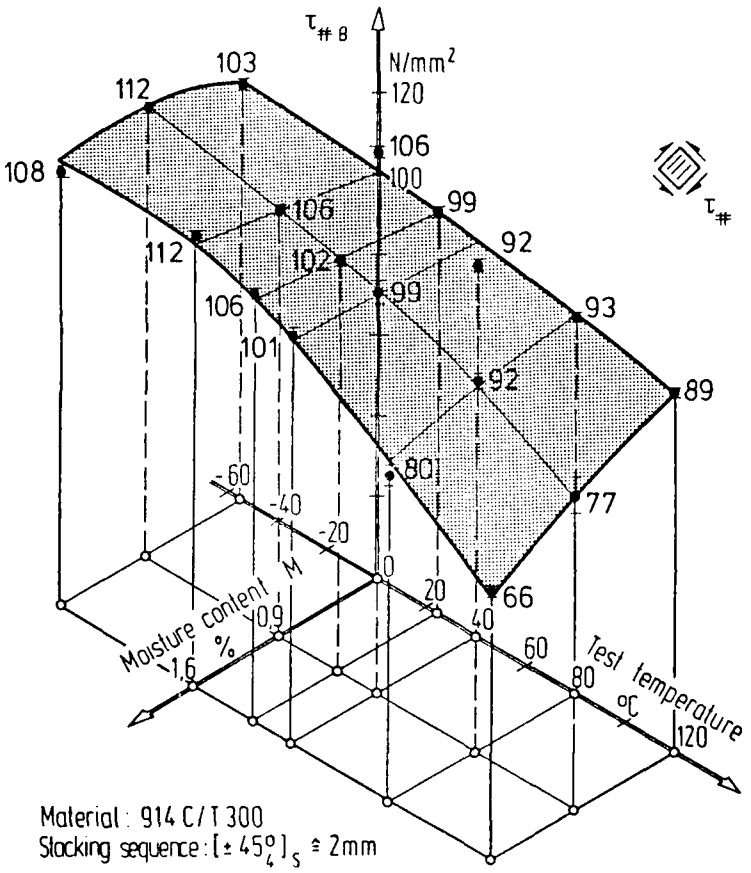

Fig. 6.20 In-plane shear strength of CFRE laminates as function of test temperature and specimen moisture content.

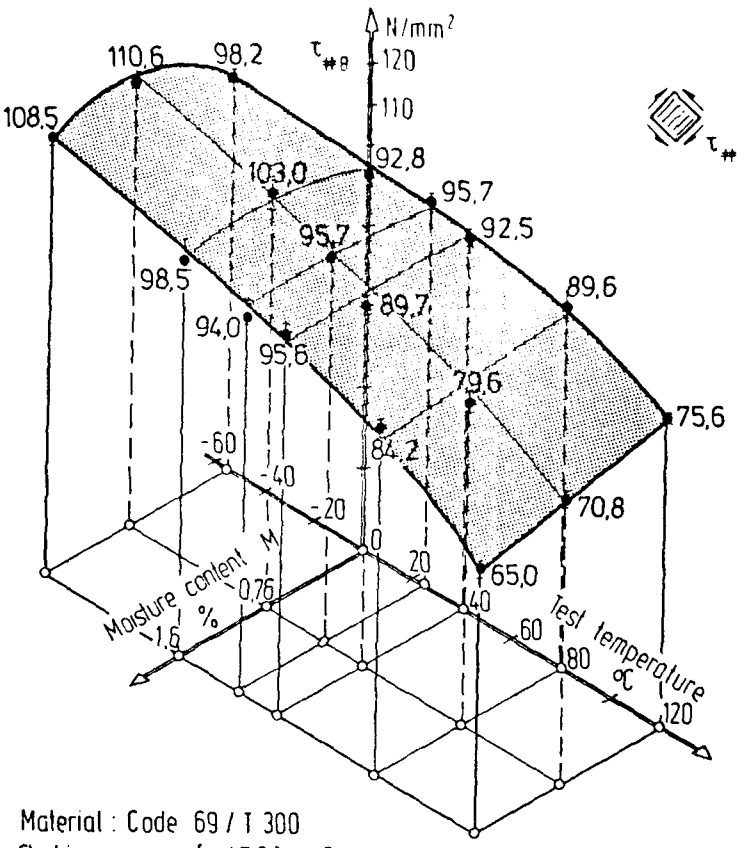

Material : Code 69 / T 300
Stacking sequence: $[\pm 45^{\circ}_{4}]_{S}$ ≙ 2 mm

Average of 6 specimens
with standard deviations

Fig. 6.21 In-plane shear strength of CFRE laminates as function of test temperature and specimen moisture content.

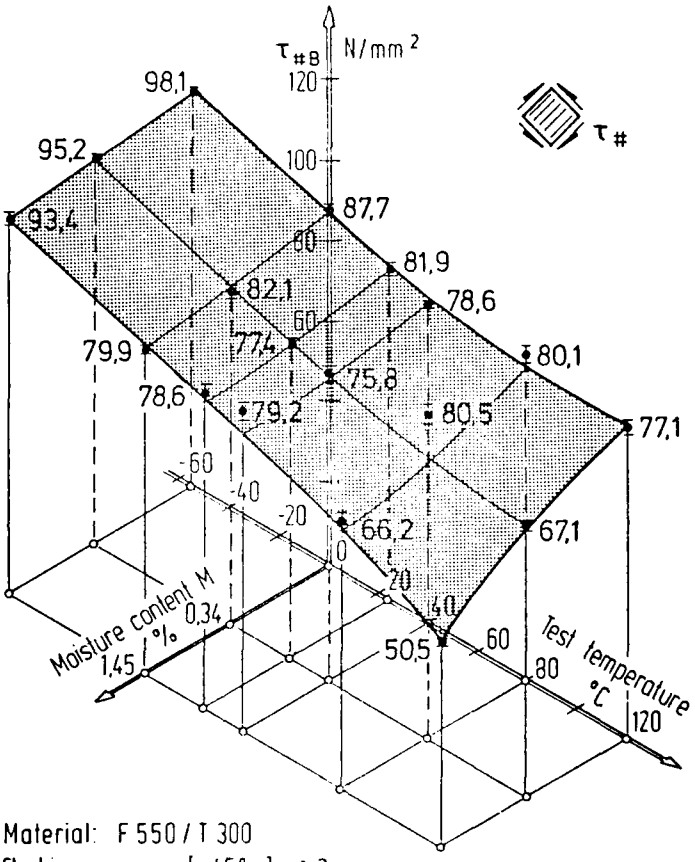

Material: F 550 / T 300
Stacking sequence: $[\pm 45°_4]_s \hat{=} 2$ mm
Average of 6 specimens
with standard deviations

Fig. 6.22 In-plane shear strength of CFRE laminates as function of test temperature and specimen moisture content.

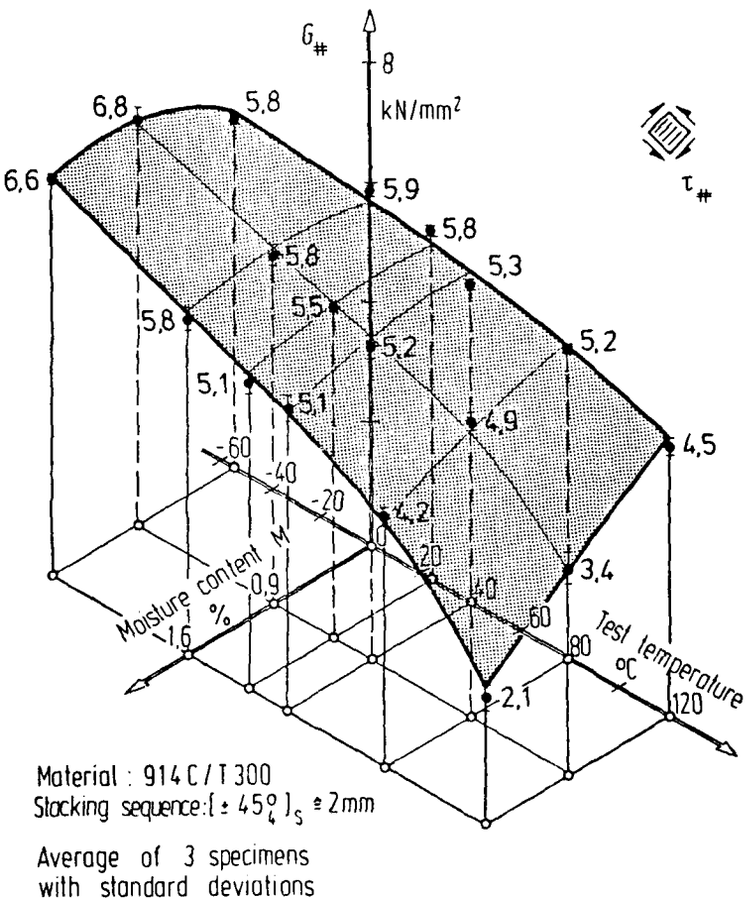

Fig. 6.23 In-plane shear modulus of CFRE laminates as function of test temperature and specimen moisture content.

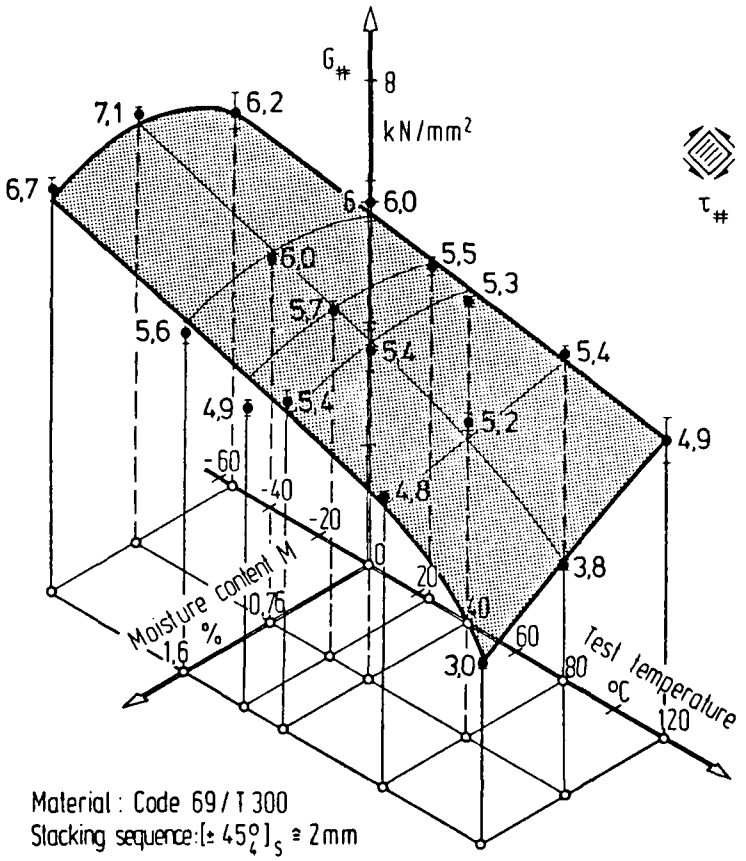

Material : Code 69 / T 300
Stacking sequence: $[\pm 45^{\circ}_{2}]_{S}$ ≙ 2mm

Average of 3 specimens
with standard deviations

Fig. 6.24 In-plane shear modulus of CFRE laminates as function of test temperature and specimen moisture content.

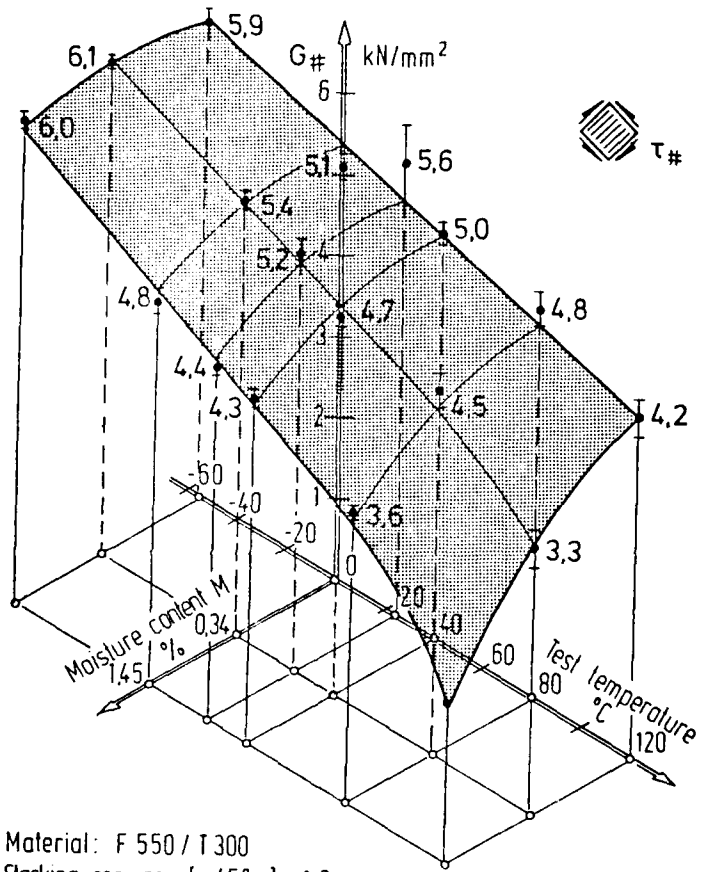

Material: F 550 / T 300
Stacking sequence: $[\pm 45°_4]_s \hat{=} 2$ mm
Average of 3 specimens
with standard deviations

Fig. 6.25 In-plane shear modulus of CFRE laminates as function of test temperature and specimen moisture content.

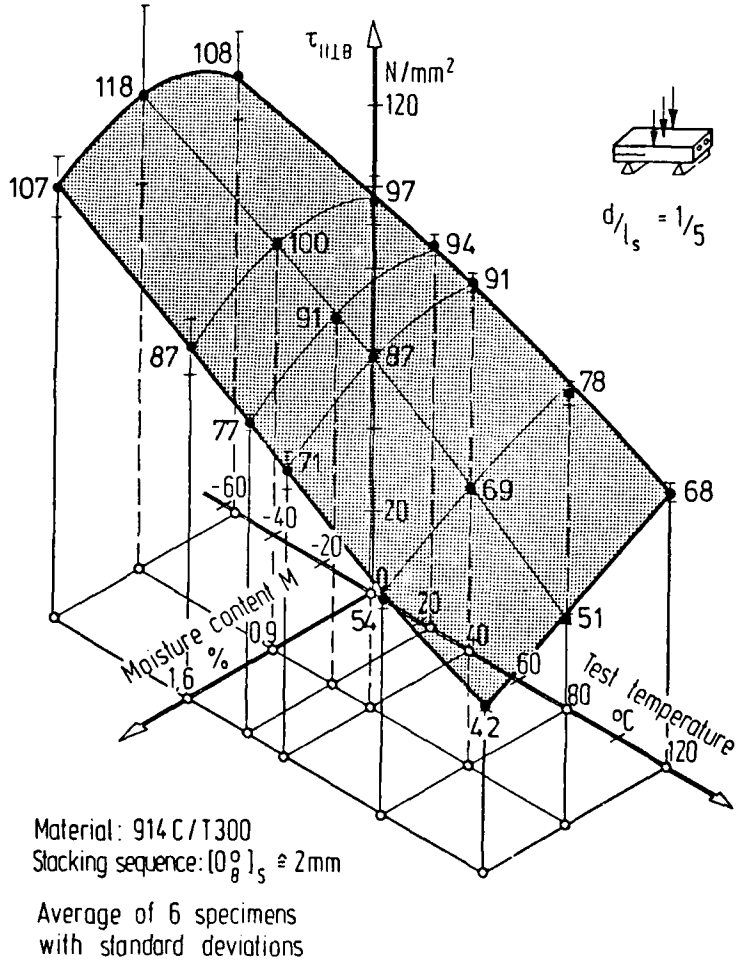

Fig. 6.26 Interlaminar shear strength of CFRE laminates as function of test temperature and specimen moisture content.

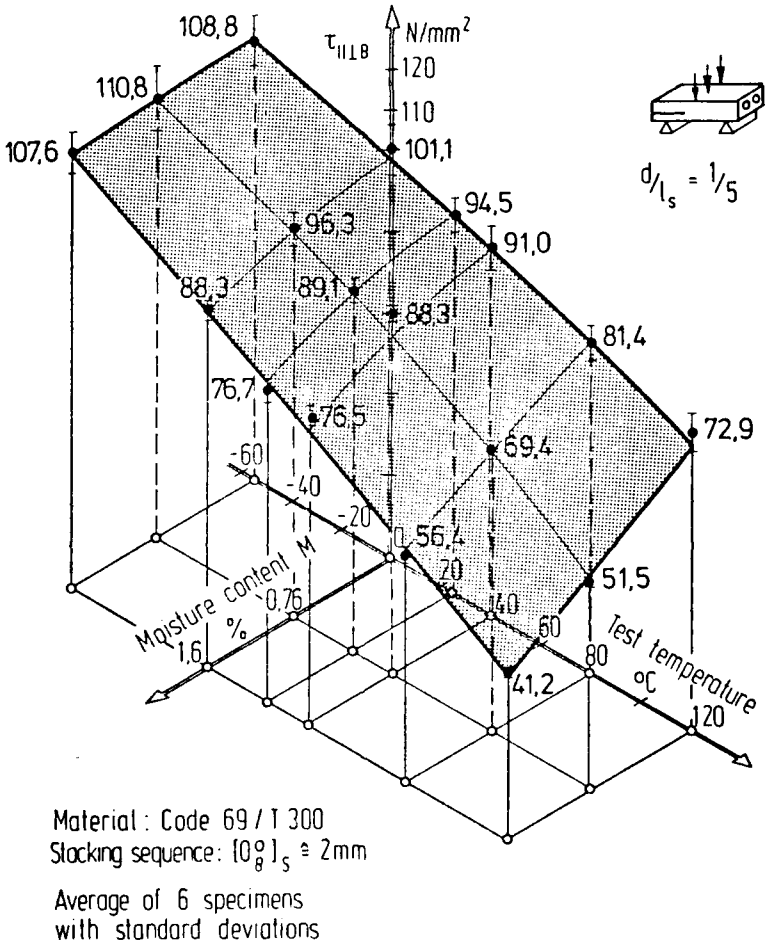

Fig. 6.27 Interlaminar shear strength of CFRE laminates as function of test temperature and specimen moisture content.

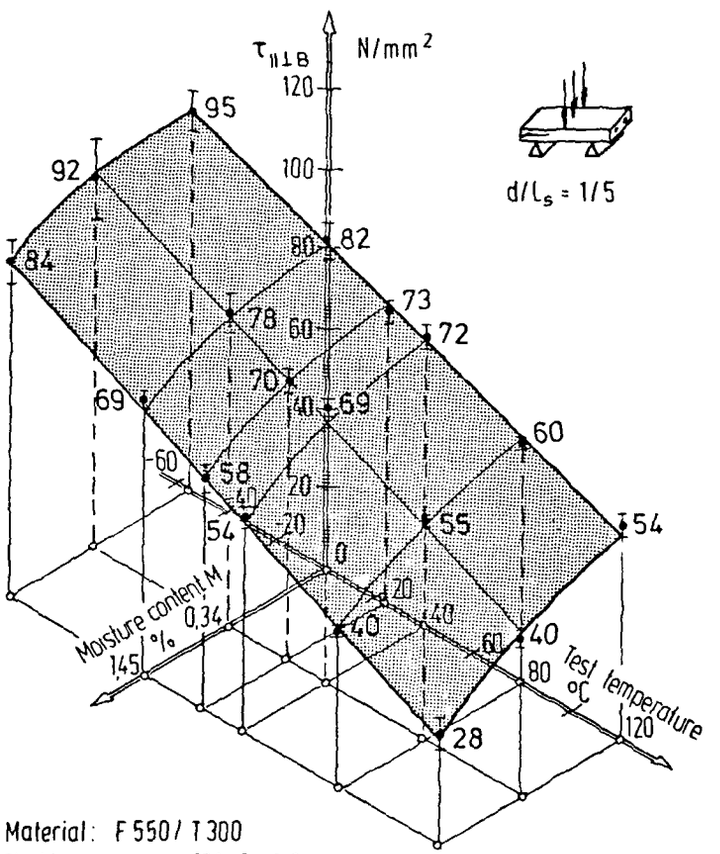

Material: F 550 / T 300
Stacking sequence: $[0°_8]_s \hat{=} 2$ mm
Average of 6 specimens
with standard deviations

Fig. 6.28 Interlaminar shear strength of CFRE laminates as function of test temperature and specimen moisture content.

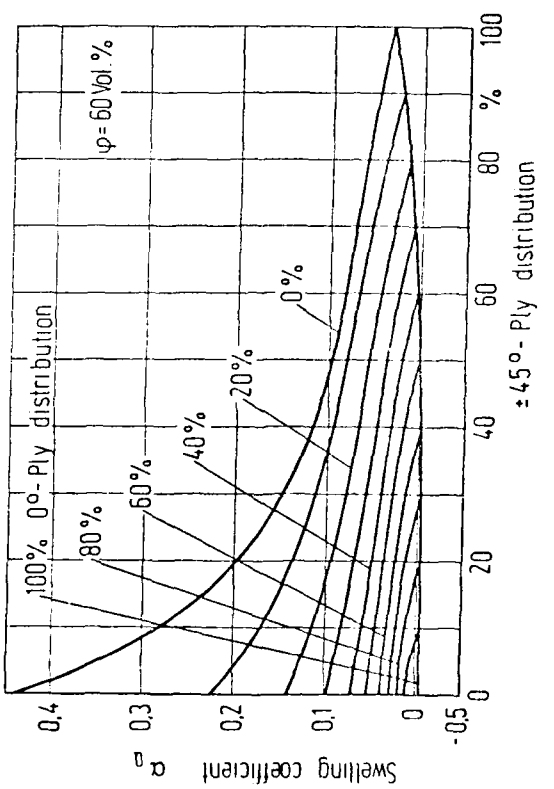

Fig. 6.29 Swelling coefficient of 0°,±45°,90° - laminate family as function of ply distribution.

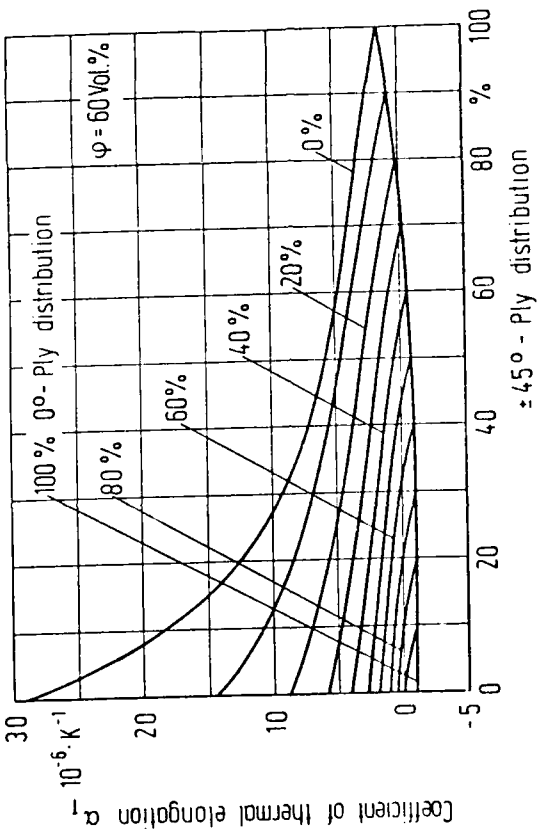

Fig. 6.30 Coefficient of thermal elongation of 0°,±45°,90° - laminate family as function of ply distribution.

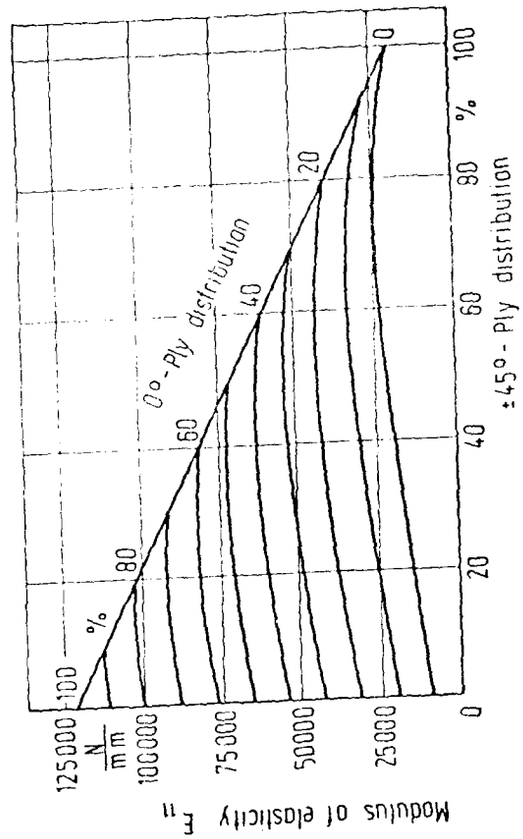

Fig. 6.31 Modulus of elasticity of 0°,±45°,90° - laminate family as function of ply distribution.

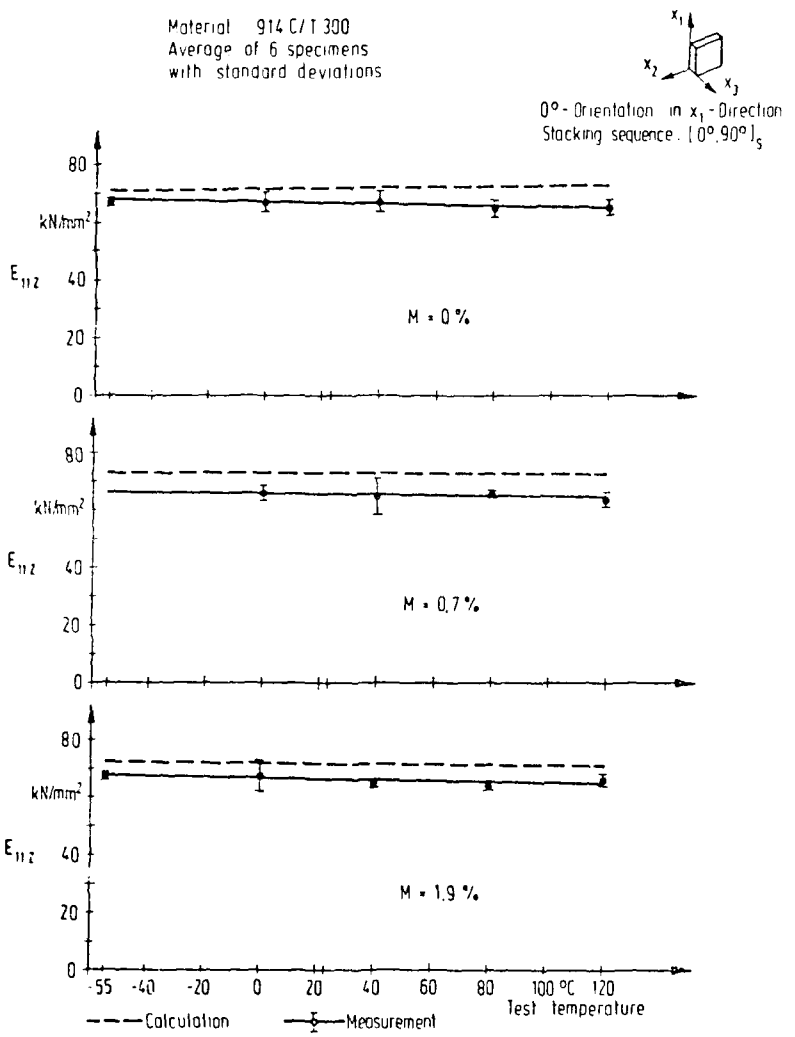

Fig. 6.32 Comparison of measured and calculated longitudinal modulus of elasticity of multidirectional CFRE laminate as function of test temperature and specimen moisture content.

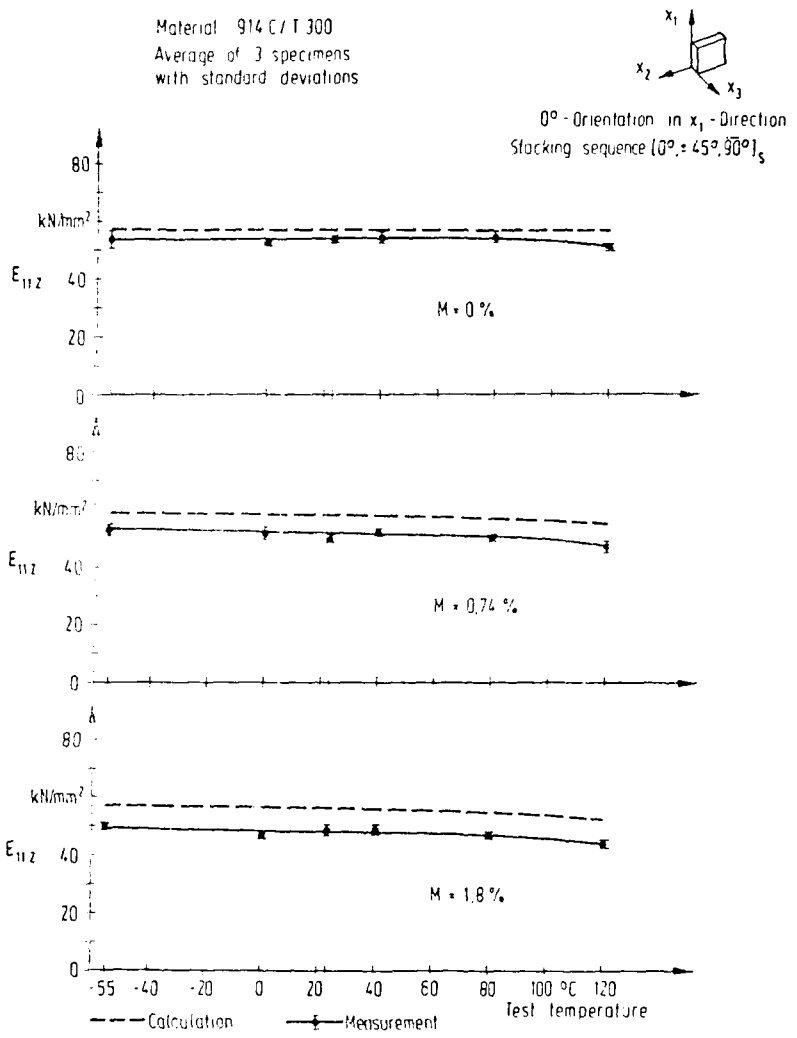

Fig. 6.33 Comparison of measured and calculated longitudinal modulus of elasticity of multidirectional CFRE laminate as function of test temperature and specimen moisture content.

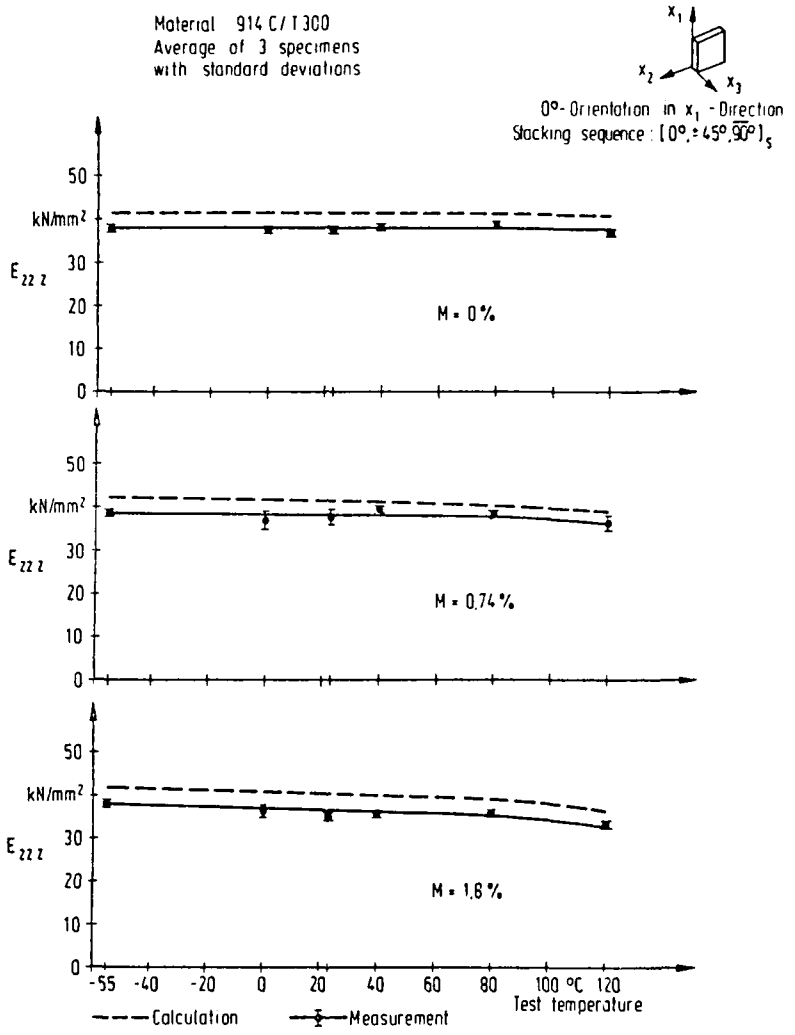

Fig. 6.34 Comparison of measured and calculated transverse modulus of elasticity of multidirectional CFRE laminate as function of test temperature and specimen moisture content.

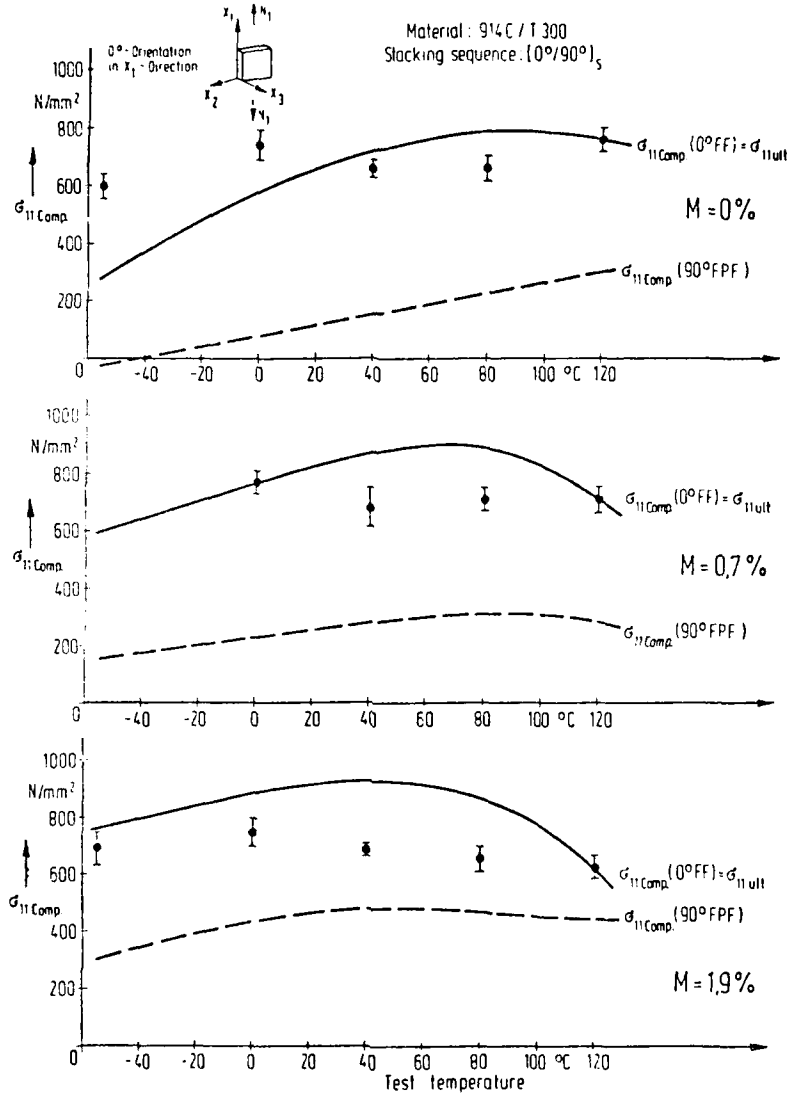

Fig. 6.35 Calculated average stresses of multidirectional CFRE laminates at first ply and ultimate failure as functions of test temperature and specimen moisture content
(Comparison with measured strength).

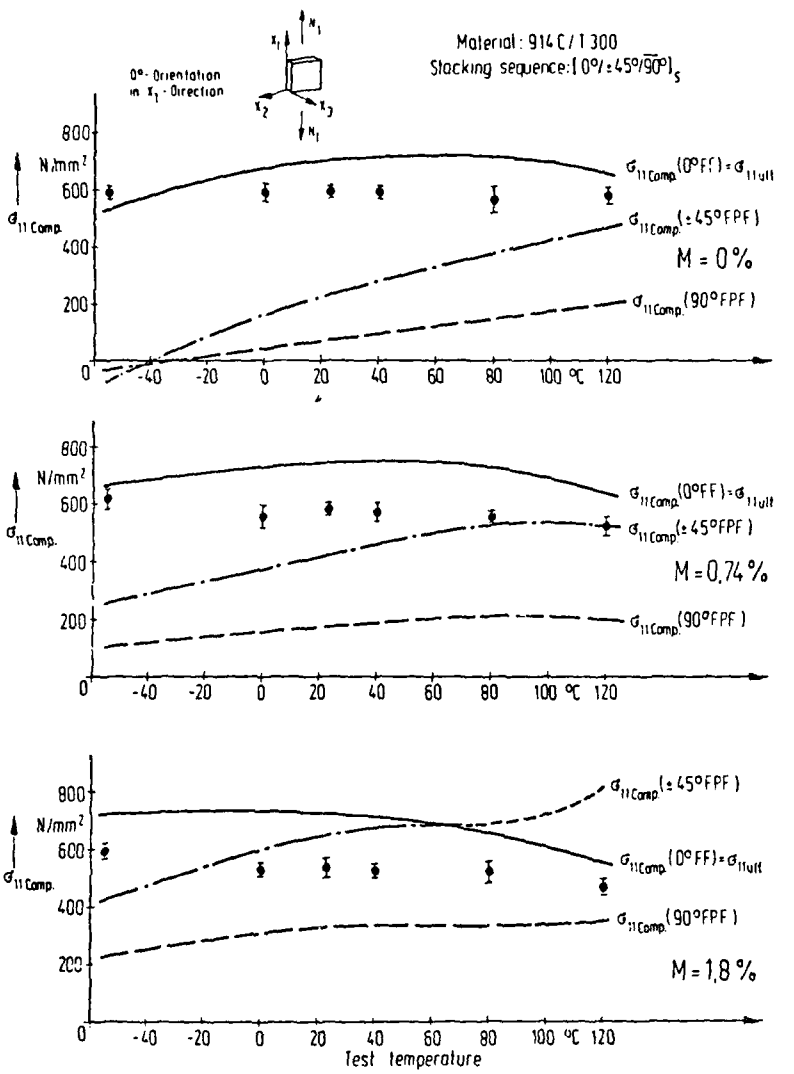

Fig. 6.36 Calculated average stresses of multidirectional CFRE laminates at first ply and ultimate failure as functions of test temperature and specimen moisture content
(Comparison with measured strength).

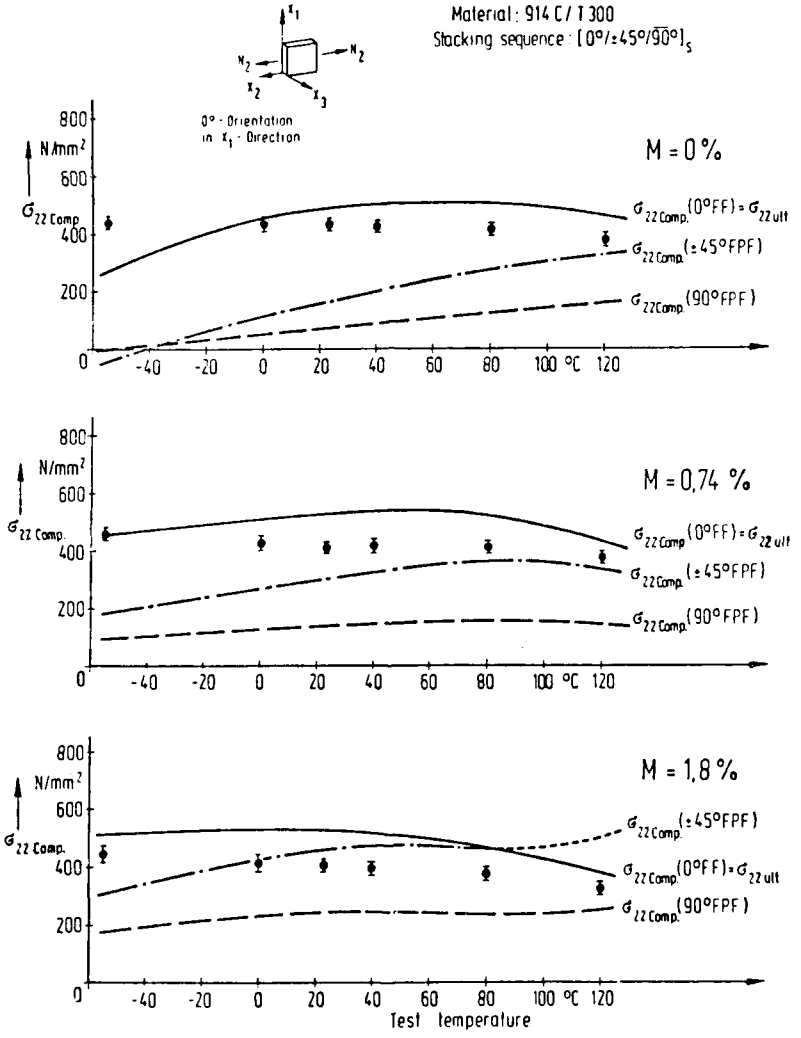

Fig. 6.37 Calculated average stresses of multidirectional CFRE laminates at first ply and ultimate failure as functions of test temperature and specimen moisture content
(Comparison with measured strength).

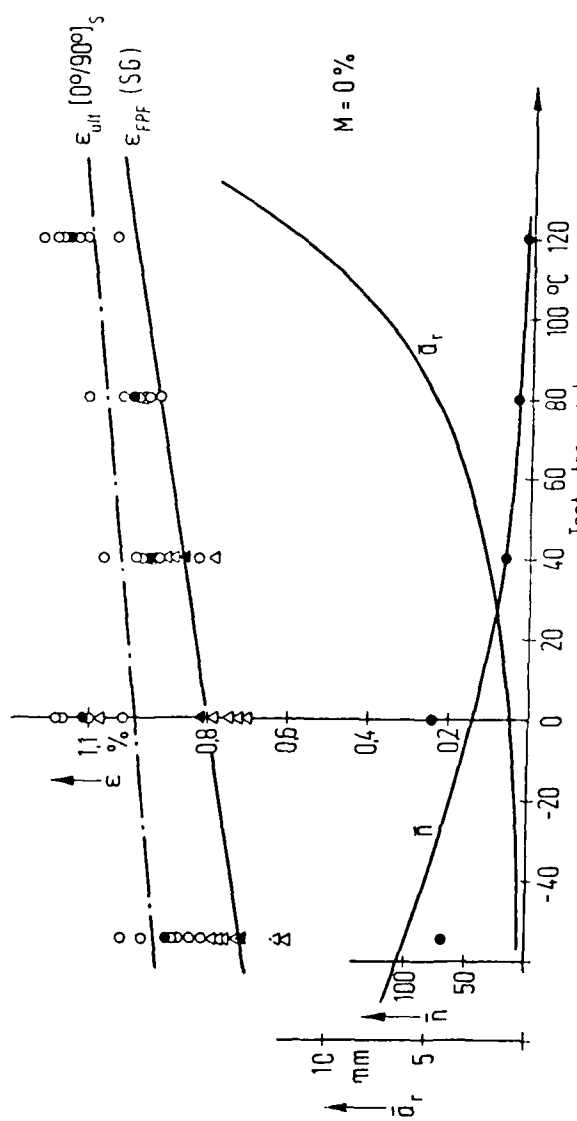

Fig. 6.38 Elongation at rupture, elongation at 90° ply failure, number of cracks $\bar{n}$ and crack distance $\bar{a}_r$ of multidirectional CFRE as functions of test temperature and specimen moisture content.

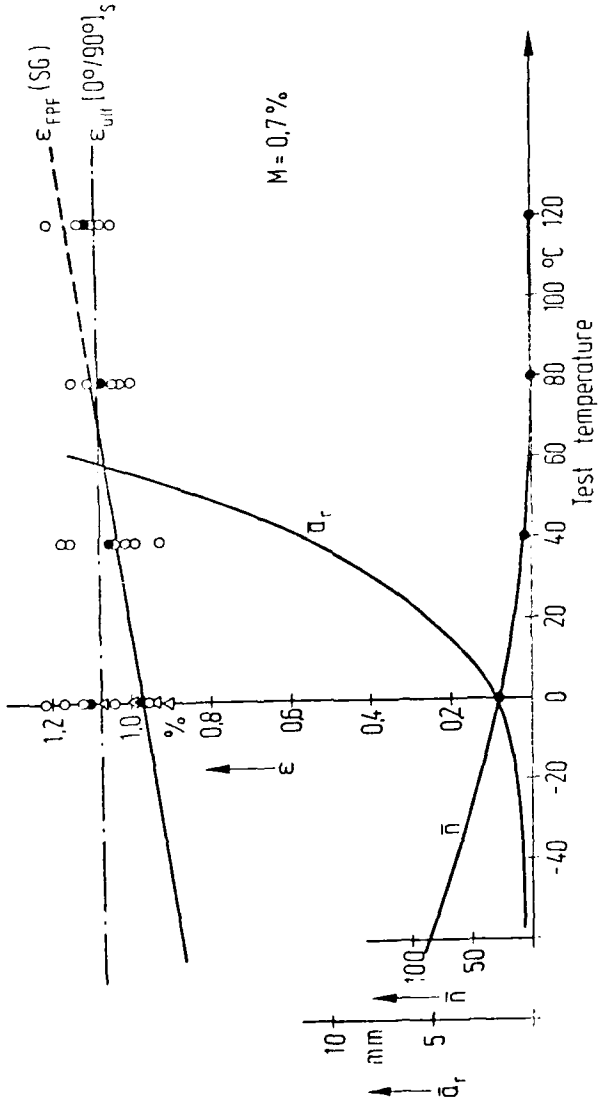

Fig. 6.39 Elongation at rupture, elongation at 90° ply failure, number of cracks $\bar{n}$ and crack distance $\bar{a}_r$ of multidirectional CFRE as functions of test temperature and specimen moisture content.

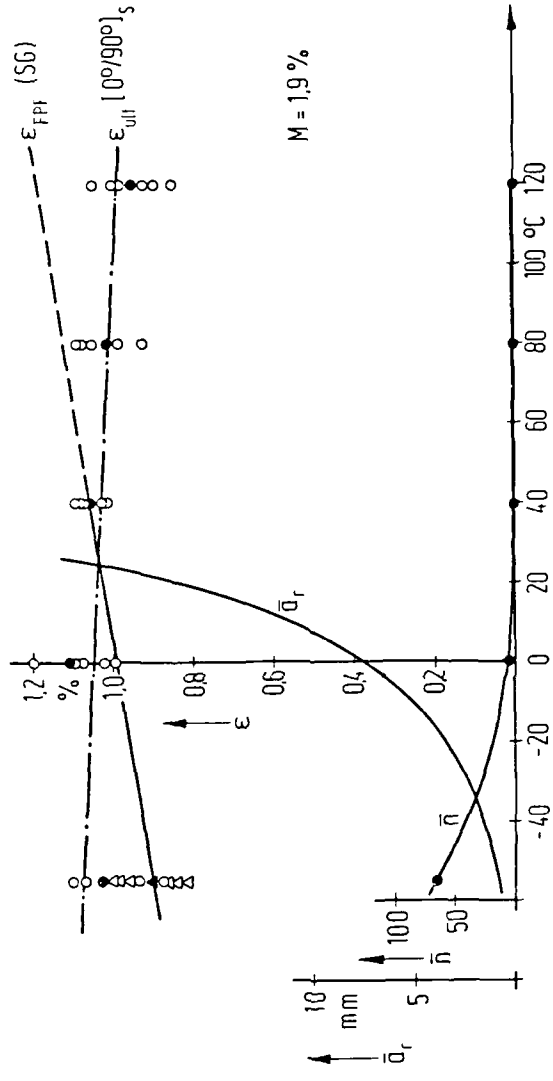

Fig. 6.40 Elongation at rupture, elongation at 90° ply failure, number of cracks $\bar{n}$ and crack distance $\bar{a}_r$ of multidirectional CFRE as functions of test temperature and specimen moisture content.

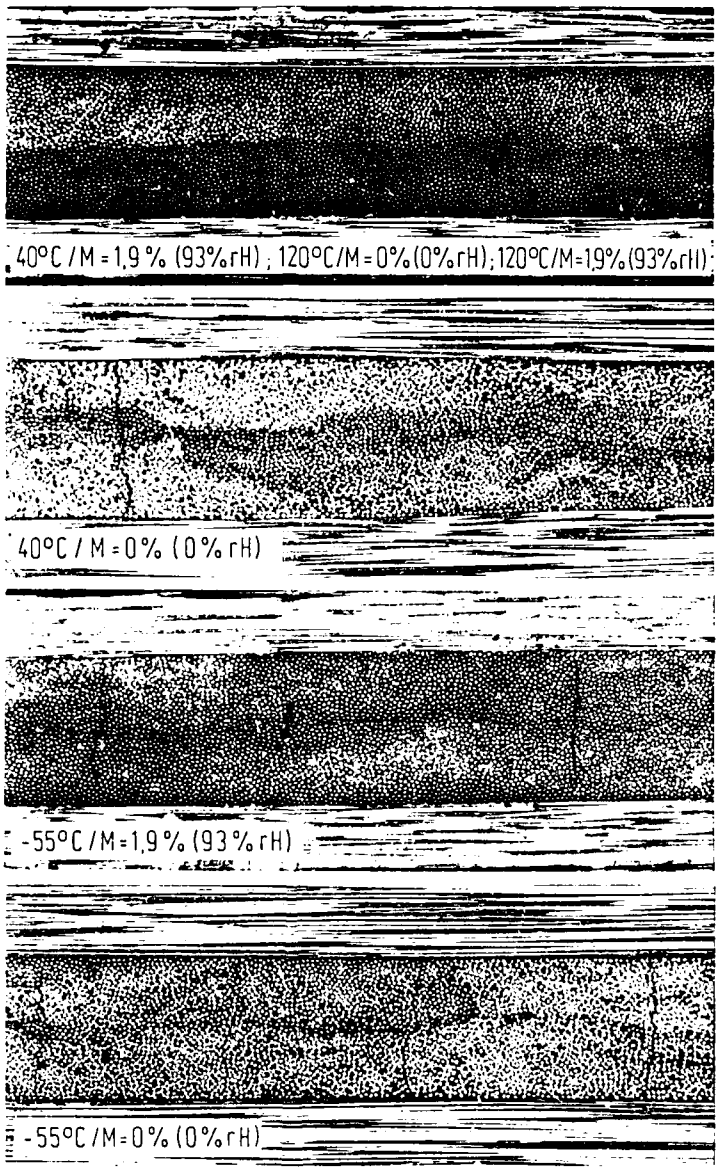

Fig. 6.41 Crack formation in a $[0°/90°]_s$ - laminate as function of test temperature and specimen moisture content (x100).

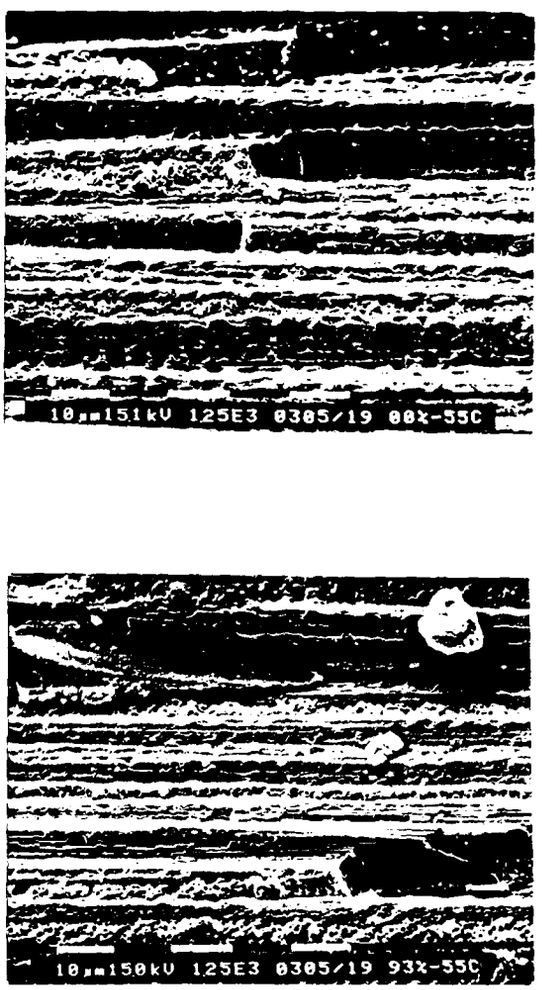

Fig. 6.42 Fracture surface of $[90°_8]_s$ - laminate at T=-55°C with different specimen moisture contents (914C/T300).

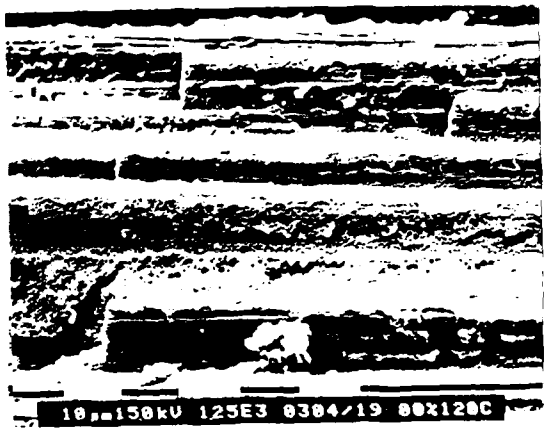

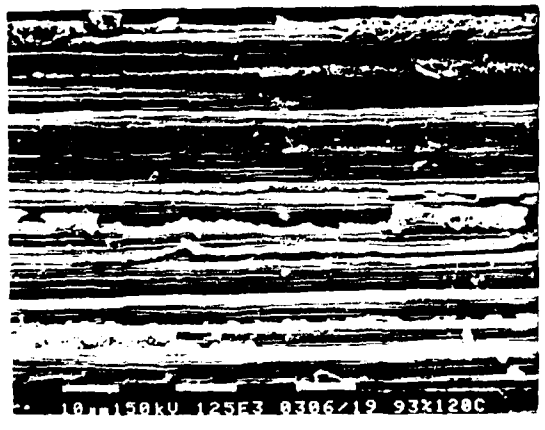

Fig. 6.43 Fracture surface of $[90°_8]_L$ - laminate at T=120°C with different specimen moisture contents 914C/T300).

7. RESPONSE OF STATICALLY TESTED NOTCHED SPECIMENS

7.1 Summary

By combining experimental and analytical investigations, an attempt was made to comprehend the significance of notches in carbonfiber-reinforced epoxy resins (CFRE). The test program included quasi-static tension tests with unidirectional on-axis and off-axis specimens as well as multidirectional specimens containing either a single central notch or two symmetrical notches at the edges. During the loading of the specimens the crack-opening displacements, the local strains, the overall displacements, and the length of the cracks emanating from the notch tips were observed. The tests were supported by radiographical and fractographical investigations. Based on the test results, parameters were determined which characterize the state of damage and the influence of stacking order, type of notch and length of crack. A general understanding of crack initiation and crack progression could be gained. Parallel to the test effort, numerical calculations were performed with the aim of establishing failure criteria for incorporation into the computer program LAMINA. The analyses presupposed that for several of the test specimen configurations the precepts of linear elastic fracture mechanics are applicable. By means of the finite element programs ASKA and LAMINA the states of stress at the crack tips in unidirectional laminates were analyzed for different crack lengths at load intensities under which crack extension was observed. The critical stress intensity factors K_1^c and K_2^c were established by different evaluation methods and the strain energy release rate concept was found to be the most promising. Using this approach it was possible to identify the total energy release as well as the two energy release components which associate with the two crack opening modes, from which both K_1^c and K_2^c can be obtained.

Fitting curves for the test results are discussed in detail in Appendix D.

7.2 Test Program

All of the investigations were performed on parallel-sided specimens with unidirectional and multidirectional laminate arrangements. The specimens were provided either with two symmetrically placed notches at the free edges, or with a single center notch. Fig. 7.1 is a summary of the scope of the test program.

For the determination of the strain field in the vicinity of the notch tip, and for the monitoring of the crack initiation, crack growth rates and crack lengths, the following techniques were employed (ref. Fig. 7.2):

- Electric strain gages (Hottinger 6/120 LY and 3/120 KY 13)
- Crack propagation gages (Micro-Measurement TK-09 CPB 02/005)
- COD-transducers (in-house development, DFVLR-patent)
- Displacement transducers (Hottinger W1)
- Light and electron beam scanning microscopes
- Radiographic, ultrasonic and acoustic emission techniques

All of the quasi-static tension tests were performed with extremely stiff hydro-pulse test machines. Preliminary investigations had shown that the crack propagation in notched specimens was sensitive to the choice of force vs. displacement control, to continuous vs. step vs. saw-tooth loading, and to the rate of loading in context with creep effects. In order to achieve compatible test results, all tests were performed under identical loading and environmental conditions.

The test machines were operated in the load-controlled mode. The loading rates were chosen such that the stress rate over the net cross-sections of the specimens was in all cases $\Delta\dot{\sigma}_{net} = 9$ N/mm² per minute.

Upon crack initiation and after distinct crack propagation in unidirectional laminates and distinct damage progression in multidirectional laminates, the load was held constant for 5 seconds and subsequently reduced by the equivalent of $\Delta\sigma_{net} = 25$ N/mm². In this fashion it was avoided that further damage could take place during the approximately 100 seconds necessary for the

microscopic measurement of the crack lengths. Subsequently, the load was continuously raised until the next marked damage progression took place.

7.3 Types of Damage Progression

The tensile loading of a notched specimen leads to high tensile and shearing stresses in the vicinity of the notch tip. If these stresses exceed their critical values, non-linear deformations result followed by individual macrocracks in unidirectional laminates, or by an assembly of microcracks in multidirectional laminates, emanating from the very tip of the notch. In unidirectional laminates the crack initiation phase (<0.5 mm) occurs either suddenly or gradually. Contrary to metallic materials, where cracks extend always in the direction perpendicular to the highest normal stress, the crack extension in fiber-reinforced resinous materials is determined by the fiber directions of the laminate. During the tests of unidirectional laminates the cracks developed always parallel to the fiber direction as shown, typically, in Fig. 7.3. In the $[0°]_n$-laminates, always two cracks developed at each of the notch tips, while in the $[\alpha°]_n$-laminates one crack only proceeded from each of the notch tips toward the center of the test specimen, indicating pure matrix failures.

Unidirectional laminates with large off-axis angles ($\alpha \geq 30°$) always failed suddenly by complete separation without a recognizable crack initiation or extension.

In multidirectional laminates matrix failures within and between plies were observed as well as fiber breaks and fiber pull-outs. The damage, therefore, is characterized not by a single crack but by a multitude of cracks within an extended damage region, typically depicted in Fig. 7.4.

The extension of the cracks under continuously increasing load is, independent of the type of laminate, not a continuous process but takes place at variable extension rates. Erratic crack extensions were also observed under constant load due to creep of the

resin. Figs. 7.5, 7.6 and 7.7 describe the progress of crack extension by means of COD-records for uni- and multidirectional laminates.

With respect to the non-continuous crack propagation in unidirectional laminates two explanations can be offered. Detailed stress analyses show that the stress field around the crack tip changes during the propagation of the crack. While the normal and shear stresses in the fiber direction remain more or less constant, the tensile stresses in the transverse direction clearly diminish with increasing crack length as shown in Fig. 7.8, which also indicates the change in the deformation patterns. Additionally, the crack propagation is affected by misaligned fibers which sporadically cross the well-aligned fibers in the path of the crack and thereby retard its propagation. In accordance with Fig. 7.9, a new crack may form ahead of the original crack tip and a sudden jump in the crack length may be expected following the break of the misaligned fibers as illustrated in Fig. 7.10.

The above processes were observed microscopically during the tests and substantiated by subsequent investigations based on radiography and scanning electron beam microscopy. Fig. 7.11 is evidence of the latter.

7.4 Characteristic Quantities

The test program proved that insight can be gained by COD- and strain gage (SG) measurements, typically displayed in Figs. 7.12 and 7.13, into the extension of cracks and damage zones in notched laminates.

In unidirectional laminates a quasi-linear relationship exists between crack length and crack opening displacements, as shown in Fig. 7.14. It is, therefore, possible to deduce the crack length from the COD-measurements. Within the measured range an approximately linear dependence also exists between the total elongation of the test specimens and the crack lengths, Figs. 7.15 and 7.16.

In $[0°_2/+45°/0°_2/-45°/0°/90°]_s$-laminates the COD- and strain measurements produced results similar to those of unidirectional laminates as is evident from a comparison of Fig. 7.6 with Fig. 7.12. This leads to the supposition that also in the case of multidirectional laminates the extent of the damage zone, or the aggregate of the crack lengths, can be deduced by COD-measurements. A direct determination of the individual crack lengths seems hardly possible.

In order to assess the damage process and to describe the damage state the COD-measurements, as functions of the loading, were evaluated with respect to the following properties:

- Limit of linearity
- First minor jump (first microcrack at notch tip)
- First pronounced jump (first distinct crack)
- Maximum values

7.4.1 Characteristic Quantities of Uniaxial Laminates

Figs. 7.17 and 7.18 contain measured data relative to crack initiation and failure of on- and off-axis unidirectional laminates. Laminate failure is defined as the condition where the cracks extend to the region of the grips of the test machine. Each of the symbols represents an average of 4 to 10 tests, whose numerical values are given in Fig. 7.19. According to Fig. 7.17, laminates with $\alpha = 0°$, $5°$, $10°$ and $15°$ developed initially matrix cracks, which led to crack extensions and eventual failure under increasing load. The failure load diminished rapidly with increasing values of the off-axis angle, $\alpha°$. In laminates with $\alpha \geq 30°$ the failures occurred suddenly without noticeable evidence of crack initiation and extension.

In Fig. 7.18 the failure stresses of notched laminates relative to the rupture stresses of unnotched laminates for various laminate configurations are shown. It is apparent that variations of the thickness and width, and of the off-axis angle of the laminates, have only a minor influence on their failure characteristics.

The majority of the experiments led to fracture modes which were point-symmetrical relative to the center of the specimens. The consistency of this phenomenon could be confirmed by finite-element calculations on a notched $[0°]_8$-laminate with a single 10 mm long crack at one of the notch tips. The calculated stresses in the direction of the potential crack propagations are given in Fig. 7.20. A comparison of the stress components shows that the fracture process is influenced predominantly by the normal stresses transverse to the crack and hardly by the shear stresses. The stress fields around the different crack tips are apparently quite similar. The aberrations from the point-symmetrical fracture mode, observed in ca. 30% of the test specimens, may be due to scatter of the material strength properties. The test results were evaluated in terms of the average far-field stresses versus crack lengths, overall specimen elongations and crack opening displacements. Figs. 7.21, 7.22 and 7.23 show compilations of test data as well as approximated curve-fits for a $[5°]_8$-laminate. The corresponding digital values are given in Fig. 7.24.

7.4.2 Characteristic Quantities of Multidirectional Laminates

The test results for $[0°_2/+45°/0°_2/-45°/0°/90°]_s$-laminates with center and edge notches of different configurations and lengths are shown in Fig. 7.25. Obviously, the net stress levels at which crack initiation, propagation and eventual laminate rupture occurred, are significantly higher than those registered for unidirectional laminates. The type of notch and the notch length seem to have little influence on the test specimen performance. Fig. 7.26 and 7.27 summarize further pertinent test results.

7.5 Analytical Approach

For the analytical treatment of the experiments the unidirectional laminates were considered to be orthotropic, so that the crack propagation could be approximated by the principles of linear elastic fracture mechanics. The test results served as validation of this assumption and supported the derivation of fracture cri-

teria necessary for the further development of the computer program LAMINA.

In linear fracture mechanics the crack propagation is governed essentially by two parameters: the stress intensity factors and the strain energy release rate. While critical values of the stress intensity factors identify the incipient crack propagation, the crack direction is characterized by the maximum of the strain energy release rate.

In accordance with the theory of elasticity the stresses at the crack tip are singular. In homogeneous isotropic materials they increase in proportion to $1/\sqrt{r}$, where r denotes the distance from the crack tip. Singular solutions exist for different specimen geometries, load intensities and crack configurations [7.1]. In contrast, similar closed-form solutions are hardly known for orthotropic materials because of the larger number of material parameters [7.2].

In the vicinity of the crack tip in a membrane, the stresses are approximated by the equation

$$\sigma^{\alpha\beta} = \frac{1}{\sqrt{2\pi r}} \cdot S_{\lambda}^{\alpha\beta}(a_{ij}, \varphi) \cdot K_{\lambda} + \sigma_{H}^{\alpha\beta} \tag{7.1}$$

in which (r,ϕ) are polar cordinates referred to the crack tip, a_{ij} the coefficients of the constitutive law, K_{λ} the stress intensity factors and $\sigma_{H}^{\alpha\beta}$ the continuous homogeneous solution for the matching of the boundary conditions. In front of the crack tip the functions $S_{\lambda}^{\alpha\beta}$ are partially independent of the material coefficients so that equation (7.1) can be solved explicitly for K_{λ}:

$$\begin{aligned} K_1 &= \sqrt{2\pi r} \cdot (\sigma^{22} - \sigma_H^{22}) \\ K_2 &= \sqrt{2\pi r} \cdot (\sigma^{12} - \sigma_H^{12}) \end{aligned} \tag{7.2}$$

The bracketed expressions in equation (7.2) denote particular solutions for an unbounded cracked disk.

Near the crack tip the continuous boundary term $\sigma_H^{\alpha 2}$ is negligible in comparison to the singular solution $\sigma^{\alpha 2}$. Upon substitution of the exact solution for $\sigma^{\alpha 2}$ by a finite element approximation, $K_\lambda(r)$ may be expressed as a linear function in the vicinity of the crack tip. The extrapolation of the straight branch for $r = 0$ then yields the stress intensity factors (Fig. 7.28). In the literature this procedure is known as the extrapolation method. It requires a very fine element mesh at the crack tip so that a sufficiently long straight branch for the extrapolation can be established. In a coarse mesh the function develops as sketched by the upper curve in Fig. 7.28, which does not allow a straight extrapolation. In the case of off-axis unidirectional laminates, however, the extrapolation method has been observed to diverge in extremely fine element meshes.

The stress intensity factors can also be determined by means of the energy released during the crack propagation. The basis for this procedure are the Rice integrals [7.3] which presuppose an affine type of crack propagation (Fig. 7.29).

$$
\begin{aligned}
G &= \int_{\delta c} \sigma^{\alpha 2}(r = x,\ \varphi = 0) \cdot \Delta u_\alpha (r = \delta c - x,\ \varphi = \pm\pi)\, dx \\
&= \oint_S (W(\gamma_{\rho\lambda}) \cdot n_1 - \bar{p}_s^\rho \cdot u_{\rho,1})\, dS \qquad (7.3) \\
&= R_1^{\rho\lambda}(\sigma_{ij}) \cdot K_\rho \cdot K_\lambda
\end{aligned}
$$

The first equation (7.3-1) describes the energy release associated with the propagation interval δc directly. This expression was tranferred by Rice into a path-independent line integral (7.3-2), where the closed integration path includes the crack tip. The term $W(\gamma_{\rho\lambda})$ denotes the specific strain energy, n_ρ the components of the unit vector normal to the boundary of the membrane segment isolated by the integration path, and $\bar{p}_s^\rho$ the corresponding tractions. The evaluation of the integrals for the particular solution given in equation (7.1) allows the coupling of the energy release rate G with the stress intensity factors K_λ. The constants $R_1^{\rho\lambda}$ depend only on the constitutive law and assume in the case of orthotropic materials the following values

$$
\begin{aligned}
R_1^{11} &= \varkappa / \sqrt{a_{11}} \\
R_1^{22} &= \varkappa / \sqrt{a_{22}} \\
R_1^{12} &= R_1^{21} = 0 \\
\varkappa &= \sqrt{(\sqrt{a_{11} \cdot a_{22}} + a_{11} - a_{66}/2) \cdot a_{11} \cdot a_{22}/2}
\end{aligned}
\tag{7.4}
$$

The energy release rate G as such provides only one equation for the determination of the two stress intensity factors. By means of the finite element method, however, the energy release rate G can be split into two terms depending only on K_1 and K_2, respectively, as follows:

$$G = G_1(K_1^2) + G_2(K_2^2) \tag{7.5}$$

In the finite element model, a fictitious propagation of the crack over the length of one element is introduced such that an opening of the crack is admitted only normal to the crack axis, while the tangential displacements of the adjacent elements remain coupled. The evaluation of equation (7.3-2) for this case provides the energy release rate component $G_1(K_1^2)$ from which the corresponding stress intensity factor K_1 can be determined. For the calculation of $G_2(K_2^2)$, analogously, only the tangential displacements are disconnected, while normal to the fictitious crack the displacements remain coupled. This "modified J-integral method" yields useful results even when the extrapolation method fails. However, it is numerically demanding as the displacement components associated with the fictitious crack propagation must be calculated explicitly rather than by affinity relationships as in the Rice integral.

The approximation of the stresses in the vicinity of the crack tip by means of standard finite elements techniques is poor. Therefore, equation (7.3-1) is unsuitable to determine the energy release rates G_α. In [7.4], Buchholz replaced the stresses and displacements resulting from a cracked element by the corresponding forces and displacements in the nodal points (Fig. 7.30) and thereby obtained highly accurate energy release rates. This procedure, known as the "modified crack closure integral method", is

equivalent to the "modified J-integral method" at a substantially lower numerical effort.

Both methods were used for the evaluation of the experimental results with the aim to determine the energy release rate and the stress intensity factors in dependence on the crack length and on the off-axis angle of the fibers in unidirectional laminates. Emphasis was placed on the identification of parameters suitable, perhaps in the form of interaction diagrams, for the description of the crack progression.

7.6 Results of Analysis

7.6.1 Material Properties

The experimental results were evaluated on the basis of the material properties listed in Fig. 7.31. An initial comparison of measured forces and displacements with analytically derived values showed that the elasticity constants, established for unidirectional laminates at 30% of ultimate load, were too high for direct application to the test program, in which the applied stresses did not exceed 10% of their ultimate values. At such low stress levels, the carbonfibers are still being straightened so that, according to Fig. 7.32, the stress-strain diagram is non-linear. In order to support the actual test conditions the elasticity constants listed in Fig. 7.31 were proportionately reduced until the calculated displacements corresponded to the measured displacements at the elastic limit load. The such modified constants were also used for higher load levels.

Fig. 7.33 shows a comparison of measured and calculated force-displacement curves for the test specimen elongation, w1, and for the notch opening displacement, COD. Discrepancies between measured and calculated values occur only in the w1-curves when the crack tips approach the terminals of the displacement transducer. The terminals are not attached to discrete points at the specimen center line but to clamped-on yokes extending over the entire specimen width so that, in the presence

of long cracks, the longitudinal displacements over the width of the specimen are not constant and, because of the yoke deformations, the clamping stresses at the edges of the specimen are higher than at the center. Therefore, a more pronounced curvature should be expected in the measured w1-curve than in the calculated curve which relates to the specimen center line. The discrepancies are not indicative of a possible plastic deformation at the crack tip as is evident from the unloading curve in Fig. 7.12, which terminates at the point of origin.

7.6.2 Element Net

The reference calculations for the $[0°]_8$- and $[90°]_8$-laminates were performed with the program LAMINA. As short cracks do not appreciably disturb the prevailing double-symmetries, only a quarter of the test specimen needed to be modelled. Two different element nets were chosen: A coarse net, shown in Fig. 7.34, covered the entire length of the specimen to the rigid clamping head of the test machine, while in a finer net the clamping was introduced at the location of test point w1 (Fig. 7.35). In both nets the influence of the notch on the stress distribution extended beyond the clamping location. However, as displayed in Fig. 7.36, the magnitude of the stress differences in the case of short cracks is minor, so that the investigations could be based on the shorter, but finer, element net.

The off-axis laminates were analysed with the TRIM6-element of the ASKA-program. Because ASKA is not equipped to accomodate point-symmetry, the entire test specimen needed to be modelled as shown in Fig. 7.37.

In all element nets the loads were introduced through imposed constant longitudinal displacements at the assumed clamping location. The resulting longitudinal forces were correlated with the measured test values.

7.6.3 $[0°]_8$-Laminates

Stress intensity factors were determined for $[0°]_8$-laminates on the basis of measured loads and crack lengths. Fig. 7.38 is an example of a numerical evaluation using the extrapolation method, while Fig. 7.39 displays the resulting stress intensity factors as a function of the crack length. They fall on approximately straight lines for both crack opening modes and increase with increasing crack length. The slope of the lines may be due to the clamping effects which have not faded out completely at the crack tips, and ought to disappear in very long test specimens.

Straight-line extrapolations for crack lengths $l_c \to 0$ lead to the critical stress intensity factors at crack initiation:

$$K_1^c = 48 \text{ N/mm}^{3/2} \qquad (7.6)$$
$$K_2^c = 123 \text{ N/mm}^{3/2}$$

Fig. 7.40 shows the associated energy release rates for different crack lengths. The circled values were calculated with the use of J-integrals, and the solid line was established from the stress intensity factors given in Fig. 7.39. Both procedures, apparently, are in excellent agreement. In $[0°]_8$-laminates the crack begins to move at an energy release rate of

$$G_c = 0.48 \text{ N/mm}. \qquad (7.7)$$

The mean value of

$$G_m = 0.52 \text{ N/mm}. \qquad (7.8)$$

indicated in Fig. 7.40 corresponds well with the energy release rate chosen by ESI in their crack propagation calculations (Fig. 7.41).

7.6.4 $[90°]_8$-Laminates

The evaluation of test results for $[90°]_8$-laminates is summarized in Figs. 7.42 and 7.43. The critical stress intensity factors calculated by the extrapolation method

$$K_1^c = 52 \text{ N/mm}^{3/2} \qquad (7.9)$$
$$K_2^c = 0 \text{ N/mm}^{3/2}$$

correspond with those determined by the modified J-integral method. The critical energy release rate in $[90°]_8$-laminates is only

$$G_c = 0.187 \text{ N/mm}. \qquad (7.10)$$

and much smaller than in $[0°]_8$-laminates.

7.6.5 $[\alpha°]_8$-Laminates

The evaluation of unidirectional off-axis laminates is still incomplete. As is evident from Figs. 7.44 to 7.46, the extrapolation method leads to divergent results. Even extremely fine element nets and different evaluation directions did not improve the convergence. First results based on the modified J-integral method are being evaluated and appear promising.

7.6.6 Failure Criteria

The critical energy release rates given in equations (7.7) and (7.10) for the $[0°]_8$- and $[90°]_8$-laminates, respectively, are quite different and therefore unsuitable for the description of the crack propagation in unidirectional laminates. The stress intensity factors, however, are useful and can be displayed in the form of the interaction diagram presented in Fig. 7.47. From the current efforts it may be concluded that the crack propagation depends principally on the crack opening mode which is characterized by the stress concentration factor K_1. The influence of shear stresses is believed to be of subordinate

importance which is also evident in the work of Wang [7.5]. However, the accuracy of his test results is suspect since, in the presence of transverse tension, a reduction of the crack velocity on account of superimposed shear stresses is hardly sensible.

7.6.7 Influence of Laminate Thickness

The influence of the laminate thickness on the strength properties of test specimens are displayed in Figs. 7.48 through 7.50, where the crack lengths l_c, the specimen elongations w1 and the notch opening displacements COD of $[0°]_8$- and $[0°]_{16}$-laminates are compared. It is evident that the thin laminates tend to exhibit less crack propagation but fail at lower stress levels than the thicker laminates. A numerical evaluation of this phenomenon is hampered by the considerable complexity of the three-dimensionality of the problem.

7.7 Observations

7.7.1 Notched Unidirectional Laminates

For notched unidirectional laminates the results can be summarized as follows:

- Cracks develop always parallel to the fibers.
- Crack propagation is significantly delayed by inevitable misalignment of fibers or fiber bundles.
- Thin laminates show earlier crack initiation and slower crack propagation than thick ones.
- The energy release rate is not a material constant and therefore not suitable for a description of the crack propagation.
- Cracks initiate at a critical combination of the stress intensity factors (K_λ-interaction).

- Crack propagation predominantly depends on the crack opening mode I and very little on the shear mode II.

As a conclusion from the second observation, the cracking of multidirectional laminates containing multiple unidirectional layers might be reduced, if the fiber angles of the individual layers alternate by perhaps ±5° from their main direction.

7.7.2 Notched Multidirectional Laminates

For notched multidirectional laminates the results can be summarized as follows:

- Damage progression occurs as a multitude of single cracks within a damage zone. The direction of these cracks are determined by the fiber directions of the individual layers.

- Damage progression occurs as matrix failure within or between layers, or as fiber breaks, or as fiber matrix debonds.

- Damage progression is not always a continuous process. The speed may vary and sudden jumps may occur as observed in the tests with unidirectional laminates.

- The type of damage - notch type, notch length - has only a minor influence on the damage progression.

- Damage progression and eventual failure occur at considerably higher load levels than for unidirectional laminates.

7.8 References

[7.1] Rooke, .P. Cartwright, D.J. — Stress Intensity Factors. Uxbridge, UK: Hillingdon Press, 1976.

[7.2] Lekhntskii, S.G. — Theory of Elasticity of an Anisotropic Elastic Body. San Francisco, USA: Holden-Day Inc., 1963.

[7.3] Rice, J.R. — A Path Independent Integral and the Approximate Analysis of Strain Concentration by Notches and Cracks. J. Applied Mech. *35*(1968), pp. 379-386.

[7.4] Buchholz, F.-G. — Improved Formulae for the FE-Calculation of the Strain Energy Release Rate by the Modified Crack Closure Integral Method. Accu acy, Reliability, Training in FEM Technology, Editor J. Robinson, Robinson and Associates, Horton Road Woodlands Weinborne Dorset BH216 NB England, 1984.

[7.5] Wang, A.S.D. — Fracture Mechanics of Sublaminate Cracks in Composites. Composites Technology Review *6*(1984), pp. 45-62.

I. Specimen with edge notches

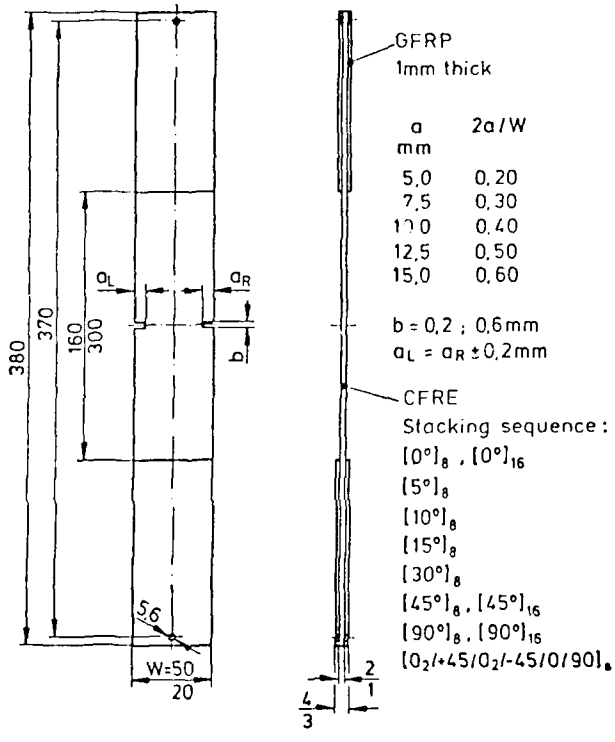

II. Specimen with center notch

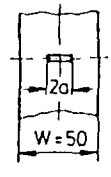

For a, 2a/W variations, see specimen I

Figure 7.1 Dimensions of the notched CFRE-specimens.

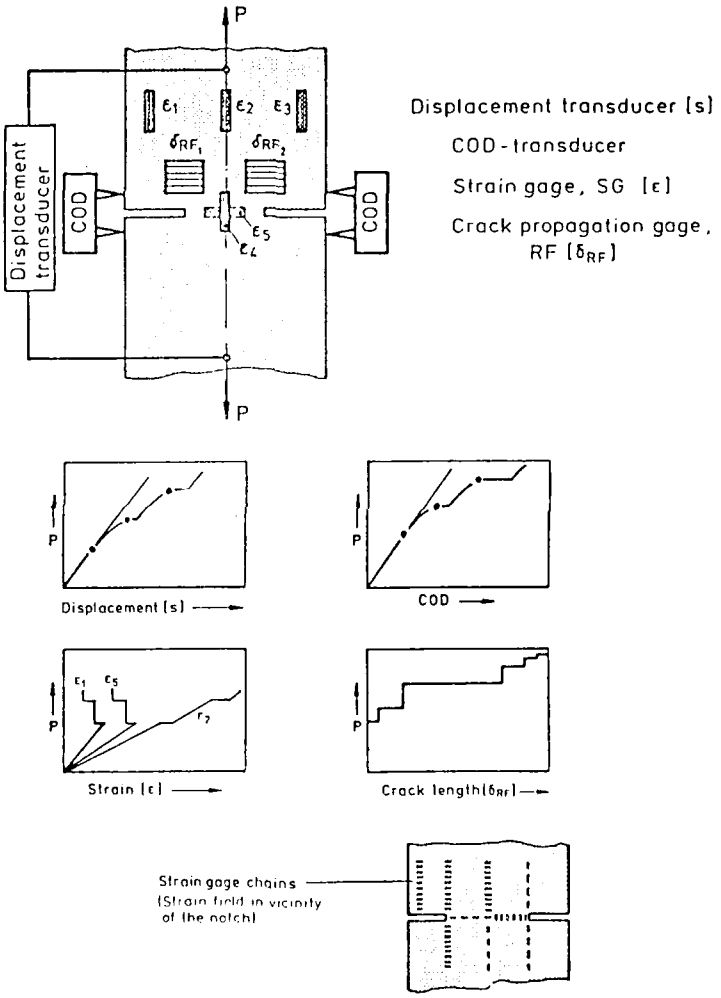

Figure 7.2 Measurement techniques to determine the crack propagation in notched CFRE-laminates.

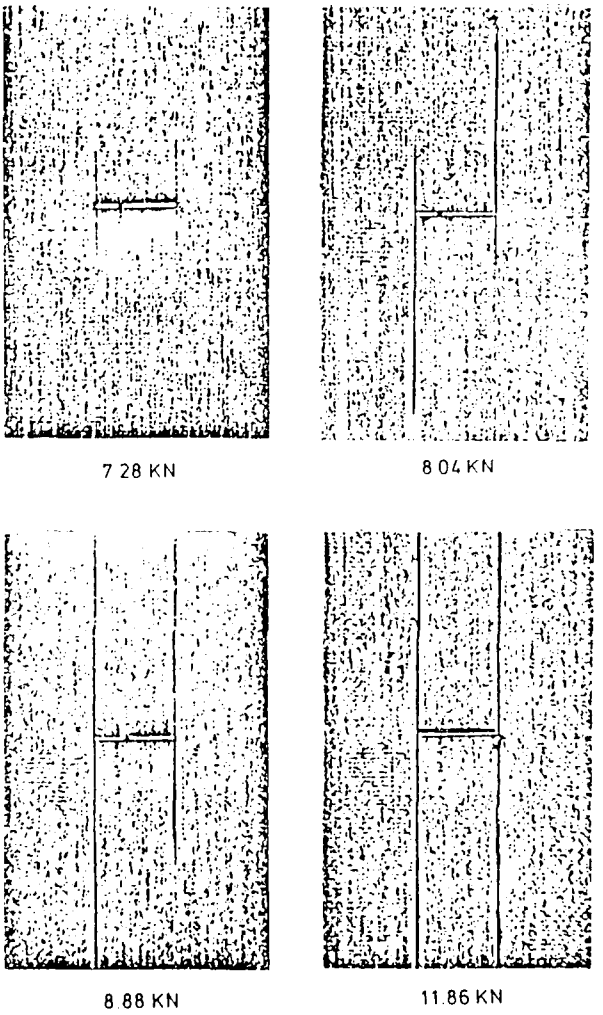

Figure 7.3 Crack propagation in a CFRE-specimen with a center notch under tensile load (Contrast-enhanced X-ray photographs).
Specimen width : 25 mm
Stacking sequence: $[0°]_8$

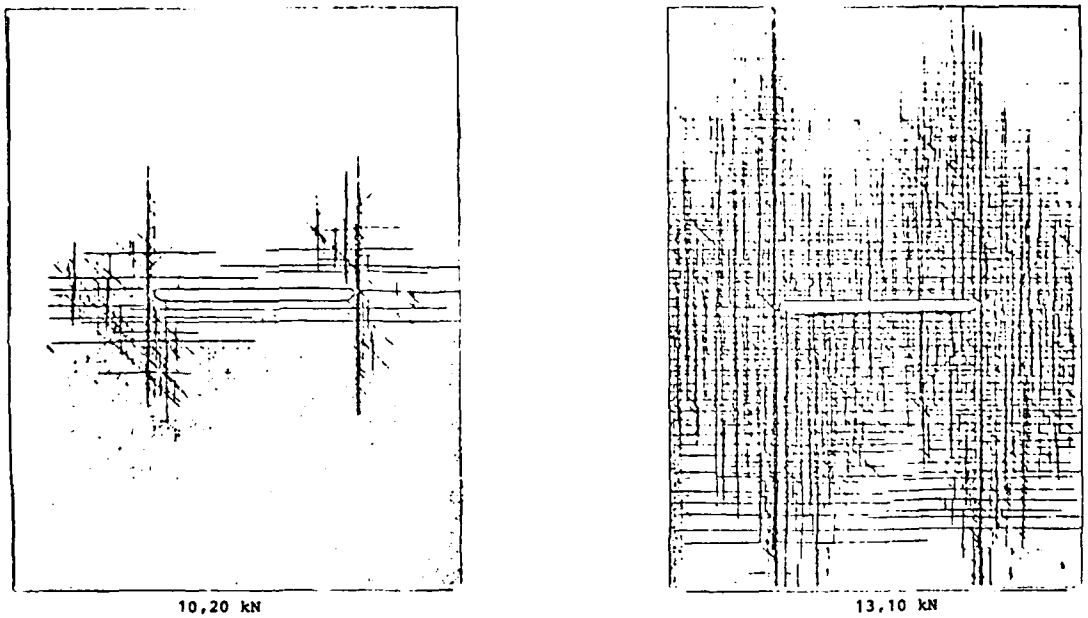

Figure 7.4 Crack propagation in a multidirectional CFRE-specimen with a center notch under tensile load (Contrast-enhanced X-ray photographs).
Specimen width : 25 mm
Stacking sequence: $[0°_2/+45°/0°_2/-45°/0°/90°]_s$

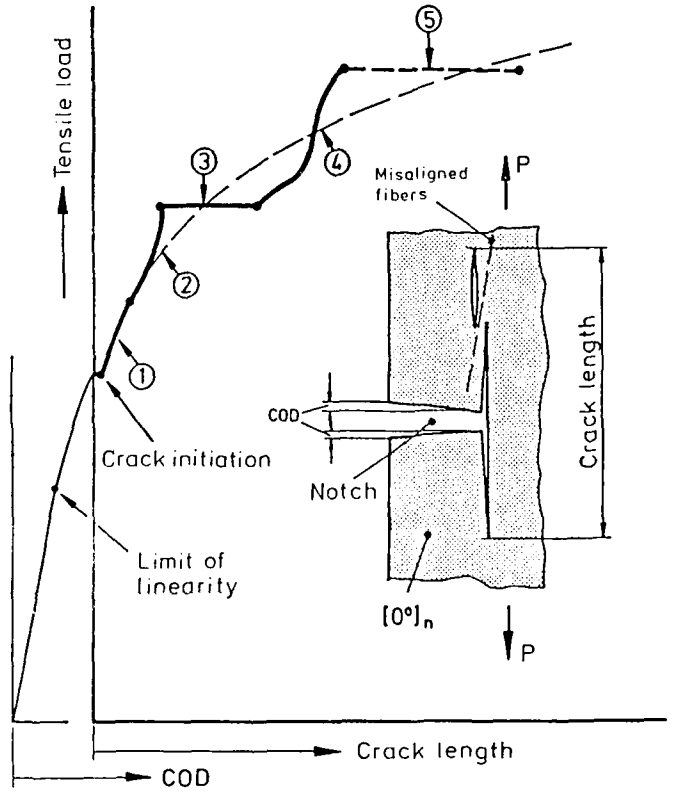

① Crack propagation with increasing rate of propagation
② Crack propagation with decreasing rate of propagation (Retardation by misaligned fibers)
③ Crack propagation abrupt (Fracture of misaligned fibers)
④ Increase/Decrease/Increase of the rate of propagation (Second crack develops above the misaligned fibers)
⑤ Crack propagation abrupt under increasing load, or Crack propagation slow under constant load.

Figure 7.5 Typical forms of crack propagation in unidirectional CFRE-laminates under tensile load.

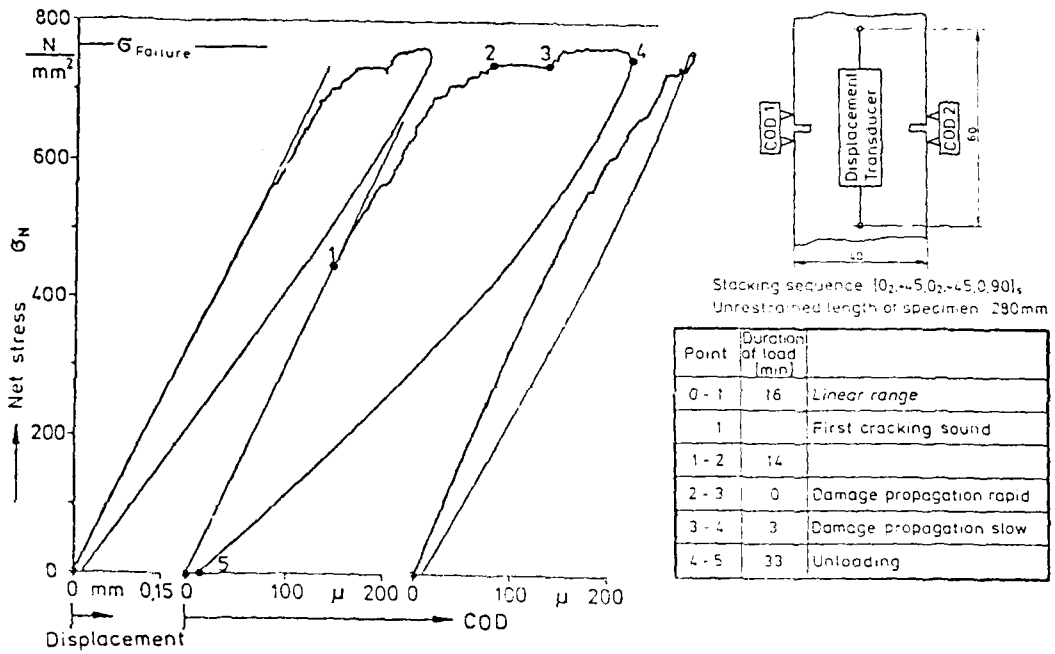

Point	Duration of load (min)	
0 - 1	16	*Linear range*
1		First cracking sound
1 - 2	14	
2 - 3	0	Damage propagation rapid
3 - 4	3	Damage propagation slow
4 - 5	33	Unloading

Figure 7.6 Displacement- and COD-measurements during a tensile test on a notched $[0°_2/+45°/0°_2/+45°/0°_2/-45°/0°/90°]_s$-CFRE-specimen.

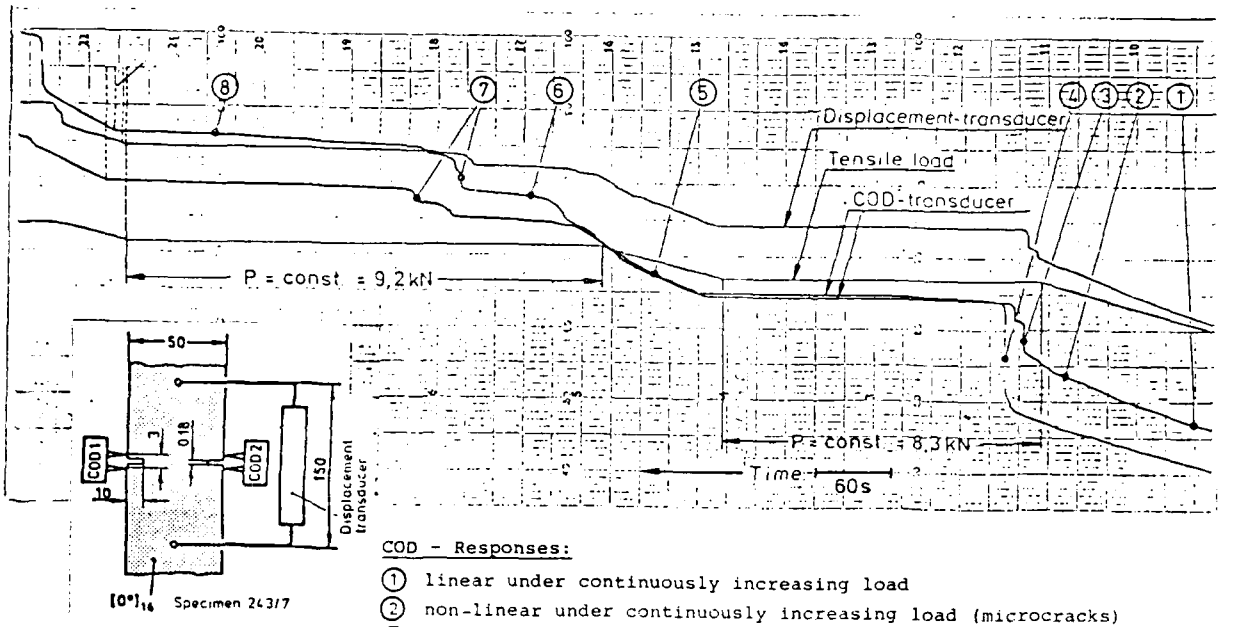

COD - Responses:

① linear under continuously increasing load
② non-linear under continuously increasing load (microcracks)
③ discontinuous under continuously increasing load (crack initiation)
④ discontinuous under constant load (crack initiation)
⑤ non-linear under continuously increasing load (crack propagation slow)
⑥ ⑧ gradual under constant load (" " ")
⑦ discontinuous under constant load (crack propagation rapid)

Figure 7.7 Unidirectional CFRE-laminate with edge notches under tensile load and continuous step-wise load increases under load control.

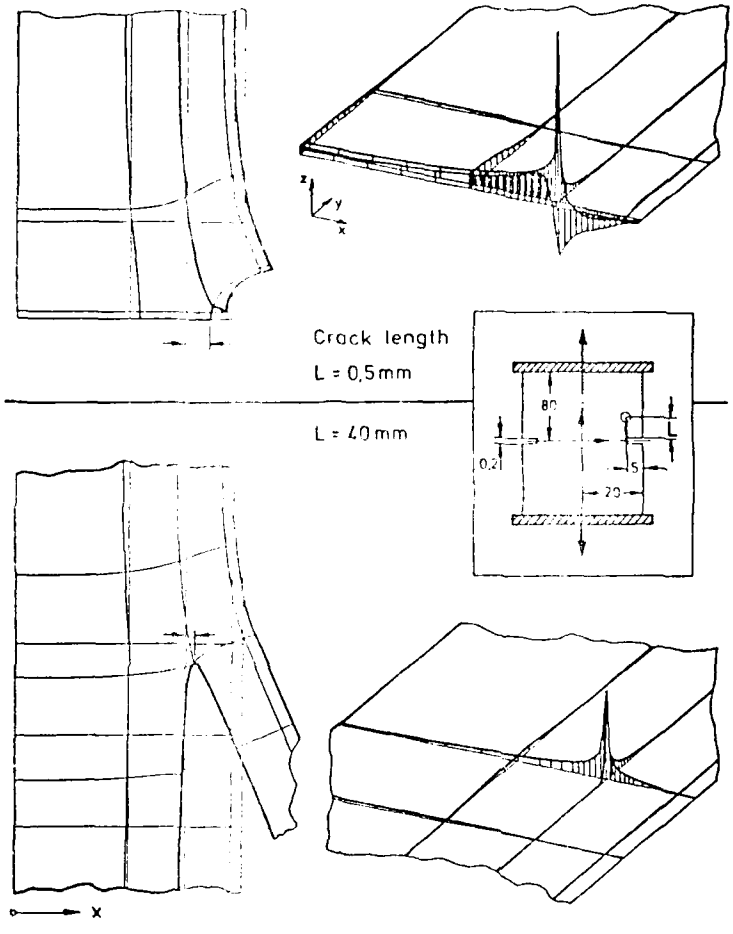

Figure 7.8 Deformation and tensile stress σ^{xx} in the transverse direction at the tip of cracks with different lengths L in notched unidirectional CFRE-laminates.

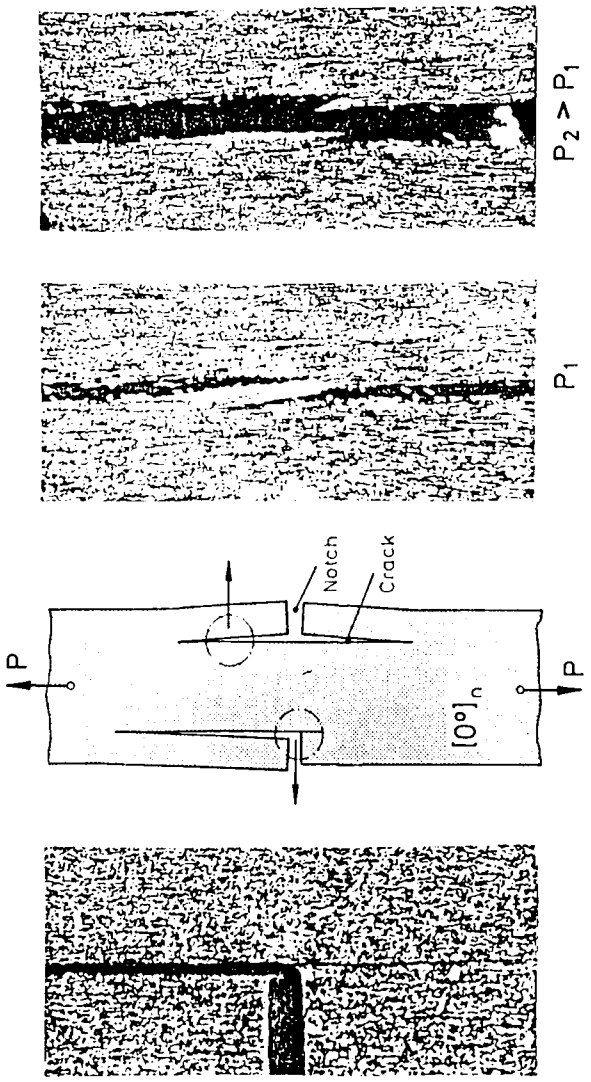

Figure 7.9 Retardation of crack propagation by misaligned fibers in a notched unidirectional laminate under tensile load.

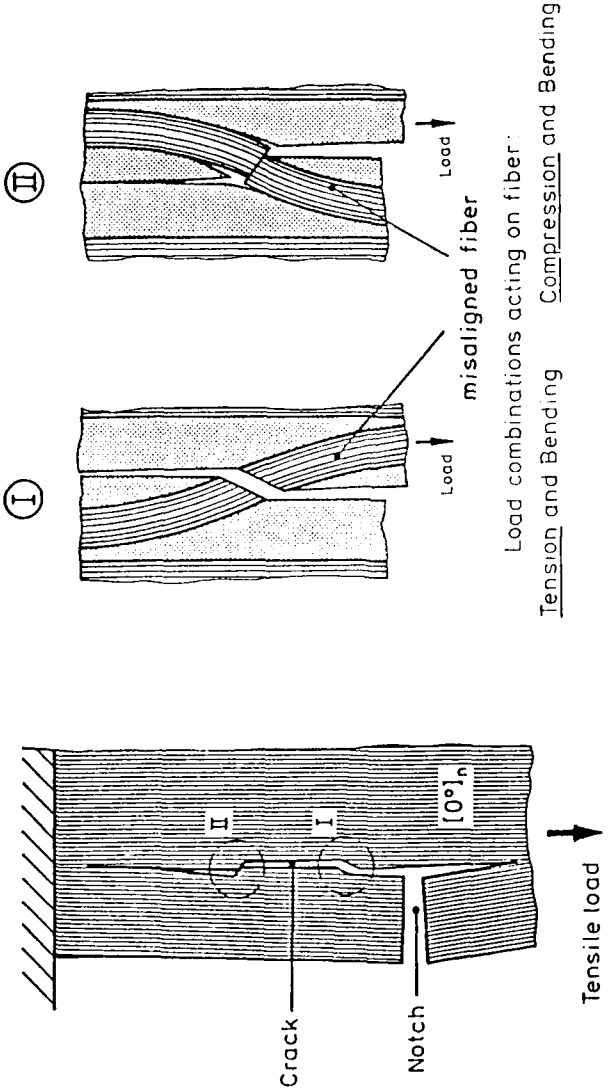

Figure 7.10 Different failure modes of misaligned fibers in an unidirectional laminate under tensile load.

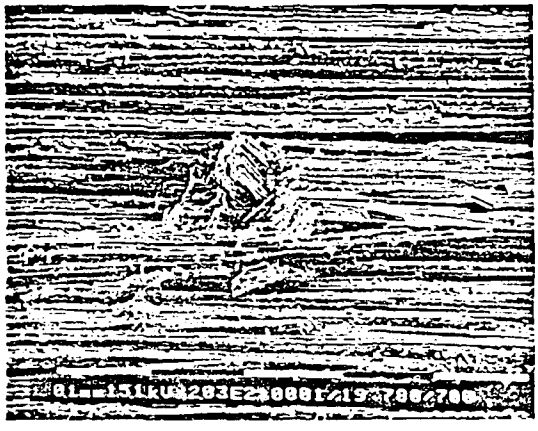

a)

b) : pendant of a)

Figure 7.11 SEM-photograph of the fracture surface with breaks of misaligned fibers, stressed by compression and bending, in an unidirectional CFRE-laminate under tensile load.

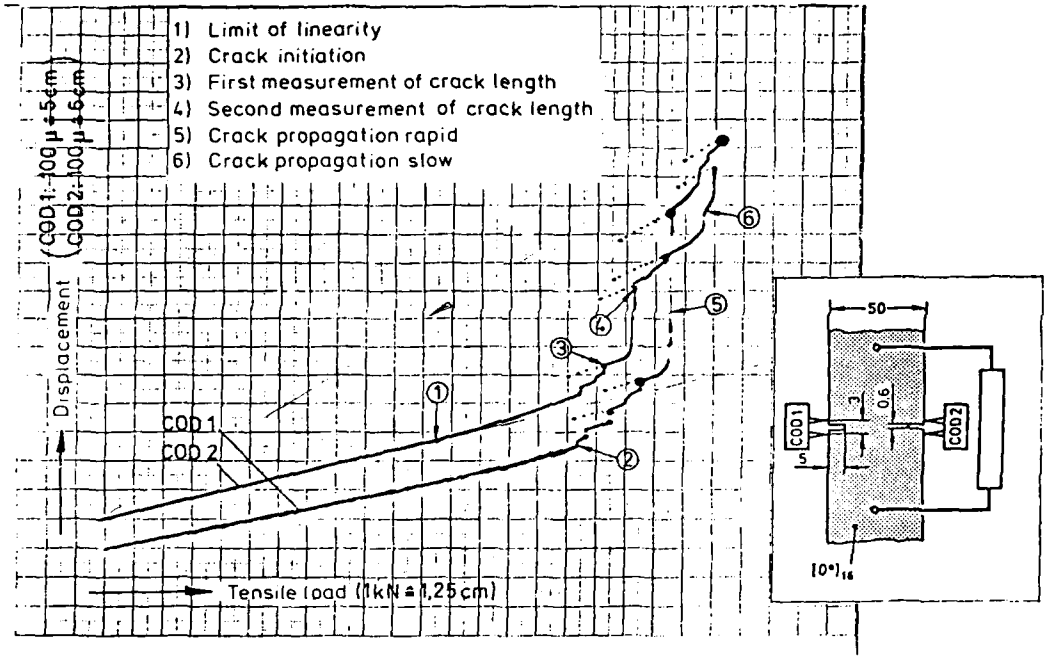

Figure 7.12 COD-measurements during a tensile test on a notched unidirectional CFRE-specimen.

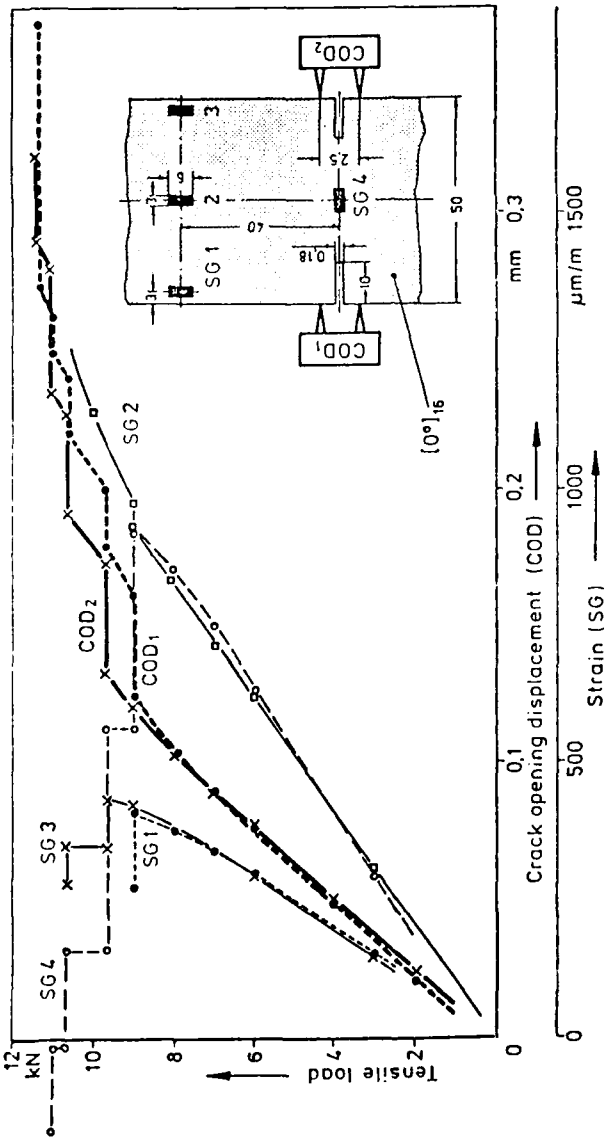

Figure 7.13 Measurements of the crack-opening displacements (COD) and of local strains (SG) in longitudinal and transverse directions for a notched CFRE-specimen under tensile load.

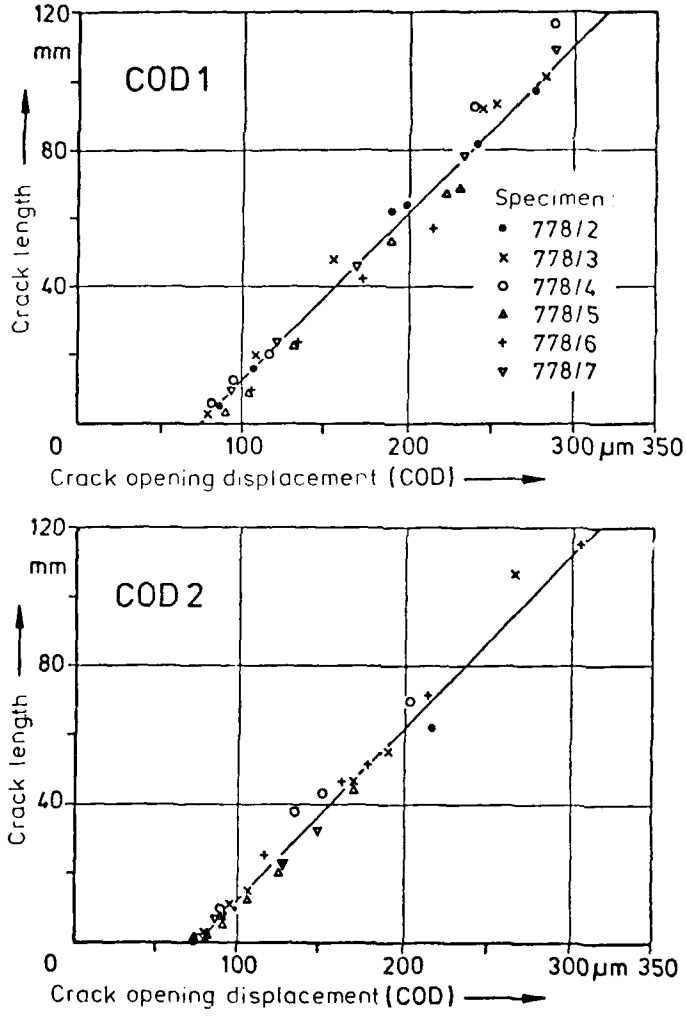

Figure 7.14 Relationship between crack length and crack-opening displacements (COD1, COD2) in unidirectional CFRE-laminates with two edge notches under tensile load.

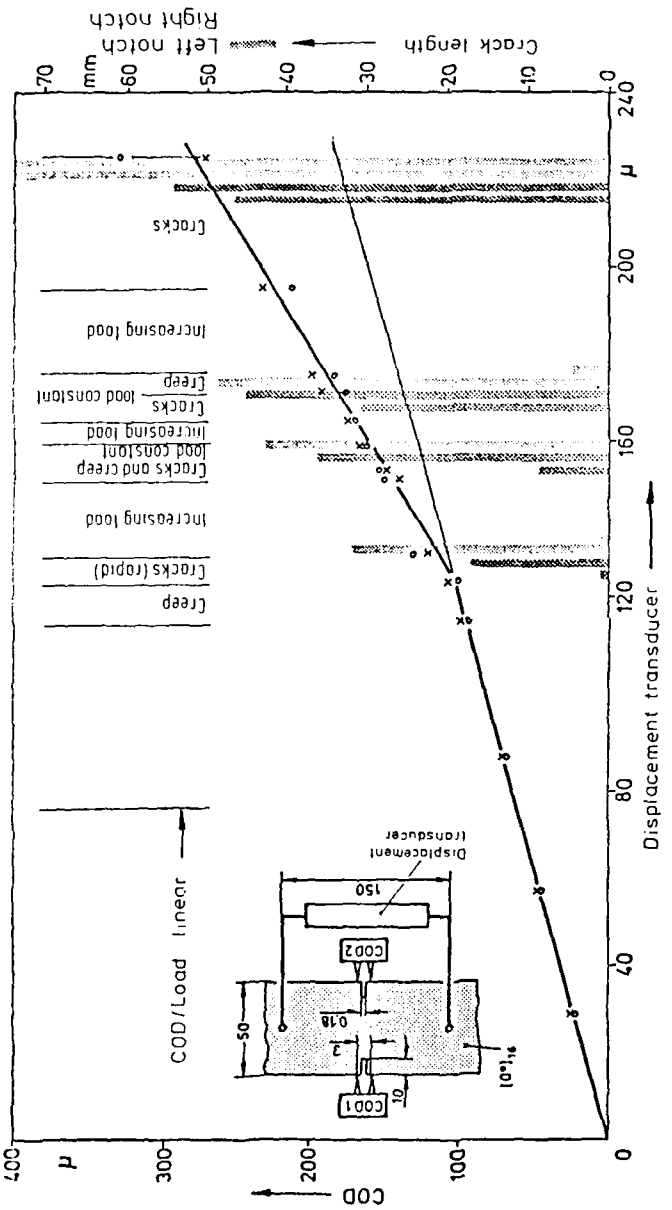

Figure 7.15 Displacement-, COD- and crack length measurements during a quasi-static tensile test on a notched unidirectional CFRE-specimen under continuous and step loading.
Load controlled load rate: 1 kN/84s

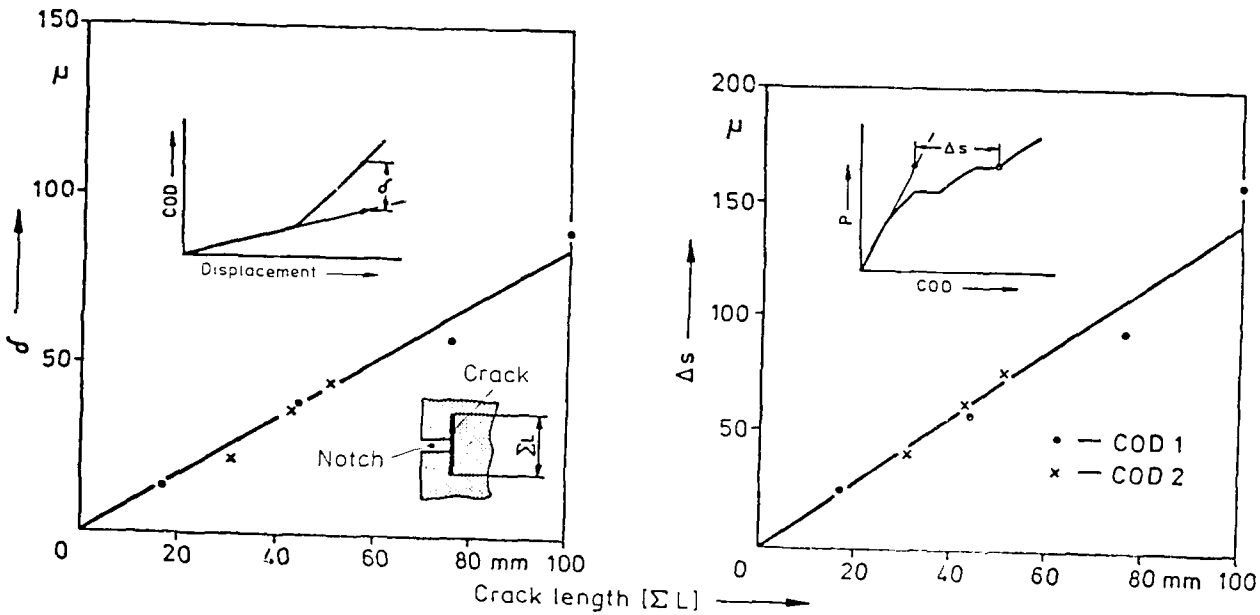

Figure 7.16 Relationship between crack length and crack-opening displacement on an unidirectional CFRE-laminate.
(Two different methods of evaluation)

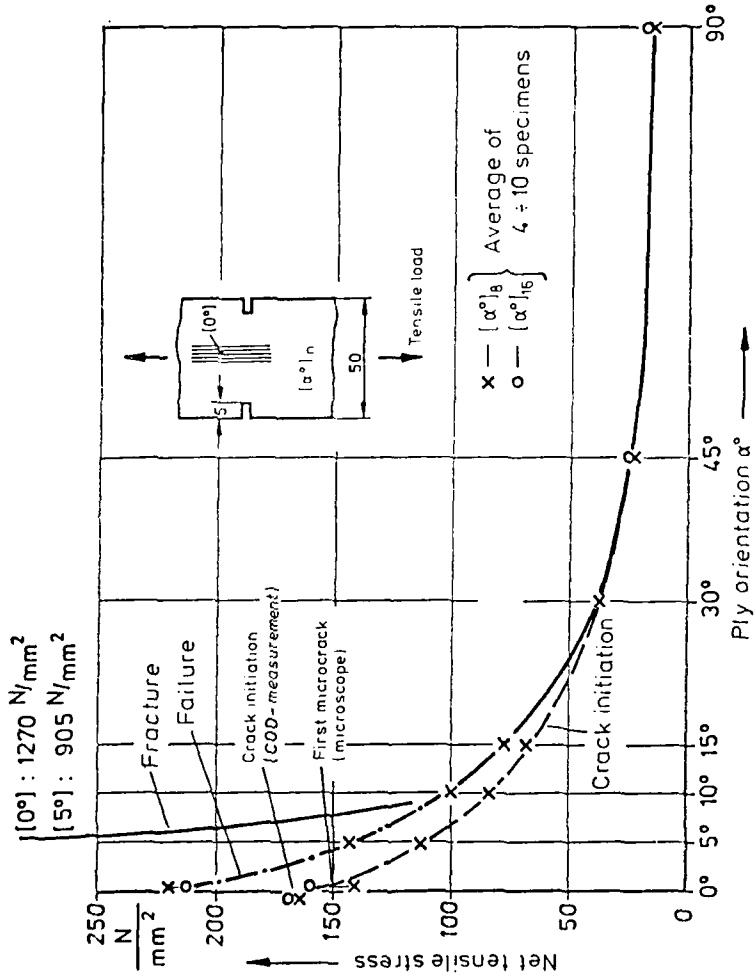

Figure 7.17 Crack initiation, crack extension to the grips of the test machine (failure) and fracture of notched unidirectional CFRE-laminates with different ply orientations under static tensile load.

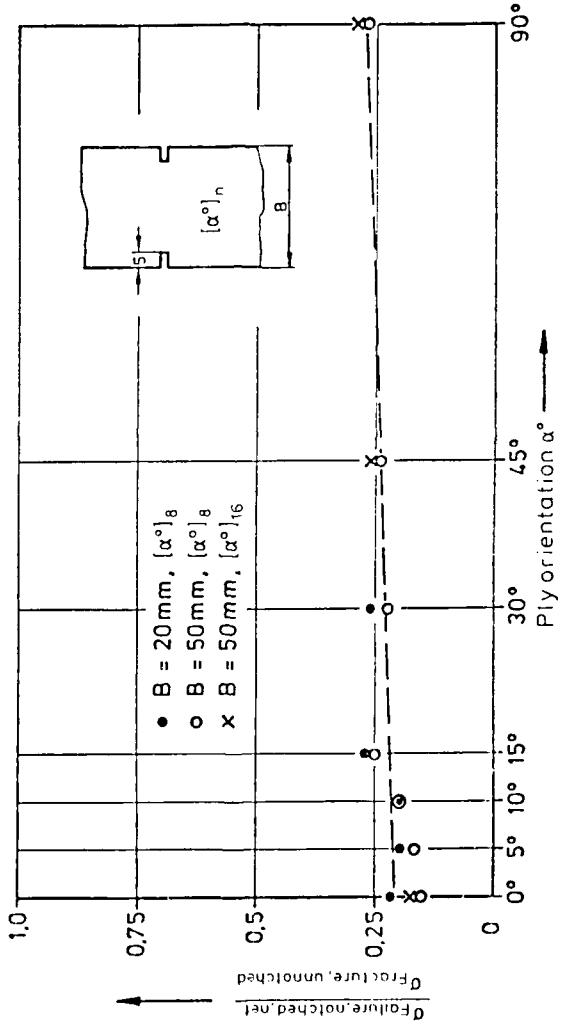

Figure 7.18 Failure of notched unidirectional CFRE-laminates with different ply orientations under static tensile load (averages of 4 to 10 tests).

Laminate	Width of specimen mm	Stress in net cross section x) σ [N/mm²] Crack initiation	Failure	Fracture	Unnotched specimen σ_{Fr} [N/mm²]	$\frac{\sigma_{Failure,notched}}{\sigma_{Fracture,unnotched}}$
$[0°]_8$	20	210	300	1.270	1.362	0,22
	50	140	220	-	-	0,16
$[5°]_8$	20	140	147	220	750	0,20
	50	119	145	905!	850	0,17
$[10°]_8$	20	98	→	→	484	0,20
	50	84	100	→	492	0,20
$[15°]_8$	20	85	→	→	(326)	(0,26)
	50	70	76	→	297	0,25
$[30°]_8$	20	44	→	→	167	0,26
	50	35,2	→	→	150	0,23
$[45°]_8$	50	21,8	→	→	92	0,24
$[45°]_{16}$	50	24,1	→	→	91,8	0,26
$[90°]_8$	50	15,2	→	→	55	0,26
$[90°]_{16}$	50	17,3	→	→	56,3	0,30

Figure 7.19 Edge-notched unidirectional CFRE-specimens under static tensile load.

x) Averages of 4 ÷ 10 tests, notch depth 5 mm

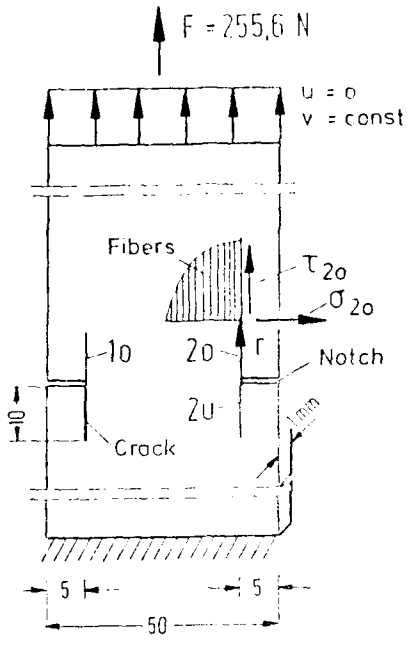

r mm	σ_{2o} N/mm²	τ_{2o} N/mm²	σ_{2u} N/mm²	τ_{2u} N/mm²	σ_{1o} N/mm²	τ_{1o} N/mm²
0	1,000	0,519	0,973	0,493	0,788	0,823
1,8	0,197	0,631	0,193	0,616	0,139	0,673
3,4	0,048	0,504	0,046	0,496	0,040	0,540
5,4	-0,001	0,401	-0,001	0,389	-0,001	0,434
7,6	-0,027	0,333	-0,024	0,322	-0,023	0,360
10,0	-0,039	0,283	-0,037	0,271	-0,034	0,304
15,3	-0,043	0,218	-0,040	0,212	-0,037	0,230

Figure 7.20 Stress distribution in a cracked notched $[0°]_8$-laminate along expected crack directions calculated by finite elements.

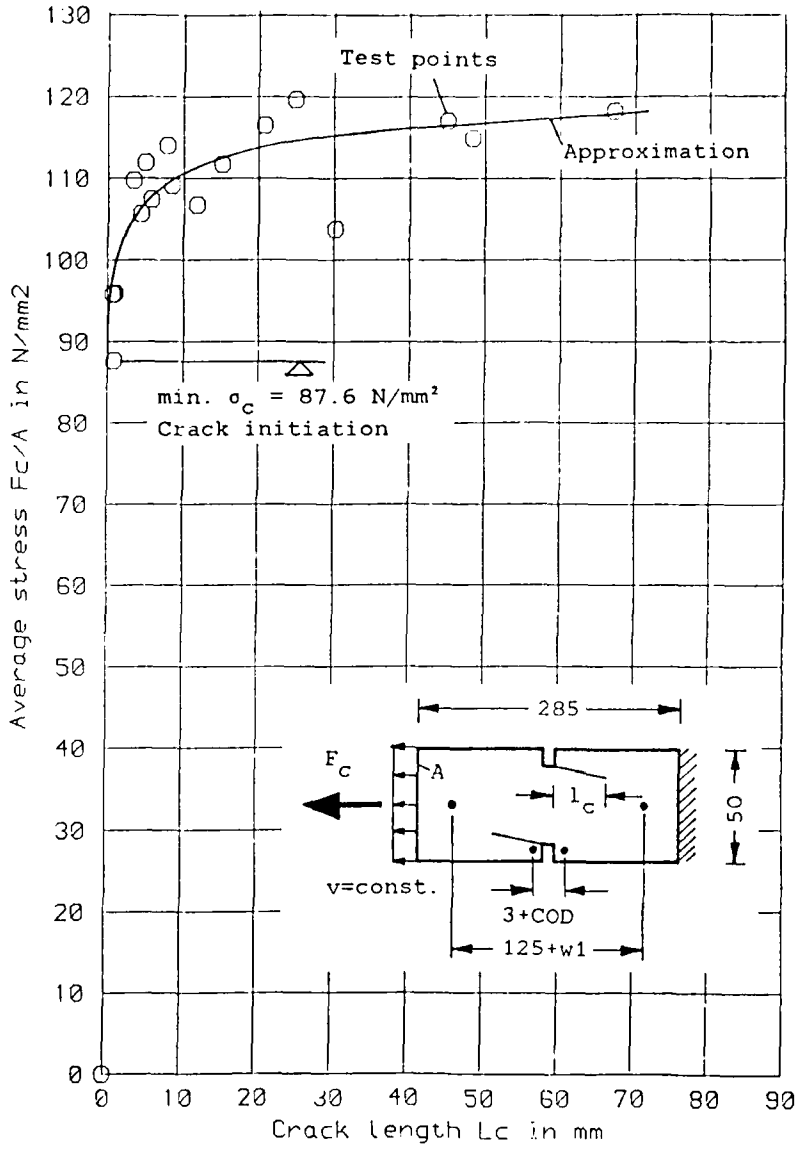

Figure 7.21 Measured average crack length under static load.
Specimen width 50 mm
Material T300-914C
Stacking sequence $[5°]_8$

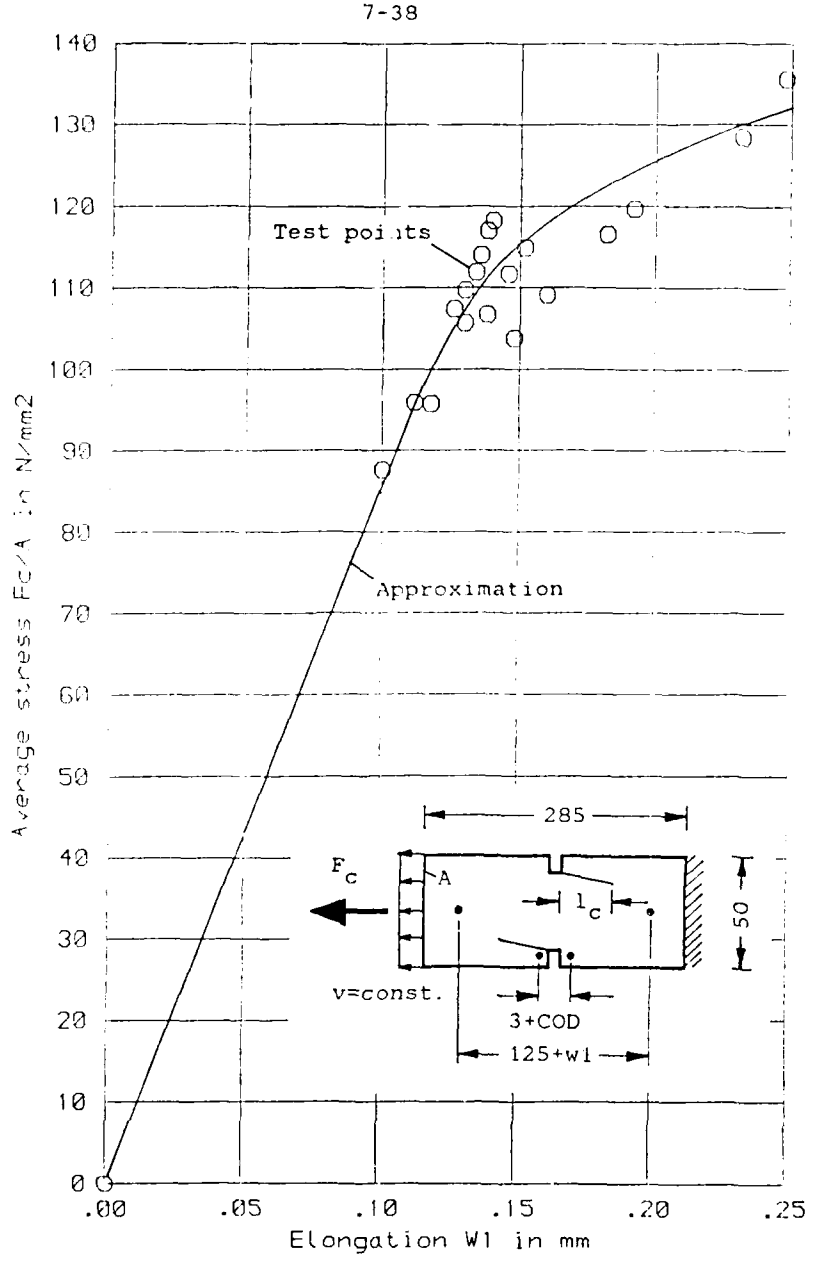

Figure 7.22 Measured elongation under static load.
Specimen width 50 mm
Material T300-914C
Stacking sequence $[5°]_8$

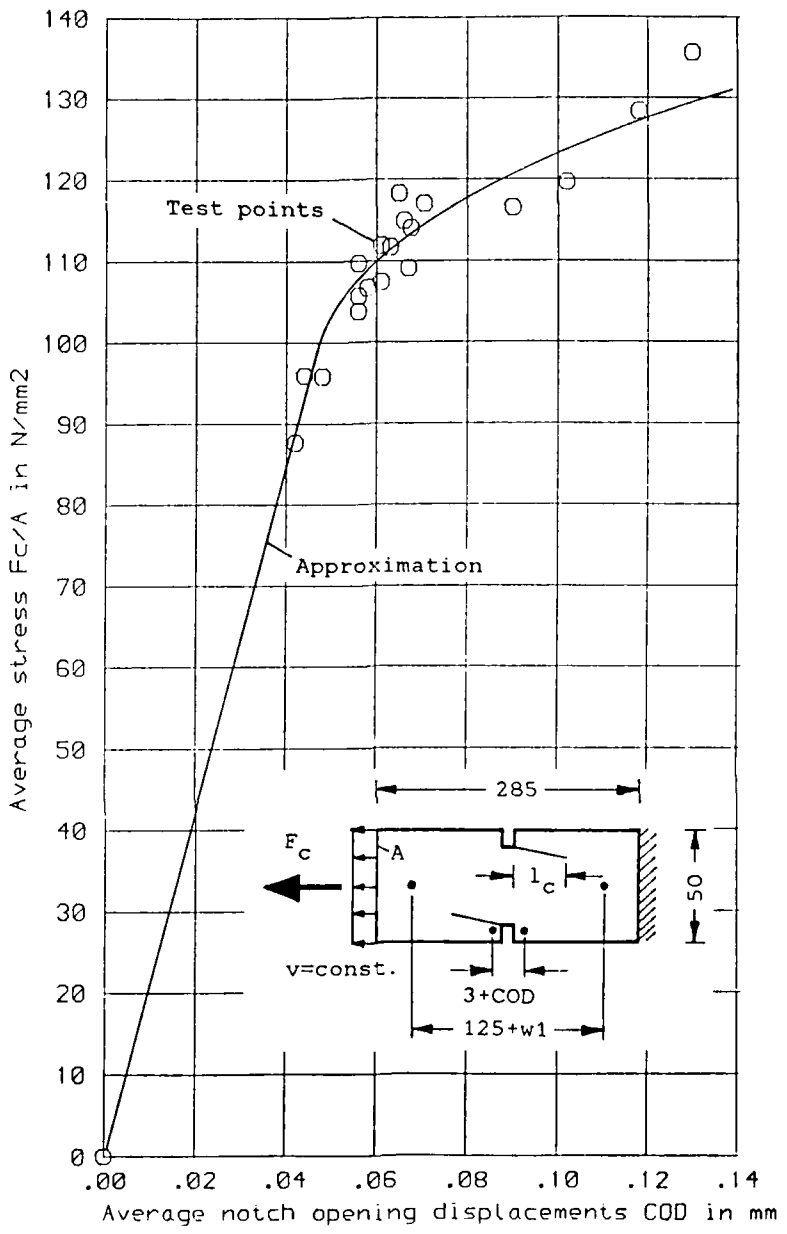

Figure 7.23 Measured average notch opening displacements under static load.
Specimen width 50 mm
Material T300-914C
Stacking sequence $[5°]_8$

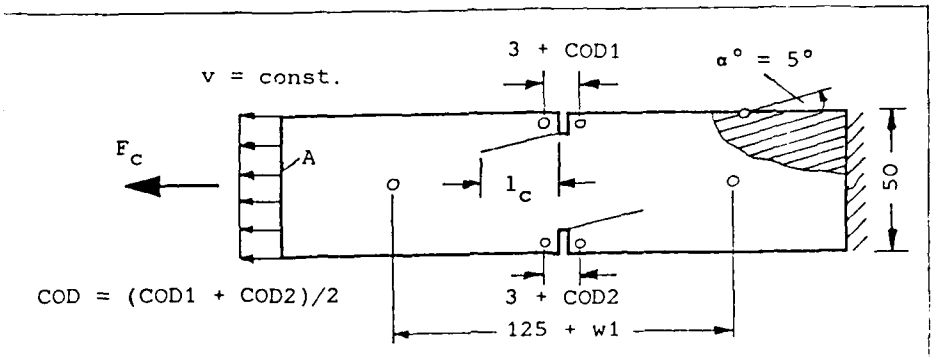

Specimen no.	Width mm	l_c mm	F_c/A N/mm²	w1 mm	COD mm
891/1-4	50	0.	87.6	0.103	0.041
		1.25	100.4	0.118	0.048
		2.5	103.9	0.123	0.050
		3.75	106.2	0.127	0.053
		5.	107.5	0.129	0.055
		7.5	109.3	0.131	0.058
		10.	110.6	0.136	0.061
		15.	112.4	0.141	0.065
		20.	113.9	0.144	0.069
		25.	114.7	0.147	0.071
		30.	115.5	0.149	0.073
		40.	116.1	0.153	0.075
		50.	116.7	0.155	0.077
		60.	117.3	0.157	0.079
		70.	117.9	0.160	0.081

Notch: Ultrasonic knife cut,
5mm deep, 0.6 mm wide, 0.1 mm tip radius
Young's Modulus in load direction: E = 111000 N/mm²

Figure 7.24 Averaged test results for $[5°]_3$-laminates under static load.
Material T300-914C

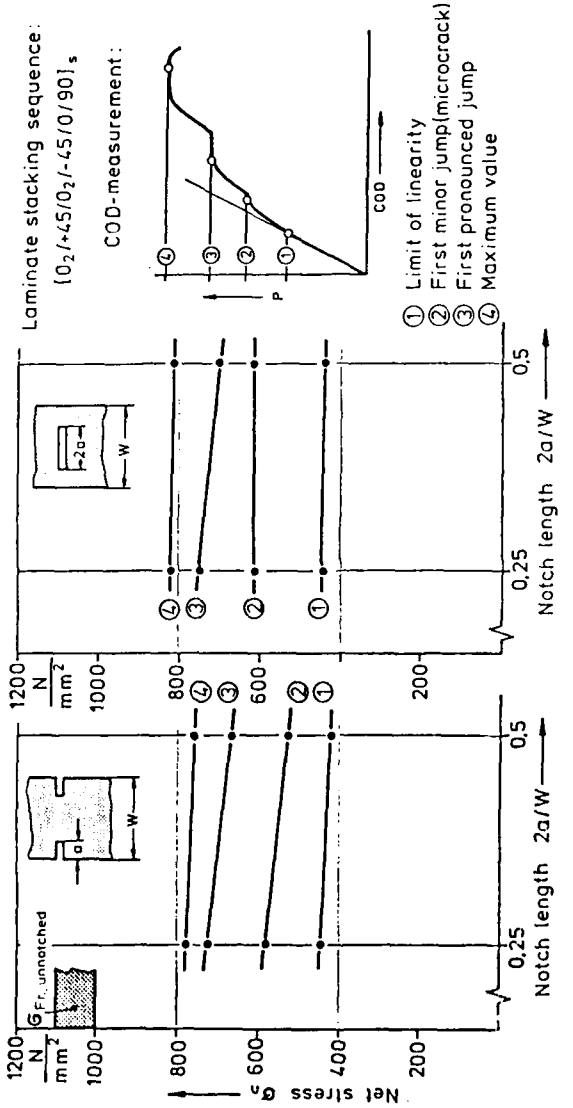

Figure 7.25 Damage and fracture of notched multidirectional CFRE-laminates under tensile load.

	Tensile load [kN]	Displacement W1 [µm]	Displacement COD 1 [µm]	Displacement COD 2 [µm]	Crack length [mm] Notch 1 (left) above	Notch 1 (left) below	Notch 2 (right) above	Notch 2 (right) below
Limit of linearity	3,6	76	35	34	⁄	⁄	⁄	⁄
first microcrack	5,39	116	56	53	⁄	⁄	⁄	⁄
1. Crack length measurement	6,1	134	66	64	1,48	0,82	2,22	0,48
2. "	6,68	148	82	72	9,35	1,21	3,43	0,88
3. "	7,3	164	100	88	12,56	3,16	6,74	5,19
4. "	7,9	190	114	143	15,79	5,04	23,12	20,04
5. "	8,25	212	200	153	57,88	10,51	23,48	21,20
6. "	8,76	242	232	221	63,6	11,96	26,1	63,76
7. "								

Specimen Nr.: 781/4

Date: 14.4.1984

Stacking sequence: $[0°]_8$
Cross section of specimen: 50x[illegible] mm
Notch lengths : 5 mm
Net cross section: 40 mm²

Control : load
Rate of loading: [illegible] kN/168 s
Duration of test: 52 Minutes

Figure 7.26 Test record for an unidirectional CFRE-specimen with two edge notches under tensile load.

Specimen	Laminate	Specimen Nr.	$\sigma_{Fracture}$ [N/mm²]	Elongation at fracture of reference length W1 (125mm) [µm]	$\varepsilon_{Fracture}$ [µm/m]	Observations
notched	$[45°]_8$	776/1 ÷ 776/5	21,8	188	$1{,}504 \times 10^3$	Fracture abrupt. One specimen: Microcrack before fracture. Some specimens: Creep under constant load. COD-increasing non-linearly immediately before fracture.
	$[45°]_{16}$	777/1 ÷ 777/5	24,1	209	$1{,}672 \times 10^3$	Fracture abrupt. Only one specimen: COD-increasing non-linearly immediately before fracture.
unnotched	$[45°]_8$	776/6 776/7	99,2 86,0	1 280 1 120	$10{,}24 \times 10^3$ $8{,}96 \times 10^3$	Fracture abrupt.
	$[45°]_{16}$	777/6 777/8	(62,6) *) 91,8	(700) 1 214	$(5{,}6 \times 10^3)$ $9{,}71 \times 10^3$	x) Fracture premature on the fixing of one COD-transducer.

Figure 7.27 Test results for $[45°]_n$-CFRE-specimens under tensile load.
Notched Specimens : Averages of 5 measurements
Unnotched Specimens: Single measurements
Specimen width : 50 mm
Notch length : 5 mm

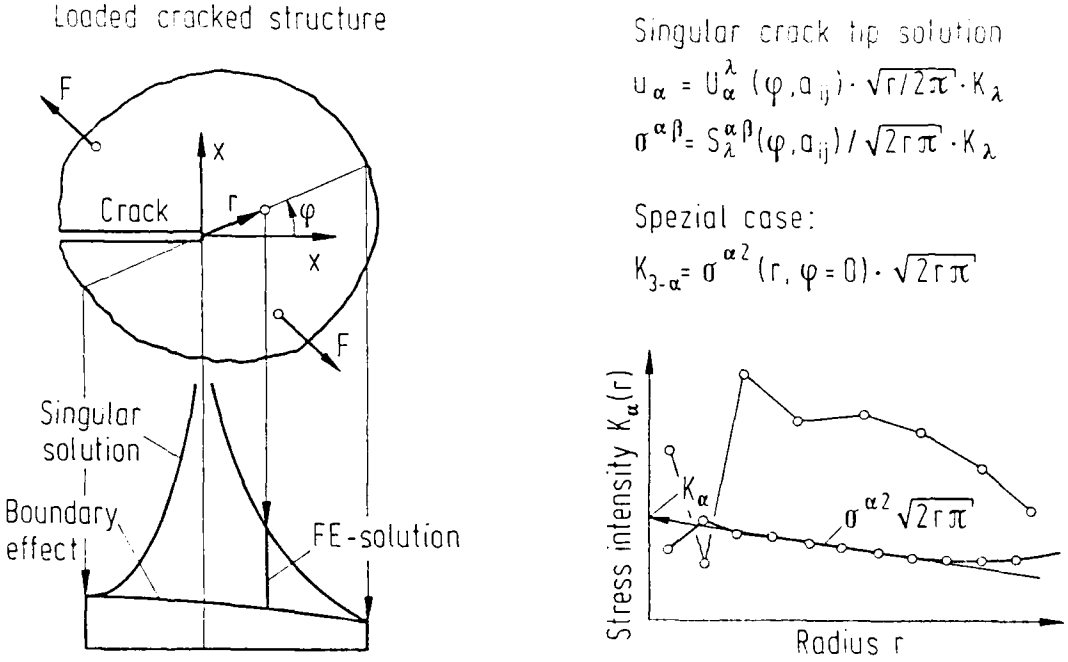

Figure 7.28 Extrapolation method for the stress intensity factor.

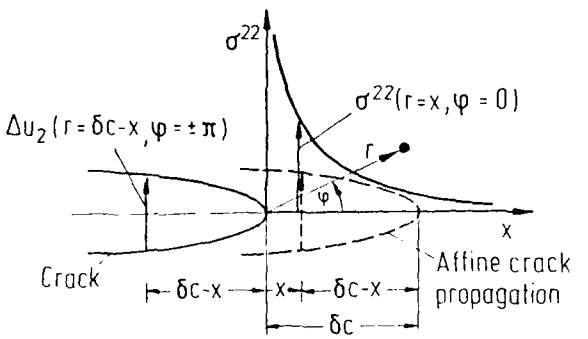

Rice's path-indepedent integral

$$G = \int_{\delta c} \pi^{\alpha 2}(r=x,\varphi=0)\cdot \Delta u_{\alpha}(r=\delta c-x,\varphi=\pm\pi)\,dx$$

$$= \oint_{S} (W(\gamma_{\varrho\lambda})\cdot n_1 - \bar{p}_s^{\varrho}\cdot u_{\varrho,1})\,dS$$

$$= R_1^{\varrho\lambda}(a_{ij})\cdot K_{\varrho}\cdot K_{\lambda}$$

Figure 7.29 Notation for the energy release rate.

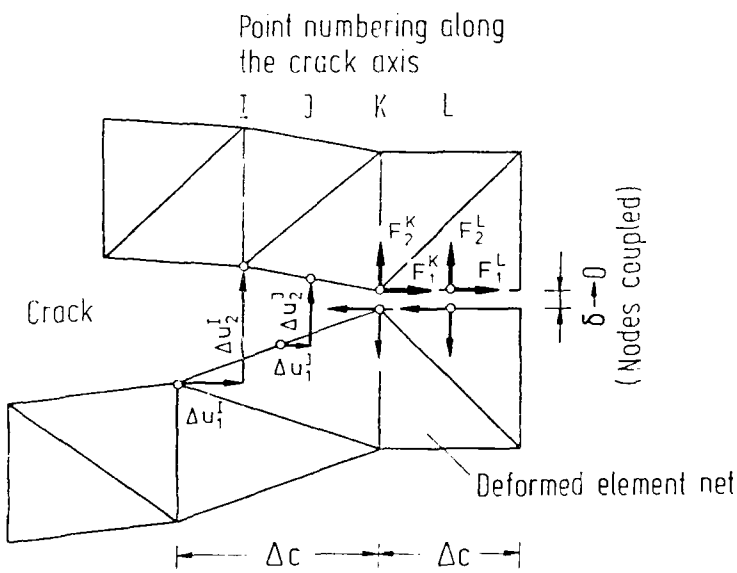

Figure 7.30 Modified crack closure method.

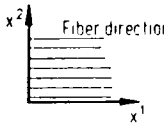

Cartesian coordinates

$$\begin{bmatrix}\varepsilon_{11}\\ \varepsilon_{22}\\ 2\varepsilon_{12}\end{bmatrix} = \begin{bmatrix}\frac{1}{E_1} & & \text{Sym}\\ -\frac{\nu_{21}}{E_1} & \frac{1}{E_2} & \\ 0 & 0 & \frac{1}{G}\end{bmatrix} \cdot \begin{bmatrix}\sigma^{11}\\ \sigma^{22}\\ \sigma^{12}\end{bmatrix} + \begin{bmatrix}\alpha_{11}\\ \alpha_{22}\\ 0\end{bmatrix} \cdot T$$

Constitutive equations

T	23		Temperature in °C
M	0	50	Moisture in %
σ_z^{11}	1784	1889	Ultimate stresses in N/mm² ( )$_z$: Tension ( )$_0$: Compression
σ_0^{11}	- 1086	- 1090	
σ_z^{22}	64.8	55.6	
σ_0^{22}	- 215	- 212	
σ_{12}^{u}	92.4	94.4	
E_1	143 242	150 782	Elasticity constants in N/mm², measured at 30% of the ultimate stresses
ν_{21}	0.317	0.325	
E_2	10 165	9 987	
G	6 239	5 859	
T_G	190°		Glass transition point in °C, Thermal expansion coefficient in °C^{-1}
α_{11}	$-0.8 \cdot 10^{-6}$		
α_{22}	$28.8 \cdot 10^{-6}$		

Figure 7.31 Material constants for UD-laminates.
Material T300-914C

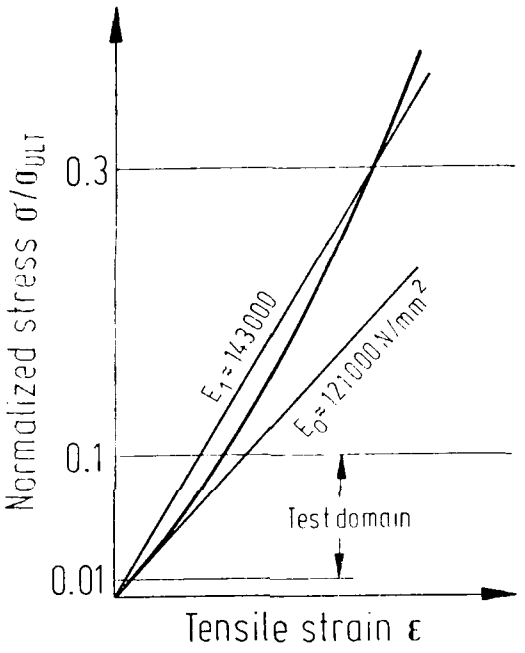

Figure 7.32 Stress-strain curve for UD-laminates.
Material T300-914C

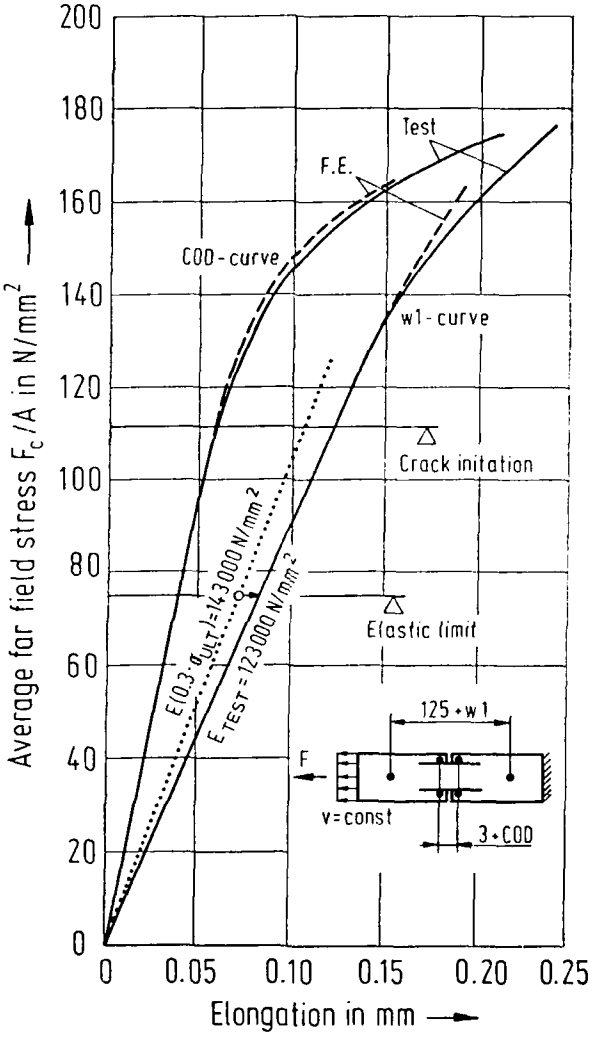

Figure 7.33 Elongation of the specimen verified by tests and calculations.
Material T300-914C
Stacking sequence $[0°]_8$

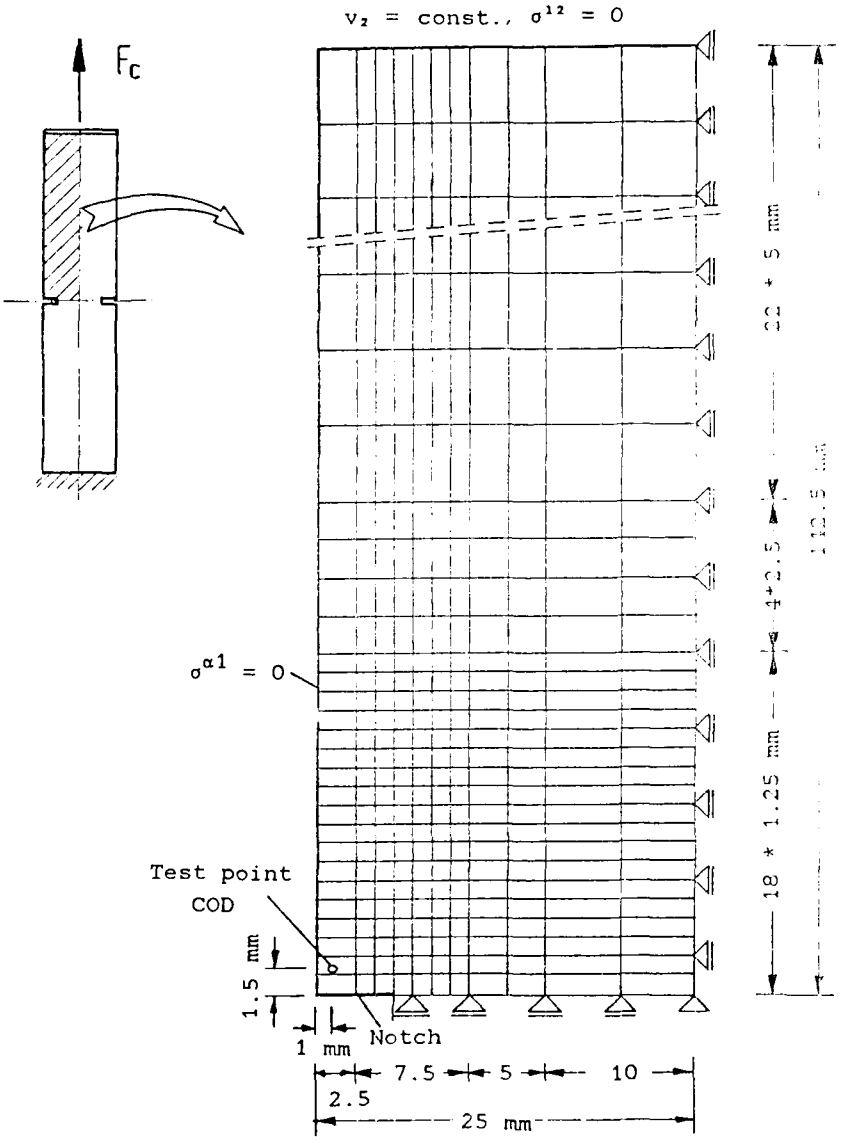

Figure 7.34 Coarse mesh for the approximation of $[0°]_n$- and $[90°]_n$-laminates.

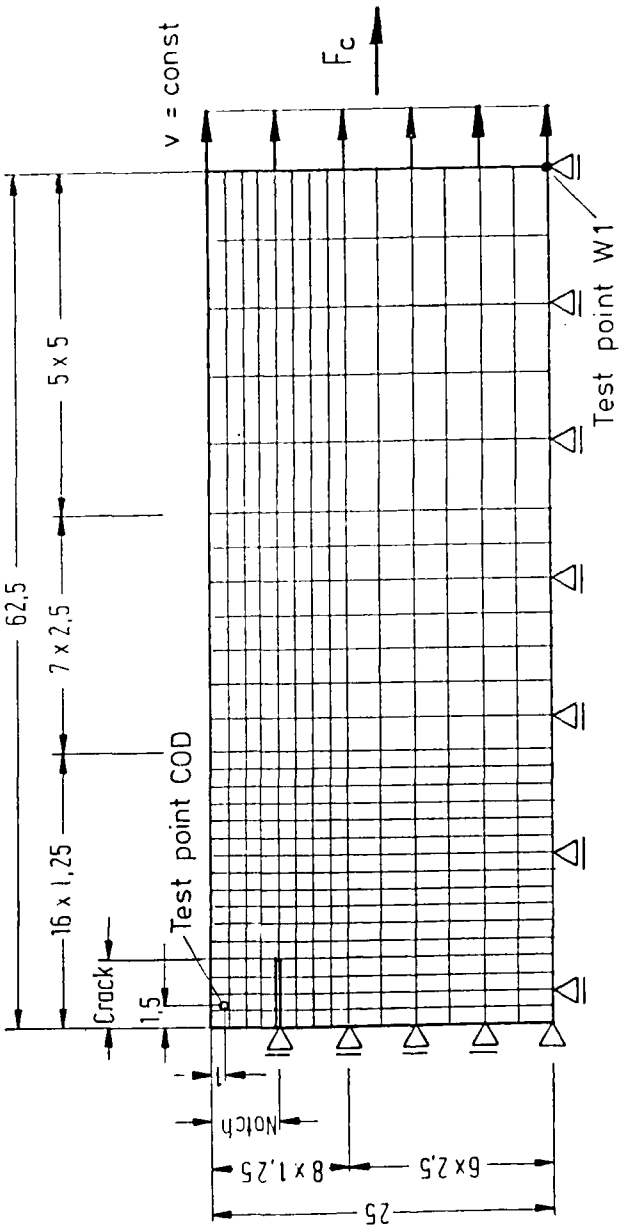

Figure 7.35 Fine mesh for the approximation of $[0°]_n$- and $[90°]_n$-laminates.

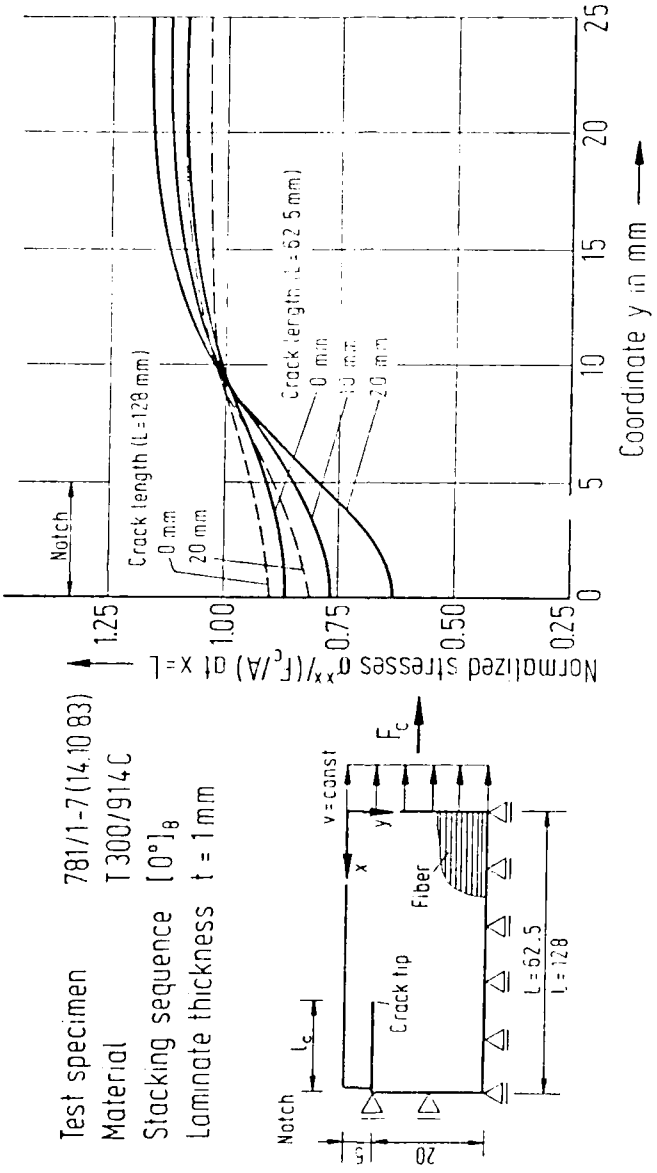

Figure 7.36 Tensile stress distribution at the clamped end of a the finite element net.

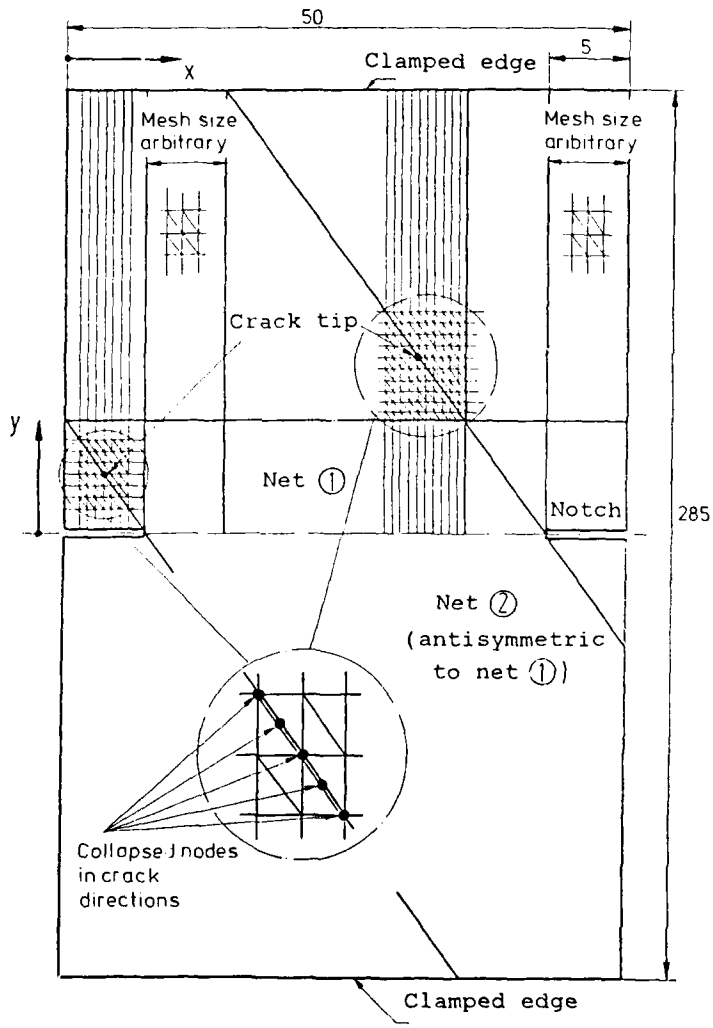

Figure 7.37 Fine mesh for the approximation of off-axis UD-laminates.

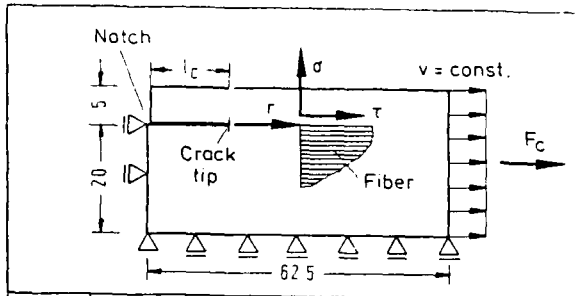

Stress intensity factors for crack propagation

Test specimen:	781/1-7 (14.10.83)
Material:	T300/914C
Laminate thickness:	t = 1 mm
Tensile force:	F_c = 3900 N
Crack length:	l_c = 12.5 mm

$\varrho = \frac{r}{1.25}$	$\sqrt{2\pi r}$	J N/mm²	τ N/mm²	$\sigma\sqrt{2\pi r}$ Nmm$^{-3/2}$	$\tau\sqrt{2\pi r}$ Nmm$^{-3/2}$
0.5	1.9817	20.709	43.750	41.03	86.70
1.0	2.8025	13.818	39.464	38.73	110.60
1.5	3.4323	9.939	35.582	34.11	122.13
2.0	3.9633	7.030	32.226	27.86	127.72
2.5	4.4311	4.986	29.343	22.09	130.02
3.0	4.8541	3.406	27.139	16.53	131.73
3.5	5.2430	2.180	25.210	11.43	132.18
4.0	5.6050	1.229	23.723	6.89	132.97
4.5	5.9450	0.454	22.383	2.70	133.07
5.0	6.2666	-0.140	21.318		133.60
5.5	6.5724		20.332		133.60
6.0	5.8647		19.380		133.03

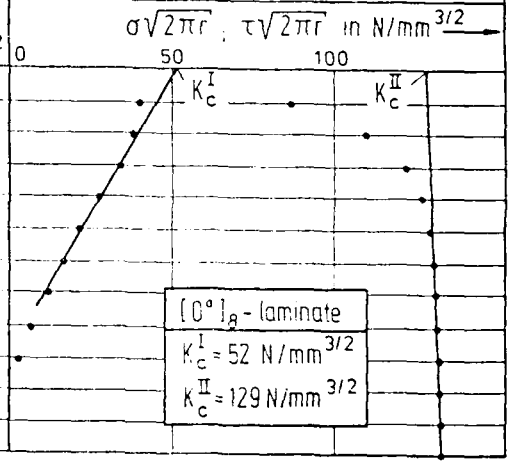

Figure 7.38 Evaluation of the stress intensity factors by extrapolation method for $[0°]_8$-laminates.

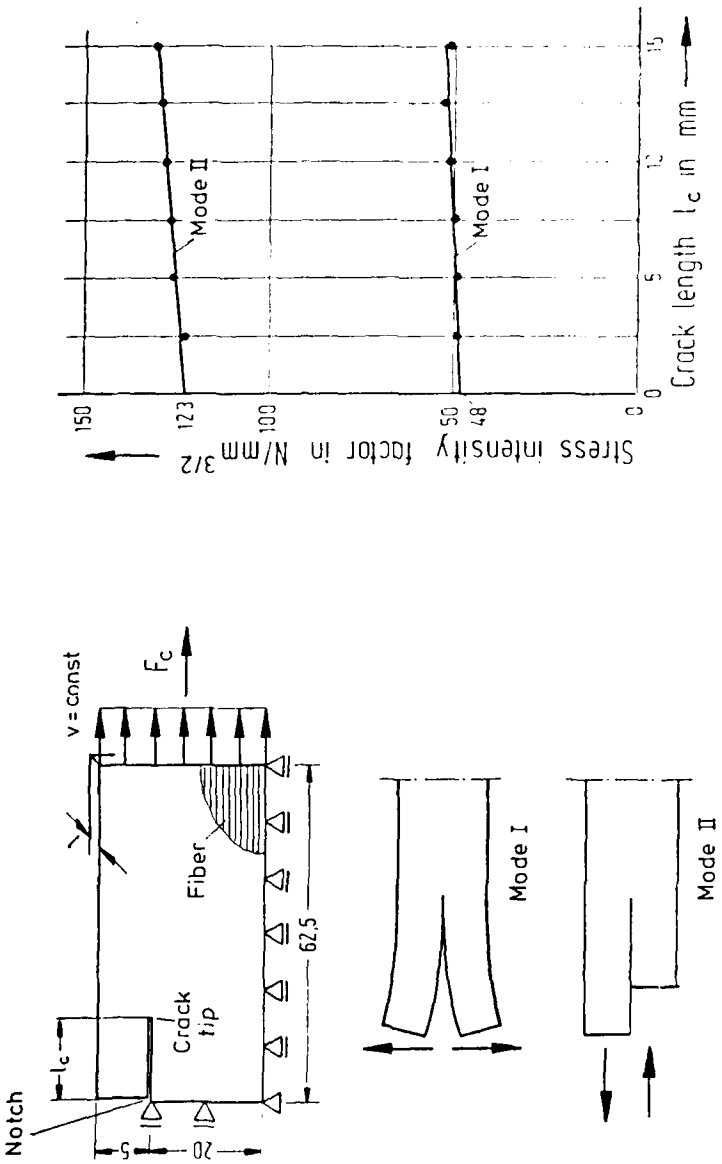

Figure 7.39 Critical stress intensity factors for various crack lenths in $[0°]_8$-laminates. Material T300-914C

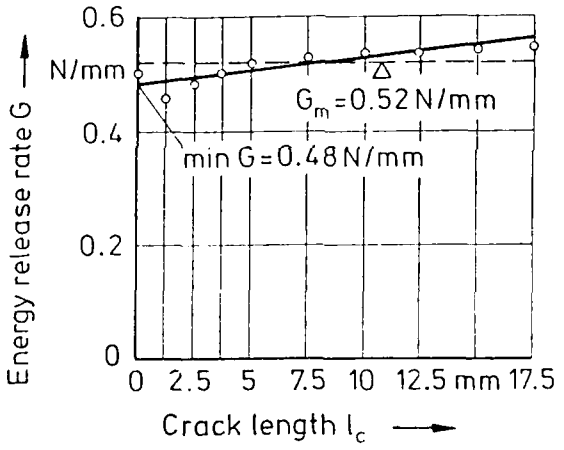

Figure 7.40 Energy release rate G_c for notched $[0°]_8$-laminates.

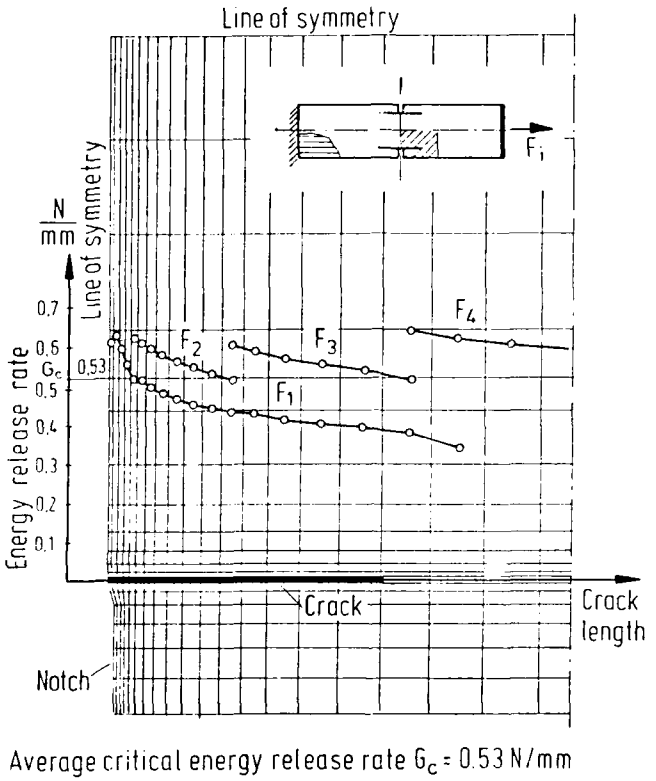

Figure 7.41 Energy release rate versus crack length in edge notched $[0°]_{16}$-laminates.
Material T300-914C
(Source: Dr. Haugh, ESI, Paris)

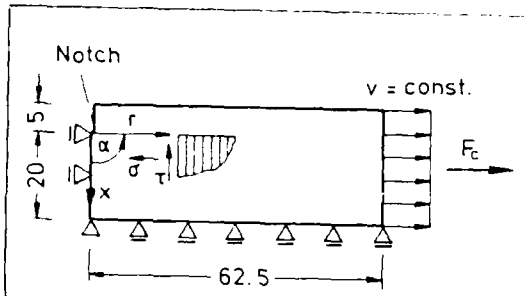

Stress intensity factors for crack propagation

Test specimen : 785/1-5
Material : T300/914C
Stacking sequence : $[90°]_8$
Tensile force : F_c = 302.5 N
Specimen failed suddenly

$\varphi = \frac{r}{1.25}$	σ N/mm²	τ N/mm²	$K_1(r)$ $Nmm^{-3/2}$	$K_2(r)$ $Nmm^{-3/2}$
0.5	31.922	-9.396	82.2	78.9
1.0	15.984	-8.319	50.2	-3.5
1.5	15.435	-6.270	64.2	31.4
2.0	13.983	-5.191	68.7	44.2
2.5	12.932	-4.631	71.6	50.1
3.0	12.316	-4.082	76.0	61.6
3.5	11.895	-3.706	80.0	71.0
4.0	11.569	-3.334	84.6	83.2
4.5	11.387	-3.028	89.5	95.7
5.0	11.255	-2.729	94.6	109.4
5.5	11.162	-2.477	99.6	122.6
6.0	11.103	-2.228	104.7	136.8

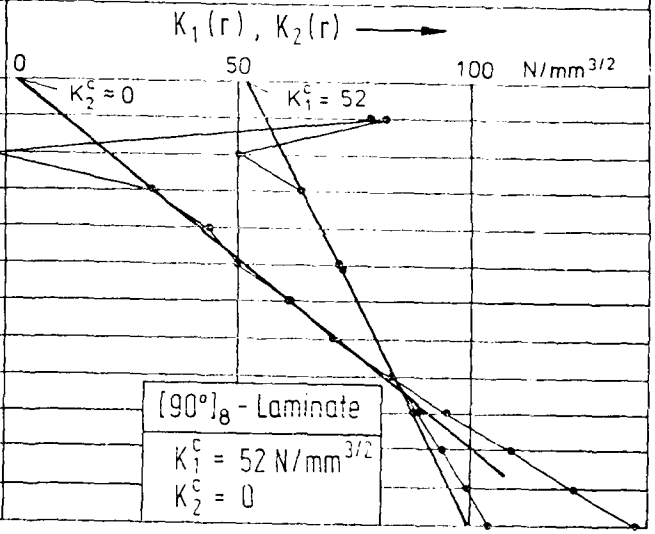

Figure 7.42 Evaluation of the stress intensity factors by extrapolation method for $[90°]_8$-laminates.

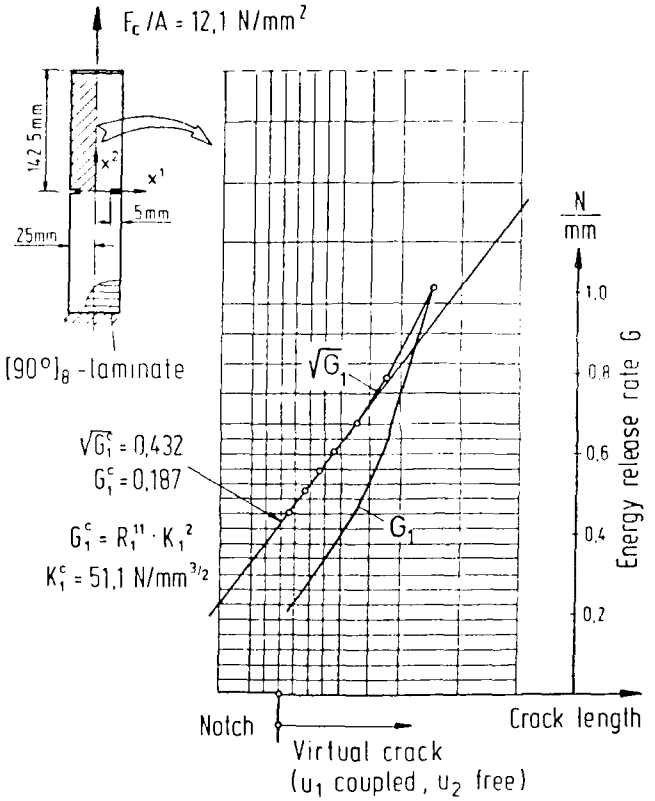

Figure 7.43 Energy release rate for various crack lengths in $[90°]_8$-laminates.

AD-A168 002 DEVELOPMENT OF FRACTURE MECHANICS MAPS FOR COMPOSITE MATERIALS VOLUME 1(U) DEUTSCHE FORSCHUNGS- UND VERSUCHSANSTALT FUER LUFT- UND RAUMF.. H W BERGMANN 3/3

UNCLASSIFIED DEC 85 AFWAL-TR-85-4150-VOL-1 F/G 11/4 NL

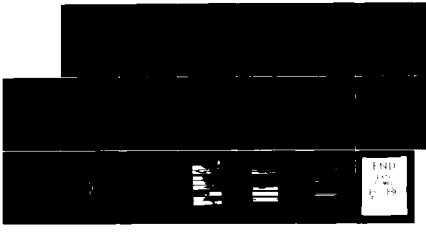

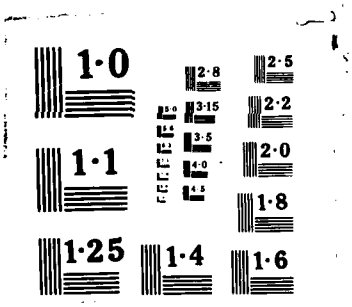
1·0
1·1
1·25
2·8
3·15
3·5
4·0
1·4
2·5
2·2
2·0
1·8
1·6

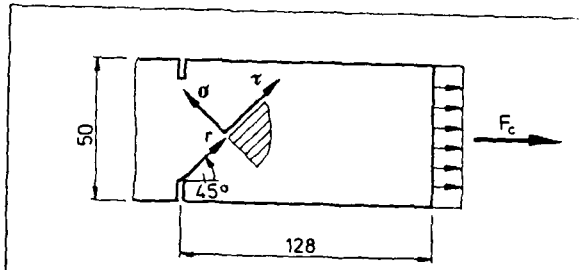

Stress intensity factors for crack propagation

Test specimen : 776/1-7
Material : T300/914C
Laminate thickness : t = 1.0 mm
Tensile force : F_c = 872 N
Specimen failed suddenly

r mm	$\sqrt{2\pi r}$	σ N/mm²	τ N/mm²	$K_1(r)$ $Nmm^{-3/2}$	$K_2(r)$ $Nmm^{-3/2}$
0.5					
1.0	2.8025	15.62	-10.91	46.6	32.5
1.5					
2.0	3.9633	12.37	-10.21	52.1	43.0
2.5					
3.0	4.8541	10.89	- 9.90	56.2	51.1
3.5					
4.0	5.6050	10.09	- 9.76	60.2	58.2
4.5					
5.0	6.2666	9.59	- 9.70	63.9	64.7
5.5					
6.0					
7.0	6.6319	9.05	- 9.65	71.4	76.1

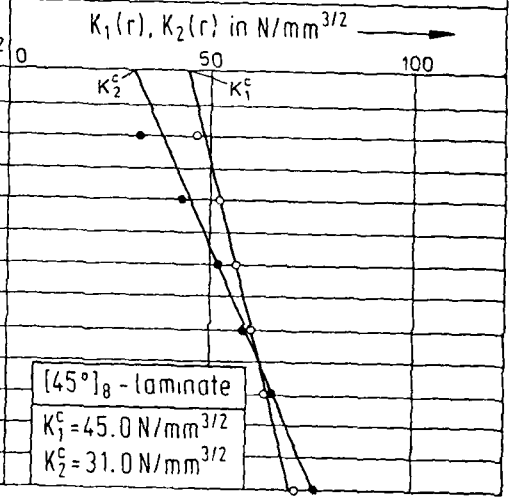

Figure 7.44 Evaluation of the stress intensity factors by extrapolation method for $[45°]_8$-laminates.

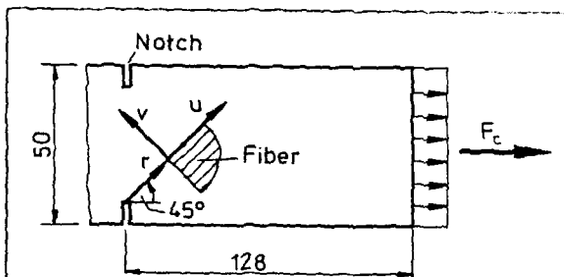

Stress intensity factors for crack propagation

Test specimen : 776/1-7
Material : T300/914C
Laminate thickness : t = 1.0 mm
Tensile force : F_c = 872 N
Specimen failed suddenly

r mm	$\Delta u/10^5$ mm	$\Delta v/10^5$ mm	$K_1(r)$ $Nmm^{-3/2}$	$K_2(r)$ $N\,mm^{-3/2}$
0.5	-55.90	-18.90	34.7	11.7
1.0	-98.47	-52.84	43.2	23.2
1.5	-131.95	-77.69	47.3	27.9
2.0	-148.8	-131.1	46.2	35.1
2.5	-167.1	-140.0	46.4	38.9
3.0	-183.4	-164.9	46.5	41.8
3.5	-198.3	-187.2	46.6	44.0
4.0	-208.7	-208.7	45.8	45.8
4.5	-223.2	-228.8	46.2	47.2
5.0	-233.6	-247.1	45.9	48.5
5.5				
6.0	-254.3	-280.2	45.6	50.2

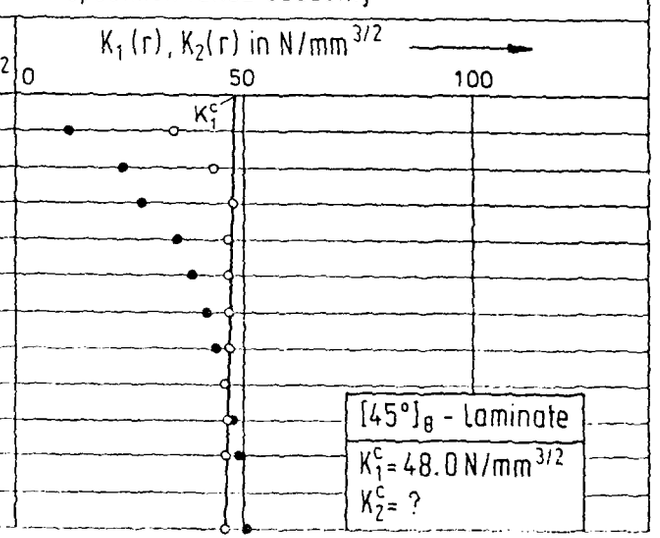

Figure 7.45 Evaluation of the stress intensity factors by extrapolation method for $[45°]_8$-laminates.

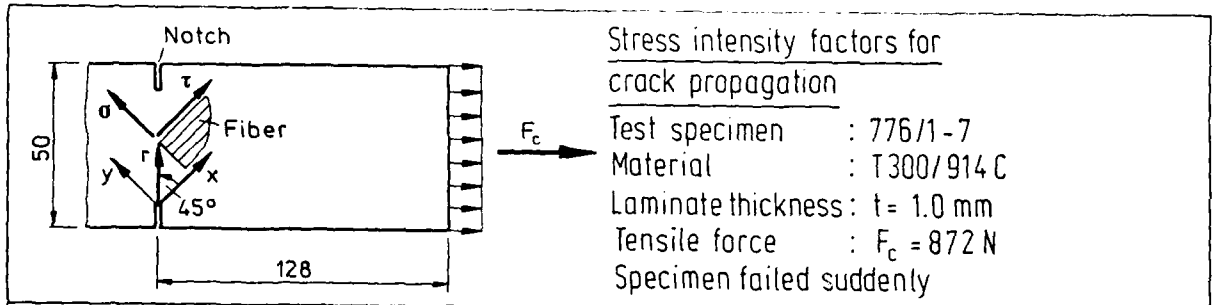

Stress intensity factors for crack propagation

Test specimen : 776/1-7
Material : T300/914C
Laminate thickness : t = 1.0 mm
Tensile force : F_c = 872 N
Specimen failed suddenly

r mm	σ N/mm²	τ N/mm²	$K_1(r)$ $Nmm^{-3/2}$	$K_2(r)\pi$ $N\,mm^{-3/2}$
1.0	21.51	-6.13	48.6	27.80
2.0	16.41	-7.30	52.4	47.17
3.0	14.11	-7.53	55.1	59.72
4.0	12.78	-7.73	57.6	70.89
5.0	11.89	-7.94	59.9	81.49
6.0				
7.0	10.85	-8.22	64.7	99.92
8.0				
9.0				
10.0	10.09	-8.46	71.8	123.01
11.0				
12.0				
13.0	9.70	-8.57	78.7	142.13

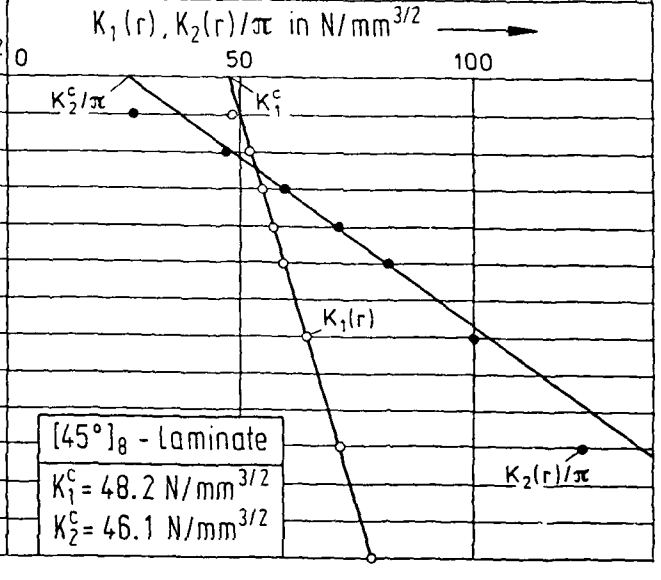

Figure 7.46 Evaluation of the stress intensity factors by extrapolation method for $[45°]_8$-laminates.

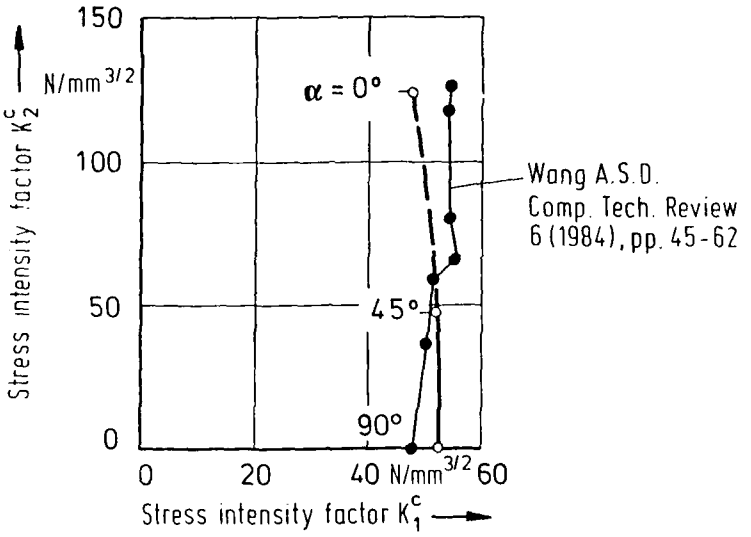

Figure 7.47 K_1^c - K_2^c interaction for $[\alpha°]_8$-laminates.
Material T300-914C

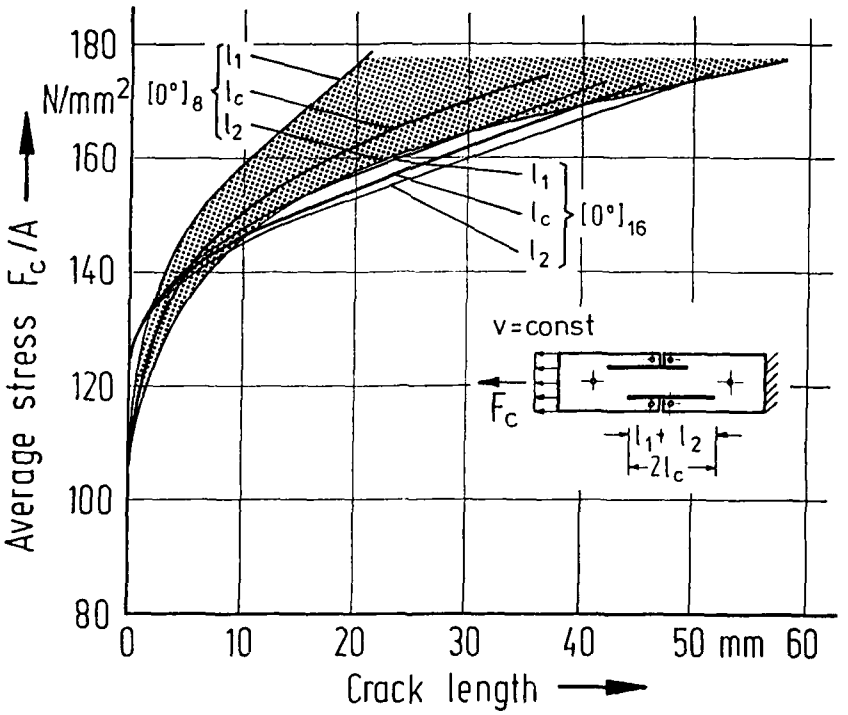

Figure 7.48 Comparison of crack lenths for $[0°]_8$- and $[0°]_{16}$-laminates. Material T300-914C

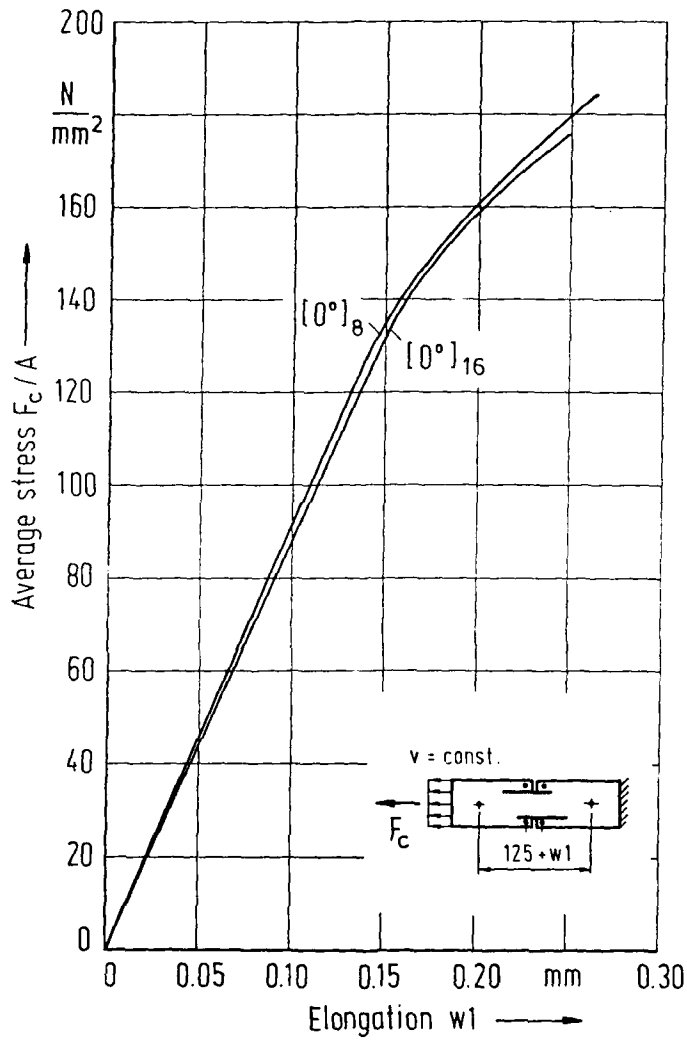

Figure 7.49 Comparison of elongations for $[0°]_8$- and $[0°]_{16}$-laminates. Material T300-914C

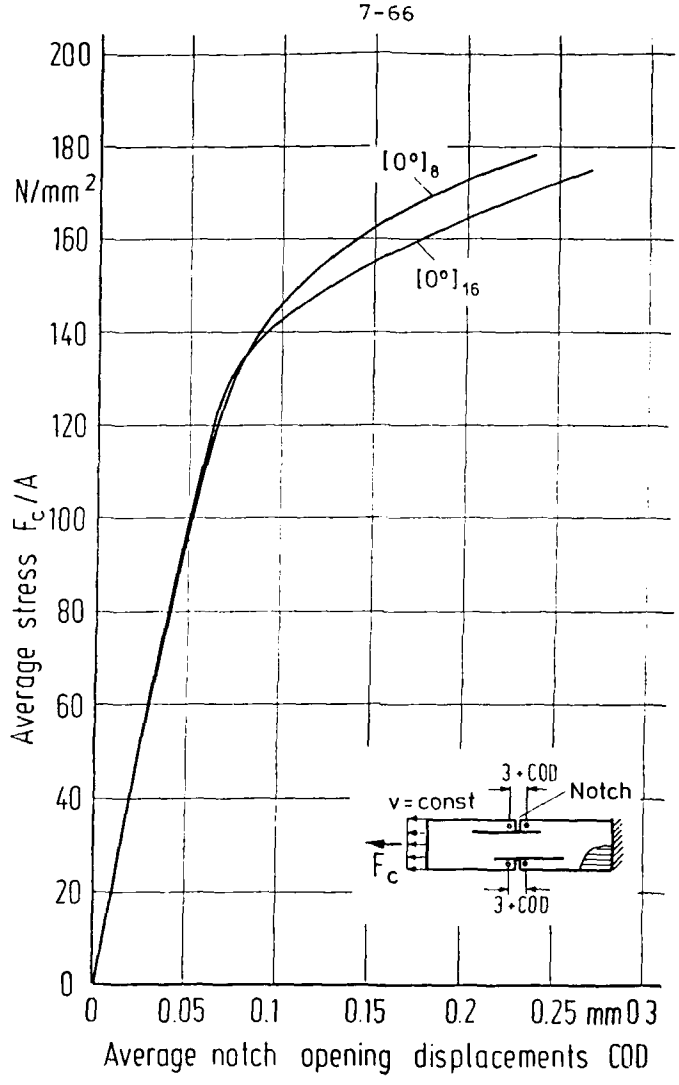

Figure 7.50 Comparison of notch opening displacements $[0°]_8$- and $[0°]_{16}$-laminates.
Material T300-914C

8. RESPONSE OF MECHANICALLY FATIGUED UN-NOTCHED SPECIMENS

8.1 Summary

Tensile fatigue tests of unidirectional, angle-ply and multidirectional laminates were performed under four different environmental conditions in order to investigate the influence of temperature and moisture on the fatigue strength and on the damage mechanisms of un-notched carbonfiber-reinforced laminates.
The unidirectional on-axis laminates exhibited no significant degradation due to the combined effects of temperature and moisture. The presence of moisture at ambient temperature had a beneficial effect on the fatigue life because of the relaxation of the curing prestresses by the swelling of the matrix. Macromechanical damage like matrix-cracks or delaminations could not be detected by means of NDT-techniques. In angle-ply laminates elevated temperature alone as well as moisture alone led to significant degradations of the fatigue strength. Additional degradation was observed if both moisture and temperature are present simultaneously.Typical damage patterns are matrix-cracks and edge-delaminations in increasing degrees of severity which correspond to measured stiffness losses of the test specimens during fatigue.
Similar to the unidirectional laminates, the multidirectional laminates exhibited only slight degradations at elevated temperature and slight improvements with increasing moisture contents. Even the simultaneous presence of both did not influence the fatigue strength. In all of the tested laminates a typical characteristic damage state (CDS) could be observed [8.1].
It may be stated generally that the fatigue properties of matrix-controlled laminates are sensitive to temperature and moisture, whereas the more fiber-controlled laminates show no significant degradative effects. However, the fatigue performance of carbon fiber-reinforced laminates under "worst-case" environments clearly exceeds that of metallic materials even in the presence of occasionally large data scatter.
Additional information regarding the response of mechanically fatigued un-notched specimens is contained in Appendix E:

"Einfluß von Temperatur und Feuchte auf die Schwingfestigkeit ungekerbter CFK-Laminate".

8.2 Scope of Test Program

A comprehensive test program was conducted to evaluate the fatigue performance of carbon-fiber-reinforced un-notched laminates with different stacking orders. Emphasis was placed on a quantitative assessment of temperature and moisture effects on the fatigue life, and on the investigation of the mechanisms of dominant failure modes. The test program comprised ca. 600 specimens of which 420 were cycled to failure. The balance of 180 specimens was used for initial and residual stiffness tests and for non-destructive and destructive evaluations. The types and numbers of the tested specimens are presented in Table 8.1. Despite the fact that comprehensive test results for dry specimens at ambient temperature already exist [8.1], [8.2], [8.3], tests under these conditions were included in order to arrive at compatible test data.

The fatigue tests were performed in four different environments:

- ambient temperature-dry;
- high temperature-dry;
- ambient temperature-wet;
- high temperature-wet.

The environments were simulated in climatic chambers designed such that only the 140 mm long test sections of the specimens were located within the chamber in order to avoid failure in the bond lines of the tabs and to minimize the chamber volume. After preconditioning of the test specimens over periods of at least 6 weeks, the following test conditions were realized:

- ambient-dry (ad) : 22°C - 40% RH
- hot-dry (hd) : 80°C - 5% RH
- ambient-wet (aw) : 28°C - 95% RH
- hot-wet (hw) : 80°C - 95% RH

All of the fatigue test were conducted in the tension regime with a stress ratio of R = 0.1. The loading was applied by means of preprogrammed and computer-controlled function generators with a frequency of 5 Hz. In ca. 70% of the tests the strain response of the specimens was monitored in order to assess the stiffness reduction prior to failure. σ-N-curves were established by a statistical evaluation of the cycles to failure of three to six test specimens at three or four different stress levels. Curves indicating 10%, 50% and 90% probability of survival were represented in terms of logarithms of the load cycles, N.

As a major part of the test program, various non-destructive test procedures were used for the quality control of the test specimens and for the detection and identification of developing defects. In addition to microscopic, radiographic and ultrasonic techniques, an in situ grid-reflection method was introduced especially for the observation of edge delaminations. Further, a computerized procedure was developed allowing interruption of the load cycling and inspection of the specimen upon reaching a predetermined stiffness reduction or secant modulus value.

8.3 Effects of Temperature and Moisture on Fatigue Life

Test performed at 22°C and moisture saturation at 40% RH confirmed the pronounced dependence of the fatigue life on the fiber orientation and the stacking sequence of the test specimens. Fig. 8.1 shows the life characteristics for unidirectional $[\alpha^\circ]_8$-laminates with fiber directions relative to the load axis of $\alpha^\circ = 0^\circ$, 5°, 15° and 45° for a survival probability of 50%. Evidently, the fatigue life of unidirectional specimens is remarkably reduced even by minor departures from the 0°-orientation. A similar comparison is given in Fig. 8.2 for balanced $[\pm 15^\circ]_8$-, $[\pm 30^\circ]_8$- and $[\pm 45^\circ]_8$-laminates. The more fiber-controlled $[\pm 15^\circ]_8$- laminate exhibits the highest fatigue

strengths but also the highest rate of decline of the σ-log N-line.

The influence of temperature and moisture on the fatigue life of the $[0°]_8$-laminates is presented in Fig. 8.3. Again, for the sake of clarity, only the 50% probability of survival lines are shown. It is apparent that the presence of moisture at ambient temperature has a beneficial effect probably due to the relaxation of the curing prestress. Relative to the tests at ambient temperature the σ-log N-line has a distinctly higher slope.

In all test series, especially in those with moist specimens, appreciable scatter of the test data occurred so that additional tests ought to be performed for statistical substantiation of the data interpretation. Figs. 8.4, 8.5 and 8.6 illustrate the extent of the scatter and the shift of the mean values in the form of a Weibull-distribution. Fig. 8.7 indicates the need for more test data for the prediction of useful confidence limits. Fig. 8.8 summarizes the effects of temperature and moisture on the $[\pm 15°]_8$-, $[\pm 30°]_8$- and $[\pm 45°]_8$-laminates. Especially the former two exhibit noticeable degradations of their fatigue lives. According to Fig. 8.9, again appreciable scatter occurred at some of the stress levels.

A comparison of the influence of temperature and moisture on the fatigue life of the $[0_2°/+45°/0_2°/-45°/0°/90°]_s$- and the $[0°/+45°/-45°/\overline{90}°]_s$-laminate is depicted in Fig. 8.10. Apparent is a slight degradation at elevated temperature but also a certain improvement in the moist condition. Fig. 8.11 shows the σ-log N-line for the $[0_2°/+45°/0_2°/-45°/0°/90°]_s$-laminate tested at 80°C and 95% RH. In comparison to Fig. 8.10 the mean values are lower and the scatter is partially greater but the relatively small slope is maintained.

It must be recognized that in the preparation of the test specimens a certain variability in the material supplies, the curing process or the machining operation, in spite of all reasonable safeguards, cannot be avoided and will contribute to the fatigue life scatter. A separation of these effects will require a statistical evaluation of much larger data sets.

In summary, it may be stated that the influence of temperature and moisture on the fatigue life of carbon-fiber-reinforced laminates is only moderate and not always detrimental. In matrix-controlled laminates elevated temperature as well as moisture saturation tend to degrade the fatigue strength while in fiber-controlled laminates the presence of moisture seems to be beneficial. The simultaneous presence of temperature and moisture causes in multidirectional laminates an increase in scatter but the slope of the σ-log N-line remains essentially unaffected. A clear separation of the individual effects is difficult in view of the scatter problem. Additional insight may be expected from statistical significance tests and from fractographical observations. Regardless of the outcome of such studies it is already evident that even in "worst-case" environments the fatigue performance of carbonfiber-reinforced laminates exceeds that of metallic materials by far.

8.4 Mechanisms of Damage

In numerous publications, *e.g.* [8.4], the mechanisms of damage occurring under fatigue loading have been identified as matrix cracks and delaminations on a macroscopic scale, and as microcracks, fiber breaks and debonds on a microscopic scale. In the context of the current research effort only the effects traceable by optical, ultrasonic and radiographic means were investigated.

An assessment of the stiffness response of test specimens under sustained cyclic loading proved that their behavior is predominantly influenced by the stacking order of the laminates and hardly at all by environmental conditions or by the test frequency. A classification of the stiffness response into three regions, as suggested in [8.5], revealed that the sharp decline of stiffness in Region III is found only in the $[\pm\alpha^\circ]_8$- laminates. Both the unidirectional and the multidirectional laminates did not exhibit this decline, i.e., the specimens failed without a preceding stiffness change. Fig. 8.12 and Fig. 8.13 show, typically, the response of a $[0^\circ/+45^\circ/-45^\circ/\overline{90}^\circ]_s$-laminate and a $[\pm45^\circ]_8$-laminate. Since a reduction of stiffness may be interpreted as damage accumulation or progression, several

$[\pm\alpha^\circ]_8$-specimens were cycled to a predetermined degree of reduction and then radiographically evaluated. Fig. 8.14 contains a representative selection of damage patterns in the $[\pm\alpha^\circ]_8$-laminates at several percentages of residual stiffness which, in the case of the $[\pm45^\circ]$-laminate, may fall off to 40%. Fig. 8.15 shows the progression of damage in the form of matrix cracks and edge delaminations in multidirectional laminates. Localized internal delaminations could not be detected in any of the test specimens. A comprehensive evaluation of the recognized damage patterns leads to the following conclusions.

8.4.1 Unidirectional Laminates

Cracks and edge delaminations could not be observed by radiographic or ultrasonic means in any of the on-axis and off-axis specimens. The fracture surfaces of on-axis specimens showed splitting and rupture of fiber bundles while the off-axis specimens failed smoothly in planes parallel to the fibers. The presence of temperature and/or moisture had no influence on the fracture modes.

8.4.2 Angle-Ply Laminates

In the $[\pm45^\circ]_8$-laminates only matrix cracks developed parallel to the fibers favoring one direction. The number of cracks increased with increasing load intensity. Intense accumulations of cracks locally preceded the tension failure of the specimens. Edge delaminations did not form in $[\pm45^\circ]_8$-laminates.

Consistent with Fig. 8.14, matrix cracks in $[\pm30^\circ]_8$-laminates emanated from the edges of the test specimens and proceeded in the fiber directions. Simultaneously, edge delaminations occurred between the outside and next-to-outside plies. Tension failure took place in locations where the matrix cracks had traversed over the entire width of the test specimens. The $[\pm15^\circ]_8$-laminates exhibited very similar damage patterns.

8.4.3 Multidirectional Laminates

In the $[0_2°/+45°/0_2°/-45°/0°/90°]_s$-laminates matrix cracks in the 90°-plies developed quite early and extended partially over the entire width of the test specimens. Parallel to the development of a characteristic state of crack damage, the first localized edge delaminations occurred. Under increasing load cycles, they converged and formed solid edge delaminations of rather uniform width. In some cases the edge delaminations eventually merged, splitting the test specimens into two halves.

The $[0°/+45°/-45°/90°]_s$-laminates behaved similarly except that here matrix cracks developed quite early also in the 45°-directions as noticeable in Fig. 8.15. The matrix cracks again extended over the width of the specimen but the boundaries of the edge delaminations were less uniform.

The investigation of temperature and moisture effects is still incomplete. At this point it can only be stated that at elevated temperature as well as in the moist condition the matrix-cracks are less long and sometimes limited to the areas of the edge delaminations. Fig. 8.16 contains a representative selection of typical damage patterns.

8.5 References

[8.1] Reifsnider, K.L. (Editor) — Damage in Composite Materials. STP 775, American Society for ...ing and Materials, 1982.

[8.2] Gerharz, J.J., Schütz, D. — Schrifttumsrecherche zum Festigkeitsverhalten von Faserverbundwerkstoffen. - Analyse des Standes der Technik - LBF-Report Nr. TB-145 (1979).

[8.3] Talreja, R. — Fatigue of composite materials: damage mechanisms and fatigue-life diagrams. Proc.R.Soc.Lond. 1981 A 378, pp. 461-475.

[8.4] Reifsnider, K.L., Jamison, R. — Fracture of fatigue-loaded composite laminates. Int.J.Fatigue 4 (1982), pp. 187-197.

[8.5] Highsmith, A.L., Reifsnider, K.L. — Stiffness Reduction Mechanisms in Composite Laminates. ASTM, STP 775 (1982), pp. 103-117.

Stacking sequence	Plies	Number of specimens
Unidirectional:		
On-axis 0°	8	85
Off-axis 5°	8	30
Off-axis 15°	8	70
Off-axis 45°	8	20
Multidirectional:		
$[0_2°/+45°/0_2°/-45°/0°/90°]_s$	16	105
$[0°/+45°/-45°/\overline{90}°]_s$	7	90
Angle-ply:		
$[\pm 15°]_8$	8	70
$[\pm 30°]_8$	8	65
$[\pm 45°]_8$	8	70

Table 8.1 Types and numbers of tested specimens

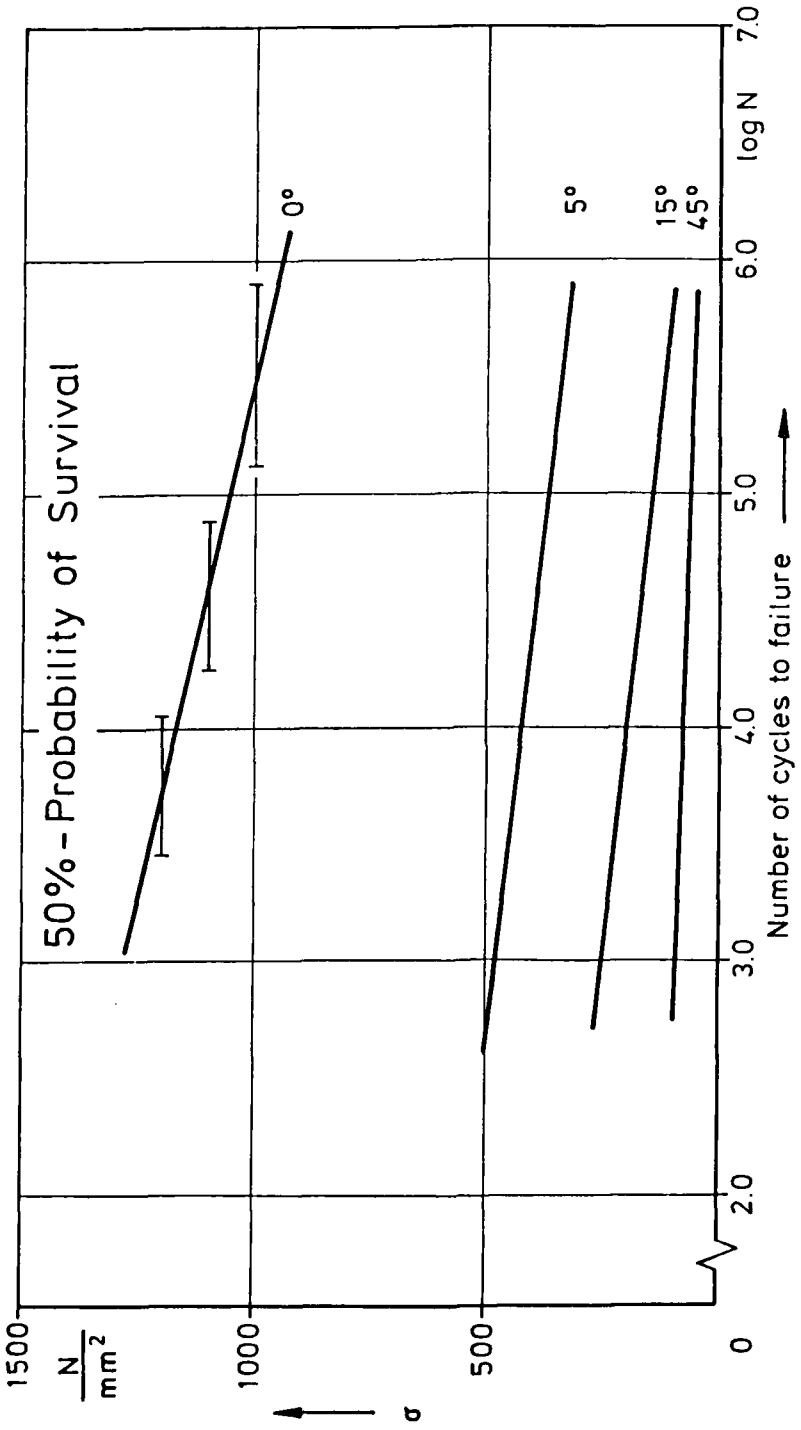

Fig. 8.1 Influence of fiber orientation on fatigue strength of unidirectional laminates

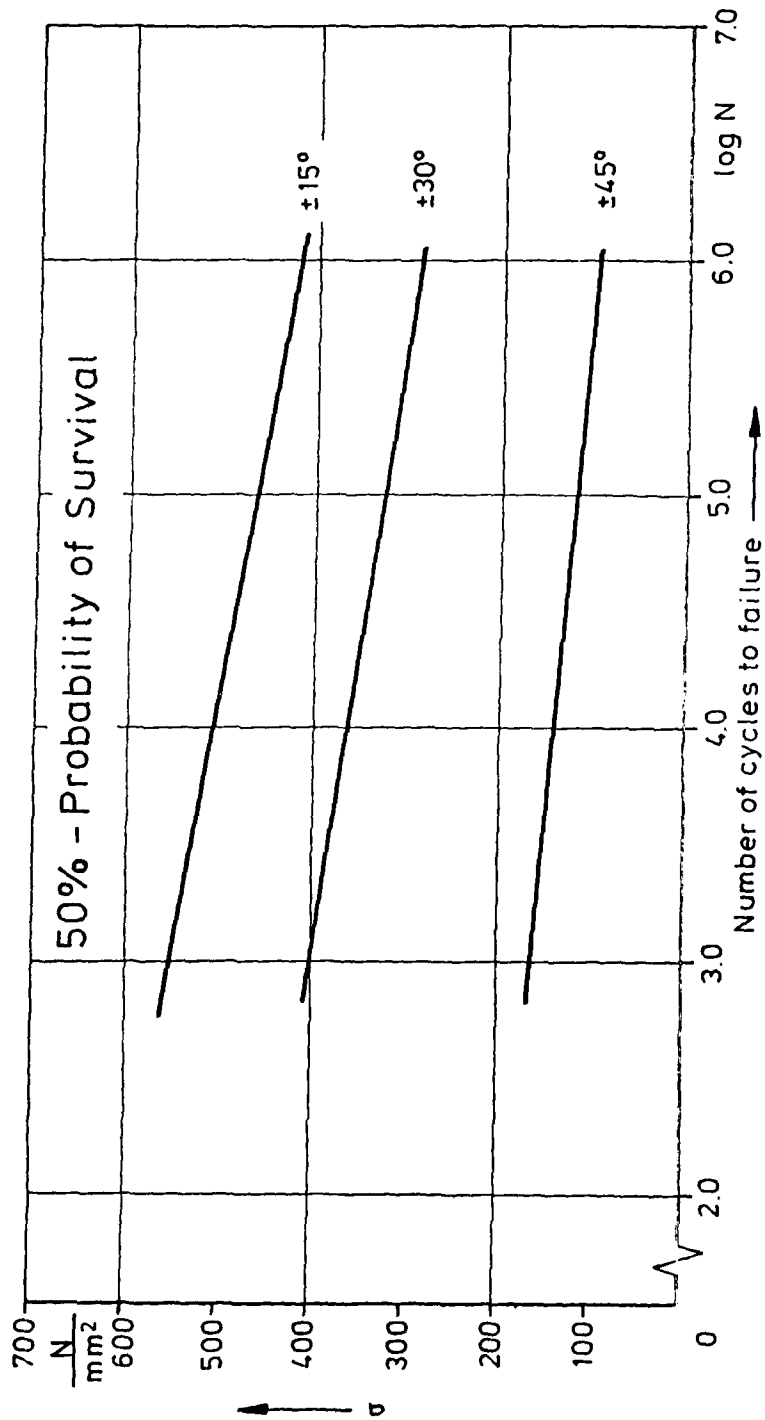

Fig. 8.2 Influence of fiber orientation on fatigue strength of angle-ply laminates

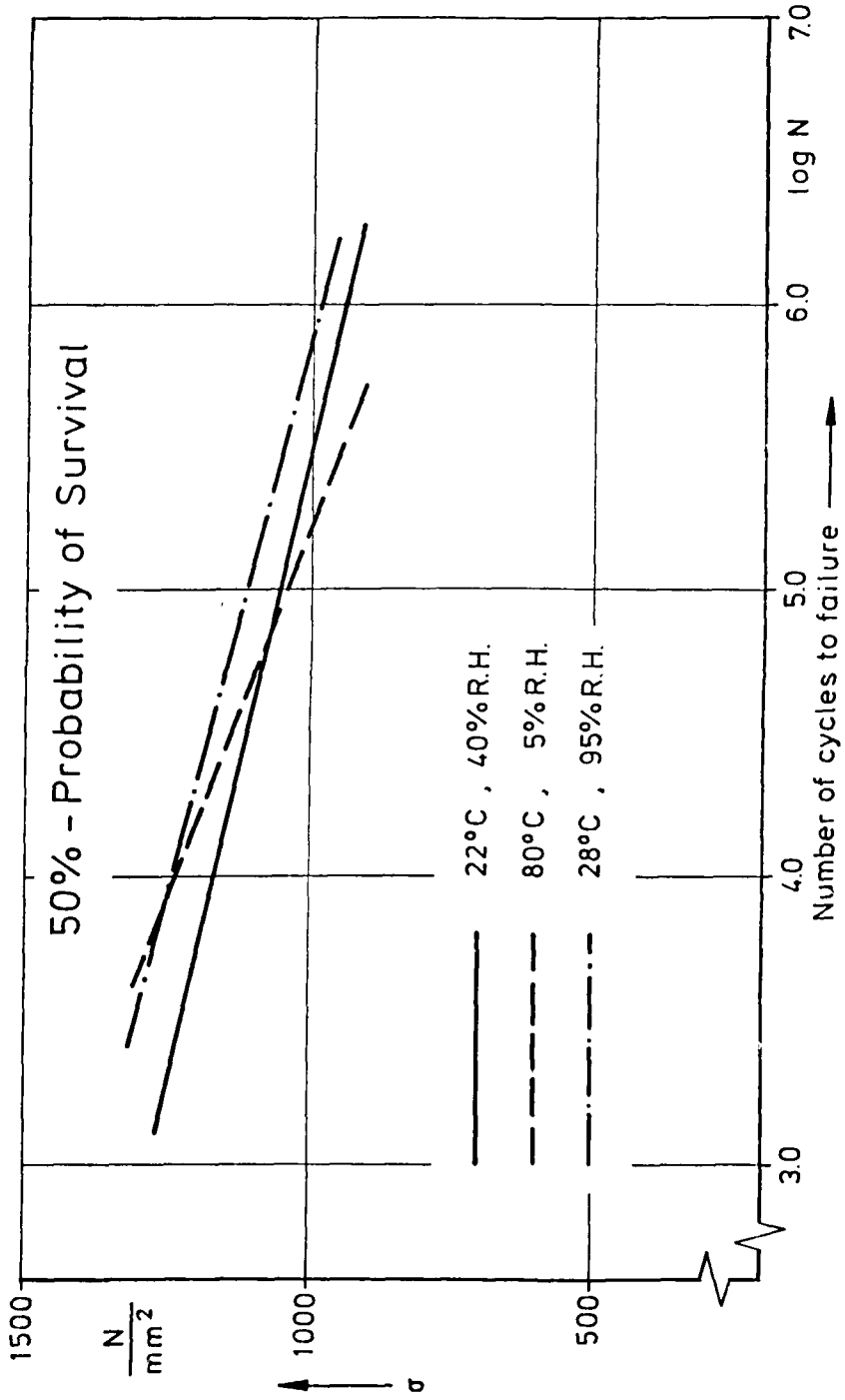

Fig. 8.3 Influence of temperature and moisture on fatigue strength of unidirectional 0°-laminates

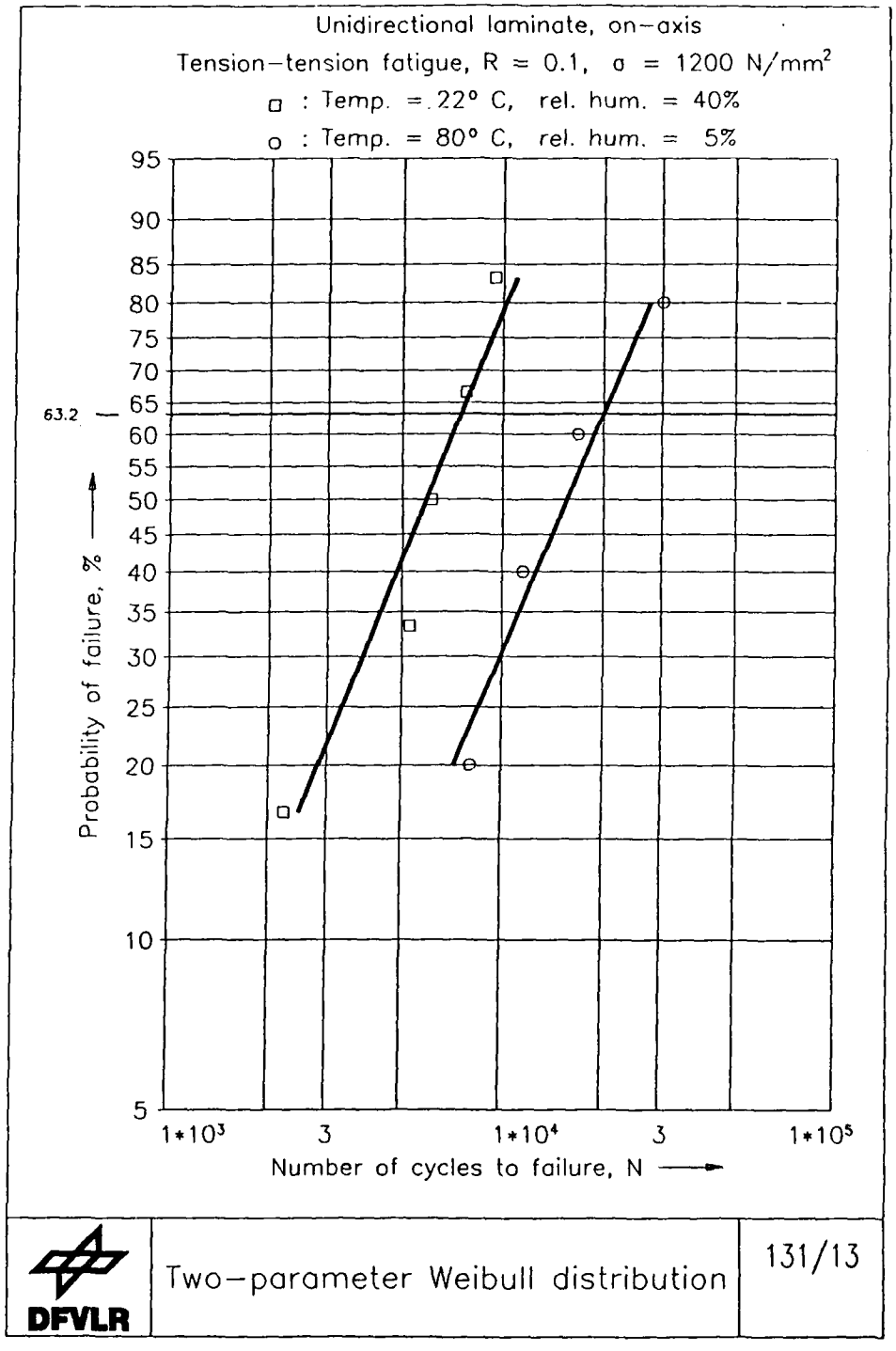

Fig. 8.4 Weibull-distributions of unidirectional 0°-laminates, $\sigma = 1200\ N/mm^2$

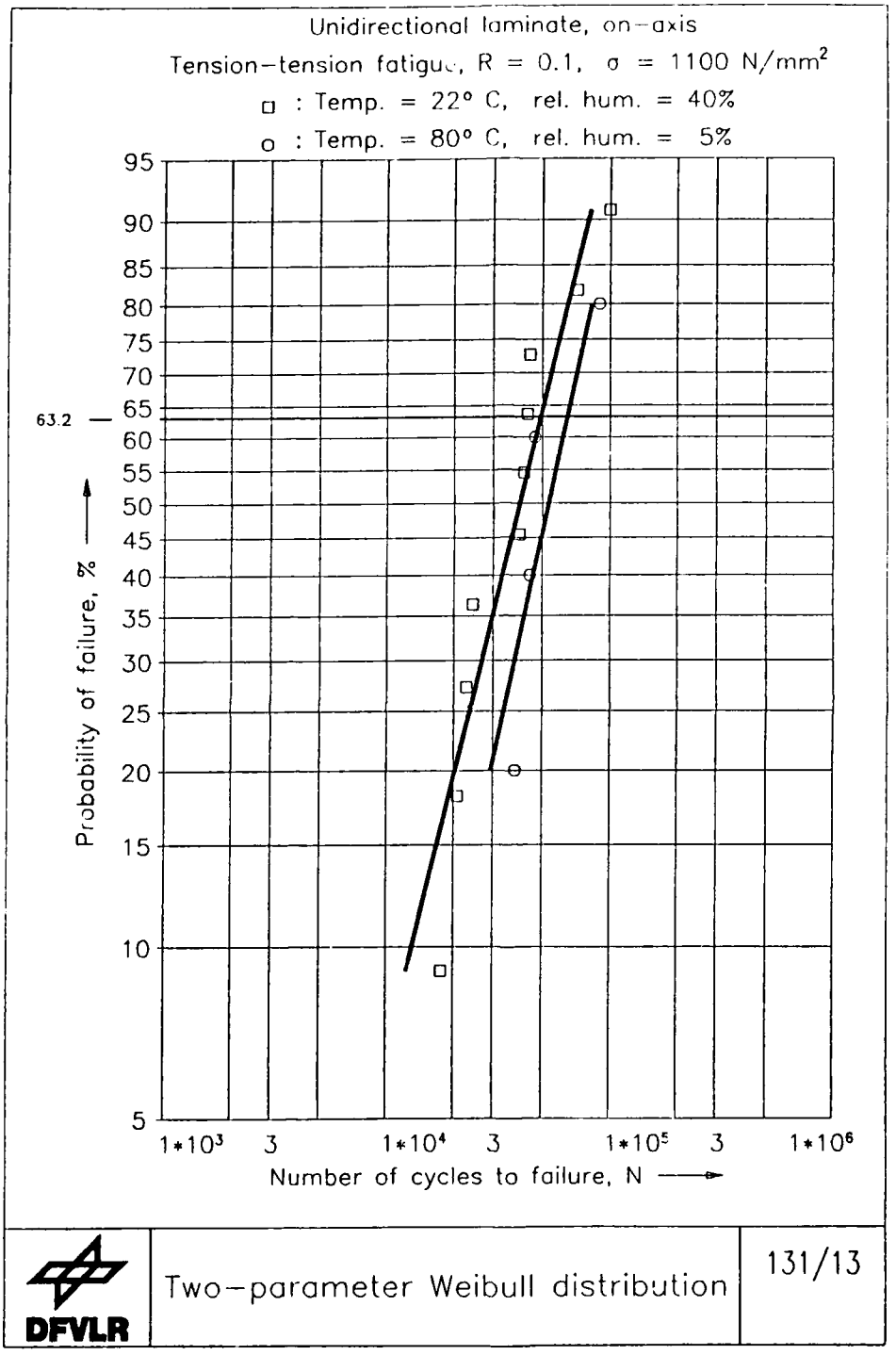

Fig. 8.5 Weibull-distributions of unidirectional 0°-laminates, σ = 1100 N/mm²

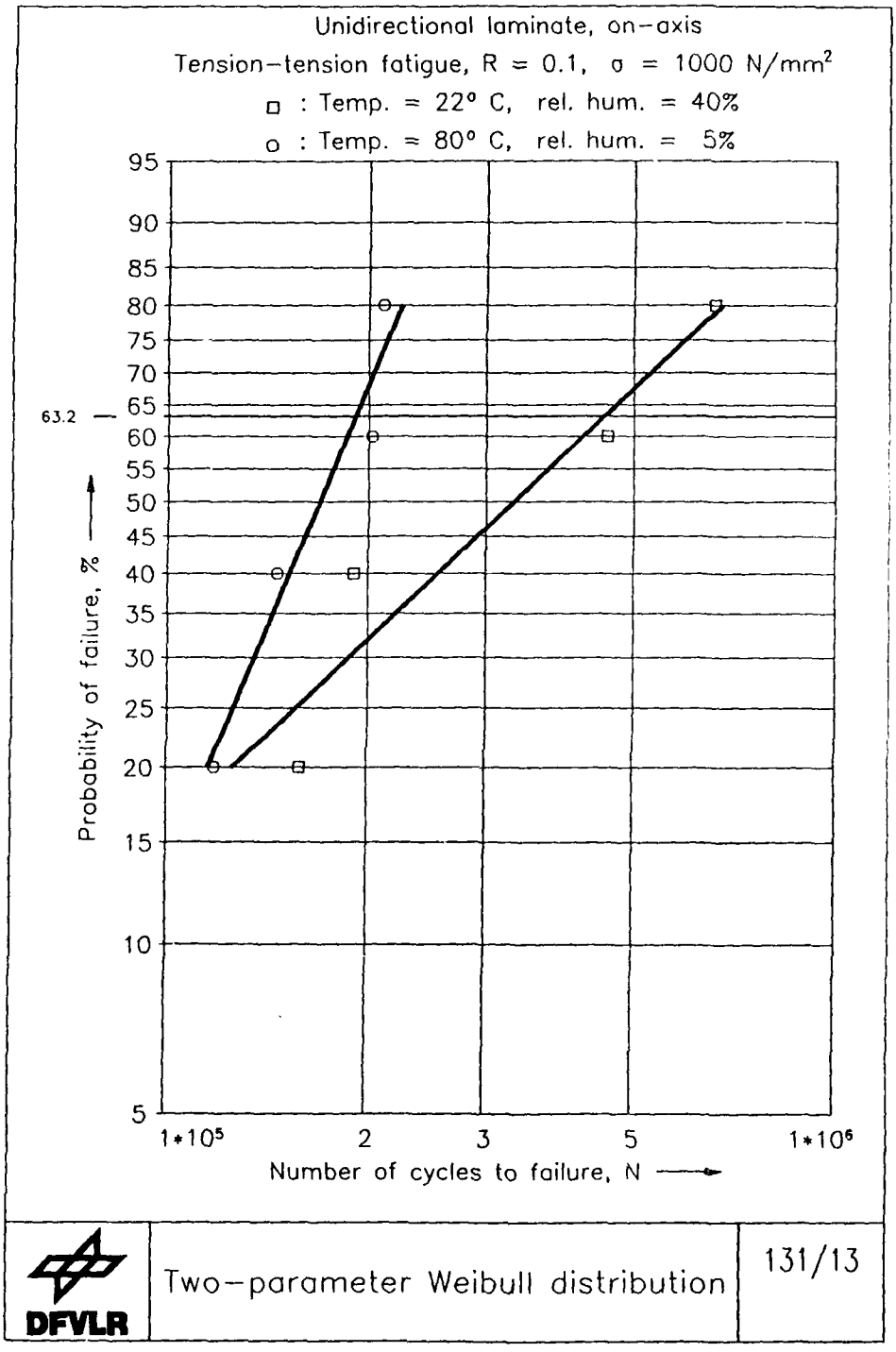

Fig. 8.6 Weibull-distributions of unidirectional 0°-laminates, σ = 1000 N/mm²

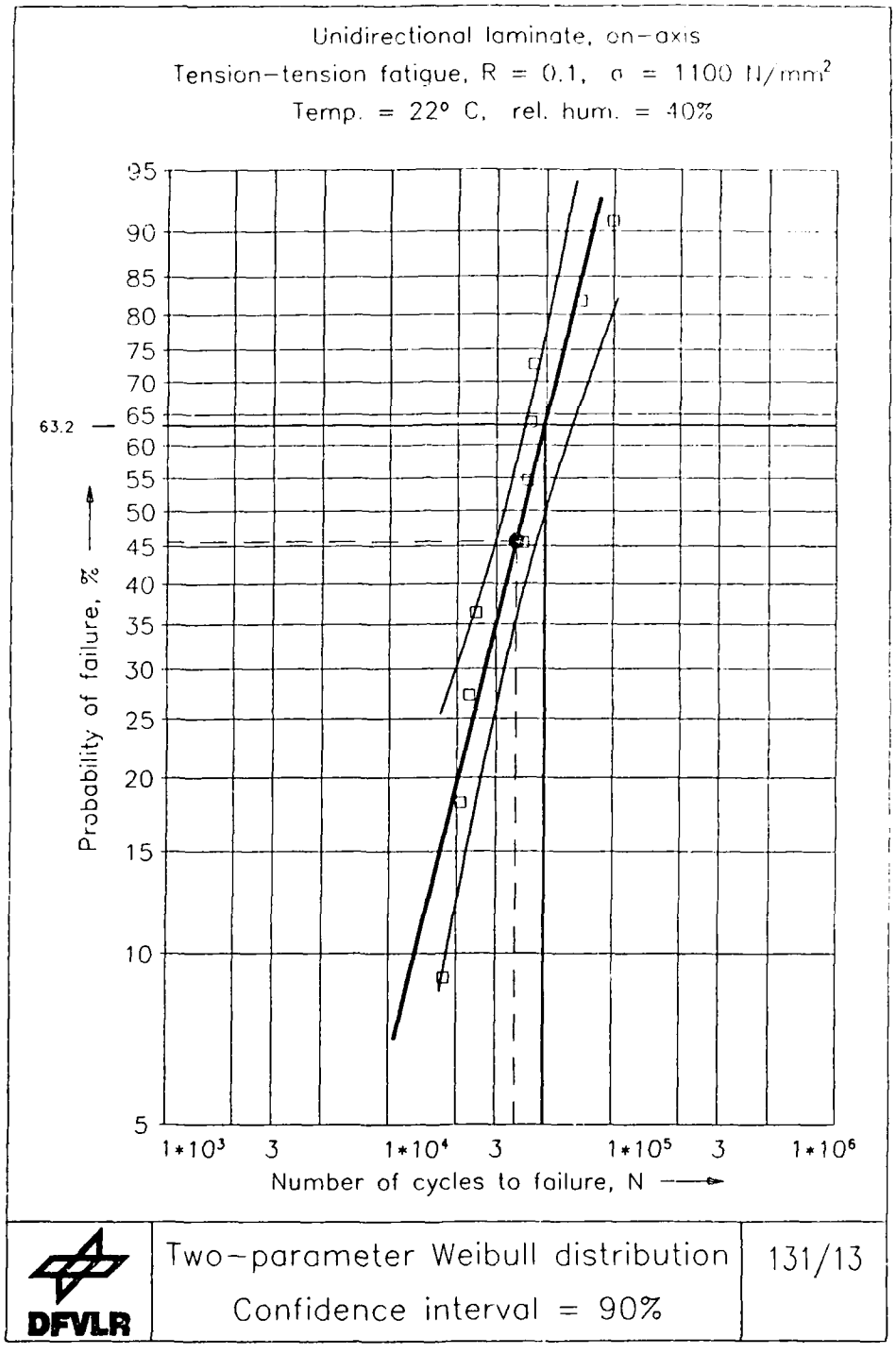

Fig. 8.7 Weibull-distribution with 90% confidence limits

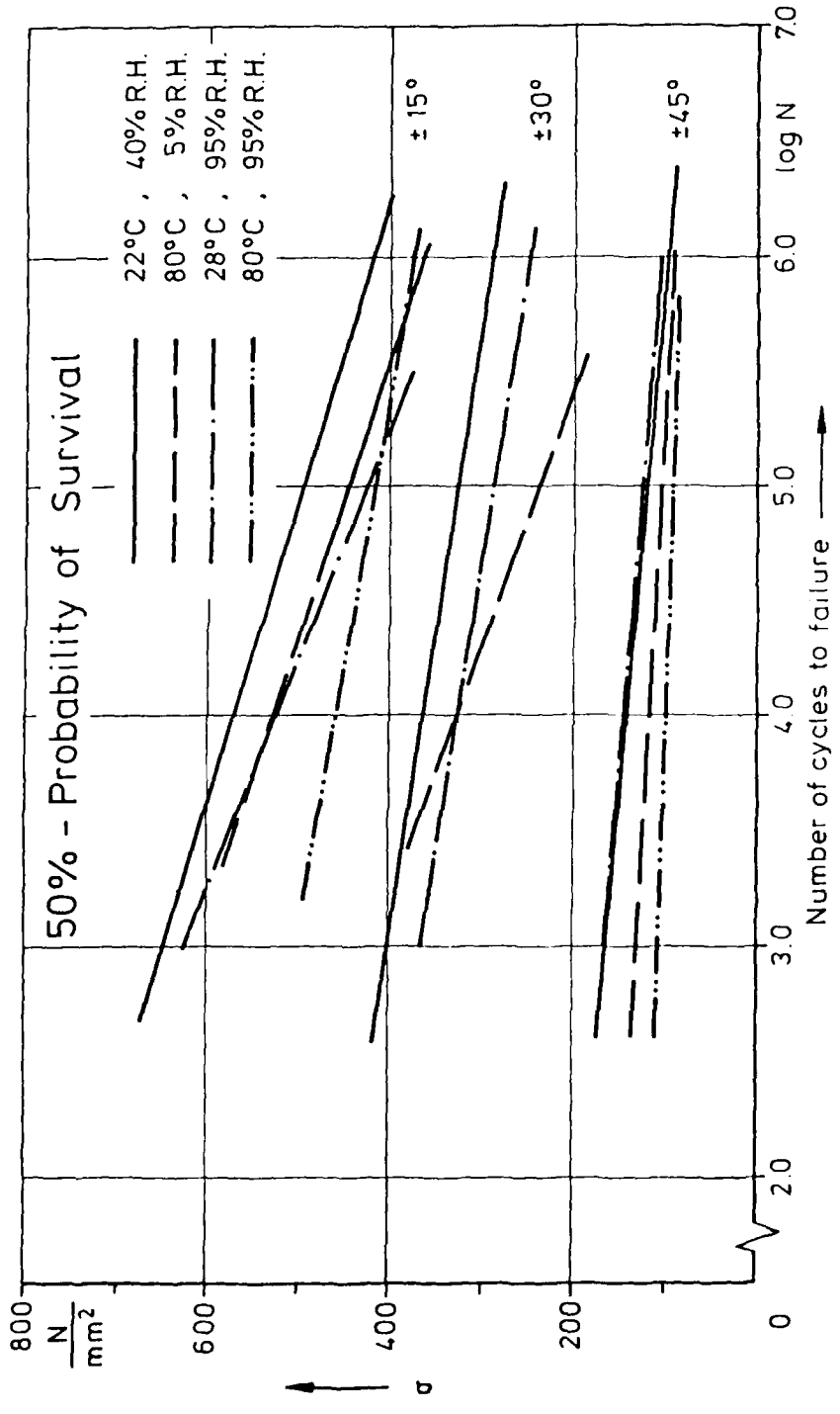

Fig. 8.8 Influence of temperature and moisture on fatigue strength of angle-ply laminates

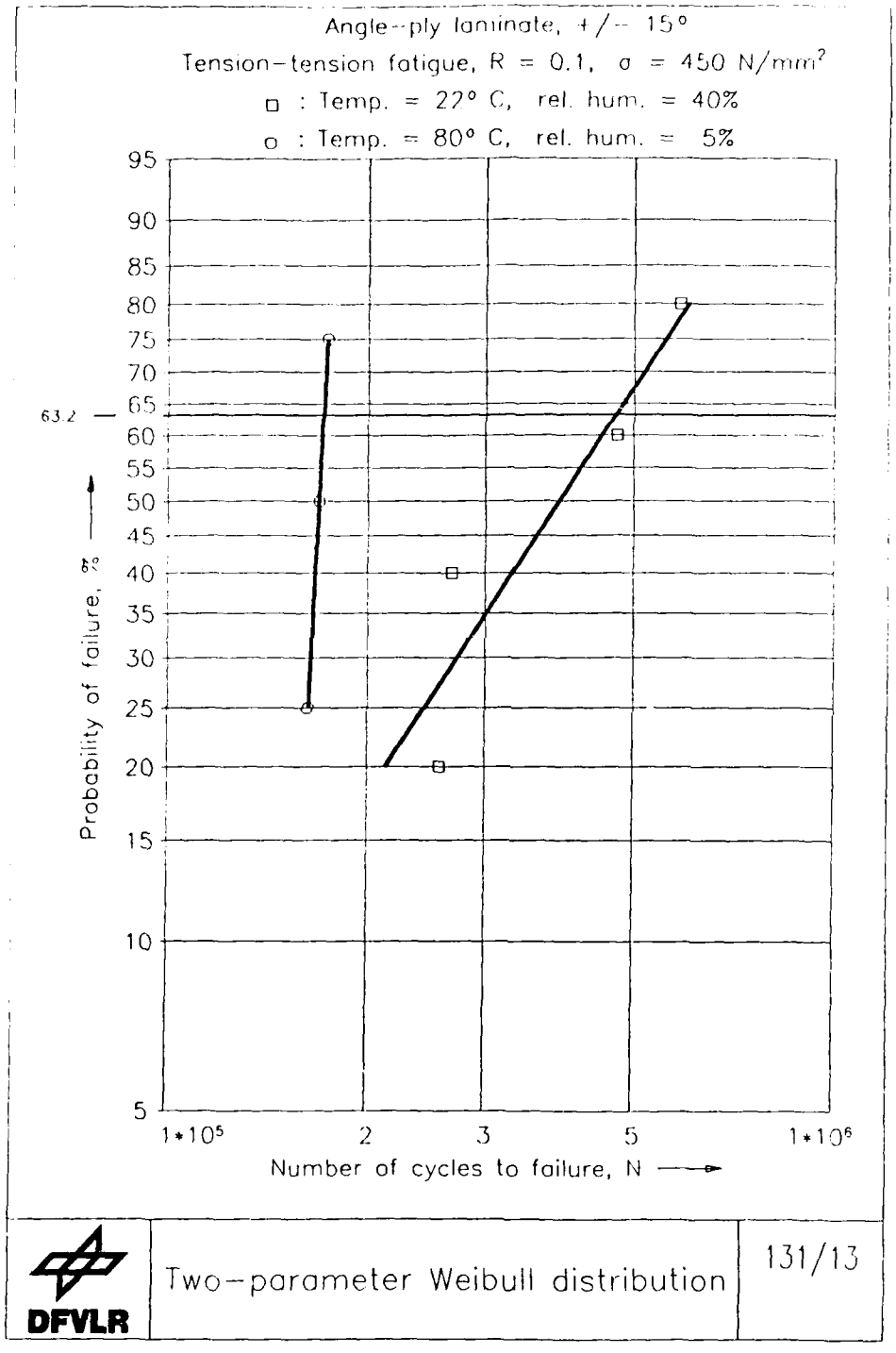

Fig. 8.9 Weibull-distributions of ±15° angle-ply laminates, σ = 450 N/mm²

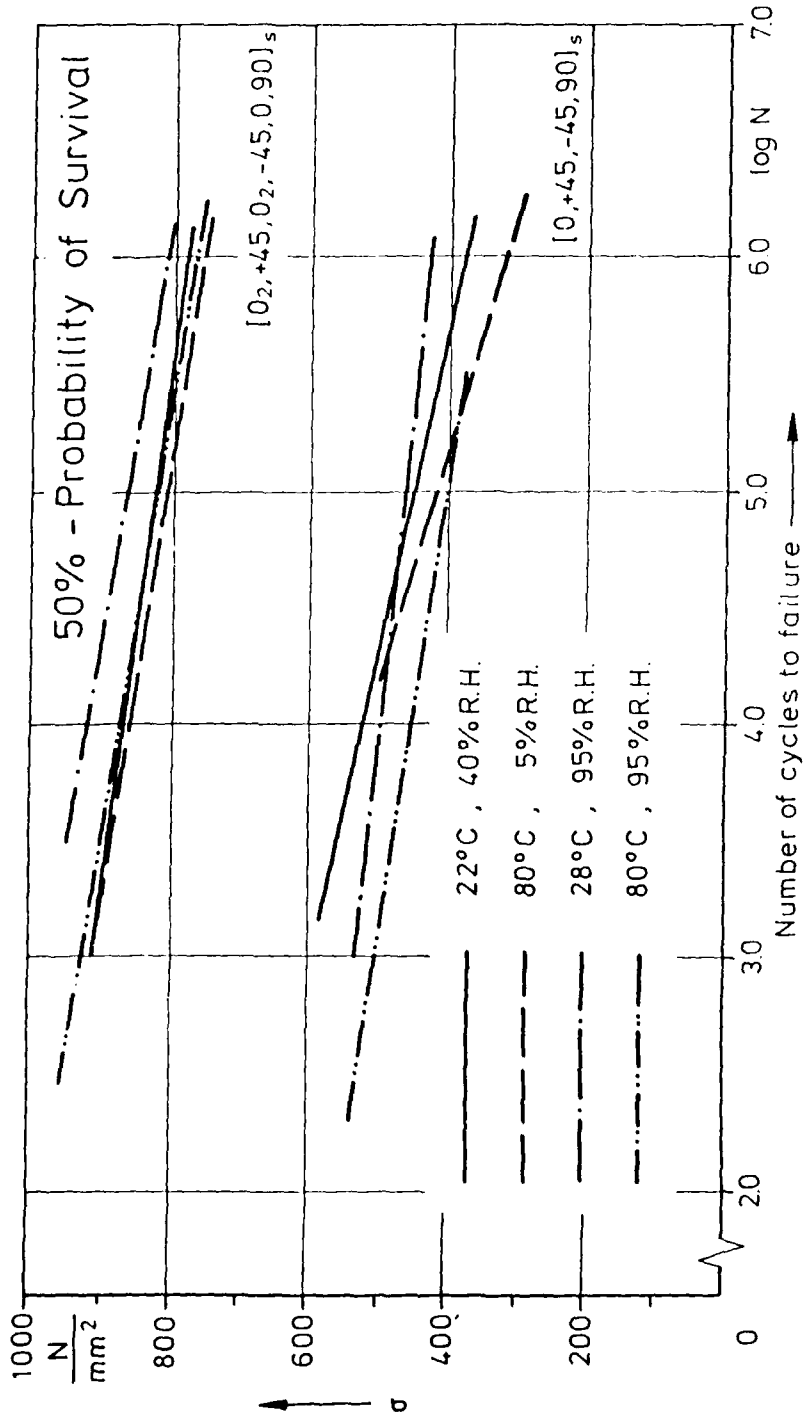

Fig. 8.10 Influence of temperature and moisture on fatigue strength of multidirectional laminates

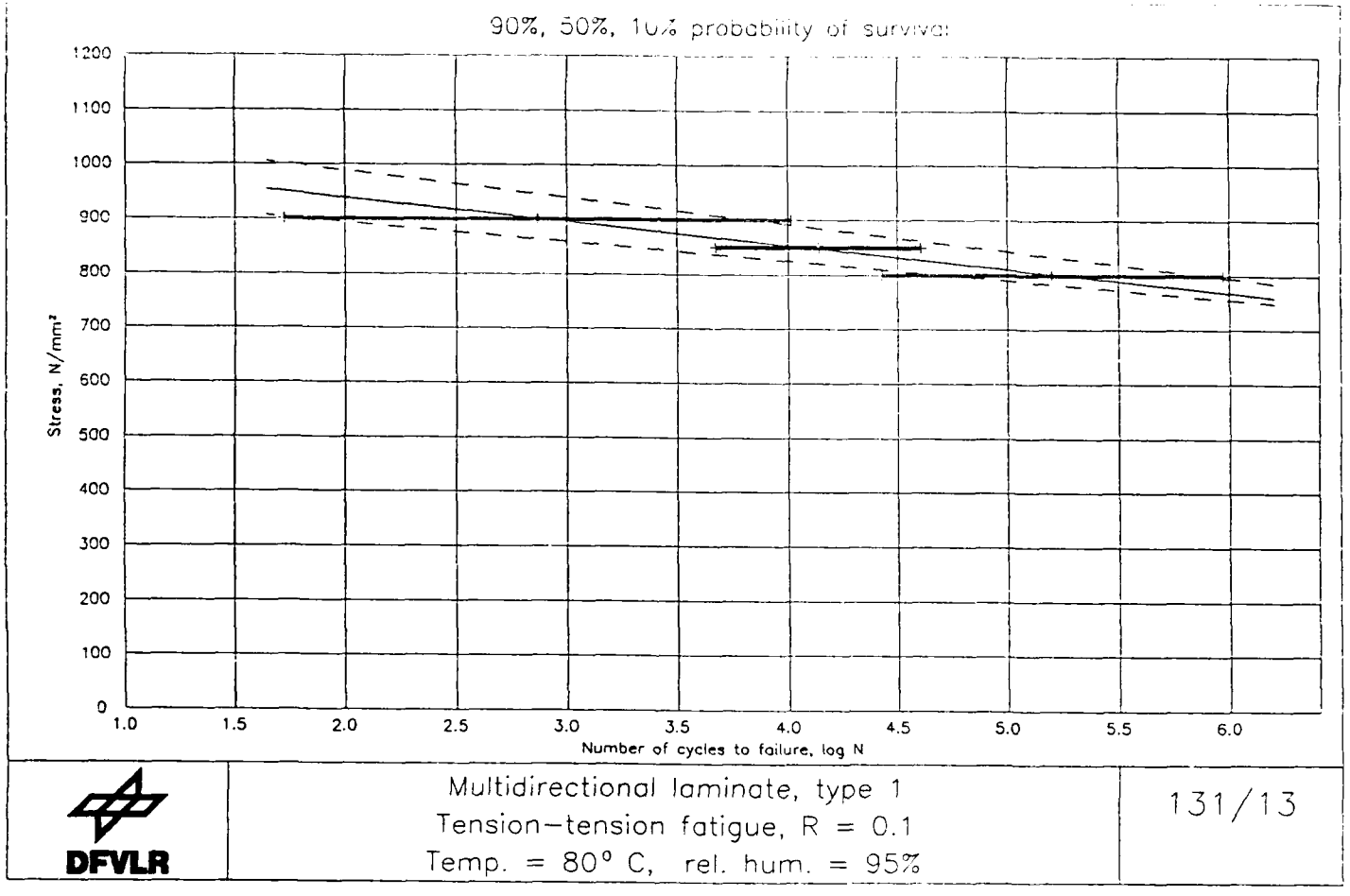

Fig. 8.11 σ-log N-line of $[0_2°/+45°/0_2°/-45°/0°/90°]_s$ multidirectional laminates under 80° C and 95% R.H.

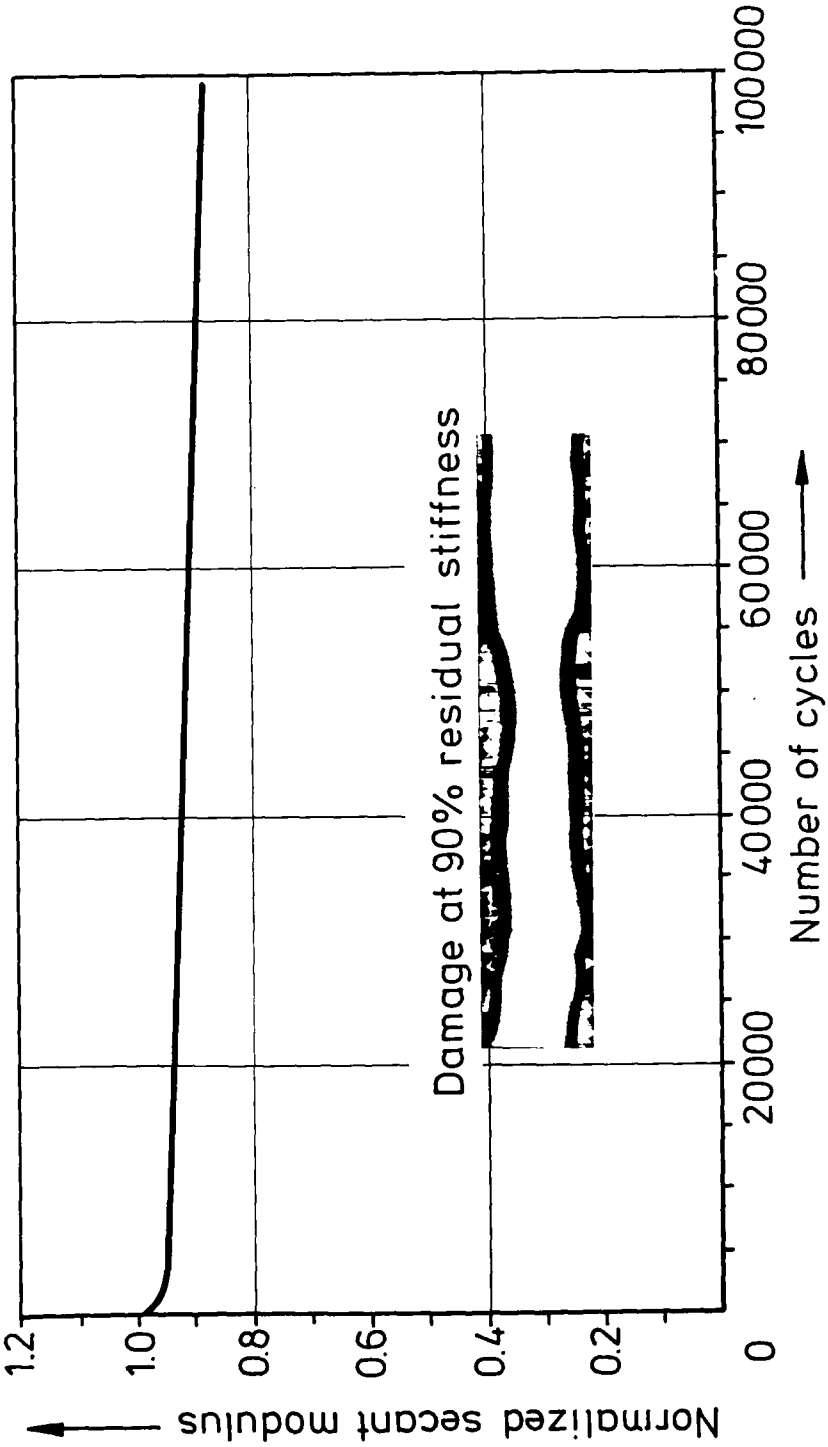

Fig. 8.12 Stiffness reduction and corresponding damage of a multidirectional laminate $[0°/+45°/-45°/\bar{9}0°]_s$

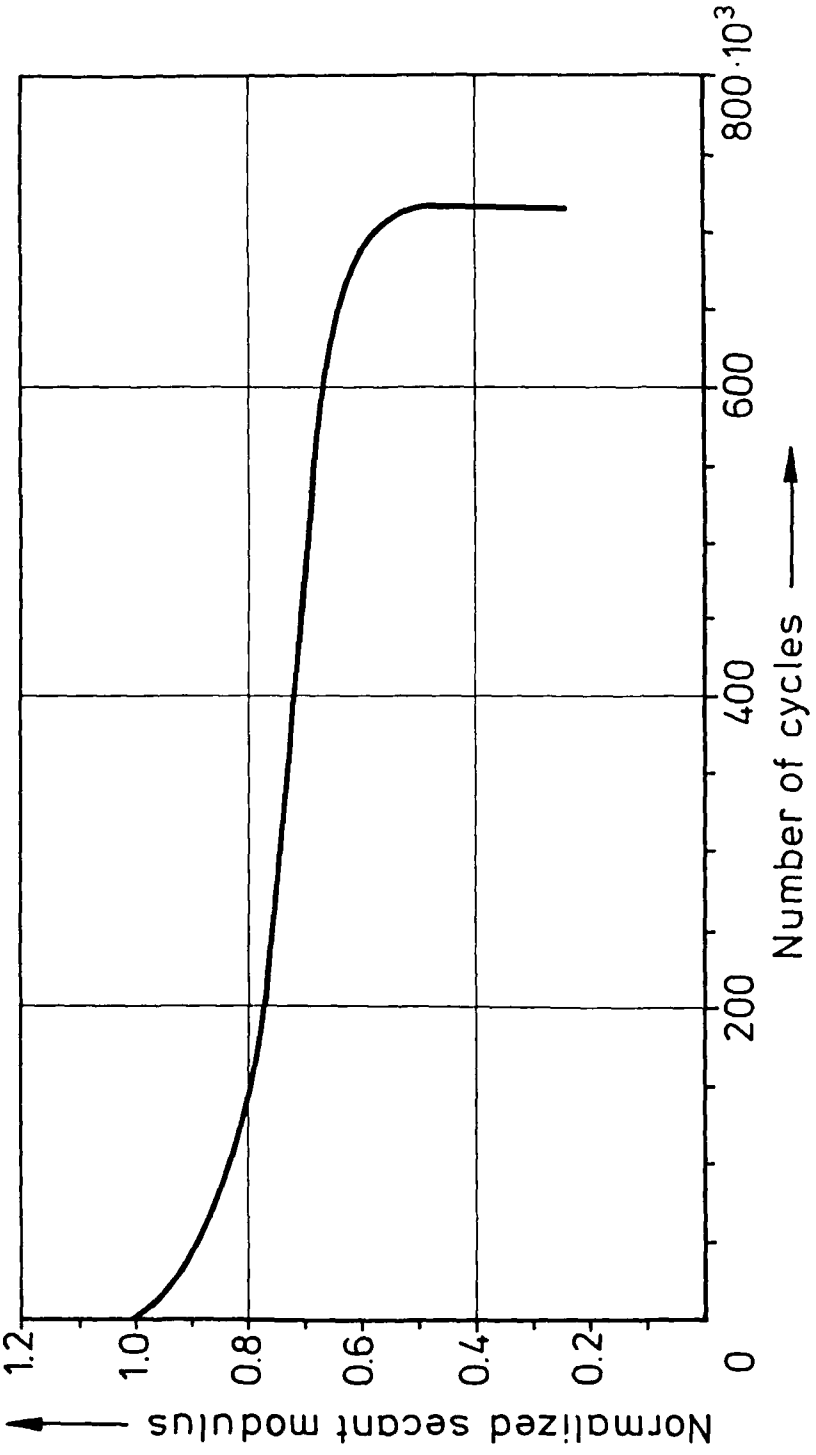

Fig. 8.13 Stiffness reduction of an angle-ply laminate (±45°)

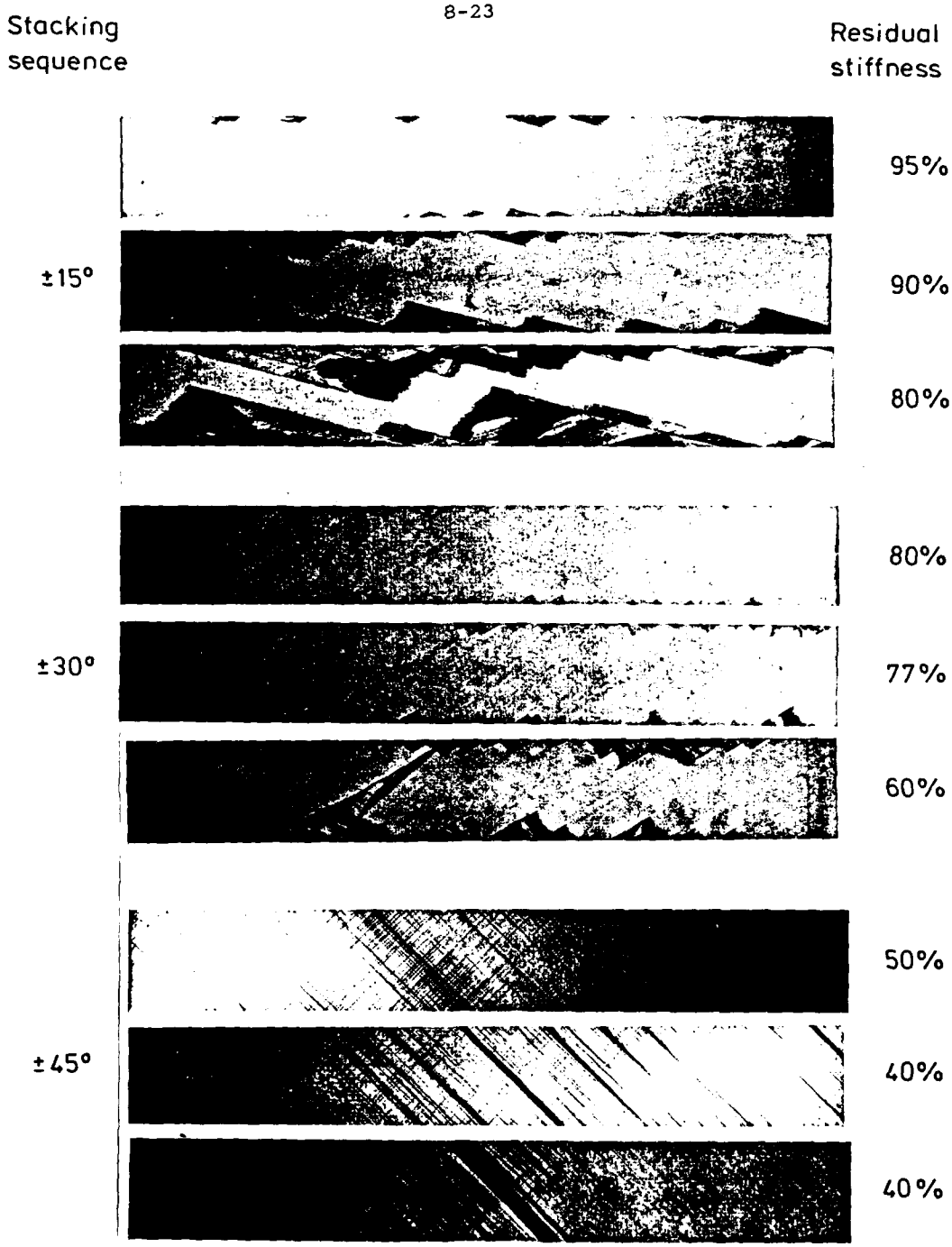

Fig. 8.14 Damage pattern development in angle-ply laminates

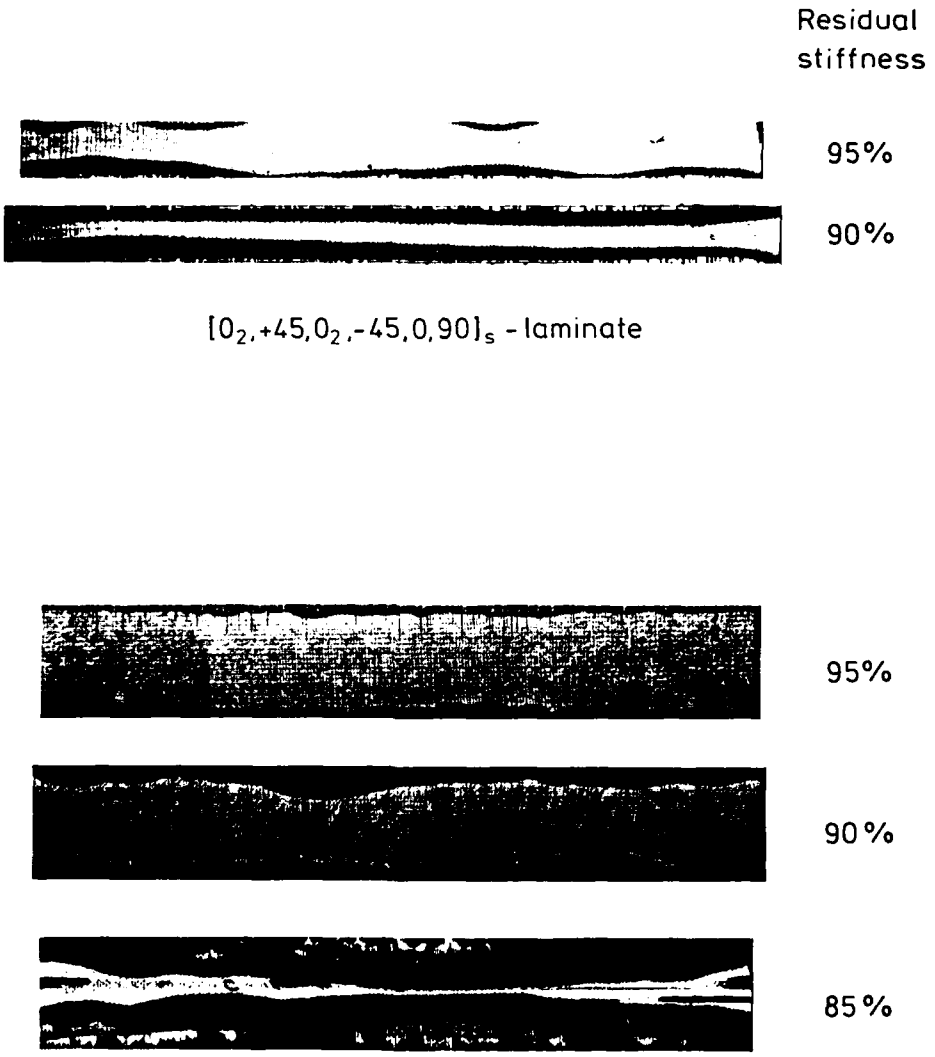

Fig. 8.15 Damage pattern development in multidirectional laminates

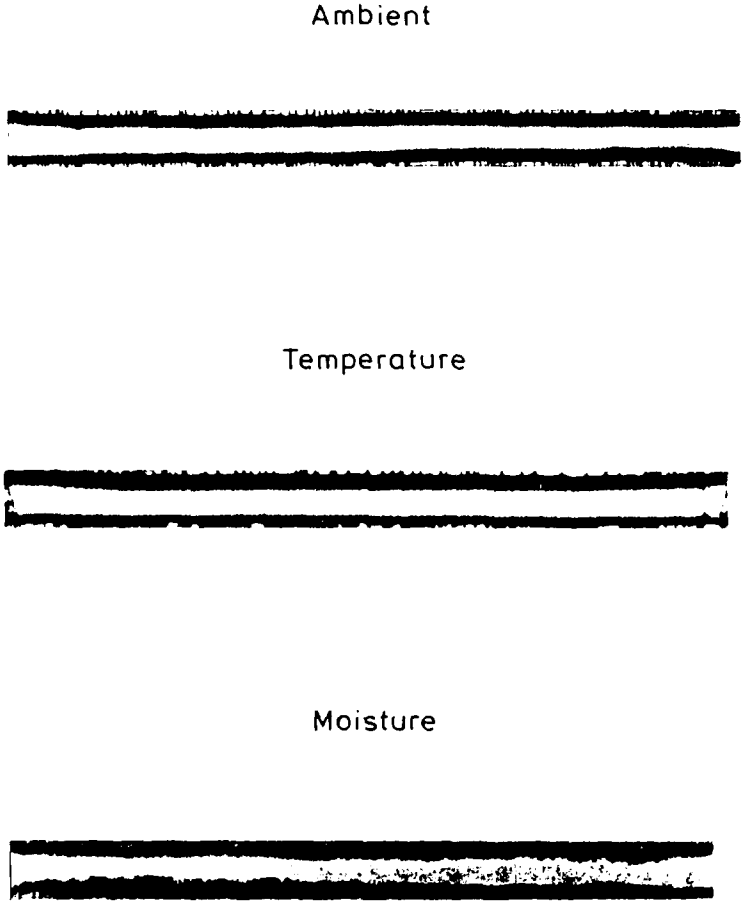

Fig. 8.16 Influence of temperature and moisture on damage patterns of multidirectional laminates

END

DATE
FILMED

6 -86

DTIC